

FROM MULTIDIRECTIONAL-VECTOR-BASED SEISMIC REVERSE TIME MIGRATION
AND ANGLE-DOMAIN COMMON-IMAGE GATHERS TO FULL WAVEFORM
INVERSION USING PHASE-MODIFIED AND DECONVOLVED IMAGES
IN ACOUSTIC AND ELASTIC MEDIA

by

Chen Tang



APPROVED BY SUPERVISORY COMMITTEE:

George A. McMechan, Chair

John F. Ferguson

John W. Geissman

Susan E. Minkoff

Copyright © 2018

Chen Tang

All Rights Reserved

Dedicated to my family and teachers

FROM MULTIDIRECTIONAL-VECTOR-BASED SEISMIC REVERSE TIME MIGRATION
AND ANGLE-DOMAIN COMMON-IMAGE GATHERS TO FULL WAVEFORM
INVERSION USING PHASE-MODIFIED AND DECONVOLVED IMAGES
IN ACOUSTIC AND ELASTIC MEDIA

by

CHEN TANG, BS, MS

DISSERTATION

Presented to the Faculty of
The University of Texas at Dallas
in Partial Fulfillment
of the Requirements
for the Degree of

DOCTOR OF PHILOSOPHY IN
GEOSCIENCES

THE UNIVERSITY OF TEXAS AT DALLAS

May 2018

ACKNOWLEDGMENTS

When I was young, I often dreamed that I would become a scientist when I grew up. Now I am finally finishing my Ph.D. dissertation, although the path has been long and full of thorns. First, I would like to express my sincere gratitude to my supervisor, Professor George A. McMechan. George not only provides guidance and advice to me on my research, but also, he has shared his life philosophy and his elegant character with me. George shows understanding to me when I hold a different academic opinion from him. He uses encouragement and patience in his supervision. This education mode greatly inspires my innovative thinking and critical thinking, which has led me to propose novel academic opinions in several research areas. This mode not only benefits me a lot in research, but also has a great influence on my life. It makes me have more confidence and patience when dealing with tasks, more understanding and tolerance when getting along with other people, and has given me a wider vision when thinking about my career.

I also appreciate the time and help from other members of my doctoral committee, Professor John F. Ferguson, Professor John W. Geissman and Professor Susan E. Minkoff. They provided valuable suggestions during my qualifying exam and annual committee-member meetings. I also would like to thank the two new professors, Professor Hejun Zhu and Professor David Lumley, for their help during my Ph.D. period.

I am sincerely grateful for the help from Dr. Yu Zhang (now at ConocoPhillips). I have known Yu for more than seven years. During this period, he provided a lot of valuable suggestions and encouragement to me. I respect him as a pioneer of science, a mentor of career and life, and a friend with loyalty.

I also would like to thank Professor Huazhong Wang from Tongji University, Professor Deli Wang, Professor Ligu Han, and Professor Danian Huang from Jilin University. They provided valuable help during my master's degree. In 2017, Danian passed away at 58 years, but he always lives in my heart.

I also thank the following of my fellow students in our geophysics section during my stay at Dallas; Xiao Liang, Haonan Zhu, Jun Li, Bao D. Nguyen, Yulang Wu, Jidong Yang, Xueyan Li, Shuo Zhang, Linghao Chen and Chen Sun for their help during my Ph.D. period. I am also grateful to my friend Hao Jiang for his concern and encouragement during my Ph.D. period. Hao graduated from the same university as me and now is a student in Geophysics at Mines Paris Tech. We have been good friends for many years.

Finally, and the most important, I am very, very grateful to the love from my parents. I know they sacrificed a lot for me. Without their love, I would not be here. I also thank the care from my family members, especially my grandfather, who taught me a lot since I was a young child.

March 2018

FROM MULTIDIRECTIONAL-VECTOR-BASED SEISMIC REVERSE TIME MIGRATION
AND ANGLE-DOMAIN COMMON-IMAGE GATHERS TO FULL WAVEFORM
INVERSION USING PHASE-MODIFIED AND DECONVOLVED IMAGES
IN ACOUSTIC AND ELASTIC MEDIA

Chen Tang, PhD
The University of Texas at Dallas, 2018

Supervising Professor: George A. McMechan

Angle-domain common-image gathers (ADCIGs) are an important product from reverse time migration (RTM). Using the Poynting vector (PV) to calculate propagation angles is efficient but suffers from instability problems. First, the PV can give only a single direction per grid point per time step, and thus it fails to give the multiple directions at wavefield overlaps. Second, the current PV formula is only kinematically correct, which leads to an undefined propagation angle at the magnitude peak of the wavefield. Third, the receiver wavefield reconstructed from the observed data is often not as stable as the source wavefield simulated from the synthetic source. We address the first two issues by proposing a dynamically-correct multidirectional PV (MPV) that decomposes the wavefield into several vector bins in the frequency-wavenumber (ω - \mathbf{k}) domain and then uses PV to calculate the propagation directions of each decomposed wavefield

in the time-space (t - \mathbf{x}) domain. We also provide an improved flow to calculate the ADCIGs by using the source wavefield propagation direction and the reflector normal in the \mathbf{k} domain.

We propose an improved system for the elastic RTM, which involves three parts. For the P/S wave mode separation, we put forward a scheme to relax the assumption of the (locally) constant shear modulus caused by the Helmholtz theorem. We also give the elastic imaging conditions based on multidirectional vectors, which can give the correct polarities for PP, PS, SP, and SS images without using the reflector normal. For the ADCIG calculation, we give two methods to calculate the multiple propagation directions.

For full waveform inversion (FWI), we propose a new scheme that provides a self-contained and physically-intuitive derivation which establishes a natural connection between the amplitude-preserved RTM, the Zoeppritz equations (the amplitude versus [reflection] angle [AVA] inversion) and the reflectivity-to-impedance inversion and combines them into a single framework to produce a preconditioned inversion formula. The formula also works for inverting only the velocity. For impedance inversion, we propose using rock-physics information to separate the impedance into velocity and density for wavefield extrapolation. Because of the complexity of the rock-physics relationship in the real world, we also suggest combining Machine Learning with this scheme for future development.

TABLE OF CONTENTS

ACKNOWLEDGMENTS	v
ABSTRACT.....	vii
LIST OF FIGURES	xiv
LIST OF TABLES	xxi
CHAPTER 1 INTRODUCTION	1
1.1 Motivation and objectives.....	1
1.2 Overview.....	2
1.3 Publication status	4
1.4 Declaration.....	5
CHAPTER 2 COMBINING MULTIDIRECTIONAL SOURCE VECTOR WITH ANTI- TRUNCATION-ARTIFACT FOURIER TRANSFORM TO CALCULATE ANGLE GATHERS FROM REVERSE TIME MIGRATION IN TWO STEPS.....	7
2.1 Summary.....	7
2.2 Introduction.....	8
2.3 Theory.....	14
2.3.1 Using multidirectional PVs to calculate SACIGs	14
2.3.2 Calculating ADCIGs from SACIGs.....	24
2.3.3 Anti-leakage Fourier transform (ALFT) in local windows.....	25
2.3.4 Anti-truncation-artifact Fourier transform (ATFT) in global space.....	33
2.4 Examples.....	37
2.5 Discussion.....	45
2.6 Conclusions.....	46
2.7 Acknowledgments.....	47
2.8 Appendix 2A “Amplitude-preserving taper functions between angle bins”	47
2.9 Appendix 2B “Angle-filter design for removal of backscattering artifacts”	48
2.10 Appendix 2C “SACIG and ADCIG for a simple model”	50
2.11 Appendix 2D “A general flow of the ALFT”	51
2.12 Appendix 2E “Analysis of the amplitude in the T -window”	53

2.13	Appendix 2F “Analysis of the ATFT algorithm”	56
2.14	Appendix 2G “Discussion of computational cost of the proposed data flow”	57
2.15	Appendix 2H “Imaging condition for ADCIGs obtained using source- and receiver-side MPVs”	59
CHAPTER 3 DYNAMICALLY-CORRECT MULTIDIRECTIONAL POYNTING VECTOR WITH APPLICATION IN CALCULATING ADCIGS FROM RTM		60
3.1	Summary	60
3.2	Introduction.....	62
3.3	Derivation of the multidirectional SV.....	65
3.4	Derivation of the dynamically-correct multidirectional PV	69
3.5	Implementation	73
3.5.1	Conjugate relationship and complex-valued wavefield extrapolation for accelerating the approximate WD.....	73
3.5.2	Decreasing the cost of the dynamically-correct MPV	76
3.6	Examples.....	78
3.7	Conclusions.....	85
3.8	Acknowledgments.....	85
3.9	Appendix 3A “Difference between the original and dynamically-correct PVs and the relationship between the dynamically-correct PV and the Eikonal equation”	86
3.10	Appendix 3B “From elastic PV to acoustic PV”	88
3.11	Appendix 3C “Data flows to calculate ADCIGs from RTM in acoustic media” ..	92
CHAPTER 4 MULTIDIRECTIONAL-VECTOR-BASED ELASTIC REVERSE TIME MIGRATION AND ANGLE-DOMAIN COMMON-IMAGE GATHERS WITH APPROXIMATE WAVEFIELD DECOMPOSITION OF P AND S WAVES.....		95
4.1	Summary	95
4.2	Introduction.....	96
4.2.1	Separation of an elastic wave into P and S modes	97
4.2.2	Imaging conditions of the elastic RTM.....	98
4.2.3	Calculation of ADCIGs from E-RTM.....	99
4.2.4	The improvements in this chapter	101
4.3	Improved system of P/S wave mode separation	101
4.3.1	The first-order hyperbolic system of elastodynamic equations	102

4.3.2	Implicit assumption in the traditional system of P and S decoupled equations	103
4.3.3	Improved decoupling system with a consideration of the conversion between P and S waves at the current separation time	111
4.4	Multidirectional-vector-based imaging condition.....	114
4.4.1	Improved vector-based imaging conditions	115
4.4.2	Two methods to calculate the multidirectional propagation vectors.....	118
4.4.3	Multidirectional-vector-based imaging conditions for E-RTM and ADCIGs	122
4.5	Examples.....	125
4.5.1	Calculating the polarization and propagation vectors for wavefield overlaps	126
4.5.2	PP and PS images for two simple models with a flat reflector interface .	127
4.5.3	Applying the proposed flow to a complicated portion of the Marmousi2 model	132
4.6	Discussion and future developments	140
4.6.1	Extension of the P/S wave mode separation into 3D	141
4.6.2	Extension of the multidirectional propagation vector into 3D.....	143
4.6.3	Discussion on the amplitude-preserved imaging conditions.....	145
4.6.4	Combining multidirectional source vector with the reflection-image normal to calculate RTM ADCIGs	151
4.7	Conclusions.....	151
4.8	Acknowledgments.....	152
4.9	Appendix 4A “The transformation of equation 4.6 to equation 4.7”	152
4.10	Appendix 4B “An alternative approach to achieve equations 4.21 and 4.22”	153
4.11	Appendix 4C “The polarity of the PP image”	154
4.12	Appendix 4D “The polarity of the PS image”	158
4.13	Appendix 4E “The imaging conditions for the SP and SS images”	160
CHAPTER 5 FROM CLASSICAL REFLECTIVITY-TO-VELOCITY INVERSION TO FULL WAVEFORM INVERSION USING PHASE-MODIFIED AND DECONVOLVED REVERSE-TIME-MIGRATION IMAGES		164
5.1	Summary	164
5.2	Introduction.....	165

5.3	Theory	169
5.3.1	The relation between the FWI gradient and the RTM image.....	169
5.3.2	FWI based on reflectivity-to-velocity inversion	174
5.3.3	Using deconvolved source and residual data for inversion.....	186
5.4	Examples.....	189
5.4.1	Examples based on the SEG overthrust model	191
5.4.2	Examples based on the Marmousi model.....	197
5.5	Conclusions.....	199
5.6	Acknowledgments.....	202
5.7	Appendix 5A “Half wavelength” condition in deriving the FWI gradient”	203
5.8	Appendix 5B “Derivation from equations 5.9 and 5.10 to 5.11 and 5.12”.....	205
5.9	Appendix 5C “Relation between $ k_i $ and $ \mathbf{k}_{ref} $ ”	207
5.10	Appendix 5D “The relationship between the true reflectivity and the angle-dependent reflectivities”	208
5.11	Appendix 5E “Using the reflectivity-image residual as the objective function”	209
5.12	Appendix 5F “A transformation of Qin et al.’s (2015) formula”	210
5.13	Appendix 5G “A comparison with the spectral shaping method”	212
CHAPTER 6 FROM CLASSICAL REFLECTIVITY-TO-IMPEDANCE INVERSION TO FULL WAVEFORM IMPEDANCE INVERSION USING PHASE-MODIFIED, DECONVOLVED REVERSE-TIME-MIGRATION IMAGES AND ROCK-PHYSICS INFORMATION.....		215
6.1	Summary	215
6.2	Introduction.....	216
6.3	Full waveform impedance inversion.....	217
6.4	From impedance to velocity and density	219
6.5	A practical implementation for AP-RTM.....	221
6.6	Examples.....	224
6.7	Extension of the proposed flow into elastic media	225
6.8	Conclusion	227
6.9	Acknowledgments.....	227
CHAPTER 7 CONCLUDING REMARKS.....		229

7.1	Conclusions.....	229
7.2	Future work.....	232
	REFERENCES	233
	BIOGRAPHICAL SKETCH	242
	CURRICULUM VITAE.....	243

LIST OF FIGURES

- Figure 2.1. Schematic diagram of the relationship between the P-wave propagation and polarization vectors. The double-headed arrow in Panel (c) consists of the two single-head arrows in Panels (a) and (b). Because $\angle 1 = \angle 2 = \angle 3$, all the three arrows give an equivalent reflection angle. Therefore, for calculating reflection ADCIGs, we can include the SACIG at $\angle 1$ into the SACIG at $\angle 2$ and vice versa. This decreases the angle range of SACIGs from $[0^\circ, 360^\circ)$ to $[0^\circ, 180^\circ)$18
- Figure 2.2. A complicated source-wavefield snapshot a), and the decomposition results using twelve vector bins, b) to m). The angles are not the propagation angles, but the “approximate” propagation angles which are only used for separating the overlapping wavefields.19
- Figure 2.3. Schematic diagram using four vector bins to separate source and receiver wavefields. The shaded regions are the shared angle-tapering regions.20
- Figure 2.4. (a) Modified Marmousi velocity model and (b) the RTM image. The image is obtained using WD-AF imaging condition (with four vector bins for source and receiver wavefields), which is the same as that used for Figure 2.6b. In b), the region in the red box corresponds to the SACIGs in Figure 2.5 and the ADCIGs in Figures 2.10 to 2.12; the region in the blue box corresponds to the ADCIGs in Figure 2.13; the region in the green circle includes a truncation point where two reflectors intersect. The velocity model in Panel (a) is modified from the modified Marmousi model of Versteeg (1994).21
- Figure 2.5. SACIGs with (b) the WD, and (c) the WD-AF imaging condition, using the constrained-propagation-angle axis in the schematic diagram (a). The two arrows in panel (a) mark the directions of angle-increase. Although the CIGs at 180° are plotted in panels (b) and (c), they can be included in the CIGs at 0° . Four vector bins are used in the MPV. The asymmetry of the angle illumination in panels (b) and (c) is because the dominant reflector dip is to the left in this part of the profile (in the red box in Figure 2.4b).....23
- Figure 2.6. RTM images with the (a) WD, and the (b) WD-AF imaging condition.24
- Figure 2.7. The images at source constrained-propagation-direction angle 100° (see the red line in Panel a). Panel (b) uses the correct migration velocity. Panel (c) uses an 8% low migration velocity.27
- Figure 2.8. Image recovery by using RMS as a criterion. a) is a local window in the \mathbf{x} domain. By using a forward FT from \mathbf{x} to \mathbf{k} , a) is transformed into c) in the \mathbf{k} domain, which contains 10201 points. By using RMS as a criterion, 1577 points are selected from c), to give d). By using an inverse FT from \mathbf{k} to \mathbf{x} , d) is transformed into b), which is a recovered image of a).....28
- Figure 2.9. Schematic diagram for a local spatial window. The selected (red) point is at the center. The size of the window is 41×41 grid points, so (excluding the red point) there are 20 grid points in each arrow direction. To avoid the Fourier truncation artifacts of the

	forward FT from the \mathbf{x} to \mathbf{k} domain, the amplitudes in the shaded region need to be tapered from the inner (box) boundaries to the outer (box) boundaries; the width of the tapering region is ten grid points.	30
Figure 2.10.	Comparison of ADCIGs by a) spatially global FT, b) spatially local ALFT and c) spatially global ATFT, using the correct migration velocity of the modified Marmousi model. The spatially local ALFT in panel b) uses a local window with a size of 41x41 grid points (see Figure 2.9 for details) in the \mathbf{x} domain. The spatially global ATFT in panel c) uses a T -window with a radius of ten grid points in the \mathbf{k} domain. This example is for the region in the red box of Figure 2.4b. The Fourier truncation artifacts in Panel (a) are reduced in Panels (b) and (c); e.g., see the red and blue boxes. The ADCIGs in Panel (c) have the least artifacts.	31
Figure 2.11.	Comparison of ADCIGs by (a) spatially global FT, (b) spatially local ALFT and (c) spatially global ATFT, using an 8% lower migration velocity. The spatially local ALFT in panel (b) uses a local window with a size of 41x41 grid points (see Figure 2.9 for details) in the \mathbf{x} domain. The spatially global ATFT in panel (c) uses a T -window with a radius of ten grid points in the \mathbf{k} domain. In panel (a), the red box indicates one of several areas with artifacts, which are reduced in (b) and (c). The overall image quality is significantly improved by the ATFT (panel c).	32
Figure 2.12.	The proposed data flow. The dashed red line separates the during-imaging and post-imaging processes. During the imaging, the receiver-side MPVs are used only in performing the WD-AF imaging condition which requires less angle-resolution than calculating SACIGs/ADCIGs.	38
Figure 2.13.	Comparison of ADCIGs using a) four and b) twelve source vector bins in a relatively simple region (in the red box in Figure 2.4b) of the modified Marmousi model.	40
Figure 2.14.	Comparison of ADCIGs using a) four and b) twelve source vector bins in a relatively complicated region (in the blue box in Figure 2.4b) of the modified Marmousi model.	41
Figure 2.15.	The observed data for source 120. (a) is the synthetic observed data. (b) is (a) with noise added. Panel (b) is used as the observed data for the RTM/ADCIGs in Figures 2.16 and 2.17.	42
Figure 2.16.	(a) The simulated wavefield-snapshot from a synthetic source. (b) The reconstructed wavefield-snapshot from the observed data with noise. The time for both (a) and (b) is 0.5 s. To clearly plot the noise, the boundaries of the scale bars do not mark the maximum/minimum amplitudes of the snapshots.	43
Figure 2.17.	Comparison of ADCIGs using (b) source- and receiver-side MPVs and (c) source-side MPV and reflector normal, in a region (see the red box) of panel (a) the RTM image. This example uses four vector bins for MPV.	44

Figure 2.18. The tapering functions for two adjacent vector bins. a) is for the vector bin $(30^\circ, 60^\circ)$; b) is for the vector bin $(60^\circ, 90^\circ)$. The summation of a) and b) at each angle gives c); thus, the wavefield amplitudes in the tapering region $(55^\circ, 65^\circ)$ are preserved.49

Figure 2.19. (a) The velocity model and (b) the stacked RTM image.....52

Figure 2.20. (a) an SACIG and (b) an ADCIG using the simple model in Figure 2.19a. The horizontal location for the SACIG and ADCIG is 2000 m. Refer to Figure 2.5a for the axis of constrained-propagation-angles used to sort SACIGs in Panel (a). The CIG at 180° can be included in the CIG at 0°53

Figure 2.21. Schematic diagram for two overlapping T -windows in the \mathbf{k} domain. The red T -window involves the center (red) point ‘0’ and several tapering (blue) points including Point ‘1’, which is the center of the blue (dashed) T -window.54

Figure 3.1. Relationship between the slowness vector in the $t\text{-}\mathbf{x}$ domain and the plane-wave decomposition in the $\omega\text{-}\mathbf{k}$ domain.....68

Figure 3.2. Comparison of the widely-used and dynamically-correct PVs. Panel (a) is a snapshot of the pressure field. Panels (b) and (c) are the x - and z -components of the widely-used PV, respectively. Panels (d) and (e) are the x - and z -components of the dynamically-correct PV, respectively. The time is 420 ms.79

Figure 3.3. Comparison of the modulus of the widely-used and dynamically-correct PVs. Panel (a) is $|u|$. Panel (b) is u^2 . Panel (c) is the widely-used $|\mathbf{p}|$. Panel (d) is the dynamically-correct $|\mathbf{p}|$. The time is 420 ms.80

Figure 3.4. Comparison of using the widely-used and dynamically-correct PVs to calculate propagation angles. Panel (a) is a snapshot of the pressure field. Now we use the widely-used and dynamically-correct PVs to calculate the propagation directions of the pressure field in panel (a). Then we only show the pressure field within propagation angle aperture $30^\circ\sim 60^\circ$ (the 0° is the horizontal right; the angle increases in the clockwise direction). Using the widely-used and dynamically-correct PVs to calculate propagation angles gives the angle-limited snapshots in panels (b) and (c), respectively.81

Figure 3.5. The P-velocity of a portion of Marmousi2 model.82

Figure 3.6. The RTM image using the synthetic data obtained from the velocity model in Figure 3.5. The migration uses the true velocity.82

Figure 3.7. Comparison of ADCIGs obtained using the (a) original and (b) dynamically-correct MPVs. The synthetic data is obtained from the velocity model in Figure 3.5. The migration uses the true velocity.83

Figure 3.8. Comparison of ADCIGs obtained using the original and dynamically-correct MPVs. Panel (a) is obtained from the original MPV. Panel (b) is obtained from the dynamically-correct MPV. The synthetic data is obtained from the velocity model in Figure 3.5. The migration uses an 8% low velocity model.84

Figure 4.1. Snapshots of P and S particle velocities obtained using the traditional decoupling scheme in a heterogeneous medium with a single, flat reflector. The ‘E wave’ denotes the elastic wave. The residual is obtained by subtracting both the P and S particle velocities from the elastic particle velocity. The colored arrows point to the reflector depth. All the panels are plotted with the same amplitude scale.	108
Figure 4.2. Snapshots of P and S particle velocities obtained using the new decoupling scheme in a homogeneous medium. The ‘E wave’ denotes the elastic wave. All the panels are plotted with the same amplitude scale.	109
Figure 4.3. Snapshots of P and S particle velocities obtained using the new decoupling scheme in a heterogeneous and smooth medium. The ‘E wave’ denotes the elastic wave. All the panels are plotted with the same amplitude scale.	110
Figure 4.4. Snapshots of P and S particle velocities obtained using the new decoupling scheme in a heterogeneous medium with a single, flat reflector. The ‘E wave’ denotes the elastic wave. The residual is obtained by subtracting the P and S particle velocities from the elastic particle velocity. The colored arrows point to the reflector depth. All the panels are plotted with the same amplitude scale.	111
Figure 4.5. The proposed data flow.	126
Figure 4.6. Wavefield snapshots of the x -component of an elastic (E) particle velocities and the separated P and S particle velocities. The arrows denote the polarization directions defined by the particle velocities.	128
Figure 4.7. Wavefield snapshots of the x -component of the decomposed P and S particle velocities. The arrows denote the polarization directions defined by the particle velocities.	129
Figure 4.8. Snapshots of the x -component of decomposed P and S particle velocities. The arrows denote the polarization directions defined by the particle velocities.	130
Figure 4.9. Schematic diagram of two simple elastic models.	131
Figure 4.10. PP images using the elastic model in Figure 4.9a which contains a positive reflectivity. (a) Using P particle velocities decomposed by divergence operator. (b) Cross-correlating the x -component of the $\mathbf{v}_s^{p,tm}$ with the x -component of $\mathbf{v}_r^{p,tm}$. (c) Cross-correlating the z -component of the $\mathbf{v}_s^{p,tm}$ with the z -component of $\mathbf{v}_r^{p,tm}$. (d) Using the multidirectional-vector-based imaging condition for the PP image. The two red lines mark the open angle of 90° . Panels (b) ~ (d) are plotted with the same amplitude scale. Panel (a) is plotted with a different scale because the divergence operator changes the amplitudes of the wavefields. The low-wavenumber noise above the reflector in Panel (a) is the backscattering artifacts.	133
Figure 4.11. PS images using the elastic model in Figure 4.9a which contains a positive reflectivity. (a) Using P and S particle velocities decomposed by divergence and pseudo-curl operators. (b) Cross-correlating the x -component of the $\mathbf{v}_s^{p,tm}$ with the x -component of $\mathbf{v}_r^{s,tm}$. (c) Cross-correlating the z -component of the $\mathbf{v}_s^{p,tm}$ with the z -component of $\mathbf{v}_r^{s,tm}$	

	(d) Using the multidirectional-vector-based imaging condition for PS image. Panels (b) ~ (d) are plotted with the same amplitude scale. Panel (a) is plotted with a different scale because the divergence and pseudo-curl operators change the amplitudes of the wavefields. The minor phase-shift in the red oval in panel (d) is caused by the minor phase-shift at the top of z-component of the S-wave at normal incidence.	134
Figure 4.12.	PP images using the elastic model in Figure 4.9b which contains a negative reflectivity. Refer to the caption of Figure 4.10 for other discussion of the four panels.	135
Figure 4.13.	PS images using the elastic model in Figure 4.9b which contains a negative reflectivity. Refer to the caption of Figure 4.11 for other discussion of the four panels.	136
Figure 4.14.	A complicated portion of Marmousi2 model with a constant elastic layer added at the top. (a) The P velocity. (b) The S velocity. (c) The density.....	137
Figure 4.15.	(a) PP image and (b) PS image obtained by using the proposed flow with the true migration velocity in Figure 4.14. The region between the two red lines define the location of the PP and PS ADCIGs in Figures 4.16 and 4.17.....	138
Figure 4.16.	(a) PP ADCIGs and (b) PS ADCIGs obtained by using the proposed method with the true migration velocity (see Figure 4.14 for the elastic model and Figure 4.15 for the corresponding stacked images). The range of open angles is from 0° to 100°.....	139
Figure 4.17.	(a) PP ADCIGs and (b) PS ADCIGs obtained by using the proposed method with an 8% low migration velocity of the elastic model in Figure 4.14. The range of open angles is from 0° to 100°.....	140
Figure 4.18.	Schematic diagram of four representative situations of PP images when the PP reflectivity is positive. The ‘-’ and ‘+’ denote lower and higher P impedances, respectively. The cyan arrows denote the propagation directions and the red arrows denote the polarization directions. θ^{pp} is the open angle between source and receiver propagation vectors (see equation 4.52). \mathcal{G}^{pp} is the angle between source P and receiver P polarization vectors (see equation 4C-1). Panels (a) and (c) show two possible polarization situations with the open angle θ^{pp} below 90°; Panels (b) and (d) show two possible polarization situations with the open angle θ^{pp} above 90°.....	156
Figure 4.19.	Schematic diagram of four representative situations of PP images when the PP reflectivity is negative. Panels (a) and (c) show two possible polarization situations with the open angle θ^{pp} below 90°; Panels (b) and (d) show two possible polarization situations with the open angle θ^{pp} above 90°. \mathcal{G}^{pp} is the angle between two P polarization vectors (see equation 4C-1).	157
Figure 4.20.	Schematic diagram of two representative situations of PS images when the PS reflectivity is positive. The ‘-’ and ‘+’ denote lower and higher (P and S) impedances, respectively. Panel (a) shows a possible polarization situation with the open angle θ_{ps} below 90°; Panel (b) shows a possible polarization situation with the open angle θ_{ps} above 90°. In both the two panels, the source P wave is on the left side and the receiver S	

	wave is on the right side. The blue arrows denote the propagation directions and the red arrows denote the polarization directions.	159
Figure 4.21.	Schematic diagram of four representative polarization situations of PS images when the PS reflectivity is positive. In panel (a), the polarization direction of the source P wave is the same as its propagation direction. In panel (b), the polarization direction of the source P wave is opposite to its propagation direction.	161
Figure 4.22.	Schematic diagram of four representative polarization situations of PS images when the PS reflectivity is negative. In panel (a), the polarization direction of the source P wave is the same as its propagation direction. In panel (b), the polarization direction of the source P wave is opposite to its propagation direction.	162
Figure 5.1.	Ricker wavelet (Panel a) and the negative of its second time derivative (Panel b) have similar phases, but a) has longer wavelength than b), which means the dominant frequency of a) is lower than that of b).....	174
Figure 5.2.	Ricker wavelet a), its first time derivative b), and its time integration c). In b), the polarity of the wavelet changes three times, which correspond to three reflectors; while in (c), the polarity of the wavelet changes only at 0.1 s, which corresponds to a positive reflectivity at 0.1 s and thus is consistent with a).	187
Figure 5.3.	Schematic diagram for comparison of different phases in FWI. For a true model in a) and an initial model in b), the ideal velocity update is in c). Using the first time derivative of the residual image gives an update in d), using the time integration gives an update in e), and using a deconvolution and a time integration gives an update in f).....	188
Figure 5.4.	For a Ricker wavelet in a), deconvolving it with a zero-phase Ricker wavelet with the same dominant frequency will give a wavelet in b). The spectrum of a) is in c); the spectrum of b) is in d). The phase comparison between time integration of a) and b) is seen in Figures 5.3e and 5.3f.	189
Figure 5.5.	The source wavelet a) and its spectrum b) used for the SEG overthrust model.....	192
Figure 5.6.	Comparison of inversion results obtained by using three methods on a complicated portion of the SEG overthrust model. a) The true model. b) The initial model. c) the S-FWI result. d) the P-FWI result. e) the PD-FWI result. The red, black and blue arrows point to three reflector boundaries, respectively. The four black lines in a) denote the locations for the velocity profiles in Figure 5.7, which show more details for comparison.	194
Figure 5.7.	Comparison of velocity profiles obtained with S-FWI (Panel a), P-FWI (Panel b), and PD-FWI (Panel c), for the SEG overthrust model. The blue line is the true velocity, the green line is the initial velocity, and the red line is the inverted velocity.....	195
Figure 5.8.	Velocity profiles at different iterations of S-FWI (Panel a), P-FWI (Panel b), and PD-FWI (Panel c), for the SEG overthrust model. The horizontal location of these velocity profiles is 1000 m (see Figure 5.6a). The blue line is the true velocity, the green line is the initial velocity, and the red line is the inverted velocity.	196

Figure 5.9. Comparison of average velocity residual between the true and inverted velocities obtained with S-FWI, P-FWI, and PD-FWI, for the SEG overthrust model.	197
Figure 5.10. Comparison of (relative) total data residuals between predicted and observed data obtained with S-FWI (Panels a and b), P-FWI (Panels c and d), and PD-FWI (Panels e and f), for the SEG overthrust model. The total data residual is a summation of the square of the residual over every time, of every receiver, of every shot.....	198
Figure 5.11. The source wavelet a) and its spectrum b) used for the Marmousi model.	199
Figure 5.12. Comparison of inversion results obtained by using three methods on a complicated portion of the Marmousi model. a) The true model, b) The initial model, c) the S-FWI result, d) the P-FWI result, e) the PD-FWI result. The three black lines in a) denote the locations for the velocity profiles in Figure 5.13, which show more details for comparison.....	200
Figure 5.13. Comparison of velocity profiles obtained with S-FWI (Panel a), P-FWI (Panel b), and PD-FWI (Panel c), for the Marmousi model. The blue line is the true velocity, the green line is the initial velocity, and the red line is the inverted velocity.....	201
Figure 5.14. Comparison of average velocity residuals between the true and inverted velocities obtained with S-FWI, P-FWI, and PD-FWI, for the Marmousi model.	202
Figure 5.15. Inverted velocity profiles obtained by using a) PD-FWI-DIC and b) PD-FWI-CIC on a complicated portion of the SEG overthrust model (Figure 5.6a). The blue line is the true velocity, the green line is the initial velocity, and the red line is the inverted velocity.....	213
Figure 6.1. (a) and (b) are the true and initial P-impedance models. (c) and (d) are inverted results using equations 6.19 and 6.20, respectively. The unit of P-impedance used in Figures 6.1 and 6.3 is $\text{kg} \cdot \text{cm}^{-2} \cdot \text{s}^{-1}$	226
Figure 6.2. Average P-impedance relative residual (shown in percentage) versus iteration number. This relative residual is obtained by averaging $ I_{p,result} - I_{p,true} / I_{p,true}$ in the global space. The red and blue lines corresponding to Figure 6.1c (using equation 6.19) and Figure 6.1d (using equation 6.20), respectively.....	228
Figure 6.3. P-impedance profile at horizontal locations 2000 m. The blue, green and red lines denote the true, initial and inverted P-impedance (Figure 6.1c).....	228

LIST OF TABLES

Table 2.1. Full names of the acronyms	13
Table 3.1. A table of the SR-flow, the SI-flow and the SRSI flow.	93

CHAPTER 1

INTRODUCTION

1.1 Motivation and objectives

Angle-domain common-image gathers (ADCIGs) are an important output from reverse time migration (RTM). The Poynting vector (PV) is an efficient way to calculate the propagation direction of the propagating wavefield that can be further used to produce ADCIGs. However, the widely-used PV formula in acoustic media suffers two problems: First, the PV, that works in the time-space domain, can give only a single direction per grid point per time step, and thus it cannot give the correct multiple directions at wavefield overlaps. Second, this formula is only kinematically-correct, and the propagation direction at the magnitude peak of the wavefield is undefined. Besides these two theoretical problems, in practice, the receiver wavefield, which is reconstructed from the observed data, is often as not stable as the source wavefield that is simulated from the synthetic source. There are algorithms to use the source wavefield propagation directions and the reflector normal to calculate ADCIGs but they have some problems. We try to address these three problems by proposing new and improved algorithms.

The elastic RTM generally involves three main parts: the wave mode separation, the imaging conditions, and the ADCIG calculation. The P/S wave mode separation that is based on the Helmholtz theorem, involves the assumption of (locally) constant shear modulus, and thus we try to develop an improved decoupling system to relax this assumption. We also try to give new or improved imaging conditions to calculate the correct PP, PS, SP and SS images. For the

ADCIG calculation, we try to extend our multidirectional PV from acoustic media to the elastic media.

Besides the RTM, the full waveform inversion (FWI) is also an important research area in computational seismology. The FWI is often based on solving an optimization problem of minimizing the L2 norm of the residual between the calculated data and the observed data. Because of the complexity of the problem, approximations are often made during the derivation of the inversion formula. These approximations may not correspond to clear physical meanings. We try to develop a derivation process for the inversion formula based on physical concepts.

1.2 Overview

Chapters 2 and 3 contain the calculation of the RTM image and ADCIGs in acoustic media. Chapter 2 gives a two-step data flow to calculate angle-domain common-image gathers (ADCIGs) from reverse time migration, which makes use of the reflector normal and addresses several issues including overlapping wavefields, backscattering artifacts, and Fourier truncation artifacts that reduce reliability of ADCIGs. During imaging, we use a multidirectional Poynting vector to calculate the propagation vectors of the source wavefield at each time step and output intermediate source-angle-domain CIGs (SACIGs), during which an improved imaging condition, wavefield decomposition plus angle-filter (WD-AF), is used to remove the backscattering artifacts. After imaging, we use an anti-truncation-artifact Fourier transform (ATFT) to convert SACIGs to ADCIGs in the wavenumber domain.

Chapter 3 introduces a dynamically-correct multidirectional PV, which decomposes the wavefield into several vector bins in the ω - \mathbf{k} domain and then uses PV to calculate the propagation directions of each decomposed vector bin in the t - \mathbf{x} domain. We also prove that the

decomposition result of the wavefields with either positive- or negative-frequencies are conjugate. Because we need only the real part of the decomposition result, we can apply the approximate wavefield decomposition to the wavefield with only the positive frequencies and the multiply the real part of the decomposition result by two.

Chapter 4 develops an improved flow for elastic RTM (E-RTM), that decouples elastic waves into P and S modes in non-smooth elastic models, gives the multidirectional-vector-based elastic imaging conditions, and calculates the propagation directions either by multidirectional Poynting vectors or by converting the decomposed particle velocities that are obtained by applying the amplitude-preserved approximate wavefield decomposition to the decoupled P and S particle velocities, into propagation vectors. This flow considers the converted waves during P/S wave mode separation, gives the correct polarities for E-RTM images, and produces high-quality ADCIGs.

Chapters 5 and 6 propose a new full-waveform-inversion (FWI) scheme that provides a self-contained and physically-intuitive derivation which establishes a natural connection between the amplitude-preserved reverse time migration (RTM), the Zoeppritz equations (the amplitude-versus-(reflection)angle [AVA] inversion) and the reflectivity-to-impedance inversion, and combines them into a single framework to produce a preconditioned inversion formula. In this scheme, the relative impedance update is a phase-modified and deconvolved RTM image obtained with the residual data. The rock-physics information is used to separate the impedance into the velocity and density for wavefield extrapolation. Machine learning is also suggested to address the complexity of the rock-physics relationship in the real world. If we ignore the density,

the impedance inversion formula becomes the velocity inversion formula. Chapter 5 discusses the velocity inversion and Chapter 6 discusses the impedance inversion.

My contributions to Chapters 2~6 include initiating the ideas, proposing and improving the data flow, programming the codes, and writing and revising the corresponding papers. The work is in cooperation with my advisor George A. McMechan, whose contributions mainly focus on revising the papers. George also provides some advice during the testing of the data flows.

1.3 Publication status

I. Chapter 2: Tang C. and G. A. McMechan, 2017, Combining multidirectional source vector with anti-truncation-artifact Fourier transform to calculate angle gathers from reverse time migration in two steps: *Geophysics*, **82**, no. 5, S359-S376. Copyrighted by Society of Exploration Geophysicists. Permalink: <https://doi.org/10.1190/geo2016-0408.1>

II. Chapter 3 comes from the following two papers:

(a) Tang C. and G. A. McMechan, 2016, Multidirectional slowness vector for computing angle gathers from reverse time migration: *Geophysics*, **81**, no. 2, S11-S24. Copyrighted by Society of Exploration Geophysicists. Permalink: <https://doi.org/10.1190/geo2015-0134.1>

(b) Tang C. and G. A. McMechan, 2018, The dynamically-correct formula of Poynting vector for acoustic media with application in calculating the multidirectional propagation vector to produce angle gathers from reverse time migration: *Geophysics*. (Accepted). Copyrighted by Society of Exploration Geophysicists. Permalink: <https://doi.org/10.1190/geo2017-0331.1>

- III. Chapter 4: Tang C. and G. A. McMechan, 2018, Multidirectional-vector-based elastic reverse time migration and angle-domain common-image gathers with approximate wavefield decomposition of P and S waves: *Geophysics*, **83**, no. 1, S57-S79. Copyrighted by Society of Exploration Geophysicists. Permalink: <https://doi.org/10.1190/geo2017-0119.1>
- IV. Chapter 5: Tang C. and G. A. McMechan, 2017, From classical reflectivity-to-velocity inversion to full-waveform inversion using phase-modified and deconvolved reverse time migration images: *Geophysics*, **82**, no. 1, S31-S49. Copyrighted by Society of Exploration Geophysicists. Permalink: <https://doi.org/10.1190/geo2016-0033.1>
- V. Chapter 6: Tang C. and G. A. McMechan, 2017, From classical reflectivity-to-impedance inversion to full waveform impedance inversion using phase-modified, deconvolved reverse-time-migration image and rock-physics information: 87th International Meeting, SEG, Expanded Abstracts, 1578-1582. Copyrighted by Society of Exploration Geophysicists. Permalink: <https://doi.org/10.1190/segam2017-17791370.1>

Note, from I to IV, only the publications in, or accepted by, *Geophysics* are listed. Please see Section 1.4 for the declaration.

1.4 Declaration

Most or all contents of this dissertation come from the papers that have already been published or submitted. These papers have also been presented at, or will be submitted to, SEG annual meetings, as expanded abstracts. These are identified by an asterisk at the title of the relevant chapter. The introductory material to the published papers (above) describes my contribution to the work (and acknowledges the contribution of other coauthors). The signatures

of the Supervising Committee which precede all other material in this manuscript attest to the accuracy of this statement.

CHAPTER 2

**COMBINING MULTIDIRECTIONAL SOURCE VECTOR WITH ANTI-
TRUNCATION-ARTIFACT FOURIER TRANSFORM TO
CALCULATE ANGLE GATHERS FROM REVERSE
TIME MIGRATION IN TWO STEPS***

2.1 Summary

Angle-domain common-image gathers (ADCIGs) are an important product from reverse time migration. Because receiver wavefields reconstructed from observed data are not as stable as synthetic source wavefields, the source propagation vector and the reflector normal have often been used to calculate angle-domain common-image gathers (ADCIGs) from reverse time migration (RTM). However, the existing data flows have three main limitations: 1) Calculating the propagation direction only at the maximum amplitudes of wavefields ignores multi-arrivals; using the cross-correlation imaging condition at each time step can include the multi-arrivals but will result in backscattering artifacts. 2) Neither amplitude picking nor Poynting-vector calculations are accurate for overlapping wavefields. 3) Calculating the reflector normal in space

* Tang C. and G. A. McMechan, 2017, Combining multidirectional source vector with anti-truncation-artifact Fourier transform to calculate angle gathers from reverse time migration in two steps: *Geophysics*, **82**, no. 5, S359-S376. Copyrighted by Society of Exploration Geophysicists. Permalink: <https://doi.org/10.1190/geo2016-0408.1>

Tang C. and G. A. McMechan, 2016, Combining multidirectional-source vector with revised antileakage Fourier transform to calculate angle gathers from reverse time migration in two steps: 86th International Meeting, SEG, Expanded abstracts, 4378-4382. Copyrighted by Society of Exploration Geophysicists. Copyrighted by Society of Exploration Geophysicists. Permalink: <https://doi.org/10.1190/segam2016-13879599.1>

Tang C., 2014, Combining source direction vectors with wavefield decomposition to calculate angle gathers: 84th International Meeting, SEG, Expanded abstracts, 3831-3836. Copyrighted by Society of Exploration Geophysicists. Permalink: <https://doi.org/10.1190/segam2014-0454.1>

is not accurate for a structurally complicated reflection image and calculating it in the wavenumber (\mathbf{k}) domain may give Fourier truncation artifacts. We address these three limitations in an improved data flow with two steps: During imaging, we use a multidirectional Poynting vector (MPV) to calculate the propagation vectors of the source wavefield at each time step and output intermediate source-angle-domain CIGs (SACIGs). After imaging, we use an anti-truncation-artifact Fourier transform (ATFT) to convert the SACIGs to ADCIGs in the \mathbf{k} domain. To achieve the new flow, another three innovative aspects are included. In the first step, we develop an angle-tapering scheme to remove the Fourier truncation artifacts during the wave decomposition (of MPV) while preserving the amplitudes, and use a wavefield decomposition plus angle-filter imaging condition to remove the backscattering artifacts in the SACIGs. In the second step, we compare two algorithms to remove the Fourier truncation artifacts that are caused by the plane-wave assumption. One uses an anti-leakage FT (ALFT) in local windows; the other uses an anti-truncation-artifact FT which relaxes the plane-wave assumption and thus can be done for global space. The second algorithm is preferred. Numerical tests show this new flow (source-side MPV plus ATFT) gives high-quality ADCIGs.

2.2 Introduction

Reverse time migration (RTM), the concept of which is initially proposed by Baysal et al. (1983), McMechan (1983), and Whitmore (1983), has become increasingly mature during the past decade. RTM uses full wavefield extrapolation and thus is more accurate than conventional one-way wave-equation migration (e.g., Claerbout, 1971) and ray-based migration algorithms (e.g., Berkhout, 1985), especially for complicated geological structures. An important extension of RTM is angle-domain common-image gathers (ADCIGs), also known as angle gathers. The

ADCIGs have a variety of applications such as migration velocity analysis (e.g., Biondi and Symes, 2004; Shen and Symes, 2008; Zhang et al., 2012), scattering-angle-based full waveform inversion (e.g., Alkhalifah, 2015; Xie, 2015), amplitude-preserved migration (e.g., Zhang et al., 2007; Xu et al., 2011), illumination and migration aperture compensation (e.g., Shen et al. 2011; Yan et al., 2014), surface energy compensation (e.g., Zhang et al., 2014), and amplitude-versus-angle (AVA) inversion (e.g., Rabben and Ursin, 2011).

Calculating ADCIGs from wavefield extrapolation is not as natural as from ray-based migration (e.g., Gray and Bleistein, 2009), because the extrapolation engines do not automatically provide or use the propagation-angle information. The ADCIGs can be calculated either during or after prestack migration. In the post-migration category, Sava and Fomel (2003) calculate local offset-domain CIGs (ODCIGs) during 2D migration and then convert them into ADCIGs after migration. As there may be wavefield overlaps in the offset gathers, the conversion from local ODCIGs to ADCIGs needs to be done by using plane-wave decomposition; e.g. in the wavenumber (\mathbf{k}) domain (by Fourier transforms) or in the τ - \mathbf{p} domain (by τ - \mathbf{p} transforms), which both produce truncation artifacts when these extended images are not dominated by a few plane waves. The artifacts are similar to those produced when using the local plane-wave decomposition to calculate ADCIGs during migration (Jin et al., 2014). Sava and Fomel's (2003) method is elegant in 2D, but the corresponding 3D implementation requires a 5D Fourier transform (FT) (Fomel, 2004). Time-shift CIGs (Sava and Fomel, 2006) can decrease the cost in 3D, but need to be combined with the local offsets for calculating azimuth angles (Sava and Vlad, 2011), because the time-shift CIGs are always in the reflection plane and thus they do not contain azimuth information.

Calculating ADCIGs during migration requires computing propagation directions during wave extrapolation. The algorithms can be generally divided into two types: local plane-wave decomposition (LPD) (e.g., Xu et al., 2011), and energy-direction-based methods such as Poynting vectors (PVs) (Červený, 2001; Yoon et al., 2004; Dickens and Winbow, 2011). Modifications and alternatives such as least-squares optimization (Yan and Ross, 2013), time-shifting (Tang et al., 2013a; Tang et al., 2017a) and optical flow (Zhang, 2014; Tang et al., 2017a), are useful to increase the stability of PVs in acoustic media.

A representative LPD algorithm developed by Xu et al. (2011) calculates reflection and azimuth angles by convolving plane-wave components of source and receiver wavefields in the frequency-wavenumber (ω - \mathbf{k}) domain. In this method, the forward FT needs to be done in local spatial windows, because the algorithm has a constant-velocity assumption; decomposing the wavefield into small angle bins implies sharp truncations in the \mathbf{k} domain, which further implies that the waves propagating in local windows should be dominated by plane-wave components to suppress Fourier truncation artifacts. Furthermore, the application of anti-leakage Fourier transforms (ALFTs) (e.g., Xu et al., 2010) is suggested to decrease the size of the convolution. In Theory, the LPD has similarity with the plane-wave migration (PWM) that is efficient way to calculation ADCIGs (Tang et al., 2013b); the LPD is much more expensive because it extracts local plane wave information from the full wavefield extrapolation but the PWM uses plane-wave-based extrapolation which is often less accurate than the full wavefield extrapolation in complex media.

In isotropic media, the PV has the same direction as the slowness vector (SV) in the time-space (t - \mathbf{x}) domain; both give only a single propagation vector that is the sum of all the plane-

wave components, so it is necessary to separate overlapping wavefields before calculating their directions. Tang and McMechan (2016) propose decomposition of a wavefield into several approximate direction bins in ω - \mathbf{k} (or in t - \mathbf{k} by using complex-valued wavefields), and then using SV/PV to recalculate the directions within each bin in t - \mathbf{x} . Richardson and Malcolm (2015) propose a similar approach but use LPD to decompose the overlapped wavefields. Note, in anisotropic media, the PV and SV do not have the same direction and a conversion from the group angle to the phase angle is required; refer to McGarry and Qin (2013).

Another issue for the extraction of ADCIGs is that, in practice, the receiver wavefield, which is reconstructed from the observed data, is not as stable as the synthetic source wavefield that originates from a simulated source. To address this problem, Yoon et al. (2011) and Vyas et al. (2011) propose to use the source propagation vector and the reflector normal to calculate ADCIGs, which avoids using the propagation direction of the receiver wavefield in sorting ADCIGs; Zhang and McMechan (2011) have a similar idea but use the source polarization vector. However, these data flows have three main limitations.

The first limitation relates to the imaging condition (picking the maximum amplitude from all time steps or using the cross-correlation imaging condition at each time step). Zhang and McMechan (2011) assume that there is only one arrival at each grid point during the wave propagation; they pick the corresponding maximum amplitude of the propagating wavefields to locate the time of this arrival, and thus ignore multi-arrivals. Yoon et al. (2011) and Jin et al. (2014) propose to pick more than one maximum amplitude, but it is still not automatic to include multi-arrivals. Picking the maximum amplitude does not work well for overlapping wavefields and the velocity model needs to be smoothed to avoid overlaps of the incident and reflected

waves at each reflection point. Using the cross-correlation imaging condition at each time step (e.g., Chattopadhyay and McMechan, 2008) automatically includes the multi-arrivals; however, it also produces backscattering artifacts (e.g., Liu et al., 2011; Tang and Wang, 2012a).

The second limitation relates to the calculation of the propagation (or polarization) angles. The PV method cannot accurately calculate the propagation directions where there are wavefield overlaps. Using the LPD to calculate propagation angles is expensive and also suffers from Fourier truncation artifacts if the propagation waves in local windows are not strictly plane waves (Jin et al., 2014).

The third limitation relates to the calculation of the reflector normal. Calculating the reflector normal in the \mathbf{x} domain, including using the instantaneous wavenumber or phase (Zhang and McMechan, 2011; Jin et al., 2014) and the method of Zhao et al. (2012), gives only one reflector-normal direction (for each grid point) and cannot deal with truncations or overlaps in the reflection image. Although Vyas et al. (2011) calculate the reflector normal in the \mathbf{k} domain, they do not give a method to suppress the Fourier truncation artifacts in the ADCIGs. These artifacts are associated with the plane-wave assumption of the partitioned images when they are transformed into the \mathbf{k} domain by using the global spatial forward FTs and then are sorted into ADCIGs which are finally transformed back to the \mathbf{x} domain by inverse FTs.

To address these limitations, we propose an improved data flow, in which a multidirectional source vector is combined with an anti-truncation-artifact Fourier transform (ATFT) to calculate ADCIGs from RTM in two steps. The first step uses multidirectional source vectors to calculate intermediate source-angle-domain CIGs (SACIGs) during the migration; the second step transforms these SACIGs into ADCIGs by calculating the reflector normal in the \mathbf{k}

domain after migration, for which the ATFT is used. Several acronyms are used in this chapter; see Table 2.1.

Table 2.1. Full names of the acronyms

ACRONYM	FULL NAME
CIG	Common-image gather
ADCIG	Angle-domain common-image gather
SACIG	Source-angle-domain common-image gather
LPD	Local plane-wave decomposition
SV	Slowness vector
PV	Poynting vector
MPV	Multidirectional Poynting vector
FT	Fourier transform
FFT	Fast Fourier transform
ALFT	Anti-leakage Fourier transform
ATFT	Anti-truncation-artifact Fourier transform
WD	Wave decomposition
WD-AF	Wave decomposition plus angle-filter

2.3 Theory

This section is divided into four subsections to introduce a new data flow, which solves the three limitations stated at the end of the previous section. The first subsection addresses the first and second limitations by using a multidirectional Poynting vector (MPV) and a wavefield decomposition plus angle-filter (WD-AF) imaging condition, to output intermediate SACIGs during migration. The second subsection presents calculation of ADCIGs from SACIGs (including the solution of the third limitation) after the migration is complete. The third and fourth subsections illustrate two algorithms to remove the Fourier artifacts caused by image truncations in the \mathbf{k} domain. The formulas are for both 2D and 3D; the numerical examples are in 2D.

2.3.1 Using multidirectional PVs to calculate SACIGs

In this subsection, we address the first and second limitations defined at the end of Section 2.2 “Introduction”. In the first limitation, using the cross-correlation imaging condition at each time step will generate backscattering artifacts in the SACIGs. These artifacts will have a strongly negative influence in calculating the reflector normal from the SACIGs, and in the subsequent transformation of SACIGs into ADCIGs. In the second limitation, the single-direction PV fails at overlapping wavefields which have multiple directions. To address both the two limitations, we use the MPV (Tang and McMechan, 2016) to calculate SACIGs, which involves a WD imaging condition to remove the backscattering artifacts.

Following Tang and McMechan (2016), we can use a MPV to give the multidirectional propagation vector for a single location \mathbf{x} in a propagating wave u in space at time t ,

$$\mathbf{p} = (\mathbf{p}_1, \mathbf{p}_2, \mathbf{p}_3, \dots, \mathbf{p}_i, \dots, \mathbf{p}_{n-1}, \mathbf{p}_n), \quad (2.1)$$

where each component (in the decomposed wavefield)

$$\mathbf{p}_i(t, \mathbf{x}) = -\frac{\partial u_i(t+t_i, \mathbf{x})}{\partial t} \frac{\partial u_i(t+t_i, \mathbf{x})}{\partial \mathbf{x}}, \quad (2.2)$$

is a time-shift PV calculated from each decomposed wavefield u_i (where i is the reference index and n is the total number of vector bins), and t_i is a variable time-shift to increase the stability of the PVs, which is determined by picking the maximum-magnitude of the time derivative of u_i within a short time window; in the examples below, we use a quarter of the dominant period of the source wavelet as half of the width of the time-shift search window. The variable time-shift is to improve the stability of the PV and MPV; see Tang et al. (2017a) for details. This goal can also be achieved by using the optical flow in the multidirectional scheme to produce a multidirectional optical flow (Tang et al., 2017a). The u_i is obtained by the inverse FT of a vector bin of the analytic (positive-frequency) wavefields in $t\text{-}\mathbf{k}$,

$$u_i = 2\Re \left[\int_{(\bar{\psi}_1, \bar{\psi}_2)_{i-1}}^{(\bar{\psi}_1, \bar{\psi}_2)_i} \bar{U}_+(t, \mathbf{k}) e^{-i\mathbf{k}\mathbf{x}} d\mathbf{k} \right], \quad (2.3)$$

where $(\bar{\psi}_1, \bar{\psi}_2)$ are the ‘‘approximate’’ propagation-angle pairs used to decompose the wavefield and are different from (ψ_1, ψ_2) below in heterogeneous media. $\bar{U}_+(t, \mathbf{k})$ is the complex-valued analytic wavefield in the $t\text{-}\mathbf{k}$ domain, which can be obtained by transforming the propagating wavefields at all the time-steps from the t domain to the ω domain (used in the implementation of the 2D examples in this chapter), using complex-valued wavefield extrapolation of the

analytic source wavelet and the analytic observed data (e.g., Tang and McMechan, 2016) [this can be combined with source wavefield reconstruction (e.g., Tang and Wang, 2012b)], or using low-rank wavefield extrapolation (e.g., Zhang and Zhang, 2009; Fomel et al., 2013) which can naturally provide the analytic propagating wavefields. \Re means taking the real part of a complex value. In equation 2.3, the FTs are performed for the global space (rather than in local windows), because although the global FT can give only “approximate” propagation directions for heterogeneous velocity, the wavefield decomposition in the \mathbf{k} domain is used only to separate the overlapping wavefields. Accurate propagation angles for sorting SACIGs are recalculated by PVs for each separated source wavefield, \mathbf{p}_i (where the subscript i denotes the reference number of the angle bin):

$$\begin{cases} \psi_1 = \sin^{-1} \frac{p_{i-z}}{|\mathbf{p}_i|}, \\ \psi_2 = \tan^{-1}(p_{i-y}, p_{i-x}), \end{cases} \quad (2.4)$$

where ψ_1 and ψ_2 are polar and azimuth (propagation) angles that describe the wave propagation direction in 3D; p_{i-x} , p_{i-y} , and p_{i-z} are the components of a source vector bin \mathbf{p}_i in the x -, y -, and z -axis, respectively.

In 2D, only the polar (propagation) angle ψ exists

$$\psi = \tan^{-1}(p_{i-z}, p_{i-x}) = \begin{cases} \text{atan2}(p_{i-z}, p_{i-x}) \cdot \frac{180^\circ}{\pi}, & \text{if } \text{atan2}(p_{i-z}, p_{i-x}) \geq 0, \\ \text{atan2}(p_{i-z}, p_{i-x}) \cdot \frac{180^\circ}{\pi} + 360^\circ, & \text{if } \text{atan2}(p_{i-z}, p_{i-x}) < 0, \end{cases} \quad (2.5)$$

where the range of ψ is $[0^\circ, 360^\circ)$. The `atan2` is a mathematical function that is included in the `math.h` of the C standard library. Because the reflection angle is equivalent to the included angle between the incident wave and the reflector normal, which is always within $[0^\circ, 90^\circ)$, the constrained propagation angle

$$\psi' = \begin{cases} \psi, & 0^\circ \leq \psi < 180^\circ, \\ \psi - 180^\circ, & 180^\circ \leq \psi < 360^\circ, \end{cases} \quad (2.6)$$

can be used to replace the propagation angle ψ to denote the source vector in 2D (see Figure 2.1). A combination of equations 2.5 and 2.6 is equivalent to

$$\psi' = \sin^{-1} \frac{p_{i-z}}{|\mathbf{p}_i|} = \begin{cases} \arcsin\left(\frac{p_{i-z}}{|\mathbf{p}_i|}\right) \cdot \frac{180^\circ}{\pi}, & \text{if } \arcsin\left(\frac{p_{i-z}}{|\mathbf{p}_i|}\right) \geq 0. \\ \arcsin\left(\frac{p_{i-z}}{|\mathbf{p}_i|}\right) \cdot \frac{180^\circ}{\pi} + 180^\circ, & \text{if } \arcsin\left(\frac{p_{i-z}}{|\mathbf{p}_i|}\right) < 0. \end{cases} \quad (2.7)$$

Either of equations 2.5~2.6 and equation 2.7 can be used to calculate ψ' , the range of which is $[0^\circ, 180^\circ)$ (see Figure 2.1). This decreases the storage requirement of SACIGs and the computation time of transforming SACIGs into ADCIGs by half. Because the range of the constrained propagation angle is $[0^\circ, 180^\circ)$, it can also be calculated by the polarization vector which has the same, or opposite, direction with the propagation direction. The CIGs sorted by source-side constrained propagation angle are also referred to as SACIGs in the present context.

The MPV (that consists of equation 2.1 to 2.3) does not require a plane-wave assumption. To avoid the Fourier truncation artifacts caused by the angle-limited FT in equation 2.3, which has sharp truncations in the \mathbf{k} domain, amplitude tapering needs to be done around the two

boundaries of each angle bin to smooth the (amplitude) truncations. To preserve the total amplitude while doing the taper, the choice of taper functions for two adjacent vector bins should satisfy a condition that the tapering weight of each vector bin forms a partition of unity at each angle; see Appendix 2A (Section 2.8).

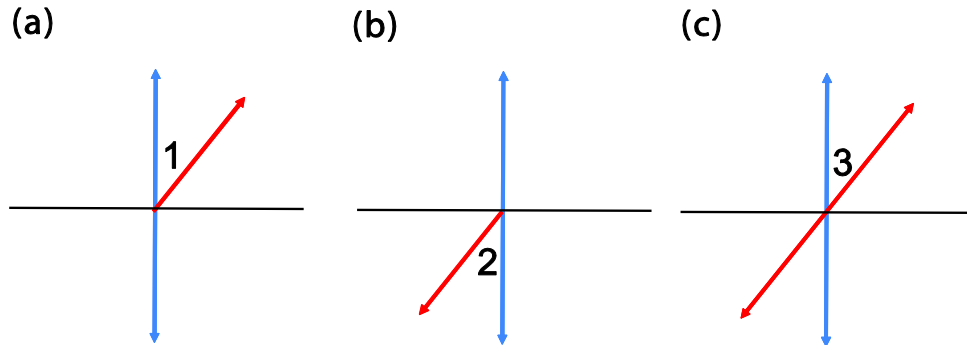


Figure 2.1. Schematic diagram of the relationship between the P-wave propagation and polarization vectors. The double-headed arrow in Panel (c) consists of the two single-head arrows in Panels (a) and (b). Because $\angle 1 = \angle 2 = \angle 3$, all the three arrows give an equivalent reflection angle. Therefore, for calculating reflection ADCIGs, we can include the SACIG at $\angle 1$ into the SACIG at $\angle 2$ and vice versa. This decreases the angle range of SACIGs from $[0^\circ, 360^\circ)$ to $[0^\circ, 180^\circ)$.

Figure 2.2 shows a wavefield decomposition example of using twelve vector bins and tapering windows with a width of 10° . Most of the overlapping wavefields in the input wavefield in Figure 2.2a have been separated in Figures 2.2b-2.2m. By using the tapering function in equation 2A-1, there are not strong Fourier truncation artifacts in Figures 2b-2m. The Fourier truncation artifacts can be further decreased by using wider tapering windows in the angle domain to make the amplitude-tapering smoother, but this reduces the resolution of the approximate wavefield decomposition (WD). For example, a tapering window of 10° -width enlarges the original range of the vector bin $(30^\circ, 60^\circ)$ to $(25^\circ, 65^\circ)$; although the amplitudes in the tapering region are progressively weakened, they still influence the resolution.

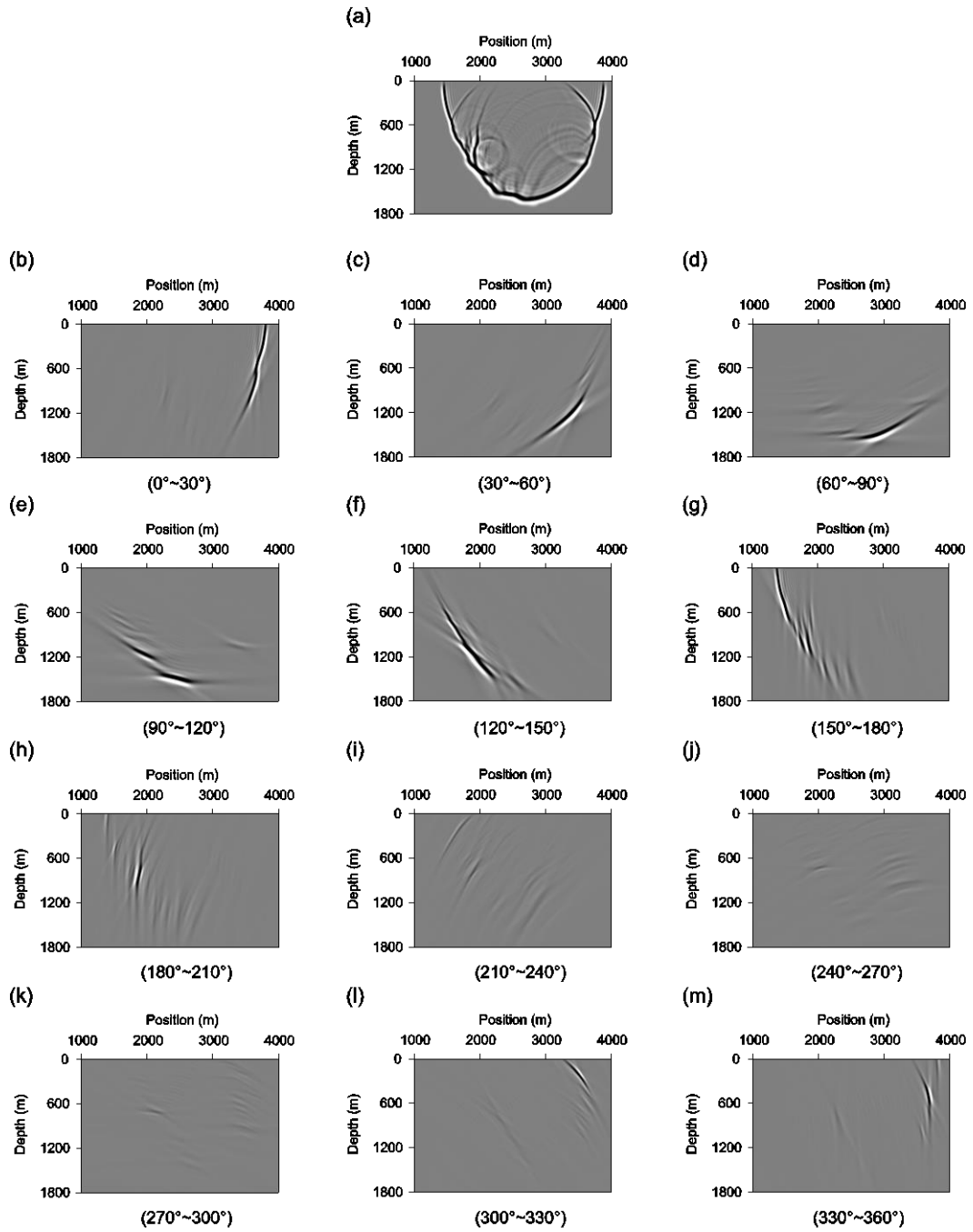


Figure 2.2. A complicated source-wavefield snapshot a), and the decomposition results using twelve vector bins, b) to m). The angles are not the propagation angles, but the “approximate” propagation angles which are only used for separating the overlapping wavefields.

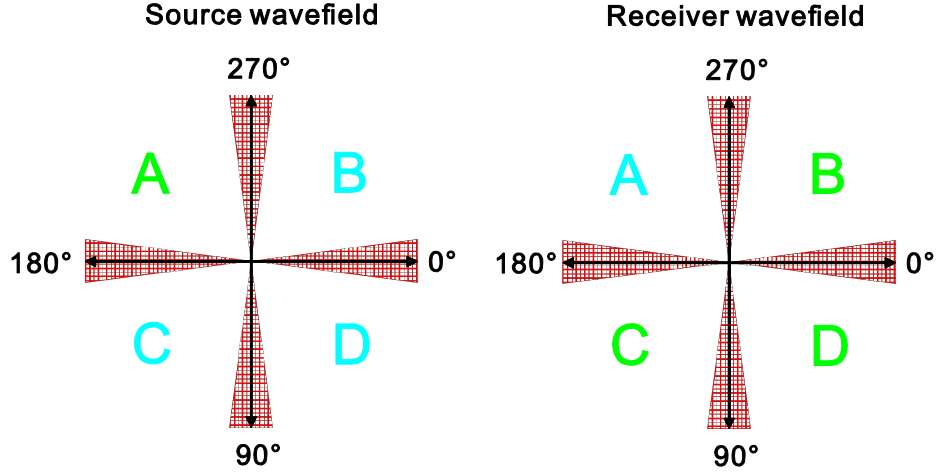


Figure 2.3. Schematic diagram using four vector bins to separate source and receiver wavefields. The shaded regions are the shared angle-tapering regions.

Based on the approximate WD in equation 2.3, a WD imaging condition

$$I(\mathbf{x}) = \int dt \sum_{i=1, j=1}^{i=N, j=M} (1 - \delta_{ij}) u_{s,i}(\mathbf{x}, t) u_{r,j}(\mathbf{x}, t), \quad (2.8)$$

is applied to reduce the backscattering artifacts, where i and j are the indices of the vector bins of the source wavefield u_s and the receiver wavefield u_r , respectively; N and M are the total numbers of vector bins for the source and receiver wavefields, respectively. The $(1 - \delta_{ij})$ means excluding the cross-correlation of source and receiver wavefields propagating in the same/similar directions, because this cross-correlation gives backscattering artifacts [e.g., Liu et al. (2011) use up- and down-going wavefields (regarded as a two-vector-bin case of MPV) to explain the reason]. For the four-vector-bin case in Figure 2.3, we can cross-correlate region A of the source wavefield with regions B, C and D of the receiver wavefield.

Equation 2.8 is a general expression for the WD imaging condition, which can remove most of the backscattering artifacts. However, this method cannot remove the backscattering artifacts

in the shared amplitude-tapering region of two adjacent vector bins (the shaded regions in Figure 2.3), because source and receiver wavefields in the same/similar directions cross-correlate in these shared bins. For the modified Marmousi model in Figure 2.4a, using a four-vector-bin MPV gives the representative SACIGs in Figure 2.5b, which contain backscattering artifacts in the vertical direction (see the detailed analysis in Appendix 2B [Section 2.9]).

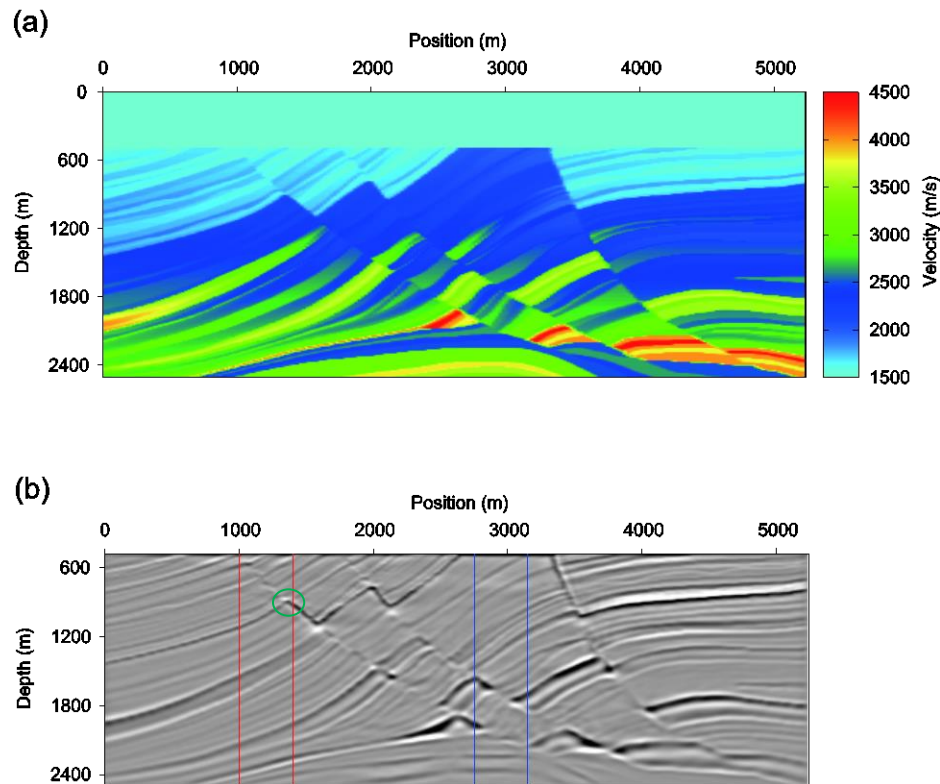


Figure 2.4. (a) Modified Marmousi velocity model and (b) the RTM image. The image is obtained using WD-AF imaging condition (with four vector bins for source and receiver wavefields), which is the same as that used for Figure 2.6b. In b), the region in the red box corresponds to the SACIGs in Figure 2.5 and the ADCIGs in Figures 2.10 to 2.12; the region in the blue box corresponds to the ADCIGs in Figure 2.13; the region in the green circle includes a truncation point where two reflectors intersect. The velocity model in Panel (a) is modified from the modified Marmousi model of Versteeg (1994).

To remove these artifacts, we propose a WD-AF (wavefield decomposition plus angle-filter) imaging condition, which uses the reflection angle θ calculated by MPV to design a filter $F(\theta)$; see Appendix 2B [Section 2.9]. The WD-AF imaging condition can be written as

$$I(\mathbf{x}) = \int dt \sum_{i=1, j=1}^{i=N, j=M} F(\theta_{i,j}) (1 - \delta_{ij}) u_{s,i}(\mathbf{x}, t) u_{r,j}(\mathbf{x}, t), \quad (2.9)$$

which can be recognized as applying an angle-dependent filter $F(\theta_{i,j})$ to the WD imaging condition in equation 2.8.

Applying the WD-AF imaging condition can suppress the backscattering artifacts in Figure 2.5b and give clean SACIGs in Figure 2.5c. The SACIGs in Figure 2.5c also give a cleaner stacked image (in Figure 2.6b) than that in Figure 2.6a (which is stacked from the SACIGs in Figure 2.5b). See Appendix 2C (Section 2.10) for the SACIG using a simple velocity model.

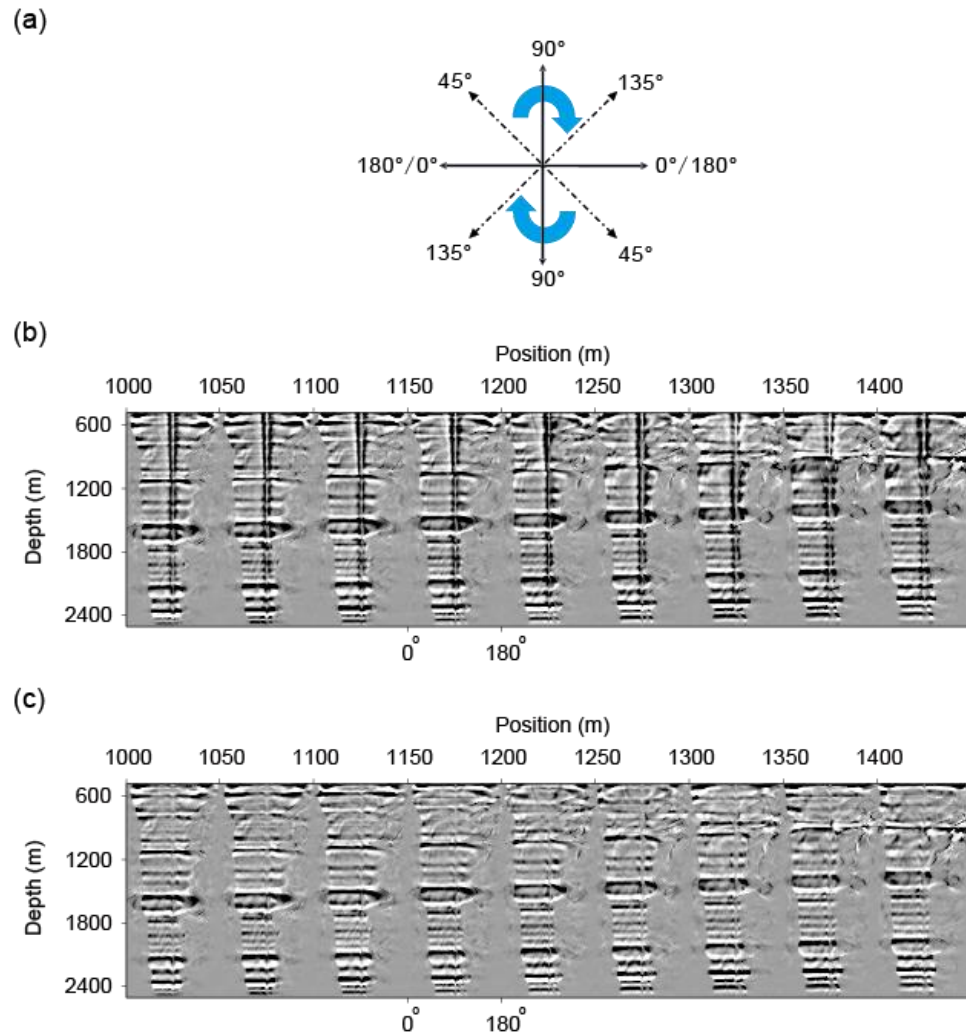


Figure 2.5. SACIGs with (b) the WD, and (c) the WD-AF imaging condition, using the constrained-propagation-angle axis in the schematic diagram (a). The two arrows in panel (a) mark the directions of angle-increase. Although the CIGs at 180° are plotted in panels (b) and (c), they can be included in the CIGs at 0° . Four vector bins are used in the MPV. The asymmetry of the angle illumination in panels (b) and (c) is because the dominant reflector dip is to the left in this part of the profile (in the red box in Figure 2.4b).

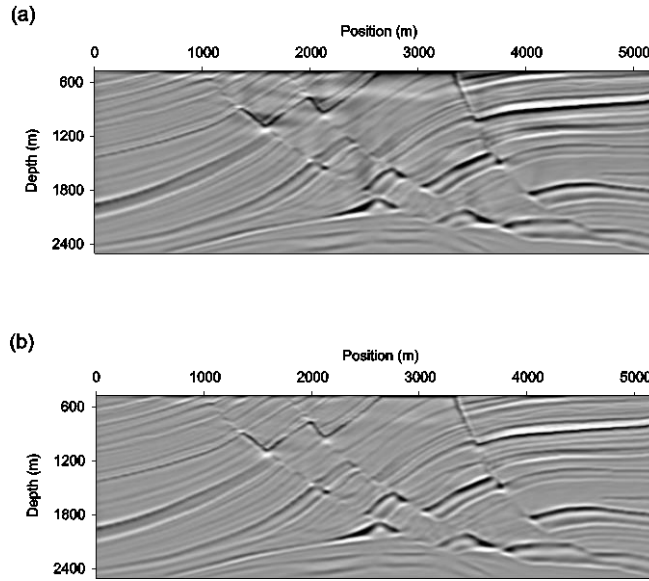


Figure 2.6. RTM images with the (a) WD, and the (b) WD-AF imaging condition.

2.3.2 Calculating ADCIGs from SACIGs

In the previous subsection, the MPV concept is used to decompose a source-wavefield snapshot into a number of angle bins to separate overlapping wavefields. This allows explicit consideration of multipathing in RTM with the WD-AF imaging condition to create SACIGs. It remains to convert the SACIGs into ADCIGs, by combining the source propagation vector and the reflector normal to calculate the incident/reflection and azimuth angles. The latter involves reordering the SACIGs into each decomposed migrated image (a “partitioned” image) corresponding to each source direction angle (Figure 2.7). In each partitioned image, at each image point, we calculate the reflection angle θ and azimuth angle ϑ in the \mathbf{k} domain,

$$\begin{cases} \theta = \cos^{-1} \frac{|\mathbf{p}_s \cdot \mathbf{k}|}{|\mathbf{p}_s| |\mathbf{k}|}, \\ \mathcal{G} = \cos^{-1} \frac{[(\mathbf{p}_s \times \mathbf{k}) \times \hat{\mathbf{z}}] \cdot \hat{\mathbf{x}}}{|\mathbf{p}_s| |\mathbf{k}|}. \end{cases} \quad (2.10)$$

Here \mathbf{p}_s is the source propagation vector converted from the source propagation angles, and \mathbf{k} is the wavenumber of the reflection image, which defines the polarization direction that is parallel to the reflector normal; the \times between two vectors is a cross product, and the dot between two vectors is a dot product; $\hat{\mathbf{x}}$ and $\hat{\mathbf{z}}$ are the unit vectors in the positive directions of the x - and z -axes.

As indicated in the ‘‘Introduction’’ section, Vyas et al. (2011) also calculate the reflection and azimuth angles in the \mathbf{k} domain (similar to equation 2.10); however, there are Fourier truncation artifacts when globally spatial FTs (FTs in the global space) are used to transform the partitioned images from the \mathbf{x} domain to the \mathbf{k} domain and transform ADCIGs from the \mathbf{k} domain back to the \mathbf{x} domain, because sorting ADCIGs in the \mathbf{k} domain (equation 2.10) has the plane-wave assumption. In the next two subsections, we discuss these artifacts and compare two schemes to remove them.

2.3.3 Anti-leakage Fourier transform (ALFT) in local windows

In the previous subsection, SACIGs are transformed into ADCIGs. The implementation is post migration and thus it is independent from the propagation velocity. However, using globally spatial FTs for this transformation will produce Fourier truncation artifacts in the ADCIGs. The reason is as follows: When the partitioned images are sorted into ADCIGs in the \mathbf{k} domain (equation 2.10), each angle corresponds to one or more sharp image-truncations; when these

image-truncations are transformed back from the \mathbf{k} domain to the \mathbf{x} domain using inverse globally-spatial FTs, each truncation point in the \mathbf{k} domain corresponds to a plane-wave component in the \mathbf{x} domain, so the plane-wave assumption is required; otherwise, there are Fourier truncation artifacts.

To satisfy this assumption as far as possible, the FTs need to be done in local windows. To decrease the computational cost of using local FTs, we use the anti-leakage Fourier transform (ALFT); the general ALFT algorithm of Xu et al. (2010) is presented in Appendix 2D (Section 2.11). This algorithm makes use of the sparse characteristic of the signal obtained using FTs, and thus only a small portion of the sampling points (those where the energy is focused) in the \mathbf{k} (or ω , or $\omega\text{-}\mathbf{k}$) domain need to be processed. The ALFT algorithm has also been used by Xu et al. (2011) and Jin et al. (2014) to calculate ADCIGs by applying LPD to the propagating wavefields.

In the general ALFT flow (Appendix 2D [Section 2.11]), because picking the maximum amplitude at each iteration increases the computational complexity, we use a different criterion to select the effective points, which avoids picking the maximum modulus in each iteration. For a local window, the data in the \mathbf{k} domain is sparse, which means the energy mainly focuses on a limited number of image points. Thus, the RMS (root-mean-square) of the modulus (of the complex-valued wavefield amplitude) is close to the background modulus of the window; thus, it can be used to separate the effective and non-effective points. If the modulus of a point $I(\mathbf{k})$ is above the RMS, this point is an effective point and needs to be transformed back into the \mathbf{x} domain; otherwise, we ignore this point. Figure 2.8a is a local window in the \mathbf{x} domain. Transforming Figure 2.8a from \mathbf{x} to \mathbf{k} by FT gives Figure 2.8c, which is sparse. In Figure 2.8c, using the RMS criterion to select 1577 effective points from the total 10201 points gives Figure

2.8d. Transforming Figure 2.8d back to the x domain gives Figure 2.8b, which successfully recovers all the salient features of the image in Figure 2.8a.

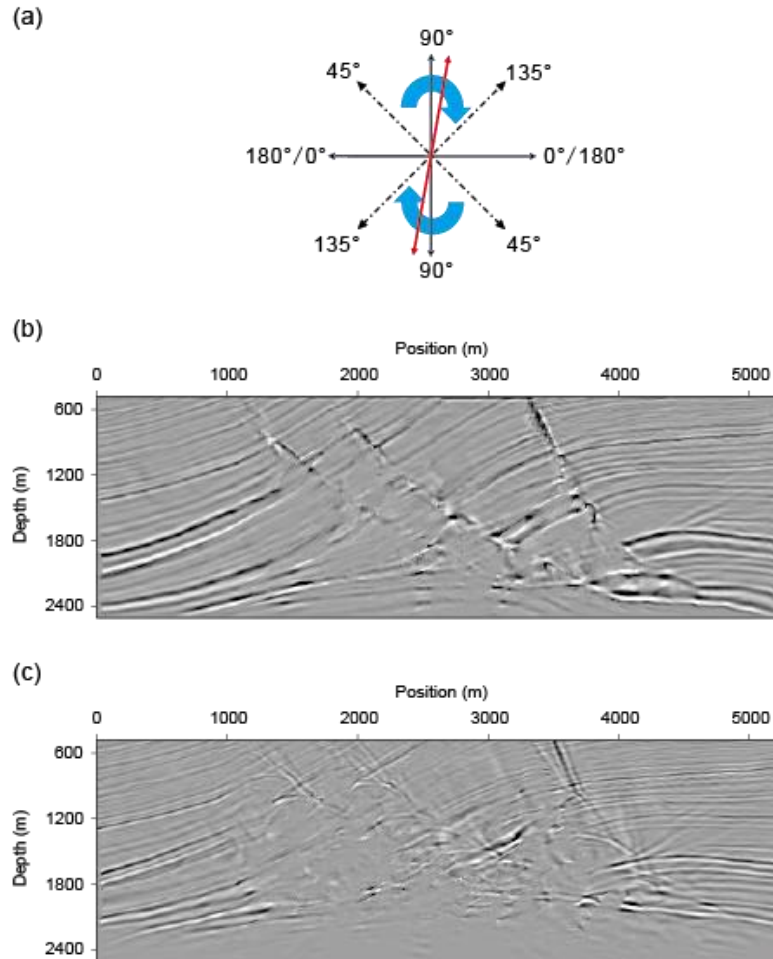


Figure 2.7. The images at source constrained-propagation-direction angle 100° (see the red line in Panel a). Panel (b) uses the correct migration velocity. Panel (c) uses an 8% low migration velocity.

The flow of using ALFT to convert SACIGs into ADCIGs in local spatial windows is as follows:

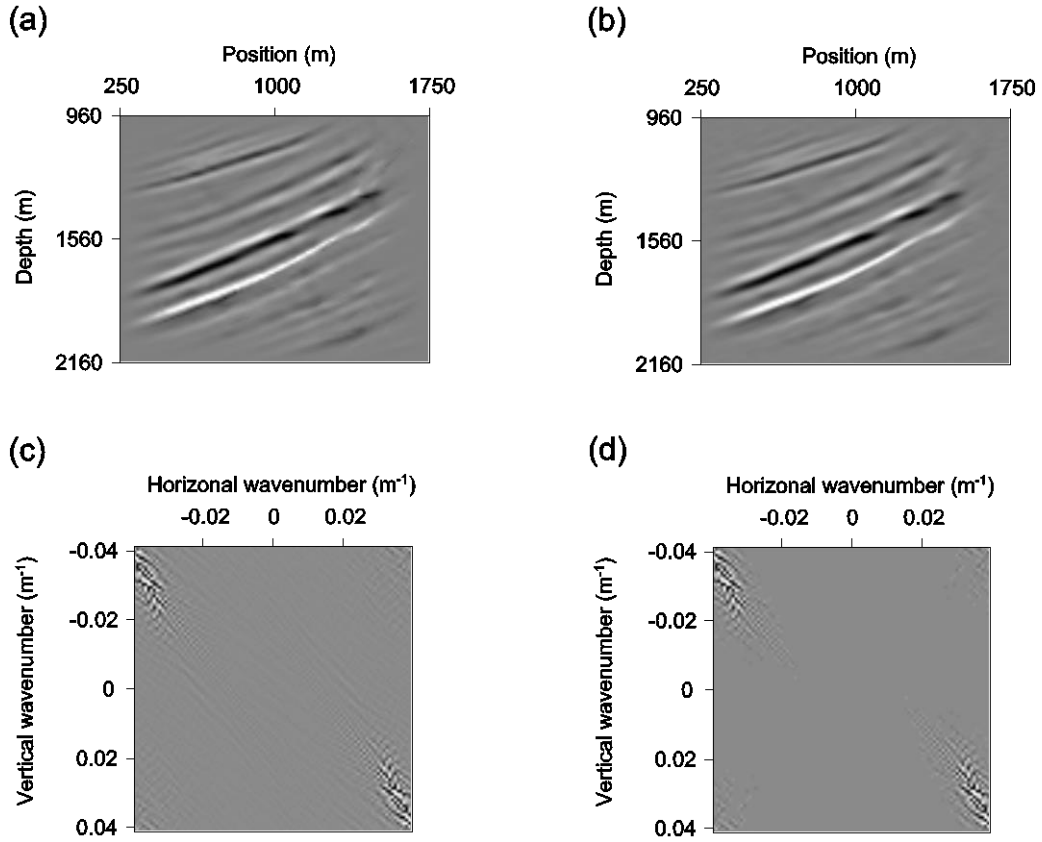


Figure 2.8. Image recovery by using RMS as a criterion. a) is a local window in the \mathbf{x} domain. By using a forward FT from \mathbf{x} to \mathbf{k} , a) is transformed into c) in the \mathbf{k} domain, which contains 10201 points. By using RMS as a criterion, 1577 points are selected from c), to give d). By using an inverse FT from \mathbf{k} to \mathbf{x} , d) is transformed into b), which is a recovered image of a).

- i. For each source direction angle, extract the corresponding partitioned RTM image from the SACIGs.
- ii. For a local grid point \mathbf{x}' in the partitioned image, construct a local square (or rectangular) window around it.
- iii. Transform the image in this local window from the \mathbf{x} domain to the \mathbf{k} domain and obtain $I(\mathbf{k})$. The boundaries of this window in the \mathbf{x} domain need to be tapered (Figure 2.9)

before the forward FT. (Note, this tapering is to avoid the truncation artifacts of the forward FT from \mathbf{x} to \mathbf{k} , and thus does not relax the plane-wave assumption, which is required to avoid the truncation artifacts caused by transforming the ADCIGs from \mathbf{k} back into \mathbf{x} by inverse FTs.)

- iv. Calculate the RMS of the moduli of all the $I(\mathbf{k})$ points.
- v. For each $I(\mathbf{k})$ point, if its modulus is less than the RMS, do nothing; otherwise, transform $I(\mathbf{k})$ from the \mathbf{k} domain back into the \mathbf{x} domain (using the inverse spatial FT) and obtain $i_{\mathbf{k}}(\theta, \varphi)$ at the local point \mathbf{x}' ,

$$i_{\mathbf{k}}(\mathbf{x}', \theta, \varphi) = I(\mathbf{k}) e^{-i\mathbf{k}\mathbf{x}'}, \quad (2.11)$$

where θ and φ are calculated from the \mathbf{k} by using equation 2.10. Adding $i_{\mathbf{k}}(\mathbf{x}', \theta, \varphi)$ to the angle gathers $i(\mathbf{x}', \theta, \varphi)$,

$$i(\mathbf{x}', \theta, \varphi) = i(\mathbf{x}', \theta, \varphi) + i_{\mathbf{k}}(\mathbf{x}', \theta, \varphi). \quad (2.12)$$

- vi. Repeat Steps iv and v until all the $I(\mathbf{k})$ points have been processed.
- vii. Repeat Steps ii to vi until all the \mathbf{x} points of the partitioned image have been processed.
- viii. Repeat Steps i to vii until all the partitioned images (each corresponds to a source angle) have been processed.

Comparisons of ADCIGs obtained using spatially global FTs and spatially local ALFTs are shown in Figure 2.10 (using the correct migration velocity) and Figure 2.11 (using an 8% low

migration velocity). ADCIGs obtained using the spatially local ALFT have fewer Fourier truncation artifacts than those using spatially global FTs (e.g., see the red and blue boxes in Figures 2.10a and 2.10b; also see the red boxes in Figures 2.11a and 2.11b).

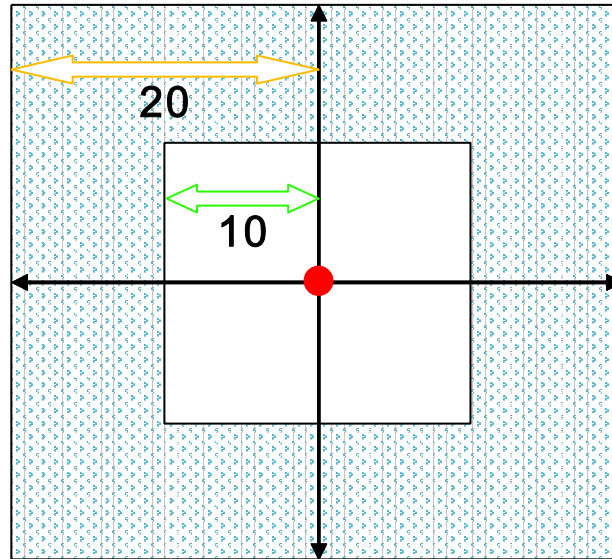


Figure 2.9. Schematic diagram for a local spatial window. The selected (red) point is at the center. The size of the window is 41x41 grid points, so (excluding the red point) there are 20 grid points in each arrow direction. To avoid the Fourier truncation artifacts of the forward FT from the \mathbf{x} to \mathbf{k} domain, the amplitudes in the shaded region need to be tapered from the inner (box) boundaries to the outer (box) boundaries; the width of the tapering region is ten grid points.

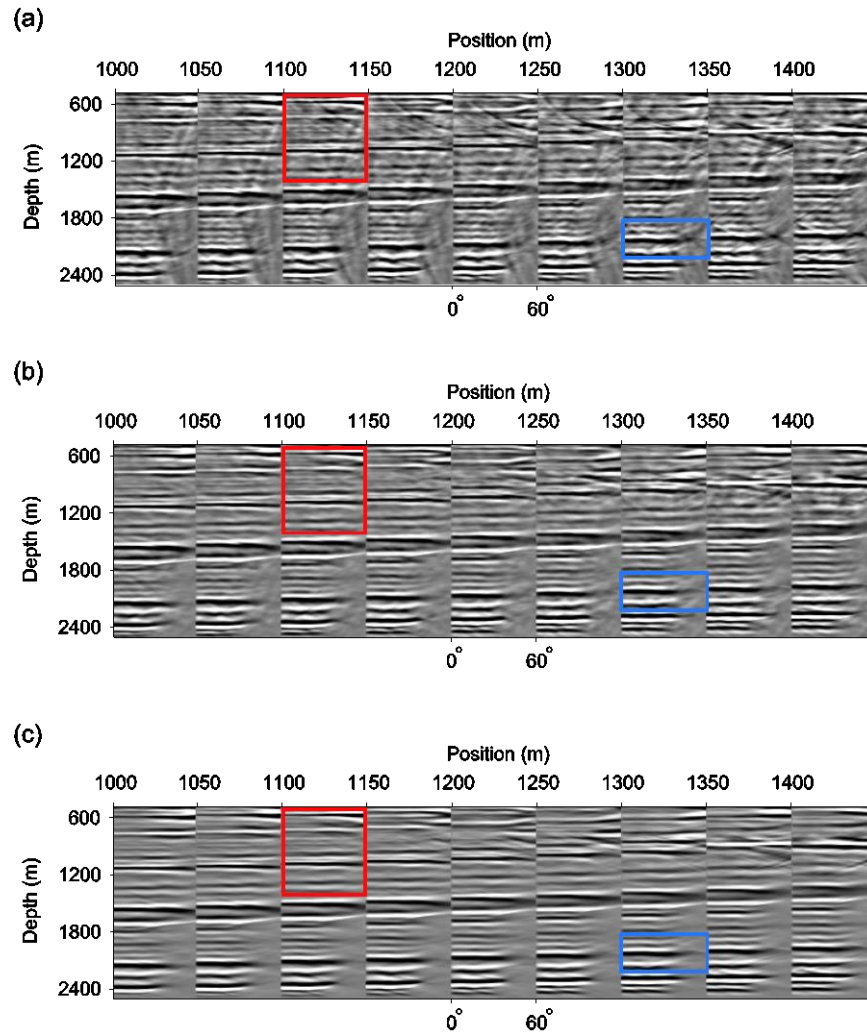


Figure 2.10. Comparison of ADCIGs by a) spatially global FT, b) spatially local ALFT and c) spatially global ATFT, using the correct migration velocity of the modified Marmousi model. The spatially local ALFT in panel b) uses a local window with a size of 41x41 grid points (see Figure 2.9 for details) in the \mathbf{x} domain. The spatially global ATFT in panel c) uses a T -window with a radius of ten grid points in the \mathbf{k} domain. This example is for the region in the red box of Figure 2.4b. The Fourier truncation artifacts in Panel (a) are reduced in Panels (b) and (c); e.g., see the red and blue boxes. The ADCIGs in Panel (c) have the least artifacts.

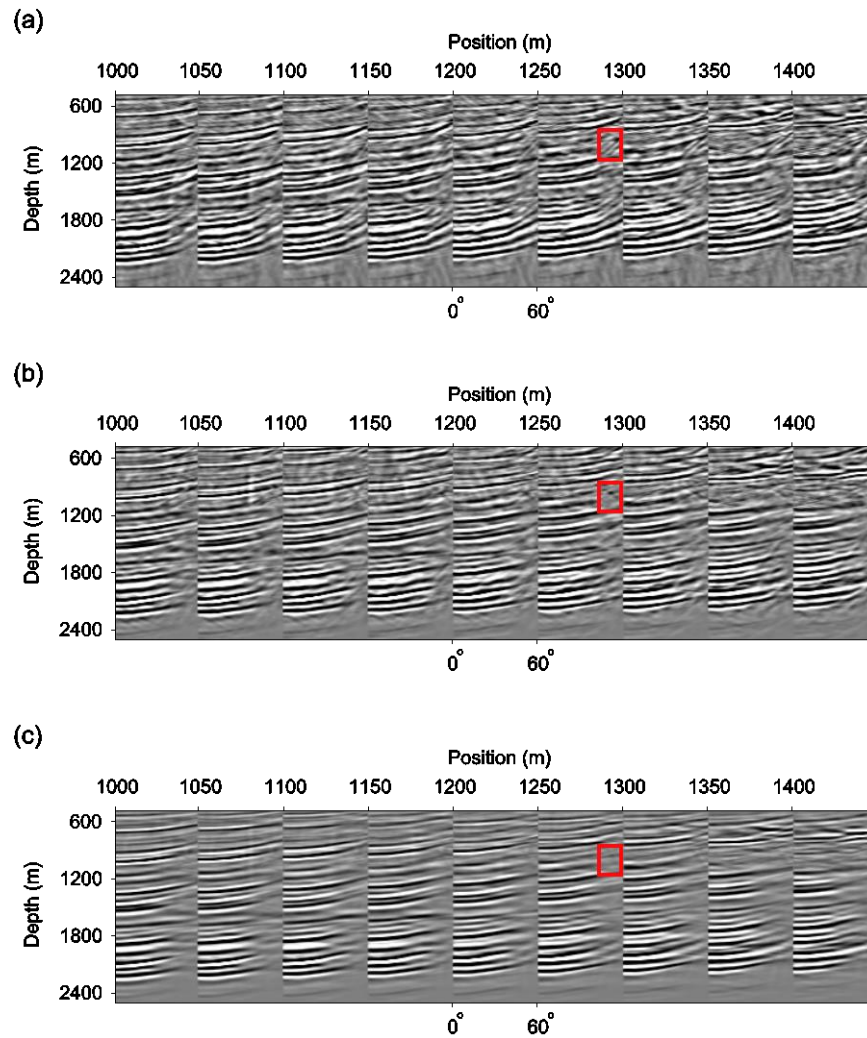


Figure 2.11. Comparison of ADCIGs by (a) spatially global FT, (b) spatially local ALFT and (c) spatially global ATFT, using an 8% lower migration velocity. The spatially local ALFT in panel (b) uses a local window with a size of 41x41 grid points (see Figure 2.9 for details) in the \mathbf{x} domain. The spatially global ATFT in panel (c) uses a T -window with a radius of ten grid points in the \mathbf{k} domain. In panel (a), the red box indicates one of several areas with artifacts, which are reduced in (b) and (c). The overall image quality is significantly improved by the ATFT (panel c).

2.3.4 Anti-truncation-artifact Fourier transform (ATFT) in global space

In the previous subsection, the Fourier truncation artifacts are reduced by using spatially local ALFTs. That method works well because the images are more likely to be primarily planar in a local window than in the global space; however, it has two disadvantages:

- 1) Calculating ADCIGs in local spatial windows does not relax the plane-wave assumption.

The images may still have curvatures in the local windows, especially when the migration velocity is not correct. For an under- or over-estimated velocity, the resulting image contains more curved (defocused) reflection events (Figure 2.7b). So artifacts still remain (e.g., the red box in Figure 2.11b). Setting a smaller local window is useful to reduce these artifacts, but a local window that is too small will lead to low angle resolution (Jin et al., 2014).

- 2) The ALFT flow requires a huge number of spatially local FTs. The calculation in each local spatial window (Steps ii-vi of the ALFT flow in Section 2.3.3) is only to obtain the ADCIG at its center point.

Fourier truncation artifacts are produced when transforming the selected single point from the \mathbf{k} domain back to the \mathbf{x} domain (in Step v of the ALFT algorithm in Section 2.3.3). Each single point in the \mathbf{k} domain corresponds to a single plane wave/image in the \mathbf{x} domain; thus, if the images are not primarily composed of planar segments in \mathbf{x} , sorting this single point into ADCIGs (equation 2.11) in the \mathbf{k} domain leads to a sharp truncation, and then transforming this truncation back to the \mathbf{x} domain using inverse FT will produce Fourier truncation artifacts. Therefore, to relax the plane-wave assumption, we propose to taper the truncation point in a

small window (surrounding this point) in the \mathbf{k} domain; this window is defined as a T -window and the algorithm is called the anti-truncation-artifact Fourier transform (ATFT). Because of the relaxation of the plane-wave assumption, the ATFT can be done in the global space rather than in local spatial windows (note, the “global space” here corresponds to the \mathbf{x} domain, and the local T -window corresponds to the \mathbf{k} domain; thus, a spatially global ATFT is done for global space and local wavenumbers). Its flow is as follows:

- i'. For each source direction-angle, extract the corresponding partitioned RTM image from the SACIGs.
- ii'. Transform this partitioned image from \mathbf{x} to \mathbf{k} by using forward FTs for the global space and obtain Γ in the \mathbf{k} domain. The boundaries of the image in \mathbf{x} need to be tapered before the forward FT.
- iii'. For each grid point \mathbf{k}_0 , set a small T -window centered at this point (this window can be circular for 2D or spherical for 3D), and taper the amplitudes from the center to the boundaries of this window. Sort and sum this T -window into the ADCIGs $I(\mathbf{k}, \theta, \vartheta)$ in the \mathbf{k} domain,

$$I(\mathbf{k}, \theta, \vartheta) = I(\mathbf{k}, \theta, \vartheta) + \int_{\Omega} d\mathbf{k} \Gamma(\mathbf{k}) f(\mathbf{k}), \quad (2.13)$$

where θ and ϑ are calculated using \mathbf{k}_0 at the central point of this T -window for equation 2.10. $f(\mathbf{k})$ is a normalized tapering function and satisfies

$$\int_{\Omega} d\mathbf{k} f(\mathbf{k}) = 1, \quad (2.14)$$

to preserve the amplitude (Appendix 2E [Section 2.12]). The Ω is the T -window, which should be small to maintain adequate resolution. A combination of equations 2.13 and 2.14 gives

$$I(\mathbf{k}, \theta, \vartheta) = I(\mathbf{k}, \theta, \vartheta) + \frac{1}{\int_{\Omega} d\mathbf{k} g(\mathbf{k})} \int_{\Omega} d\mathbf{k} \Gamma(\mathbf{k}) g(\mathbf{k}), \quad (2.15)$$

where

$$g(\mathbf{k}) = \frac{1}{2} \left(1 + \cos \left(\frac{l}{r} \pi \right) \right), \quad l \leq r, \quad (2.16)$$

is a tapering function without normalization (l denotes the distance between the center point \mathbf{k}_0 and a tapering point \mathbf{k} and r is the radius of the T -window), and

$$f(\mathbf{k}) = \frac{g(\mathbf{k})}{\int_{\Omega} g(\mathbf{k}) d\mathbf{k}}. \quad (2.17)$$

- iv'. Repeat Steps iii' until all the grid points in the \mathbf{k} domain are processed.
- v'. Repeat Step i' to iv' until all the partitioned images (each partitioned image corresponds to a source direction-angle) are processed.
- vi'. For each θ and ϑ , use spatially global inverse FTs to transform ADCIGs from the \mathbf{k} domain [defined as $I(\mathbf{k}, \theta, \vartheta)$] back to the \mathbf{x} domain [defined as $i(\mathbf{x}, \theta, \vartheta)$].

Note, the amplitude tapering at the boundaries of the global space in Step ii' here corresponds to that in Step iii of the ALFT flow in the previous subsection (Figure 2.9). This tapering is different from the tapering in the T -windows (Step iii' of ATFT), because the former

is done in the \mathbf{x} domain to avoid the truncation artifacts of the forward FT from \mathbf{x} to \mathbf{k} , which is a commonsense aspect of performing forward FTs. The tapering of the T -windows is done in the \mathbf{k} domain to smooth the truncations of \mathbf{k} when sorting the partitioned image into ADCIGs, and thus to reduce the truncation artifacts caused by transforming the ADCIGs from the \mathbf{k} domain back into the \mathbf{x} domain through the inverse FT. The tapering of the T -windows is the key point of the ATFT flow. The unit of the T -window radius r and the distance l can be either the grid point or m^{-1} (which is the unit of the wavenumber). We use the former one in our implementation and the latter one for the resolution analysis (Appendix 2F [Section 2.13]); but there is not a conflict because the horizontal and vertical grid intervals in our examples are similar (for the Marmousi examples) and same (for the simple-model example in Appendix 2C [Section 2.10]).

The ATFT relaxes the plane-wave assumption of the FT/ALFT by using the T -window to taper the amplitudes in a local window which surrounds the selected single point; thus the ATFT can be done in the global space, instead of in local spatial windows. The nature of the ATFT can also be regarded as an amplitude tapering in the angle domain (see Appendix 2F [Section 2.13]). Using the T -window in the \mathbf{k} domain will lower the angle resolution, because the entire T -window uses the angle obtained from the \mathbf{k} at its central point (\mathbf{k}_0) for the ADCIG sorting (equation 2.13). However, the resolution loss can be ignored because the ATFT is done for the global space (rather than in local spatial windows), which often gives a very high angle-resolution for the images at the dominant wavenumbers. Actually, because the angles of ADCIGs often need to be equally spaced, interpolation or angle-binning needs to be done when sorting the calculated reflection/azimuth angles into ADCIGs, so overly-high angle resolution is unnecessary. For example, the difference between an angle of 29.9° and an angle of 30° can be

ignored. The choice of the radius of the T -window is qualitative. Our ATFT examples use a circular T -window with a radius of ten grid points, which is small compared with the model dimension in the \mathbf{k} domain (420x210 grid points). Furthermore, the tapering weight of a grid point in the T -window decreases with increasing distance from the central point; less weight indicates less influence on the resolution. To maintain the resolution while using the T -window, using a smaller sampling interval for \mathbf{k} during the forward FT (from \mathbf{x} to \mathbf{k}) may also be useful.

In Figures 2.10 and 2.11, the ADCIGs obtained using the spatially global ATFT (Figures 2.10c and 2.11c) contain the least artifacts. For example, in the red boxes of Figure 2.11 (using an 8% low migration velocity), the artifacts in the ADCIGs using the spatially global FT (Figure 2.11a) are reduced by using the spatially local ALFT (Figure 2.11b), but some still remain; using the spatially global ATFT can effectively remove these artifacts and give high quality ADCIGs (Figure 2.11c).

2.4 Examples

The entire data flow of combining source-side MPV with ATFT to calculate ADCIGs from RTM is presented in Figure 2.12. Several examples have been presented in the “Theory” section to illustrate each step in the flow (see Appendix 2C [Section 2.13] for an example of an SACIG and an ADCIG for a simple layered model). A short discussion of the cost of the data flow is in Appendix 2G [Section 2.14]. In this section, we focus on the comparison between ADCIGs obtained using different numbers of vector bins in calculating the multidirectional source vectors (refer to equations 2.1~2.3).

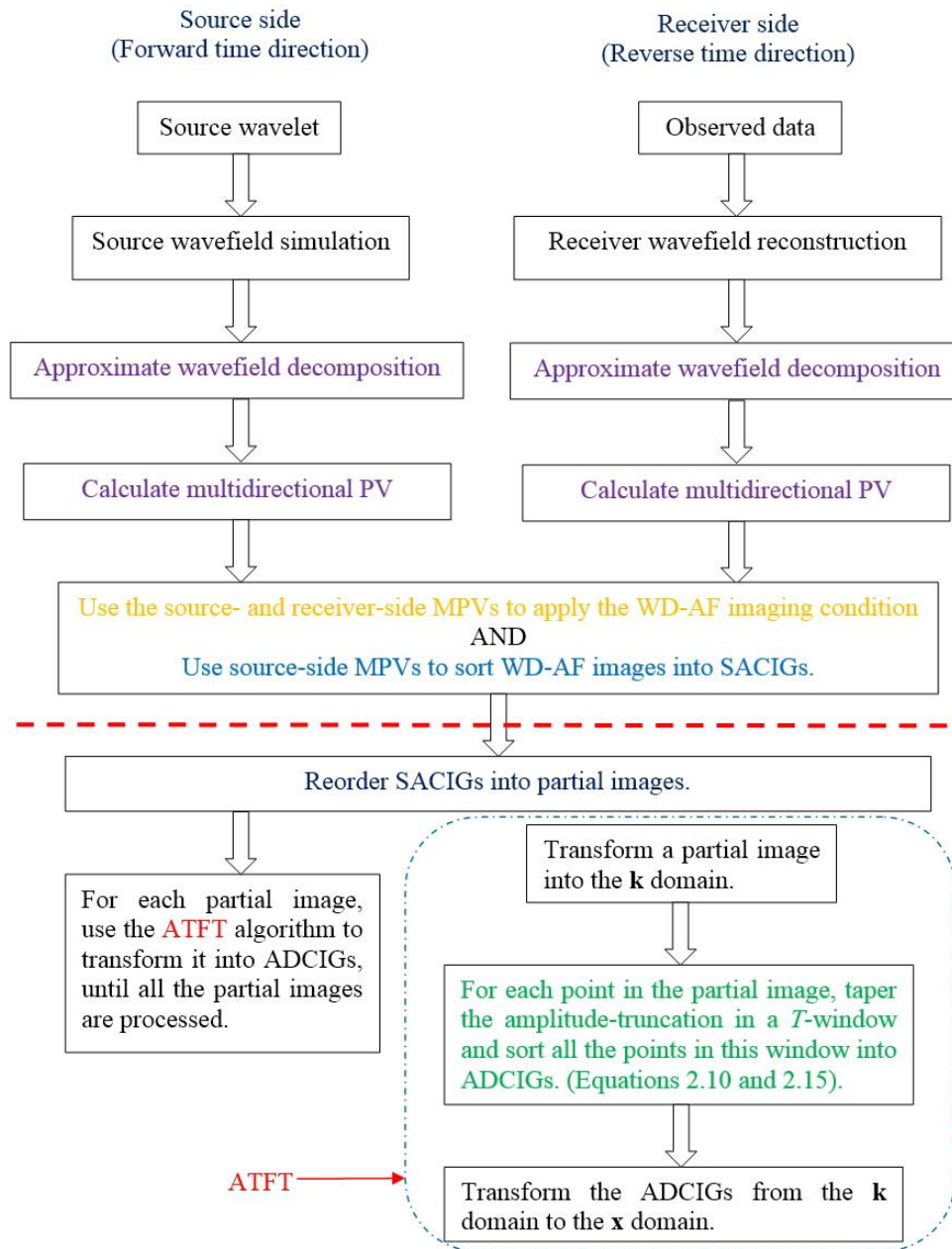


Figure 2.12. The proposed data flow. The dashed red line separates the during-imaging and post-imaging processes. During the imaging, the receiver-side MPVs are used only in performing the WD-AF imaging condition which requires less angle-resolution than calculating SACIGs/ADCIGs.

The parameters for the numerical tests (for the Marmousi examples) are: the dominant frequency is 20 Hz, the horizontal interval is 12.5 m, the vertical interval is 12.0 m, and the time interval is 1 ms. There are 240 sources; the wavefields propagated from each source are recorded by 401 receivers with the offset range -2500 ~ 2500 m. Because the angles in ADCIGs need to be equally spaced (the interval of angle sampling in all of our examples is 1°), a small Gaussian binning of the calculated angles (Tang et al., 2017a) is used, which also increases the stability of the ADCIGs. We use finite-differencing (FD) and a perfectly-matched-layer (PML) boundary condition of the scalar wave equation for the simulation/reconstruction of wavefields. The FD uses 2nd order time derivatives and 10th order space derivatives. Finite differencing is also used to calculate the time and space derivatives of the PV.

For the ADCIGs in the previous section, four vector bins are used to calculate the multidirectional source vectors. Because the velocity structure in the region from 1000 m to 1400 m (in the red box in Figure 2.4b) is not as complicated as in the central part of the modified Marmousi model (e.g., in the blue box in Figure 2.4b), using four vector bins is enough. For the WD-AF imaging condition, the number of vector bins of the receiver wavefield is the same as that of the source wavefield. Figure 2.13 contains a comparison of the ADCIGs obtained using four and twelve vector bins to calculate the multidirectional source vector in this structurally simple region; the resulting ADCIGs are similar, which means using four vector bins can separate most of wavefield overlaps in this (structurally simple) region. Their differences in the green boxes are because of the truncation point in the RTM image, where two reflectors intersect (see also the green circle in Figure 2.4b). ADCIGs obtained using twelve vector bins may have a few more artifacts than when using four vector bins (e.g., see the red boxes in Figure 2.13a and

2.13b), because more vector bins increase the proportion of the total area that is involved in the tapering windows (the shaded areas in Figure 2.3), and thus increases the possibility of Fourier artifacts. As discussed above, using a tapering window of width 10° in the MPV can significantly reduce the amplitudes of the artifacts but cannot totally remove them. The comparison in Figure 2.13 shows that using four vectors is adequate for the structurally simple region in the red box of Figure 2.4b.

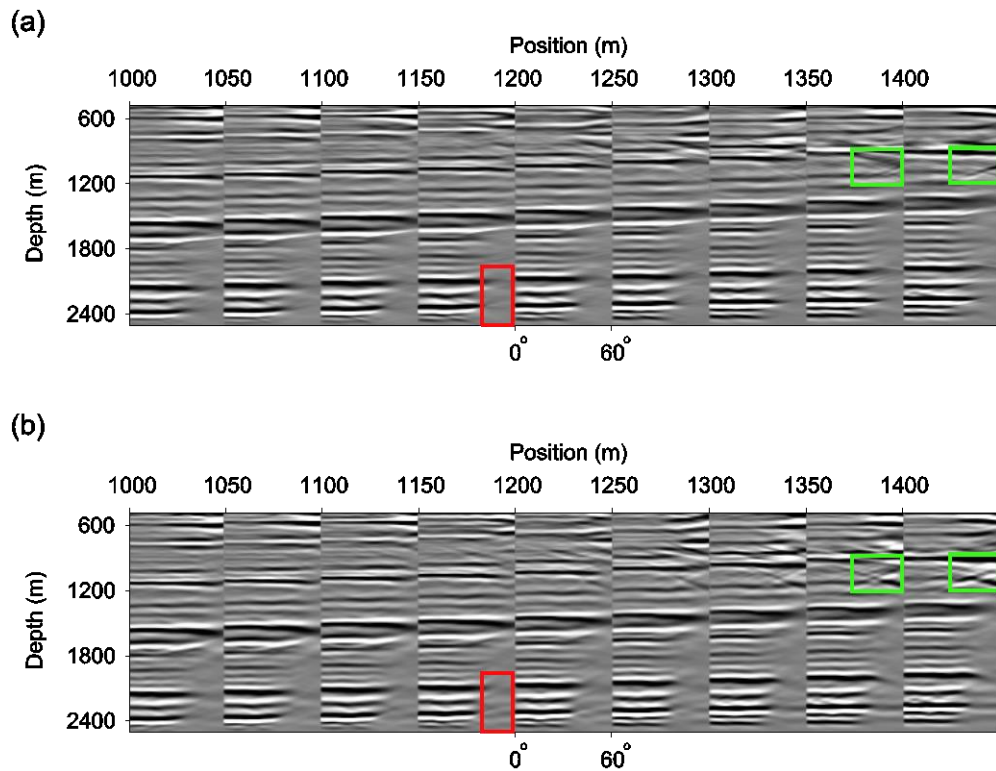


Figure 2.13. Comparison of ADCIGs using a) four and b) twelve source vector bins in a relatively simple region (in the red box in Figure 2.4b) of the modified Marmousi model.

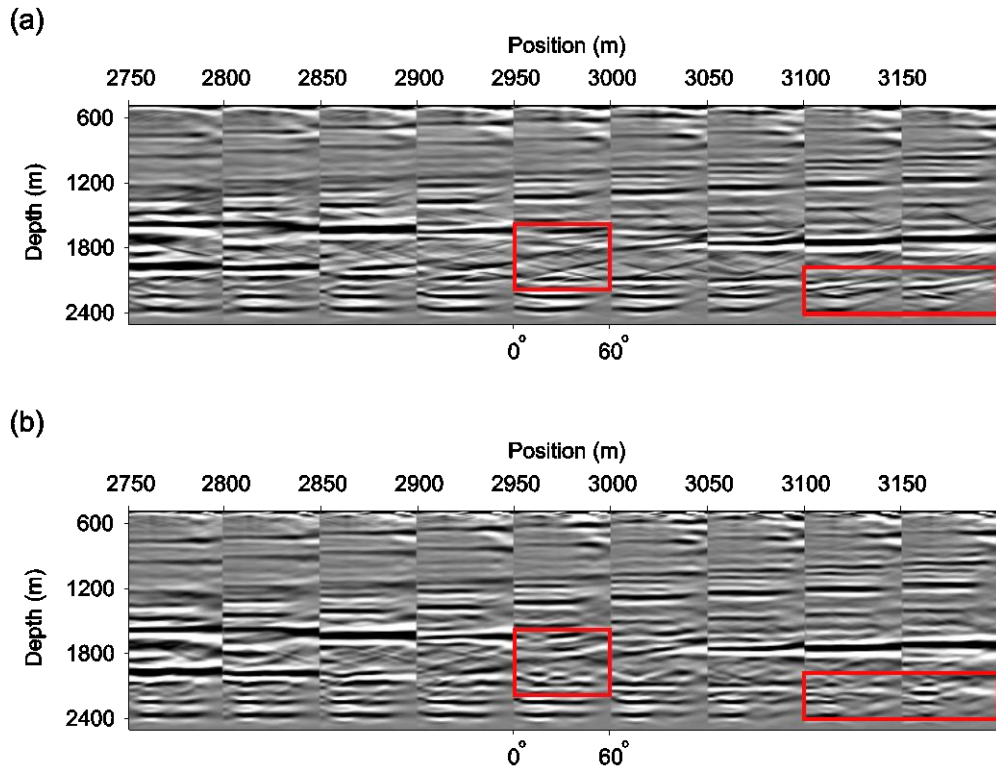


Figure 2.14. Comparison of ADCIGs using a) four and b) twelve source vector bins in a relatively complicated region (in the blue box in Figure 2.4b) of the modified Marmousi model.

For the structurally complicated region in the blue box in Figure 2.4b, using four vector bins to calculate the multidirectional source vector is not sufficient, because the complicated structure increases the possibility of wavefield overlaps. Figure 2.14 shows a comparison between ADCIGs using four and twelve vector bins in this complicated region. In Figure 2.14a (obtained by using four vector bins), there are many crossing events (e.g., in the two red boxes in Figure 2.14a); the quality of the four-vector-bin ADCIGs is not sufficient. When using twelve vector bins, these crossing events are focused to flat events in Figure 2.14b (e.g., see the two red boxes), because using twelve vector bins provides a more accurate decomposed wavefield than using only four.

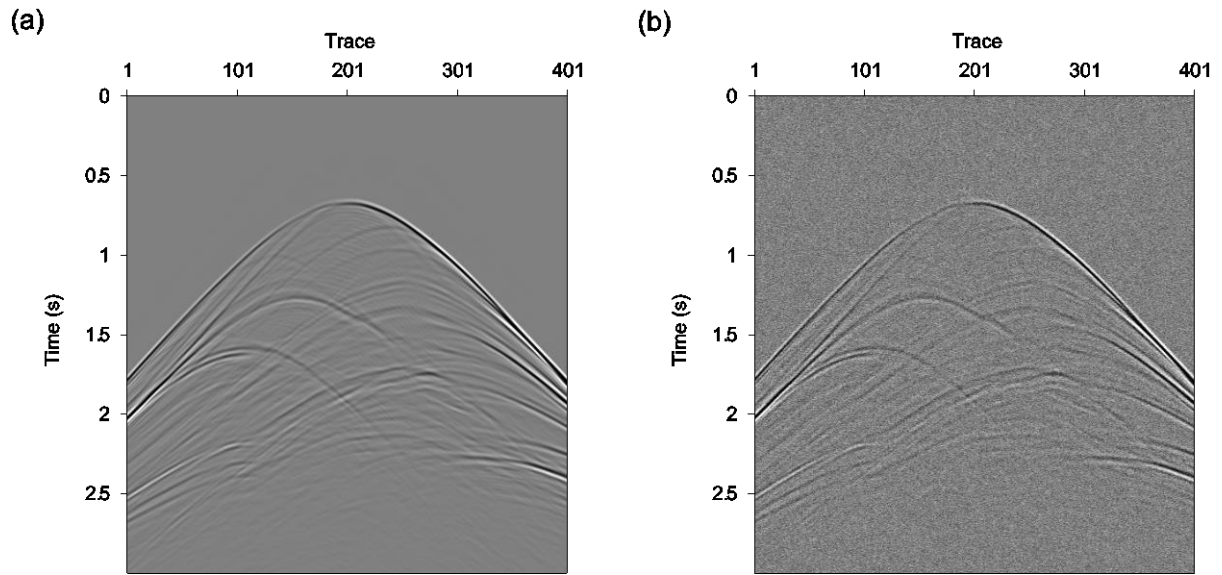


Figure 2.15. The observed data for source 120. (a) is the synthetic observed data. (b) is (a) with noise added. Panel (b) is used as the observed data for the RTM/ADCIGs in Figures 2.16 and 2.17.

The final example compares the ADCIGs obtained (a) using both the source- and receiver-side MPVs (see Appendix 2H [Section 2.15]), and (b) using the source-side MPV and the reflector normal. As explained in Section 2.2 “Introduction”, the reason to use the multidirectional source vector and reflector normal to calculate ADCIGs, is that the reconstructed wavefield from the observed data (defined as the “receiver wavefield”) is not as stable as the synthetic source wavefield (in practice, the observed data may contain different kinds of noise, seismic diffractions and other interferences). In this numerical example, we add noise to the observed data (Figure 2.15) and use it as the input for the two ADCIG-flows. In Figure 2.16, the reconstructed receiver-wavefield-snapshot (using the noisy observed data) is less stable than the simulated source-wavefield-snapshot (using a synthetic source). The comparison of ADCIGs using the two methods is shown in Figure 2.17. The ADCIGs in Figure 2.17c, which are calculated from source-side MPVs and reflector normal, has higher quality than the ADCIGs

in Figure 2.17b, which are calculated from source- and receiver-side MPVs. An important reason is that Figure 2.17c uses the reflector normal of the stacked image, rather than the reconstructed receiver-wavefield, to calculate ADCIGs. The stacked image is more stable because the data are focused by migration and the signal-to-noise ratio is increased by stacking (especially the stacking over multi-sources).

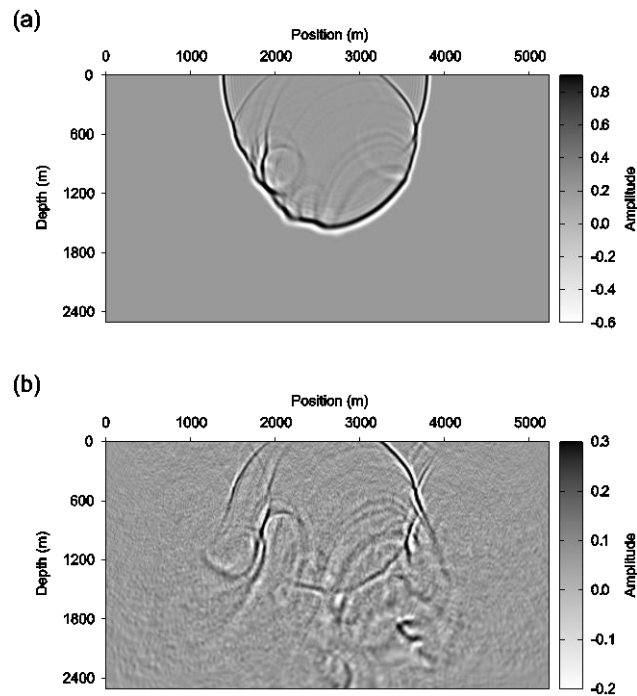


Figure 2.16. (a) The simulated wavefield-snapshot from a synthetic source. (b) The reconstructed wavefield-snapshot from the observed data with noise. The time for both (a) and (b) is 0.5 s. To clearly plot the noise, the boundaries of the scale bars do not mark the maximum/minimum amplitudes of the snapshots.

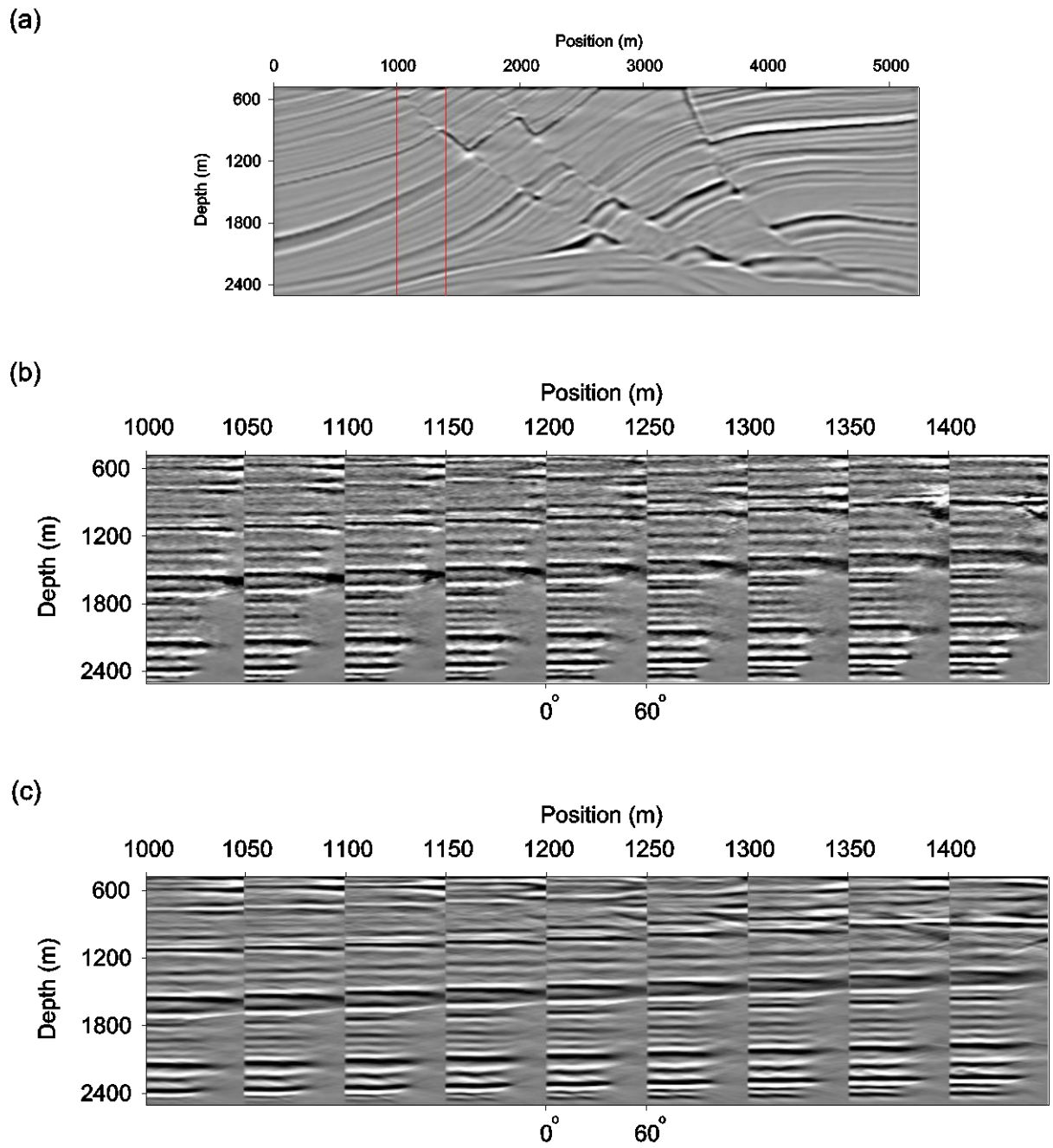


Figure 2.17. Comparison of ADCIGs using (b) source- and receiver-side MPVs and (c) source-side MPV and reflector normal, in a region (see the red box) of panel (a) the RTM image. This example uses four vector bins for MPV.

2.5 Discussion

In this chapter, a new anti-truncation-artifact Fourier transform (ATFT) is used to transform SACIGs into ADCIGs after migration. Although the numerical examples are in 2D, all the formulas of the data flow are in 3D, except equations 2.5 to 2.7 which describe the propagation/constrained-propagation-angles in 2D. Thus, the proposed data flow can also be applied in 3D, but there is an issue to be noted. In 3D, calculation of azimuth angles needs to use the 3D propagation angles (see equations 2.4 and 2.10), rather than constrained-propagation angles, to calculate the SACIGs. This is because the range of the azimuth angle ϑ in equation 2.10 is $[0^\circ, 180^\circ)$. The calculation of the reflection angle θ can use constrained-propagation angles because its range is $[0^\circ, 90^\circ)$ (see Figure 2.1 and equation 2.10). The proposed idea can also be extended to elastic media.

The SACIG-ADCIG transformation, which uses the normal directions of the reflection images, is independent of the propagation velocity. The ATFT algorithm has the potential to decrease the Fourier truncation artifacts in the ADCIG-calculation methods based on extended imaging conditions (Sava and Fomel, 2003, 2006; Fomel, 2004; Sava and Vlad, 2011); these previous algorithms involve a transformation from the local-offset or time-shift CIGs to ADCIGs, which are also post-migration and independent of the propagation velocity. The T -window of the ATFT can also be used to relax the plane-wave assumption when using the τ - \mathbf{p} transform to calculate the reflector-normal direction of an image or the polarization direction of a propagating wavefield.

As a relation between the reflectivity-to-velocity/impedance inversion, the Zoeppritz equations, and full waveform inversion (FWI) is established by Tang and McMechan (2017b), the ADCIGs may have wider applications in parameter inversions in the future by being incorporated into the FWI scheme.

2.6 Conclusions

A new data flow is proposed to use the source propagation vector and the reflector normal to calculate ADCIGs, which separates the calculation of ADCIGs into two steps. During migration, an MPV is used to calculate intermediate SACIGs. The MPV can calculate multiple directions from overlapping wavefields; tapering the amplitudes (of the wavefield) at the edges of angle bins decreases the Fourier truncation artifacts in MPV. To cleanly remove the backscattering artifacts in SACIGs, a WD-AF imaging condition is proposed.

After migration, the SACIGs are transformed into ADCIGs in the \mathbf{k} domain by using the reflector normal of the partitioned image of each source direction-angle. To reduce the Fourier truncation artifacts in ADCIGs, we compare two algorithms. One uses ALFT in local windows because the images are more similar to a plane wave in a local window than in the global space, but this method still has the plane-wave assumption in local windows and also requires a large number of spatially local FTs. The other method uses a new ATFT, which relaxes the plane-wave assumption (by using a T -window to taper the truncation point in the \mathbf{k} domain) and thus can be done in the global space. The ADCIGs obtained by using the ATFT in the global space have higher quality than using the ALFT in local spatial windows, and thus the ATFT algorithm

is preferred. Numerical tests show that the new data flow (combining multidirectional source vector with ATFT) can give high-quality ADCIGs.

2.7 Acknowledgments

The computational resources are provided by the Texas Advanced Computing Center (TACC) and the UT Dallas Geophysical Consortium (UTD GC). A research assistantship is provided via the financial support of the Sponsors of the UTD GC. We also appreciate the valuable comments from Associate Editor S. K. Foss, T. Dickens and two anonymous reviewers.

2.8 Appendix 2A “Amplitude-preserving taper functions between angle bins”

Consider an example where we separate the 360° of the “approximate” propagation angles into twelve vector bins in 2D; the width of each bin is 30° . A representative bin ($30^\circ, 60^\circ$) has two sharp angle truncations at 30° and 60° . To smooth these truncations, there needs to be two tapering windows ($30^\circ - \phi, 30^\circ + \phi$) and ($60^\circ - \phi, 60^\circ + \phi$); these two tapering windows at the edges of the angle bin ($30^\circ, 60^\circ$) are also shared by the two adjacent angle bins ($0^\circ, 30^\circ$) and ($60^\circ, 90^\circ$), respectively. Thus, to preserve the amplitude in a shared tapering window ($\bar{\psi}_{-\phi}, \bar{\psi}_{+\phi}$) with a width of 2ϕ , we choose the Raised-cosine filter (e.g., Proakis, 1995) to implement the tapering over angles,

$$\begin{cases} u'_i(\bar{\psi}) = u_i(\bar{\psi}) f'(\bar{\psi}) = u_i(\bar{\psi}) \times \frac{1}{2} \left[1 + \cos\left(\frac{\bar{\psi} - \bar{\psi}_{-\phi}}{2\phi} \times \pi\right) \right] = u_i(\bar{\psi}) \times \cos^2\left(\frac{\bar{\psi} - \bar{\psi}_{-\phi}}{2\phi} \times \frac{\pi}{2}\right), \\ u''_i(\bar{\psi}) = u_i(\bar{\psi}) f''(\bar{\psi}) = u_i(\bar{\psi}) \times \frac{1}{2} \left[1 + \cos\left(\frac{\bar{\psi}_{+\phi} - \bar{\psi}}{2\phi} \times \pi\right) \right] = u_i(\bar{\psi}) \times \sin^2\left(\frac{\bar{\psi} - \bar{\psi}_{-\phi}}{2\phi} \times \frac{\pi}{2}\right), \end{cases} \quad \bar{\psi}_{-\phi} < \bar{\psi} < \bar{\psi}_{+\phi},$$

(2A-1)

where u_i' and u_i'' are the amplitudes of the two adjacent vector bins in the shared tapering window $(\bar{\psi}_{-\varphi}, \bar{\psi}_{+\varphi})$; the \times between the two scalar values here (and in all subsequent occurrences) is a scalar product. Equation 2A-1 satisfies

$$\begin{cases} f' + f'' = 1, \\ u_i' + u_i'' = u_i, \end{cases} \quad (2A-2)$$

which means the total amplitude is preserved. For example, for the two adjacent vector bins $(30^\circ, 60^\circ)$ and $(60^\circ, 90^\circ)$ which share the tapering window $(55^\circ, 65^\circ)$ with a width of 10° , equation 2A-1 gives

$$\begin{cases} f'(\bar{\psi}) = \frac{1}{2} \left[1 + \cos \left(\frac{\bar{\psi} - 55^\circ}{10^\circ} \times \pi \right) \right], \\ f''(\bar{\psi}) = \frac{1}{2} \left[1 + \cos \left(\frac{65^\circ - \bar{\psi}}{10^\circ} \times \pi \right) \right], \end{cases} \quad 55^\circ < \bar{\psi} < 65^\circ. \quad (2A-3)$$

In this example, the first tapering function $f'(\bar{\psi})$ decreases from 1.0 at 55° to 0.0 at 65° (Figure 2.18a); the second tapering function $f''(\bar{\psi})$ decreases from 1.0 at 65° to 0.0 at 55° (Figure 2.18b). The summation of the two tapering functions at each angle is 1.0 at all $\bar{\psi}$ (Figure 2.18c), so the amplitudes are preserved.

2.9 Appendix 2B “Angle-filter design for removal of backscattering artifacts”

The RTM backscattering artifacts cannot be cleanly removed by using the wave decomposition (WD) imaging condition in equation 2.8. In Figure 2.5b, which uses four vector bins for the WD imaging condition, there are still artifacts in the vertical direction. These

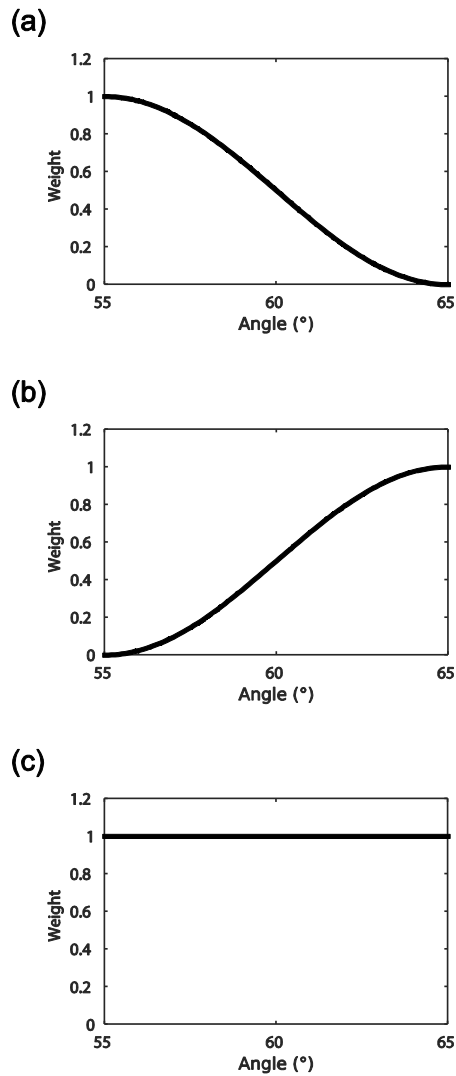


Figure 2.18. The tapering functions for two adjacent vector bins. a) is for the vector bin $(30^\circ, 60^\circ)$; b) is for the vector bin $(60^\circ, 90^\circ)$. The summation of a) and b) at each angle gives c); thus, the wavefield amplitudes in the tapering region $(55^\circ, 65^\circ)$ are preserved.

artifacts correspond to the shared tapering region $(90^\circ - \phi, 90^\circ + \phi)$ at the edges of the angle bins (see the shaded region in the vertical direction of Figure 2.4a). Note, the horizontal tapering (shaded) region in Figure 2.4a will not have corresponding artifacts, because waves propagating in the horizontal direction are hard to observe from the surface. The backscattering artifacts in

Figure 2.5b will negatively influence the transformation of SACIGs into ADCIGs, because they will be treated as reflections. To remove these artifacts, we define an angle filter,

$$F(\theta) = \begin{cases} 1, & \theta < \theta_1, \\ \frac{1}{2} \left[1 - \cos\left(\frac{\theta_2 - \theta}{\theta_2 - \theta_1} \times \pi\right) \right], & \theta_1 \leq \theta < \theta_2, \\ 0, & \theta \geq \theta_2, \end{cases} \quad (2B-1)$$

where θ_1 and θ_2 are two reflection angles that bound the taper of the reflection-angle (θ) filter.

The two-selected taper-angles need to be relatively-large reflection-angles to remove the backscattering artifacts near 90° while preserving most of the effective image; they are set empirically to 60° and 75° in our examples. The reflection angle θ in equation 2B-1 is calculated from the propagation directions of the source and receiver wavefields, but note, this does not conflict with our avoidance of using the low-reliability propagation directions of the receiver wavefields to calculate ADCIGs, because the angle resolution required by the filter in equation 2B-1 is low; the calculated reflection angle is used only for this angle filter and not to output ADCIGs. The comparisons of SACIGs and RTM images using WD and WD-AF imaging conditions are shown in Figures 2.5 and 2.6 using a complicated model.

2.10 Appendix 2C “SACIG and ADCIG for a simple model”

This appendix provides an example of an SACIG and an ADCIG using a simple layered velocity model with three flat reflectors (Figure 2.19a). The parameters for this numerical test are: the source wavelet uses a Ricker wavelet with a dominant frequency of 20 Hz, both the horizontal and vertical grid intervals are 10.0 m, and the time interval is 1 ms. There are 200 sources located from 20 m to 4000 m, which an interval of 20 m. The waves propagated from

each source are recorded by 401 receivers on the surface with the offset range -2000 ~ 2000 m; 40 points are used to taper each of the two boundaries of the observed data. For the angle sampling interval, the Gaussian binning, and the numerical method of wavefield simulation and reconstruction, please refer to the Marmousi example in the “Examples” section.

For simple models containing flat layers, or layers with small dip-angles, two vector bins (up and down) are enough to separate the incident and reflected waves. In this case, using the WD imaging condition is sufficient because the tapering region for the two vector bins are in horizontal directions (refer to Figure 2.4); waves that propagate in the horizontal direction are hard to be observed from the surface. Figure 2.19b shows the RTM image obtained using the WD imaging condition with two vector bins. Figure 2.20 contains the SACIG and ADCIG at horizontal location 2000 m. The proposed method gives high-quality ADCIGs for this simple model.

2.11 Appendix 2D “A general flow of the ALFT”

This Appendix contains a general ALFT flow as described by Xu et al. (2010). The algorithm below is between the t and ω domains; it can also be applied to the FTs between \mathbf{x} and \mathbf{k} (or $t\text{-}\mathbf{x}$ and $\omega\text{-}\mathbf{k}$).

- I. Transform the signal $f(t)$ into the ω domain to obtain $F(\omega)$.
- II. Calculate the modulus of each $F(\omega)$.
- III. Pick the $F_{\max}(\omega)$ with the maximum modulus, and convert this point (a single-frequency component) back to the t domain,

$$f_{\max}(t) = F_{\max}(\omega) e^{i\omega t}. \quad (2D-1)$$

Set the $F_{\max}(\omega)$ to be zero.

IV. Subtract $f_{\max}(t)$ from $f(t)$ at each t ,

$$f(t) = f(t) - f_{\max}(t). \quad (2D-2)$$

V. Repeat Steps III and IV until the residual, e.g.,

$$\varepsilon = \int_0^T |f(t)|^2 dt \quad (2D-3)$$

is small enough.

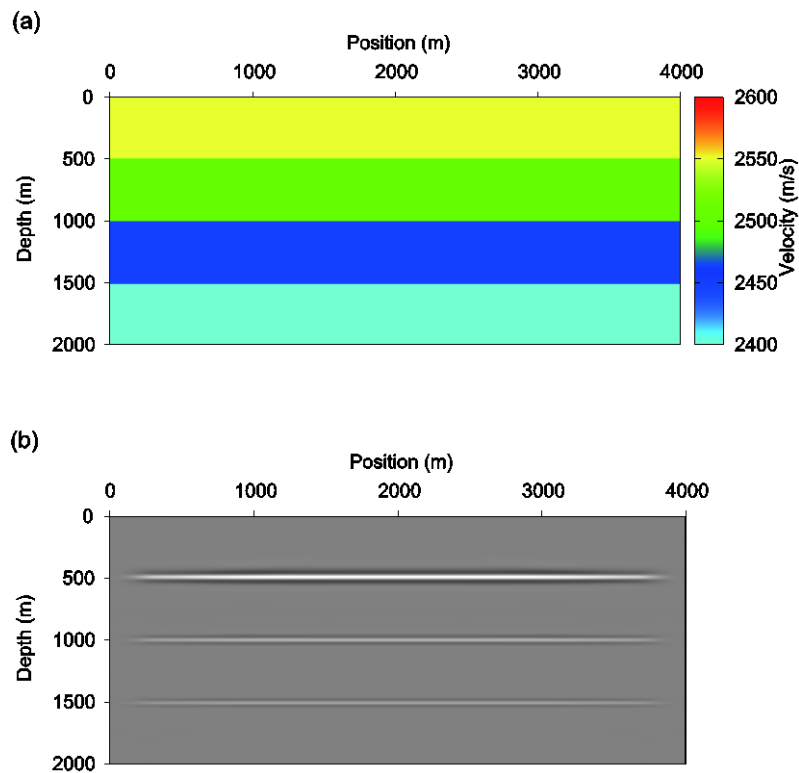


Figure 2.19. (a) The velocity model and (b) the stacked RTM image.

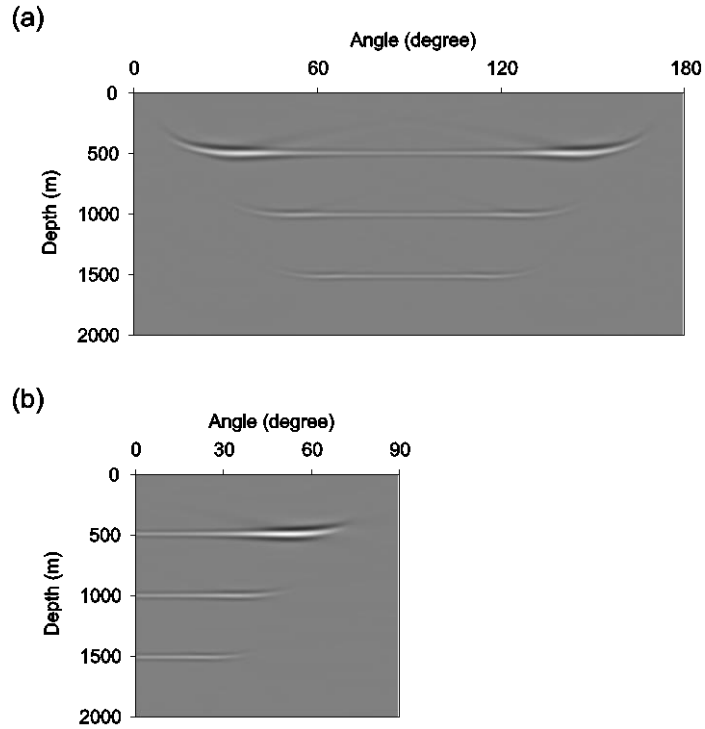


Figure 2.20. (a) an SACIG and (b) an ADCIG using the simple model in Figure 2.19a. The horizontal location for the SACIG and ADCIG is 2000 m. Refer to Figure 2.5a for the axis of constrained-propagation-angles used to sort SACIGs in Panel (a). The CIG at 180° can be included in the CIG at 0°.

2.12 Appendix 2E “Analysis of the amplitude in the T -window”

Figure 2.21 illustrates two overlapping circular T -windows in the \mathbf{k} domain, with a radius of two grid increments. Because of equations 2.16 and 2.17, in the red T -window (Ω), the normalized weight f at its central point ‘0’ is

$$f(\mathbf{k}_0) = \frac{1}{\int_{\Omega} g(\mathbf{k}) d\mathbf{k}}. \quad (2E-1)$$

The residual weight

$$f_r(\mathbf{k}_0) = 1 - f(\mathbf{k}_0), \quad (2E-2)$$

at Point ‘0’ is contributed by the other T -windows that use the blue points as center points (e.g., the blue ‘dashed’ T -window centered at the blue point ‘1’).

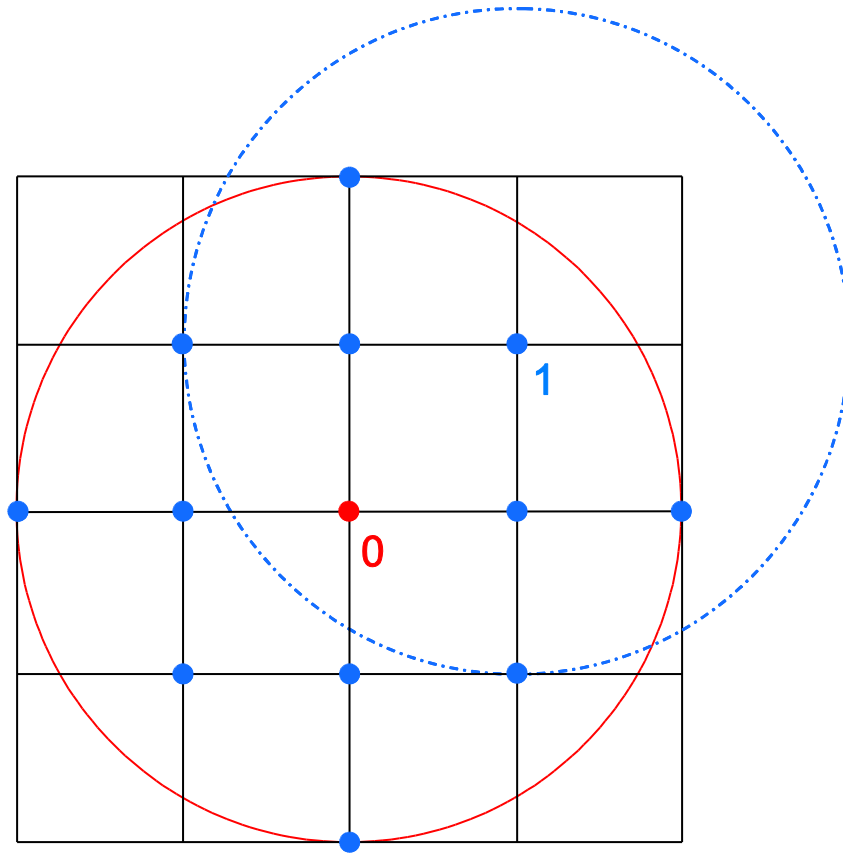


Figure 2.21. Schematic diagram for two overlapping T -windows in the \mathbf{k} domain. The red T -window involves the center (red) point ‘0’ and several tapering (blue) points including Point ‘1’, which is the center of the blue (dashed) T -window.

For example, Point ‘1’ is a tapering point for the red T -window centered at Point ‘0’, with a tapering weight of $f_{\mathbf{k}_0}(\mathbf{k}_1)$; similarly, Point ‘0’ is also a tapering point for the blue ‘dashed’ T -window centered at Point ‘1’, with a tapering weight of $f_{\mathbf{k}_1}(\mathbf{k}_0)$. Because the distance between Points ‘0’ and ‘1’ is the same for both the red and blue T -windows,

$$f_{\mathbf{k}_0}(\mathbf{k}_1) = f_{\mathbf{k}_1}(\mathbf{k}_0). \quad (2E-3)$$

which leads to

$$f_{\mathbf{k}_0}(\mathbf{k}_n) = f_{\mathbf{k}_n}(\mathbf{k}_0), \quad (2E-4)$$

for an arbitrary blue point ‘ n ’. Thus, the summation of the tapering values at point ‘0’ (in all T -windows with this point included) is

$$I_f(\mathbf{k}_0) = \sum_{n=0}^{N-1} f_{\mathbf{k}_0}(\mathbf{k}_n) = \sum_{n=0}^{N-1} f_{\mathbf{k}_n}(\mathbf{k}_0), \quad (2E-5)$$

where N is the number of the points in the red T -window (note, ‘ n ’ starts at ‘0’ and thus ends at ‘ $N-1$ ’), which is also the number of all T -windows that include point ‘0’. Because the $\sum_{n=0}^{N-1} f_{\mathbf{k}_n}(\mathbf{k}_0)$

is the discrete expression of $\int_{\Omega} d\mathbf{k} f(\mathbf{k})$ in equation 2.14,

$$\sum_{n=0}^{N-1} f_{\mathbf{k}_n}(\mathbf{k}_0) = \int_{\Omega} d\mathbf{k} f(\mathbf{k}) = 1, \quad (2E-6)$$

and thus

$$I_f(\mathbf{k}_0) = 1, \quad (2E-7)$$

which means the amplitude at Point ‘0’ is preserved. For one point, its amplitude in each T -window that involves this point is a partition of unity. This relation/conclusion is also applicable to all other points of the image in the \mathbf{k} domain (excluding the boundary points of the model, which can be ignored). Although Figure 2.21 is a 2D schematic diagram, the theory in this Appendix also works for 3D.

2.13 Appendix 2F “Analysis of the ATFT algorithm”

The ATFT algorithm (e.g. equation 2.15) is equivalent to applying an amplitude-taper over angles in the \mathbf{k} domain, which is used during the approximate WD of the MPV-calculation process (see Appendix 2A [Section 2.8]). However, different from the approximate WD, during the transformation of SACIGs into ADCIGs, the reflection angle calculated by equation 2.10 is used to output ADCIGs in the \mathbf{k} domain; thus, it requires high accuracy.

Therefore, the ATFT cannot use an angle-tapering range as large as that in the approximate WD of MPV (e.g., 10°); a small tapering window (T -window) is used in the \mathbf{k} domain to achieve a similar goal (of angle-tapering) while preserving high accuracy. Based on equation 2.10, the center point \mathbf{k}_0 of a circular T -window corresponds to a reflection angle

$$\theta_0 = \cos^{-1} \frac{|\mathbf{p}_s \cdot \mathbf{k}_0|}{|\mathbf{p}_s| |\mathbf{k}_0|}. \quad (2F-1)$$

For other points in this T -window, the vector from the center point (\mathbf{k}_0) to an arbitrary point (\mathbf{k}_l) is

$$\Upsilon = \mathbf{k}_l - \mathbf{k}_0, \quad |\Upsilon| \leq r, \quad (2F-2)$$

where r is the radius of the T -window, with a unit of m^{-1} (which is the unit of the wavenumber).

Based on equation 2.10, \mathbf{k}_l corresponds to an angle

$$\theta_l = \cos^{-1} \frac{|\mathbf{p}_s \cdot \mathbf{k}_l|}{|\mathbf{p}_s| |\mathbf{k}_l|} = \cos^{-1} \frac{|\mathbf{p}_s \cdot (\mathbf{k}_0 + \Upsilon)|}{|\mathbf{p}_s| |\mathbf{k}_0 + \Upsilon|}. \quad (2F-3)$$

For the sorting into ADCIGs, the entire T -window uses θ_0 as the reflection angle, so the angle-error of the T -window is

$$\delta\theta = \theta_l - \theta_0 = \cos^{-1} \frac{|\mathbf{p}_s \cdot \mathbf{k}_l|}{|\mathbf{p}_s| |\mathbf{k}_l|} - \cos^{-1} \frac{|\mathbf{p}_s \cdot \mathbf{k}_0|}{|\mathbf{p}_s| |\mathbf{k}_0|} = \cos^{-1} \frac{|\mathbf{p}_s \cdot (\mathbf{k}_0 + \Upsilon)|}{|\mathbf{p}_s| |\mathbf{k}_0 + \Upsilon|} - \cos^{-1} \frac{|\mathbf{p}_s \cdot \mathbf{k}_0|}{|\mathbf{p}_s| |\mathbf{k}_0|}. \quad (2F-4)$$

In equation 2F-4, if a tapering point (\mathbf{k}_l) is near the center point (\mathbf{k}_0), this point has a small $|\Upsilon|$ which results in a small angle-error magnitude $|\theta_l - \theta_0|$; otherwise, this point has a large $|\Upsilon|$ which results in a large $|\theta_l - \theta_0|$. Based on equation 2.16, the taper points with small $|\Upsilon|$ or $|\theta_l - \theta_0|$ have large tapering weights; otherwise, they have small tapering weights.

The amplitude-truncation at θ_0 is tapered in the angle-range $(\theta_{l-\min}, \theta_{l-\max})$, where $\theta_{l-\min}$ and $\theta_{l-\max}$ correspond to the minimum and maximum angles in the T -window, respectively. The reduction of resolution caused by using the T -window is defined by the tapering function (e.g., equation 2.16) and the angle-range $(\theta_{l-\min}, \theta_{l-\max})$. The $(\theta_{l-\min}, \theta_{l-\max})$ depends on the source propagation vector \mathbf{p}_s , the location of the center point \mathbf{k}_0 and the radius of T -window r . Because we use a global spatial FT, the wavenumber-sampling is very dense; a small T -window will have a limited influence on the accuracy of most \mathbf{k}_0 . For very low wavenumbers, the T -window will have a relatively large influence, but these wavenumbers are not the dominant part of the image.

2.14 Appendix 2G “Discussion of computational cost of the proposed data flow”

The proposed data flow contains two parts. One is calculation of the MPV during the imaging; the other one is the transformation of SACIGs into ADCIGs after imaging.

During the imaging, the main increase of the computational cost of the MPV over that of the single-direction PV is associated with the calculation of the approximate WD and the calculation of the time-shift PVs for each decomposed wavefield. There are two important factors that determine the computational complexity and the memory requirement. One is the number of vector bins in equation 2.3 (Tang and McMechan, 2016); the other is the width of time-shift search window that relates to equation 2.2 (Tang et al., 2017a).

For a real-valued wavefield snapshot, the computation-time complexity of the fast Fourier transform (FFT) of a complex-valued 3D slice is $O(n_x \log n_x + n_y \log n_y + n_z \log n_z)$ where n_x , n_y and n_z are the numbers of sampling points in x , y and z dimensions, respectively. If the number of vector bins is M , the approximate WD in equation 2.2 requires $(M + 1)$ spatial FTs, including one forward FT and M inverse FTs.

If the computation time of the FFT and time-shift PV for a single complex-valued slice are T_{FFT} and T_{TPV} , respectively. The entire computational time of MPV for this single slice is

$$C = (M + 1)T_{FFT} + MT_{TPV} + H, \quad (2G-1)$$

where H is the time of the other processes including calculating the approximate angles in the \mathbf{k} domain. Here we assume the forward FFT has the same computational time as the inverse FFT.

In the second step (after imaging), the number of angles of SACIGs is an important factor in the computation time of the transformation from SACIGs to ADCIGs. The number of angles in SACIGs is also the number of the partitioned images. Assuming the computational complexity of transforming one partitioned image into ADCIGs is $O_{ATFT}(1)$, the complexity of the entire

SACIG-to-ADCIG transformation is $O_{ATFT}(N_{SACIG})$ where N_{SACIG} is the number of SACIGs (or the number of partitioned images). The computation time of the second step is independent of the number of time-steps (in wavefield modelling/reconstruction) and the number of sources.

2.15 Appendix 2H “Imaging condition for ADCIGs obtained using source- and receiver-side MPVs”

The ADCIGs that are calculated by both source- and receiver-side MPVs, use a WD imaging condition (e.g., Tang et al., 2017a)

$$I(\mathbf{x}, \theta, \vartheta) = \int dt \sum_{i=1, j=1}^{i=N, j=M} (1 - \delta_{ij}) \delta(\theta_{ij} - \theta'_{ij}) \delta(\vartheta_{ij} - \vartheta'_{ij}) u_{s,i}(\mathbf{x}, t) u_{r,j}(\mathbf{x}, t), \quad (2H-1)$$

where the reflection angle θ' and azimuth angle ϑ' are obtained from

$$\begin{cases} \theta'_{i,j} = \frac{1}{2} \cos^{-1} \frac{\mathbf{p}_{s,i} \cdot (-\mathbf{p}_{r,j})}{|\mathbf{p}_{s,i}| |\mathbf{p}_{r,j}|}, \\ \vartheta'_{i,j} = \cos^{-1} \frac{\{[\mathbf{p}_{s,i} \times (-\mathbf{p}_{r,j})] \times \hat{\mathbf{z}}\} \cdot \hat{\mathbf{x}}}{|\mathbf{p}_{s,i}| |\mathbf{p}_{r,j}|}, \end{cases} \quad (2H-2)$$

where $\mathbf{p}_{r,j}$ is the propagation vector of the receiver wavefield (in the forward time direction).

The sign of $\mathbf{p}_{r,j}$ in equation 2H-2 is determined by its definition (in the forward or reverse time direction).

CHAPTER 3

DYNAMICALLY-CORRECT MULTIDIRECTIONAL POYNTING VECTOR WITH APPLICATION IN CALCULATING ADCIGS FROM RTM*

3.1 Summary

Among the existing methods to calculate ADCIGs, the Poynting vector (PV), which shares the same propagation direction with the slowness vector (SV) in the time-space (t - \mathbf{x}) domain, is efficient, but it suffers from two main problems. The first problem is that each PV can give only a single propagation direction per grid point per time step and thus fails to give multiple directions at wavefield overlaps. The SVs in t - \mathbf{x} and ω - \mathbf{k} can be connected by Fourier transforms (FTs); the forward FT from t - \mathbf{x} to ω - \mathbf{k} decomposes a t - \mathbf{x} SV into different vector components (ω - \mathbf{k} SV), and the inverse FT sums these components into a unique direction (t - \mathbf{x} PV). Thus, the PV, which can be obtained from the t - \mathbf{x} SV, can give only a single direction; while the local plane-wave decomposition (LPD), which is based on the ω - \mathbf{k} SV, can give

* Tang C. and G. A. McMechan, 2018, The dynamically-correct formula of Poynting vector for acoustic media with application in calculating the multidirectional propagation vector to produce angle gathers from reverse time migration: *Geophysics*. (Accepted). Copyrighted by Society of Exploration Geophysicists. Permalink: <https://doi.org/10.1190/geo2017-0331.1>

Tang C. and G. A. McMechan, 2018, The dynamically-correct formula of Poynting vector for acoustic media with application in calculating the multidirectional propagation vector to produce angle gathers from reverse time migration: 88th International Meeting, SEG. (Submitted).

Tang C. and G. A. McMechan, 2016, Multidirectional slowness vector for computing angle gathers from reverse time migration: *Geophysics*, 81, no. 2, S11-S24. Copyrighted by Society of Exploration Geophysicists. Permalink: <https://doi.org/10.1190/geo2015-0134.1>

Tang C. and G. A. McMechan, 2015, Time-shift multidirection slowness vector for computing angle gathers from reverse time migration: Part 1 - Multidirection slowness vector: 85th International Meeting, SEG, 4360-4364. Copyrighted by Society of Exploration Geophysicists. Permalink: <https://doi.org/10.1190/segam2015-5838306.1>

Tang C. and G. A. McMechan, 2015, Time-shift multidirection slowness vector for computing angle gathers from reverse time migration: Part 2 - Conjugate relation, complex-valued extrapolation, and time shift: 85th International Meeting, SEG, 4365-4369. Copyrighted by Society of Exploration Geophysicists. Permalink: <https://doi.org/10.1190/segam2015-5838618.1>

multiple directions. Based on this discovery, we separate the calculation of propagation vectors into two steps. First, we use the forward FT, \mathbf{k}/ω binning, and several inverse FTs to separate the wavefields into vector bins with different approximate propagation angle ranges, which contains many fewer wavefield overlaps; then, we calculate the PVs for each vector bin. The resulting PVs constitute a multidirectional PV (MPV). To complete the flow, we develop an angle-tapering scheme to remove the Fourier truncation artifacts during the wave decomposition (of MPV) while preserving the amplitudes, and use a wavefield decomposition plus angle-filter imaging condition to remove the backscattering artifacts in the SACIGs and the RTM image. Moreover, the FTs between the t and ω domains require a huge I/O time. These can be avoided by extrapolating complex-valued wavefields and using the conjugate relation between the vector bins of the positive and negative frequencies, so only the positive frequencies need to be used.

The second problem is that the current PV formula in acoustic media is only kinematically correct; a typical issue is that the PV is zero at the wavefield peaks and thus the propagation directions are undetermined there. We derive the dynamically-correct PV formula for acoustic media, which is the negative of the product of the reciprocal of the density, the pressure field (PF) itself, and a factor that is obtained by applying both a time integration and a space derivative to the PF. Combining the dynamically-correct PV with the multidirectional scheme produces a dynamically-correct MPV. Because the multidirectional scheme already involves Fourier transforms between the time and frequency domains (which facilitates implementation of the time integration), its updated version causes only a very minor increase to the computational complexity of the original one.

3.2 Introduction

In Chapter 2, we use time-shift multidirectional PV to calculate propagation angles. The work has been published by Tang and McMechan (2015a, 2015b, 2016). The MPV is kinematically correct and thus the time-shift is used to increase its stability, which is explained in detail by Tang et al. (2017a). In this chapter, we develop a dynamically-correct MPV; the process to obtain it also provides a better derivation to the multidirectional theory. Thus, this chapter is a combination of our MPV paper (Tang and McMechan, 2016) with the dynamically-correct MPV. Generally, the dynamically-correct MPV solves a similar or the same problem as the time-shift MPV, but it is theoretically cheaper. Because this dynamically-correct theory was developed after the paper of Tang and McMechan (2017c), we include it in this chapter, and thus do not need to reproduce all the results contained in the second chapter.

In isotropic media, the PV has the same direction as the slowness vector (SV) in the time-space (t - \mathbf{x}) domain [in anisotropic media, the PV and SV do not have the same direction and a conversion from the group angle to the phase angle is required; refer to McGarry and Qin (2013)]; both give only a single propagation vector that is the sum of all the plane-wave components, so it is necessary to separate the overlapping wavefields before calculating their directions.

To address this issue, we propose decomposition of a wavefield into several approximate direction bins in ω - \mathbf{k} (or in t - \mathbf{k} by using complex-valued wavefields), and then using the PV to recalculate the directions within each bin in t - \mathbf{x} ; this method is defined as a multidirectional PV. Several schemes are proposed to address some practical issues of MPV. First, the approximate decomposition in the first step does not have a plane-wave assumption, and thus we develop an

amplitude-preserved tapering (APT) scheme in the angle domain to reduce the Fourier truncation artifacts. Second, because the APT scheme has shared tapering regions that may involve backscattering artifacts, although the wavefield decomposition (WD) imaging condition is used, we propose a wavefield decomposition plus angle-filter (WD-AF) imaging condition to produce a clear image and ADCIGs. Third, to reduce the cost of the approximate WD, we prove a conjugate relationship between the decomposition results of the wavefield with positive and negative frequencies, and thus we are able to apply the approximate WD only to the wavefields with positive frequencies; to avoid the huge I/O time caused by the Fourier transform between the t and ω domains, we can use the complex-valued wavefield extrapolation to produce the positive-frequency wavefield, and then the approximate WD can be implemented in the t - \mathbf{k} domain. The idea is initially proposed by us in 2015 (Tang and McMechan, 2015a, 2015b) and later was published as a Geophysics paper (Tang and McMechan, 2016). Richardson and Malcolm (2015) also propose to calculate PVs after wavefield decomposition, but they use local plane wave decomposition (LPD) to decompose the overlapping wavefields.

Another problem of the PV is its instability at the magnitude peak of the wavefield. There are two forms of acoustic PVs. One is (Yoon et al., 2004),

$$\mathbf{p} = -u \frac{\partial u}{\partial t} \frac{\partial u}{\partial \mathbf{x}}, \quad (3.1)$$

and the other is (Yoon et al., 2011),

$$\mathbf{p} = -\frac{\partial u}{\partial t} \frac{\partial u}{\partial \mathbf{x}}, \quad (3.2)$$

where \mathbf{p} is the PV, u is the pressure field, $\mathbf{x} = (x, y, z)$ is the spatial location and t is the time.

The most widely-used is equation 3.2, which can be considered as kinematically correct.

Both equations 3.1 and 3.2 contain an instability problem. For example, the PV in equation 3.2 is the negative of the product of time and space derivatives. These two derivatives result in a phase shift between the pressure wavefield (PF) and its PV; particularly, for a PF at a local magnitude peak, its PV modulus is zero and thus the propagation direction there is undefined (e.g., Tang et al. 2013a; Tang et al., 2017a). The PV is originally derived by Poynting (1884). As given in many text books (e.g., Böhmer, 2016 [Page 108]), its original physical definition is a representation of the directional energy flux density (the rate of energy transfer per unit area) of an electromagnetic field. The PV has the same physical meaning for a pressure field. Based on this definition, the magnitude of the PV modulus should be consistent with that of the pressure field; when the pressure magnitude is large (or small), the PV modulus should also be large (or small). Thus, the “zero-modulus” problem of the widely-used PV formula is not consistent with the physical law of PV.

Several methods (Yoon et al., 2011; Tang et al., 2013a; Yan and Ross, 2013; Zhang, 2014; Tang et al., 2017a) are proposed to address the instability issue. For example, Yoon et al. (2011) integrate the PVs over four dominant periods to improve its stability; Yan and Ross (2013) use a least-squares solution of an objective function to improve the stability of the propagation angles; Zhang (2014) uses an optical-flow algorithm to stabilize the calculation of the propagation vectors; Tang et al. (2017a) search for an optimal time-shift to locate the PV with maximum magnitude. None of these methods question the widely-used PV formula.

To solve this “zero-modulus” issue, we derive the dynamically-correct PV formula for acoustic media, which is the negative of the product of the reciprocal of the density, the PF itself, and a factor that is obtained by applying both a time integration and a space derivative to the PF.

We give the dynamically-correct PV formula for acoustic media in two different ways. The first derivation relies on the fact that the PV has the same direction as the slowness vector (SV) in acoustic media; thus, we can obtain the SV in the time-space (t - \mathbf{x}) domain and thereby obtain the acoustic PV. The second derivation simplifies the PV formula for elastic media (Červený, 2001; Dickens and Winbow, 2011) to obtain the acoustic PV. Because the MPV already involves Fourier transforms between the t and ω domains (which facilitates implementation of the time integration), its updated version causes only a very minor increase to the computational complexity of the original one.

3.3 Derivation of the multidirectional SV

The wave propagation equation in acoustic media can be written as

$$\frac{\partial^2 u}{\partial t^2} = \rho v_p^2 \nabla \cdot \left(\frac{1}{\rho} \nabla u \right), \quad (3.3)$$

where v_p is the P-wave propagation velocity, ρ is the density, $\nabla \cdot$ is a divergence operator and ∇ is a gradient operator $\partial/\partial \mathbf{x}$. For a constant density, equation 3.3 can be simplified to

$$\frac{\partial^2 u}{\partial t^2} = v_p^2 \left(\frac{\partial^2 u}{\partial x^2} + \frac{\partial^2 u}{\partial y^2} + \frac{\partial^2 u}{\partial z^2} \right). \quad (3.4)$$

Define the Fourier transforms (FTs) between the t - \mathbf{x} and ω - \mathbf{k} domains as

$$\bar{U}(\omega, \mathbf{k}) = \int_{-\infty}^{\infty} dt \int_{-\infty}^{\infty} d\mathbf{x} u(t, \mathbf{x}) e^{i(\mathbf{kx} - \omega t)}, \quad (3.5)$$

and

$$u(t, \mathbf{x}) = \frac{1}{2\pi} \int_{-\infty}^{\infty} d\omega \int_{-\infty}^{\infty} d\mathbf{k} \bar{U}(\omega, \mathbf{k}) e^{i(-\mathbf{k}\mathbf{x} + \omega t)}, \quad (3.6)$$

where ω is the angular frequency and \mathbf{k} is the wavenumber. In a local window in which v_p is assumed to be constant, using the forward FT in equation 3.4 to transform equation 3.3 into the ω - \mathbf{k} domain gives

$$\begin{aligned} \omega^2 &= v_p^2 \mathbf{k}^2, \\ \mathbf{s} &= \frac{\mathbf{k}}{\omega}. \end{aligned} \quad (3.7)$$

which is equivalent to

$$\mathbf{s}^2 = \left(\frac{\mathbf{k}}{\omega} \right)^2, \quad (3.8)$$

where \mathbf{s} is the SV and

$$|\mathbf{s}| = \frac{1}{v_p}. \quad (3.9)$$

Equation 3.8 has two propagation directions; one is the forward propagation direction

$$\mathbf{s} = \frac{\mathbf{k}}{\omega}, \quad (3.10)$$

and the other is the backward propagation direction,

$$\mathbf{s} = -\frac{\mathbf{k}}{\omega}, \quad (3.11)$$

where the sign is determined by the FT definitions in equations 3.5 and 3.6 (Tang and McMechan, 2016). Note, in each of equations 3.5 and 3.6, the signs before $\mathbf{k}\mathbf{x}$ and ωt are

different; if they were the same, equation 3.11 would define the forward propagation direction and equation 3.10 would define the backward direction. Based on the FT definitions in equations 3.5 and 3.6, we have

$$i\omega \leftrightarrow \frac{\partial}{\partial t}, \quad -i\mathbf{k} \leftrightarrow \frac{\partial}{\partial \mathbf{x}}, \quad (3.12)$$

where \leftrightarrow means an equivalence between the t - \mathbf{x} and ω - \mathbf{k} domains. Thus, under the first-order (high frequency) approximation which has also been used in deriving the Eikonal equation in acoustic media, equation 3.10 (the forward propagation direction in the ω - \mathbf{k} domain) is approximately equivalent to

$$\mathbf{s} = -\left(\frac{\partial}{\partial t}\right)^{-1} \frac{\partial}{\partial \mathbf{x}}. \quad (3.13)$$

In equation 3.13, the implicit high-frequency assumption comes from using the square of the first-order derivative to approximate the second derivative in equation 3.4. Both the time-integration and space-derivative operators need to be applied to the pressure field u to make sense (because an operator needs to be applied to a variable); thus, equation 3.13 needs to be implemented as

$$\mathbf{s} = -\frac{1}{u} \left[\left(\frac{\partial}{\partial t}\right)^{-1} \frac{\partial}{\partial \mathbf{x}} u \right] = -\frac{1}{u} \int \left(\frac{\partial}{\partial \mathbf{x}} u \right) dt, \quad (3.14)$$

which gives the SV in the t - \mathbf{x} domain. Note, the time integration can also be written inside the spatial derivative; this can be applied to all the similar equations below. Because the space derivative is calculated in a local window, equation 3.14 is consistent with the constant v_p

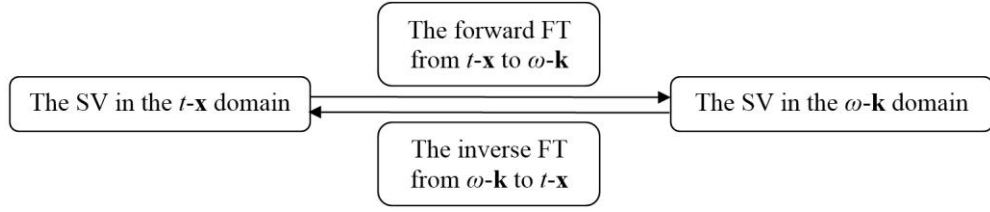


Figure 3.1. Relationship between the slowness vector in the $t\text{-}\mathbf{x}$ domain and the plane-wave decomposition in the $\omega\text{-}\mathbf{k}$ domain.

assumption that leads to equation 3.7. To make the \mathbf{s} a unit vector $\hat{\mathbf{s}}$, we can simply multiply the two sides of equation 3.14 by v_p ,

$$\hat{\mathbf{s}} = -v_p \frac{1}{u} \left[\left(\frac{\partial}{\partial t} \right)^{-1} \frac{\partial}{\partial \mathbf{x}} u \right] = -v_p \frac{1}{u} \int \left(\frac{\partial}{\partial \mathbf{x}} u \right) dt. \quad (3.15)$$

Equations 3.10 and 3.13 suggest the relationship between $\omega\text{-}\mathbf{k}$ and $t\text{-}\mathbf{x}$ SVs: The forward FT in equation 3.5 decomposes the $t\text{-}\mathbf{x}$ SV into a number of plane-wave components to give the $\omega\text{-}\mathbf{k}$ SVs; the inverse FT in equation 3.6 sums the $\omega\text{-}\mathbf{k}$ SVs to give the $t\text{-}\mathbf{x}$ SV; thus, the $\omega\text{-}\mathbf{k}$ SVs give multiple directions and the $t\text{-}\mathbf{x}$ SV gives only a single direction. This statement is the basis of the multidirectional SV (MSV) or MPV of Tang and McMechan (2016); see Figure 3.1. The MSV involves two main steps: First, decompose the wavefield into vector bins with different approximate propagation angles in the $\omega\text{-}\mathbf{k}$ domain; second, calculate the SV for each of the vector bins to construct the MSV. The MSVs can be expressed as

$$\mathbf{s} = (\mathbf{s}_1, \mathbf{s}_2, \mathbf{s}_3, \dots, \mathbf{s}_i, \dots, \mathbf{s}_{n-1}, \mathbf{s}_n), \quad (3.16)$$

$$\mathbf{s}_i = -\frac{1}{u_i} \int \left(\frac{\partial}{\partial \mathbf{x}} u_i \right) dt, \quad (3.17)$$

$$u_i = \frac{1}{2\pi} \Re \left[\int_{-\infty}^{\infty} \int_{(\alpha,\beta)_{i-1}}^{(\alpha,\beta)_i} \bar{U}(\omega, \mathbf{k}) e^{-i\mathbf{k}\mathbf{x} + i\omega t} d\mathbf{k} d\omega \right]. \quad (3.18)$$

Here, \mathbf{s}_i is an SV component of the MSV and i is a reference number for the decomposed wavefield and a SV component of the MSV. Note, the Fourier transform in equation 3.18 is for global space; thus, the wavefield decomposition uses the approximate propagation directions only to separate the wavefield overlaps. The accurate propagation direction is obtained by calculating the SV for each of the decomposed wavefields (equation 3.17); because of the global spatial FTs, the MSV does not have a plane-wave decomposition. Thus, amplitude-tapering needs to be done in the angle domain to avoid the Fourier truncation artifacts, which are discussed later in this section.

3.4 Derivation of the dynamically-correct multidirectional PV

Now, we need to obtain the acoustic PV from the t - \mathbf{x} SV in equation 3.14. As introduced in section 3.2, the physical definition of PV is the directional energy flux density, which is the rate of energy transfer per unit area, and thus the unit of it is $W \cdot m^{-2}$, which is equivalent to $J \cdot s^{-1} \cdot m^{-2}$ and $N \cdot s^{-1} \cdot m^{-1}$ because W is equal to $J \cdot s^{-1}$ and J is equal to $N \cdot m$. The PV can be obtained from the SV by using

$$\mathbf{p} = C \frac{1}{\rho} u^2 \mathbf{s}, \quad (3.19)$$

where C is a dimensionless value, the unit of the SV (\mathbf{s}) is $s \cdot m^{-1}$ (see equation 3.9), the unit of the pressure field (u) is $N \cdot m^{-2}$ which is equivalent to Pa and $kg \cdot m^{-1} \cdot s^{-2}$, and the unit of the density (ρ) is $kg \cdot m^{-3}$. Equation 3.16 can be verified by comparing the units of the two sides,

$$\begin{aligned}
\left[\frac{1}{\rho} \right] \cdot [u^2] \cdot [\mathbf{s}] &= (kg^{-1} \cdot m^3) \cdot (N \cdot m^{-2}) \cdot (N \cdot m^{-2}) \cdot (s \cdot m^{-1}) \\
&= (kg^{-1} \cdot m^3) \cdot (N \cdot m^{-2}) \cdot (kg \cdot m^{-1} \cdot s^{-2}) \cdot (s \cdot m^{-1}) \\
&= N \cdot s^{-1} \cdot m^{-1} = J \cdot s^{-1} \cdot m^{-2} = W \cdot m^{-2} \\
&= [\mathbf{p}],
\end{aligned} \tag{3.20}$$

where operator $[\]$ denotes obtaining the unit (this notation is used only in equation 3.20; the $[\]$ in other equations is a conventional square bracket). Červený (2001) gives a mathematical derivation to a similar form of equation 3.19 (refer to equation 2.4.54 on Page 65 of his book); his derivation involves a high-frequency approximation and the \mathbf{p} is an average value $\hat{\mathbf{p}}$ over a short time period. Below, we ignore the C in equation 3.19 because it does not contribute to the calculation of propagation directions.

From equations 3.14 and 3.19, we obtain

$$\mathbf{p} = -\frac{1}{\rho} u \int \left(\frac{\partial}{\partial \mathbf{x}} u \right) dt. \tag{3.21}$$

Thus, the acoustic PV is obtained. For the scalar wave equation 3.4, which does not have the density term, equation 3.21 can be simplified to (assuming the density is $1.0 \text{ kg} \cdot \text{m}^{-3}$; note the ρ^{-1} in equation 3.21 will not influence the calculation of the propagation angle)

$$\mathbf{p} = -u \int \left(\frac{\partial}{\partial \mathbf{x}} u \right) dt \cdot kg^{-1} \cdot m^3. \tag{3.22}$$

If we ignore the unit, equation 3.22 can be simply written as

$$\mathbf{p} = -u \int \left(\frac{\partial}{\partial \mathbf{x}} u \right) dt, \quad (3.23)$$

which can be used to calculate the propagation direction of the pressure field in acoustic media. Equations 3.21 and 3.23 do not have the “zero-modulus” problem which is stated as “the PV modulus at the wavefield-magnitude peak is zero”, because the corresponding variations of the PV modulus are consistent with the magnitude of the wavefield. Specifically, when the PV modulus is zero, the magnitude of the wavefield is also zero, and a correct propagation direction is not needed for a zero-magnitude wavefield. Note, the phrase “dynamically-correct” in this paper is defined as that the variation of the PV magnitude is consistent with the magnitude of the pressure, which is also consistent with the physical definition of the PV.

Note, for the widely-used PV in equation 3.2, the unit of $\partial u / \partial t$ is $N \cdot m^{-2} \cdot s^{-1}$, and the unit of $\partial u / \partial \mathbf{x}$ is $N \cdot m^{-3}$. Their product is certainly not equal to the unit of the PV ($W \cdot m^{-2}$ or $J \cdot s^{-1} \cdot m^{-2}$ or $N \cdot s^{-1} \cdot m^{-1}$). This also proves that the widely-used PV in equation 3.2 is not dynamically-correct.

Based on equations 3.14, 3.16, 3.17, 3.18 and 3.23, we give the MPV formula,

$$\mathbf{p} = (\mathbf{p}_1, \mathbf{p}_2, \mathbf{p}_3, \dots, \mathbf{p}_i, \dots, \mathbf{p}_{n-1}, \mathbf{p}_n), \quad (3.24)$$

$$\mathbf{p}_i = -\frac{1}{\rho_i} u_i \int \left(\frac{\partial}{\partial \mathbf{x}} u_i \right) dt, \quad (3.25)$$

and

$$u_i = \frac{1}{2\pi} \Re \left[\int_{-\infty}^{\infty} \int_{(\alpha, \beta)_{i-1}}^{(\alpha, \beta)_i} \bar{U}(\omega, \mathbf{k}) e^{-i\mathbf{k}\mathbf{x} + i\omega t} d\mathbf{k} d\omega \right]. \quad (3.26)$$

Here, \mathbf{p}_i is a PV component of the MPV and i is a reference number for the decomposed wavefield and a PV component of the MPV. The α and β are approximate azimuth and polar angles,

$$\alpha = \begin{cases} \frac{180^\circ}{\pi} \operatorname{atan} 2(\hat{p}_y, \hat{p}_x), & \text{if } \operatorname{atan} 2(\hat{p}_y, \hat{p}_x) \geq 0, \\ \frac{180^\circ}{\pi} \operatorname{atan} 2(\hat{p}_y, \hat{p}_x) + 360^\circ, & \text{if } \operatorname{atan} 2(\hat{p}_y, \hat{p}_x) < 0. \end{cases} \quad (3.27)$$

where $\operatorname{atan} 2$ is the multi-valued inverse tangent function with a range of $(-\pi, \pi]$ and

$$\beta = \arccos\left(\frac{\hat{p}_z}{|\hat{\mathbf{p}}|}\right), \quad (3.28)$$

where $\hat{\mathbf{p}}$ is the approximate propagation vector

$$\hat{\mathbf{p}} = \mathbf{k} \cdot \operatorname{sgn}(\omega). \quad (3.29)$$

In 2D, there is only a polar angle,

$$\beta = \begin{cases} \frac{180^\circ}{\pi} \operatorname{atan} 2(\hat{p}_z, \hat{p}_x), & \text{if } \operatorname{atan} 2(\hat{p}_z, \hat{p}_x) \geq 0, \\ \frac{180^\circ}{\pi} \operatorname{atan} 2(\hat{p}_z, \hat{p}_x) + 360^\circ, & \text{if } \operatorname{atan} 2(\hat{p}_z, \hat{p}_x) < 0. \end{cases} \quad (3.30)$$

Note, equation 3.26 is the same as equation 3.18; we rewrite it here to make the MPV formula complete. The dynamically-correct PV has a relationship with the Eikonal equation; see Appendix 3A (Section 3.9). It can also be derived by simplifying the elastic PV (Červený, 2001), from the elastic medium to the acoustic medium, see Appendix 3B (Section 3.10).

3.5 Implementation

3.5.1 Conjugate relationship and complex-valued wavefield extrapolation for accelerating the approximate WD

In MPV, most of the computation efforts focus on the approximate WD which requires Fourier transforms between the t - \mathbf{x} and ω - \mathbf{k} domains. For one approximate WD, it requires one forward FT from the t - \mathbf{x} domain to the ω - \mathbf{k} domain and several inverse FTs from the ω - \mathbf{k} domain to the t - \mathbf{x} domain. This can be simplified by separating the wavefields into positive and negative frequencies by a 1D FT between the t and ω domains first and then decomposing the wavefield in the \mathbf{k} domain. Then there are two computational issues. First, the Fourier transforms between the time and frequency domains is a great challenge for I/O time (for 3D data). The wavefields are simulated in time, so unless we store the wavefields at all the time steps in the memory, we need a large I/O time to reorder the wavefields for the Fourier transforms between the time and frequency domains. Second, after separating the wavefields into the two complex-valued parts with either positive or negative frequencies, we need to do the wave decomposition in the wavenumber domain for both of the two parts.

The first problem is easy to solve by using a complex-valued extrapolator (Zhang et al., 2007). Because the wavefield extrapolator is linear, we can use Fourier transforms between the t and ω domains to separate both the source wavelet and recorded data into two complex-valued parts with either positive or negative frequency and extrapolate the complex-valued source wavelet and recorded data. When the sign of the frequency is known, the wavefield decomposition can be done in t - \mathbf{k} . However, this solution produces another issue. The complex-

valued extrapolation has twice the computational complexity as the real-valued extrapolation; thus, if we use it to obtain both the positive- and negative-frequency wavefields, we need four times the computational time as the real-valued extrapolation.

This issue and the previously-mentioned second issue can be regarded as a single issue (referred to as the PN issue below), because both are caused by the fact that the decomposition needs to be done to both the positive- and negative-frequency wavefields. Below, we prove that the decomposition results of the wavefields with either positive or negative frequency are actually conjugate. Because we need only the real part of the decomposition result, we only need to obtain either the positive-frequency wavefield or the negative-frequency wavefield, and so the PN issue is solved.

Based on the definition in equations 3.5 and 3.6, the FT of a real function $u(t, \mathbf{x})$ has

$$\bar{U}(-\omega, -\mathbf{k}) = \bar{U}^*(\omega, \mathbf{k}), \quad (3.31)$$

where superscript * means “conjugate”. The inverse FT (equation 3.6) can be separated into two parts,

$$u(t, \mathbf{x}) = \int_{-\infty}^{\infty} d\mathbf{k} \int_0^{\infty} d\omega \bar{U}(\omega, \mathbf{k}) e^{i(-\mathbf{k}\mathbf{x} + \omega t)} + \int_{-\infty}^{\infty} d\mathbf{k} \int_{-\infty}^0 d\omega \bar{U}(\omega, \mathbf{k}) e^{i(-\mathbf{k}\mathbf{x} + \omega t)}. \quad (3.32)$$

Using equation 3.29, we can obtain

$$u(t, \mathbf{x}) = \int_{-\infty}^{\infty} d\hat{\mathbf{p}} \int_0^{\infty} d\omega \bar{U}(\omega, \hat{\mathbf{p}}) e^{i(-\hat{\mathbf{p}}\mathbf{x} + \omega t)} + \int_{-\infty}^{\infty} -d\hat{\mathbf{p}} \int_{-\infty}^0 d\omega \bar{U}(\omega, -\hat{\mathbf{p}}) e^{i(\hat{\mathbf{p}}\mathbf{x} + \omega t)}. \quad (3.33)$$

For $\omega \in (-\infty, 0)$, by using $\omega' = -\omega$ where $\omega \in (0, \infty)$, we obtain

$$u(t, \mathbf{x}) = \int_{-\infty}^{\infty} d\hat{\mathbf{p}} \int_0^{\infty} d\omega \bar{U}(\omega, \hat{\mathbf{p}}) e^{i(-\hat{\mathbf{p}}\mathbf{x} + \omega t)} + \int_{-\infty}^{\infty} -d\hat{\mathbf{p}} \int_0^{\infty} -d\omega' \bar{U}(-\omega', -\hat{\mathbf{p}}) e^{i(\hat{\mathbf{p}}\mathbf{x} - \omega' t)}. \quad (3.34)$$

Because of equation 3.31, equation 3.34 can be written as

$$\begin{aligned} u(t, \mathbf{x}) &= \int_{-\infty}^{\infty} d\hat{\mathbf{p}} \int_0^{\infty} d\omega \left\{ \bar{U}(\omega, \hat{\mathbf{p}}) e^{i(-\hat{\mathbf{p}}\mathbf{x} + \omega t)} + \left[\bar{U}(\omega, \hat{\mathbf{p}}) e^{i(-\hat{\mathbf{p}}\mathbf{x} + \omega t)} \right]^* \right\}, \\ &= 2\Re \left[\int_{-\infty}^{\infty} d\hat{\mathbf{p}} \int_0^{\infty} d\omega \bar{U}(\omega, \hat{\mathbf{p}}) e^{i(-\hat{\mathbf{p}}\mathbf{x} + \omega t)} \right], \end{aligned} \quad (3.35)$$

where \Re denotes taking the real part. The process from equation 3.32 to 3.35 states that, for each small $\hat{\mathbf{p}}$ bin with a width of $d\hat{\mathbf{p}}$, we have (ignoring $\omega = 0$)

$$\begin{cases} u(t, \mathbf{x}, \hat{\mathbf{p}}) = 2\Re [u(t, \mathbf{x}, \hat{\mathbf{p}}, \omega > 0)], \\ u(t, \mathbf{x}, \hat{\mathbf{p}}, \omega > 0) = u^*(t, \mathbf{x}, \hat{\mathbf{p}}, \omega < 0). \end{cases} \quad (3.36)$$

Equation 3.36 says that we need only the positive-frequency complex-valued wavefields, which can be obtained by extrapolation of the complex-valued source wavelet and recorded data, both of which are analytic (with only positive frequencies). The analytic wavefield can also be constructed by using Hilbert transforms (Zhang et al., 2007).

The complex-valued extrapolation helps reduce the I/O time; the conjugate relation between the decomposition results using either the positive- or negative-frequency wavefields allows the complex-valued extrapolation and decomposition to be done only for the positive-frequency wavefield. Using both, the wave decomposition can be done in t - \mathbf{k} instead of ω - \mathbf{k} . It is also useful for local plane-wave decomposition for computing angle gathers (Xu et al., 2011); although they use only the wavenumber to calculate the reflection and azimuth angles, the computation needs to be done in ω - \mathbf{k} . If using the complex-valued extrapolation and the

conjugate relation, the angle computation can be done in $t\text{-}\mathbf{k}$ instead of $\omega\text{-}\mathbf{k}$. The method can also be combined with source or receiver wavefield reconstruction (Dussaud et al., 2008; Tang and Wang, 2012b; Tang et al., 2013a) to further use computation time to reduce I/O time.

3.5.2 Decreasing the cost of the dynamically-correct MPV

Above, we give the dynamically-correct MPV (equations 3.22~3.24) for acoustic media. Equation 3.23 involves time integration. Below, we give a simplified implementation.

The dynamically-correct PV equation 3.23 (which is the original form of equation 3.25 in the dynamically-correct MPV) can be reformed as

$$\mathbf{p} = -\frac{1}{\rho} \frac{\partial \Psi}{\partial t} \frac{\partial \Psi}{\partial \mathbf{x}} = -\frac{1}{\rho} \frac{\partial \left(\int u dt \right)}{\partial t} \frac{\partial \left(\int u dt \right)}{\partial \mathbf{x}}, \quad (3.37)$$

where Ψ is the time integration of the pressure field u and thus

$$u = \frac{d\Psi}{dt}. \quad (3.38)$$

Ignoring the ρ^{-1} , equation 3.37 has the same form as the widely-used PV formula (equation 3.2) which is the negative of the product of the time and space derivatives. The difference is that equation 3.37 uses a time integration of the pressure field to replace the pressure field in equation 3.2. This also provides a physical explanation for the experience and opinion of Yoon et al. (2011) and Yan and Ross (2013) that summing the widely-used PVs in equation 3.2 over a local time or space window can improve the stability of the propagation angles. Although integrating the widely-used PVs over time (or space) is mathematically different from integrating the

pressure field over time, before calculating the PVs (equation 3.37), physically both of them lead to a phase modification of the widely-used PVs in equation 3.2.

Implementing the time integration in equation 3.37 becomes simpler in MPV because the multidirectional scheme already involves FTs between the t - \mathbf{x} and ω - \mathbf{k} domains for the approximate wavefield decomposition. Then equations 3.25 and 3.26 become

$$\mathbf{p}_i = -\frac{1}{\rho} \frac{\partial \Psi_i}{\partial t} \frac{\partial \Psi_i}{\partial \mathbf{x}}, \quad (3.39)$$

and

$$\Psi_i = \frac{1}{\pi} \Re \left[\int_{(\alpha,\beta)_{-1}}^{(\alpha,\beta)_i} \left(\int_0^\infty \frac{1}{i\omega} \bar{U} e^{i\omega t} d\omega \right) e^{-i\mathbf{k}\mathbf{x}} d\mathbf{k} \right], \quad (3.40)$$

where the $(i\omega)^{-1}$ is equivalent to the time integration in the t domain. In equations 3.39 and 3.40, the increase in computational complexity caused by incorporating the dynamically-correct PV formula into the MPV in acoustic media is very small. The decomposed P-wave can be reconstructed by using

$$u_i = \frac{d\Psi_i}{dt}. \quad (3.41)$$

By incorporating the updated MPV with the flows of our previous publications (Tang and McMechan, 2016; 2017b), we have three updated data flows to calculate ADCIGs from acoustic RTM; see Appendix 3C (Section 3.11). Because this chapter focuses on the comparison between the original and the dynamically-correct MPVs, we use only the SR-flow in Appendix 3C to produce ADCIGs in the “Examples” section below.

3.6 Examples

This section provides several 2D numerical examples to support the proposed scheme. Because here the PV is used to calculate the propagation vector of a pressure field u , the ρ^{-1} in the dynamically-correct PV and MPV formulas can be ignored. Then we can use the scalar equation 3.4 for acoustic wave propagation. First, we provide some comparisons between the widely-used PV (equation 3.2) and the dynamically-correct PV (equation 3.21) in a constant velocity model (the v_p is 2400 m/s). Equation 3.21 is implemented by using its equivalent form in equation 37 with the ρ^{-1} ignored. Note, equation 3.21 with the ρ^{-1} ignored is equation 3.23.

Figure 3.2 contains snapshots of a pressure field (panel a), the PVs calculated by the original equation 3.3 (panels b and c), and the PVs calculated by the dynamically-correct equation 3.23 (panels d and e) at the time 420 ms. The phase difference between the widely-used and dynamically-correct PVs is clearly observed. Figure 3.3 compares the modulus of the widely-used and dynamically-correct PVs. The modulus variation of the dynamically-correct PV is very similar to u^2 , which is consistent with the conclusion in equation 3.23. Thus, when $|u|$ is large (which means u^2 is also large), the dynamically-correct $|\mathbf{p}|$ is also large and thus the ‘zero-modulus’ issue does not occur for the dynamically-correct PV. By comparing Figures 3.3b and 3.3c, the phase shift between the u^2 and the widely-used $|\mathbf{p}|$ is clearly seen, which results the ‘zero-modulus’ problem.

Then, we use the widely-used and the dynamically-correct PVs in Figures 3.2 and 3.3 to calculate the propagation angles for the pressure field at 420 ms. These propagation angles are used to output two angle-limited snapshots between propagation angles 30° and 60° . In Figure 3.

4b, there are many unstable points and the two truncations at 30° and 60° are not sharp. These indicate the propagation angles calculated by the widely-used PV are neither accurate nor stable. In Figure 3.4c, there are not apparent unstable points and the two truncations are also sharp, which indicate that the propagation angles calculated by the dynamically-correct PV are accurate.

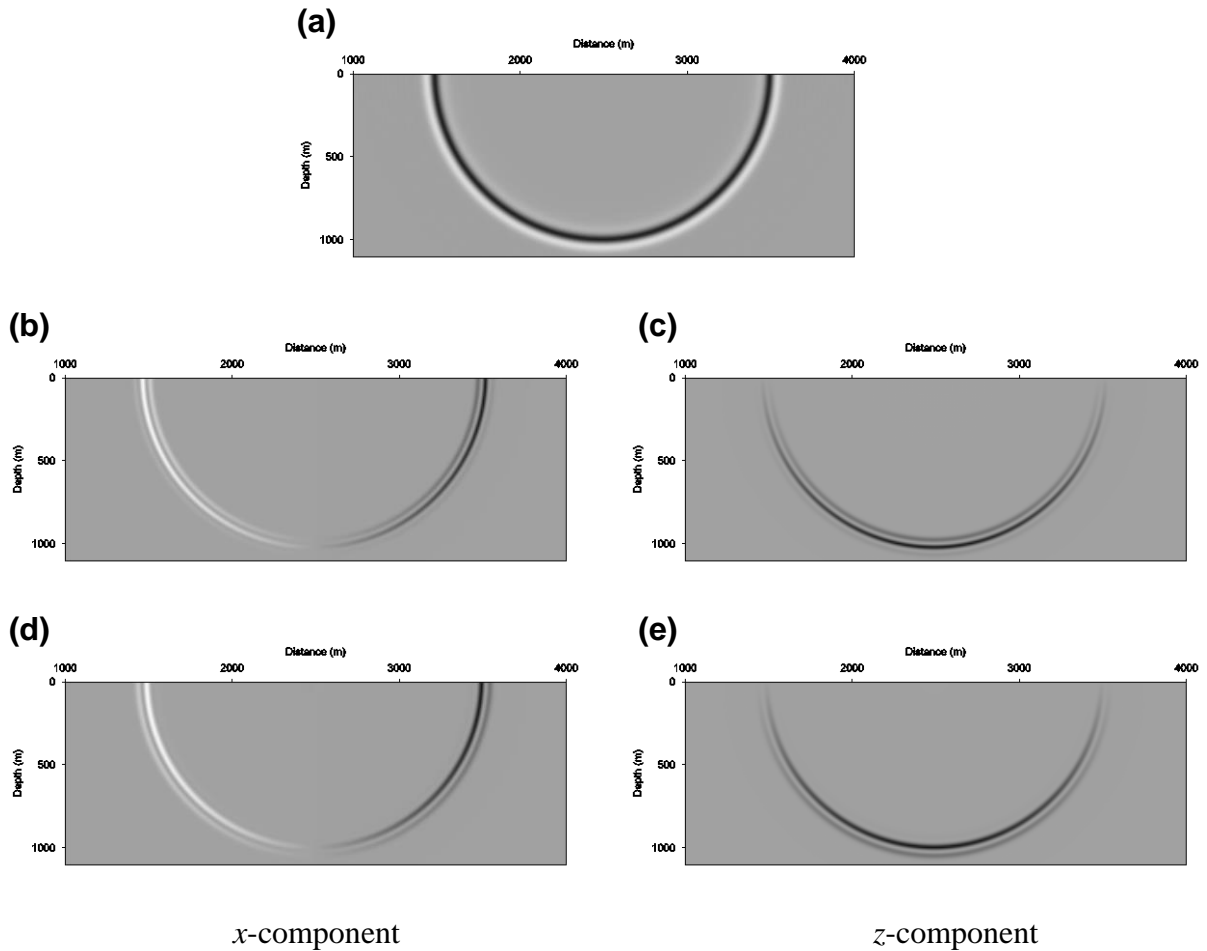


Figure 3.2. Comparison of the widely-used and dynamically-correct PVs. Panel (a) is a snapshot of the pressure field. Panels (b) and (c) are the x - and z -components of the widely-used PV, respectively. Panels (d) and (e) are the x - and z -components of the dynamically-correct PV, respectively. The time is 420 ms.

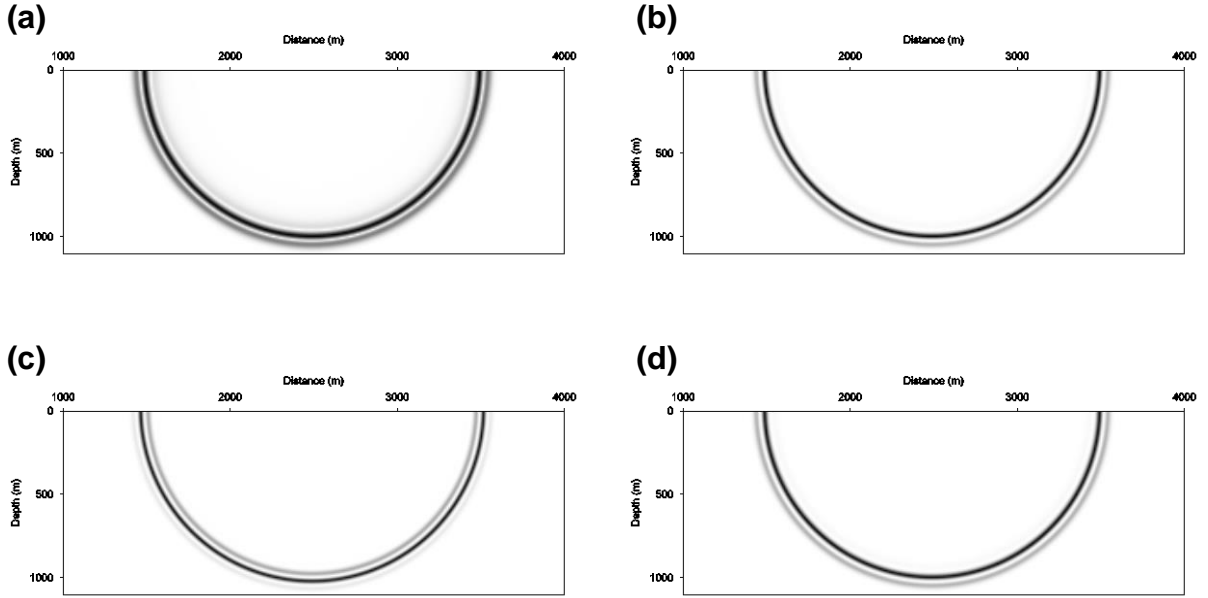


Figure 3.3. Comparison of the modulus of the widely-used and dynamically-correct PVs. Panel (a) is $|u|$. Panel (b) is u^2 . Panel (c) is the widely-used $|\mathbf{p}|$. Panel (d) is the dynamically-correct $|\mathbf{p}|$. The time is 420 ms.

The second example provides comparisons between the ADCIGS obtained using the original MPV and the updated MPV. The original MPV uses

$$\mathbf{p}_i = -\frac{\partial u_i}{\partial t} \frac{\partial u_i}{\partial \mathbf{x}}, \quad (3.42)$$

to calculate the propagation direction of each decomposed wavefield in equation 3.26. So it consists of equations 3.24, 3.42 and 3.26. The updated MPV consists of equations 3.24, 3.39, 3.40; the ρ^{-1} in equation 3.25 is ignored and the decomposed wavefield u_i is obtained from Ψ_i through equation 3.40.

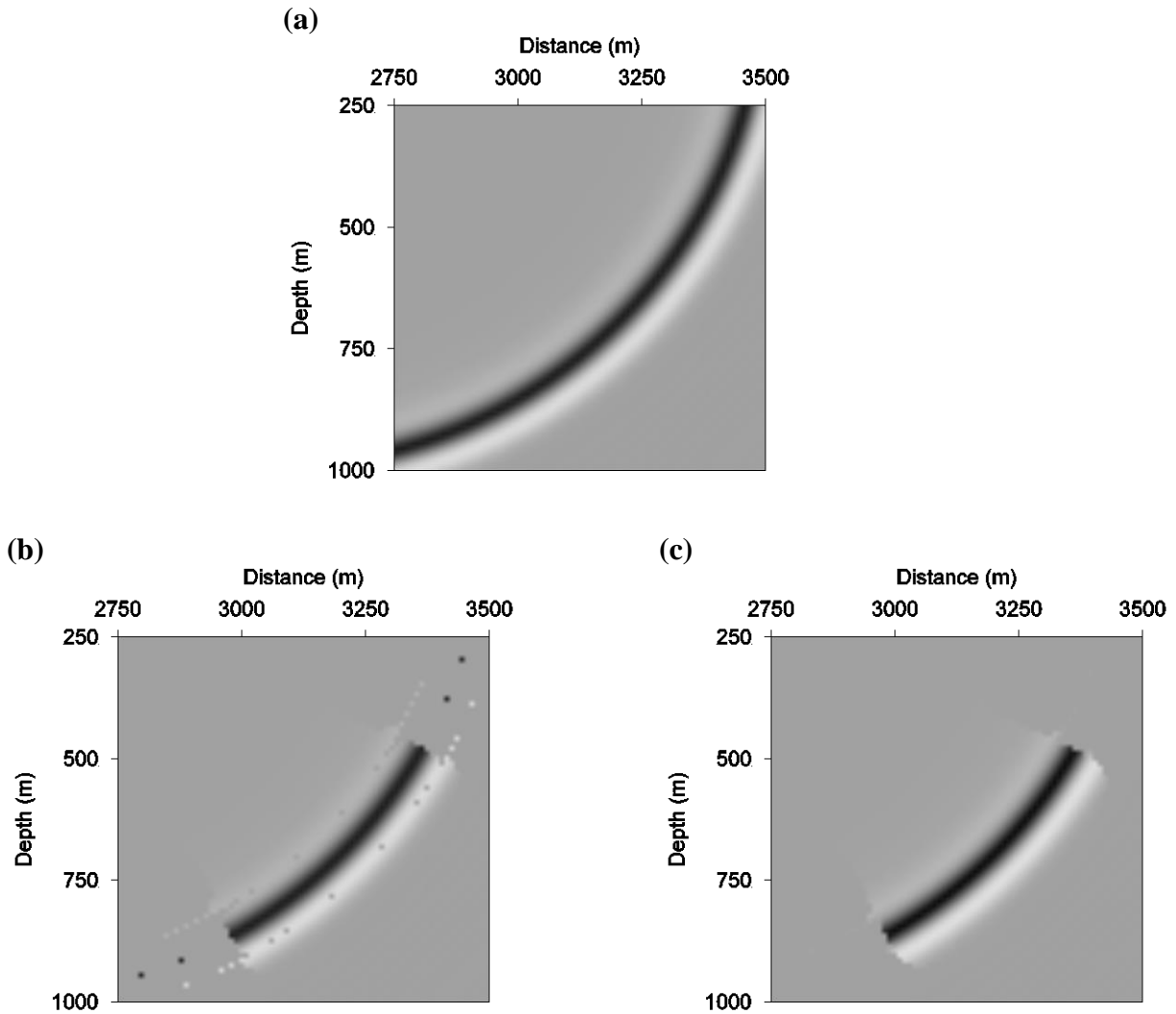


Figure 3.4. Comparison of using the widely-used and dynamically-correct PVs to calculate propagation angles. Panel (a) is a snapshot of the pressure field. Now we use the widely-used and dynamically-correct PVs to calculate the propagation directions of the pressure field in panel (a). Then we only show the pressure field within propagation angle aperture $30^{\circ}\sim 60^{\circ}$ (the 0° is the horizontal right; the angle increases in the clockwise direction). Using the widely-used and dynamically-correct PVs to calculate propagation angles gives the angle-limited snapshots in panels (b) and (c), respectively.

The P-velocity model uses a portion of Marmousi2 model (Martin et al., 2006); see Figure 3.5. There are 200 sources from 20 m to 4000 m along the surface, with an interval of 20 m. The pressure field from each source is observed by 401 receivers on the surface; the range of offsets

is from -2000 m to 2000 m relative to the location of each source. The source uses a Ricker wavelet with a dominant frequency of 25 Hz. Because the velocity above 500 m is constant, the target image zone is below 500 m; the RTM image is in Figure 3.6.

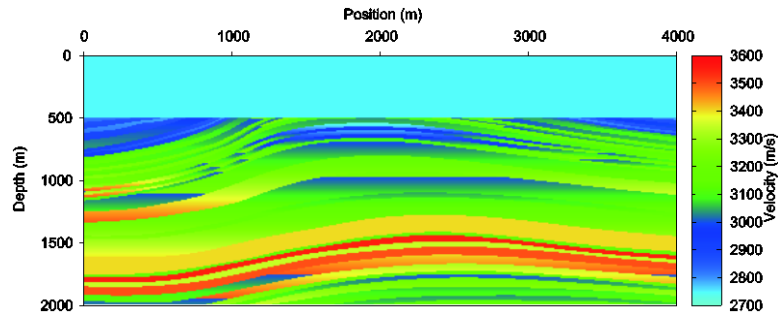


Figure 3.5. The P-velocity of a portion of Marmousi2 model.

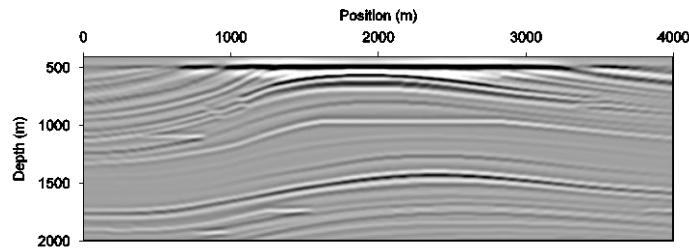


Figure 3.6. The RTM image using the synthetic data obtained from the velocity model in Figure 3.5. The migration uses the true velocity.

In Figure 3.7, the ADCIGs produced by original MPV have unreasonably high-amplitude images at the very large angles, particularly in the deep region (e.g., see the red box); this is not correct because of the limited migration aperture. These unreasonable images in Figure 3.7a are caused by the unreliable propagation angles calculated by the original MPV. The ADCIGs (in Figure 3.7b) produced by the updated MPV do not have these unreasonable images (e.g., see in the red box), and thus have higher reliability and sharp truncations in the angle domain.

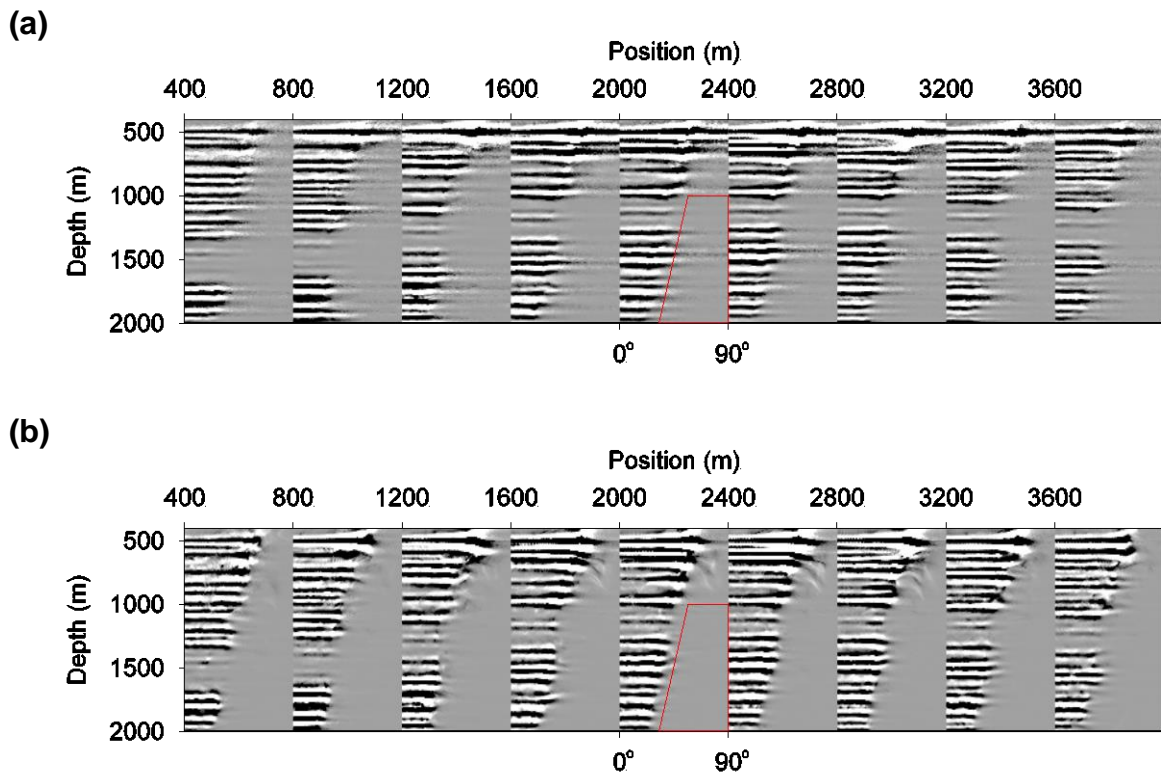


Figure 3.7. Comparison of ADCIGs obtained using the (a) original and (b) dynamically-correct MPVs. The synthetic data is obtained from the velocity model in Figure 3.5. The migration uses the true velocity.

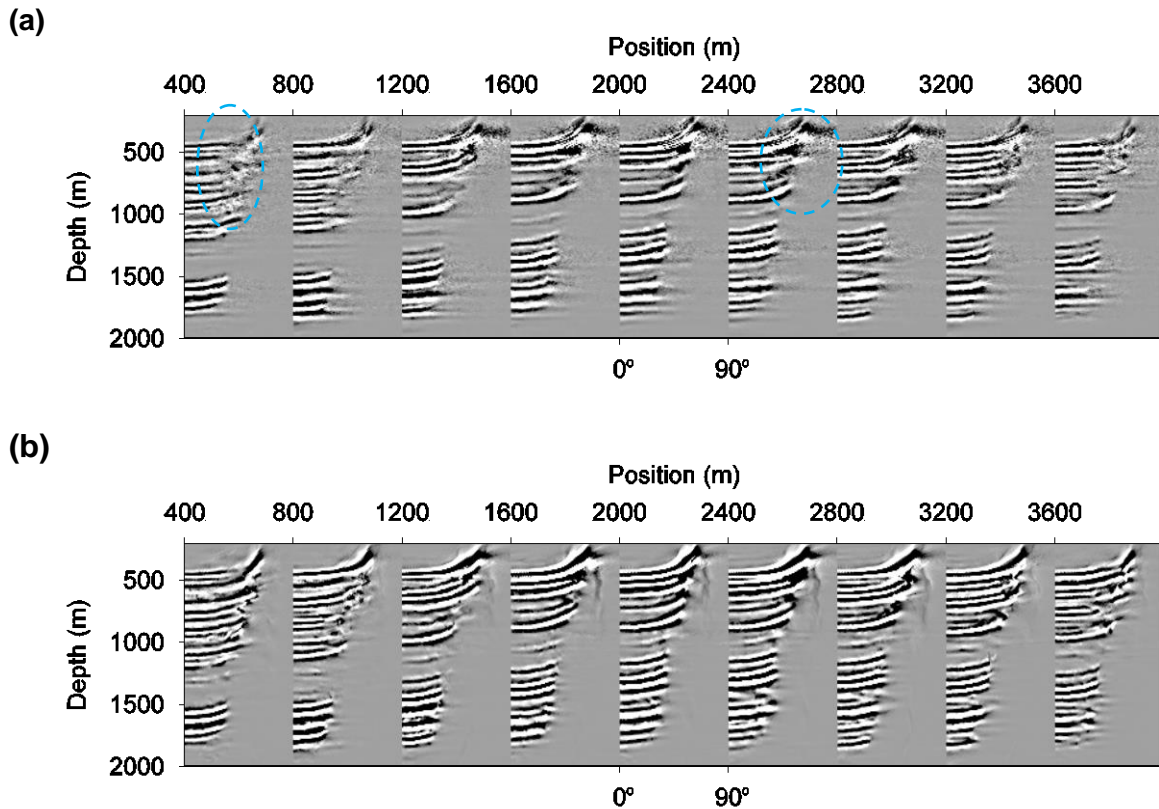


Figure 3.8. Comparison of ADCIGs obtained using the original and dynamically-correct MPVs. Panel (a) is obtained from the original MPV. Panel (b) is obtained from the dynamically-correct MPV. The synthetic data is obtained from the velocity model in Figure 3.5. The migration uses an 8% low velocity model.

Figure 3.8 provides a comparison between ADCIGs produced by the original MPV (Panel a) and the updated MPV (Panel b) when the migration velocity is incorrect (8% low). In Figure 3.8a, the ADCIGs calculated by the original MPV are noisy and unstable, particularly at large angles (e.g., see in the blue dashed ovals). This phenomenon is caused by the inaccurate and unstable propagation angles calculated by the original MPV which negatively influence the calculation of the curvature for migration velocity analysis (e.g., Biondi and Symes, 2004; Zhang et al. 2012). In Figure 3.8b, the ADCIGs calculated by updated MPV have less noise and are more focused and continuous than those in Figure 3.8a.

3.7 Conclusions

We address the two problems of PVs by deriving the dynamically-correct MPV. We separate the wavefield into approximate propagation angle ranges and then use the dynamically-correct PV to calculate accurate propagation directions for each of the decomposed wavefields. The dynamically-correct PV formula for acoustic media is a product of the reciprocal of the density, the pressure itself and a factor that is obtained by applying a time integration plus a space derivative to this pressure. To decrease the implementation cost, we prove a conjugate relationship between the decomposition result of the wavefields with either the positive or negative frequencies. Because we need only the real part, we are able to apply the approximate WD only to the wavefields with positive frequencies. We also give a practical scheme to implement the dynamically-correct MPV, which applies a time integration to the wavefields during the decomposition and use an equivalent form of the dynamically-correct PV to calculate the propagation directions.

3.8 Acknowledgments

The computational resources are provided by the Texas Advanced Computing Center (TACC) and the UT Dallas Geophysical Consortium (UTD GC). A research assistantship is provided via the financial support of the Sponsors of the UTD GC. We also appreciate the comments from Associate Editor V. Vinje and four anonymous reviewers.

3.9 Appendix 3A “Difference between the original and dynamically-correct PVs and the relationship between the dynamically-correct PV and the Eikonal equation”

Equation 3.21 is the dynamically-correct PV formula in acoustic media. Compared with equation 3.2, there are two differences if the ρ^{-1} in equation 3.21 is ignored (which gives equation 3.23). One is that the time derivative in equation 3.2 becomes a time integration in equation 3.21. The other is that, in equation 3.2, both the time and space derivatives are applied to the pressure field u independently; while in equation 3.21, a serial combination of the time-integration and space-derivative operations is applied to u . The space derivative (or time integration) leads to a phase modification and then the time integration (or space derivative) compensates for it. Thus, from a physical perspective, the $\left| \int \left(\frac{\partial}{\partial \mathbf{x}} u \right) dt \right|$ should be approximately proportional to $|u|$.

Equation 3.15 can be written as

$$u\hat{\mathbf{s}} = -v_p \int \left(\frac{\partial}{\partial \mathbf{x}} u \right) dt, \quad (3A-1)$$

the modulus of which is

$$|u\hat{\mathbf{s}}| = v_p \left| \int \left(\frac{\partial}{\partial \mathbf{x}} u \right) dt \right|. \quad (3A-2)$$

Because $\hat{\mathbf{s}}$ is a unit vector,

$$|u\hat{\mathbf{s}}| = |u| |\hat{\mathbf{s}}| = |u|. \quad (3A-3)$$

Thus,

$$|u| = v_p \left| \int \left(\frac{\partial}{\partial \mathbf{x}} u \right) dt \right|. \quad (3A-4)$$

Equation 3A-4 involves the first-order (high-frequency) approximation (see equation 3.13 which is a precursor to equation 3.15). From equations 3.15 and 3.21, we obtain

$$|u|^2 = \rho v_p \left| -\frac{u}{\rho} \int \left(\frac{\partial}{\partial \mathbf{x}} u \right) dt \right| = \rho v_p |\mathbf{p}|, \quad (3A-5)$$

which can also be written as

$$|\mathbf{p}| = \frac{u^2}{\rho v_p}. \quad (3A-6)$$

Equation 3A-6 means that when the magnitude of the pressure field is large, the modulus of the PV is also large; when the magnitude of the pressure field is small, the modulus of the PV is also small. Thus, the dynamically-correct PV formula in equation 3.21 does not suffer from the “zero-modulus” problem of the widely-used PV formula in equation 3.2. This is consistent with the physical definition of the PV which is the “directional energy flux density” of a pressure field.

The derivations of both the SV equation 3.14 and the PV equation 3.21 require equation 3.13, which can be reformed as

$$\mathbf{s} = -\frac{\partial t}{\partial \mathbf{x}}. \quad (3A-7)$$

Equation 3A-7 is the well-known Eikonal equation (or the Travel-time equation) that is widely used in ray theory. This is consistent with the fact that solving the Eikonal equation can give the

propagation angles, which is the basis of using ray-based migrations (e.g., Kirchhoff or Gaussian-beam migration) to calculate ADCIGs. Now we see that the PV and the ray-based methods actually do the same thing: the latter calculates the propagation angle from a smooth migration velocity by solving the Eikonal equation and the former calculates the propagation angle from the pressure field that is obtained from the full wave equation. Calculating ADCIGs from ray-based migration is cheaper; however, the ray-based migrations involve several assumptions and approximations which are not discussed in detail here as they are beyond the scope of this chapter.

3.10 Appendix 3B “From elastic PV to acoustic PV”

In the previous two subsections, we derive the dynamically-correct PV formula (equation 3.21) for acoustic media and discuss its difference from the widely-used PV equation 3.2. In this subsection, we obtain the same PV formula through another approach, which is reducing the PV formula for elastic media to that for acoustic media. Wave extrapolation in an elastic medium can be approximated using the first-order hyperbolic system of elastodynamic equations (Virieux, 1986),

$$\frac{\partial \mathbf{v}}{\partial t} = \begin{bmatrix} \frac{\partial v_x}{\partial t} \\ \frac{\partial v_y}{\partial t} \\ \frac{\partial v_z}{\partial t} \end{bmatrix} = \begin{bmatrix} \frac{1}{\rho} \left(\frac{\partial \tau_{xx}}{\partial x} + \frac{\partial \tau_{yx}}{\partial y} + \frac{\partial \tau_{zx}}{\partial z} \right) \\ \frac{1}{\rho} \left(\frac{\partial \tau_{xy}}{\partial x} + \frac{\partial \tau_{yy}}{\partial y} + \frac{\partial \tau_{zy}}{\partial z} \right) \\ \frac{1}{\rho} \left(\frac{\partial \tau_{xz}}{\partial x} + \frac{\partial \tau_{yz}}{\partial y} + \frac{\partial \tau_{zz}}{\partial z} \right) \end{bmatrix}, \quad (3B-1)$$

and

$$\begin{aligned}
\frac{\partial \boldsymbol{\tau}}{\partial t} &= \begin{bmatrix} \frac{\partial \tau_{xx}}{\partial t} & \frac{\partial \tau_{xy}}{\partial t} & \frac{\partial \tau_{xz}}{\partial t} \\ \frac{\partial \tau_{yx}}{\partial t} & \frac{\partial \tau_{yy}}{\partial t} & \frac{\partial \tau_{yz}}{\partial t} \\ \frac{\partial \tau_{zx}}{\partial t} & \frac{\partial \tau_{zy}}{\partial t} & \frac{\partial \tau_{zz}}{\partial t} \end{bmatrix} \\
&= \begin{bmatrix} (\lambda + 2\mu) \frac{\partial v_x}{\partial x} + \lambda \left(\frac{\partial v_y}{\partial y} + \frac{\partial v_z}{\partial z} \right) & \mu \left(\frac{\partial v_x}{\partial y} + \frac{\partial v_y}{\partial x} \right) & \mu \left(\frac{\partial v_x}{\partial z} + \frac{\partial v_z}{\partial x} \right) \\ \mu \left(\frac{\partial v_x}{\partial y} + \frac{\partial v_y}{\partial x} \right) & (\lambda + 2\mu) \frac{\partial v_y}{\partial y} + \lambda \left(\frac{\partial v_x}{\partial x} + \frac{\partial v_z}{\partial z} \right) & \mu \left(\frac{\partial v_y}{\partial z} + \frac{\partial v_z}{\partial y} \right) \\ \mu \left(\frac{\partial v_x}{\partial z} + \frac{\partial v_z}{\partial x} \right) & \mu \left(\frac{\partial v_y}{\partial z} + \frac{\partial v_z}{\partial y} \right) & (\lambda + 2\mu) \frac{\partial v_z}{\partial z} + \lambda \left(\frac{\partial v_x}{\partial x} + \frac{\partial v_y}{\partial y} \right) \end{bmatrix},
\end{aligned} \tag{3B-2}$$

where v is the particle velocity, $\boldsymbol{\tau}$ is the stress tensor, λ is the first Lamé parameter and μ is the shear modulus. Also,

$$v_p = \sqrt{\frac{\lambda + 2\mu}{\rho}}, \tag{3B-3}$$

and

$$v_s = \sqrt{\frac{\mu}{\rho}}, \tag{3B-4}$$

where v_s is the S wave propagation velocity. The propagation direction of an elastic wave can be calculated by (Červený, 2001; Dickens and Winbow, 2011) as

$$\mathbf{p} = \begin{bmatrix} P_x \\ P_y \\ P_z \end{bmatrix} = \begin{bmatrix} -(\tau_{xx} v_x + \tau_{xy} v_y + \tau_{xz} v_z) \\ -(\tau_{yx} v_x + \tau_{yy} v_y + \tau_{yz} v_z) \\ -(\tau_{zx} v_x + \tau_{zy} v_y + \tau_{zz} v_z) \end{bmatrix}. \tag{3B-5}$$

In an acoustic medium, the shear modulus μ is zero and the S velocity v_s is also zero. So equation 3B-2 becomes

$$\frac{\partial \boldsymbol{\tau}}{\partial t} = \begin{bmatrix} \frac{\partial \tau_{xx}}{\partial t} & \frac{\partial \tau_{xy}}{\partial t} & \frac{\partial \tau_{xz}}{\partial t} \\ \frac{\partial \tau_{yx}}{\partial t} & \frac{\partial \tau_{yy}}{\partial t} & \frac{\partial \tau_{yz}}{\partial t} \\ \frac{\partial \tau_{zx}}{\partial t} & \frac{\partial \tau_{zy}}{\partial t} & \frac{\partial \tau_{zz}}{\partial t} \end{bmatrix} = \begin{bmatrix} \lambda \frac{\partial v_x}{\partial x} & 0 & 0 \\ 0 & \lambda \frac{\partial v_y}{\partial y} & 0 \\ 0 & 0 & \lambda \frac{\partial v_z}{\partial z} \end{bmatrix}, \quad (3B-6)$$

which gives

$$\begin{cases} \tau_{xx} = \tau_{yy} = \tau_{zz} = \tau_p = -u, \\ \tau_{xy} = \tau_{yx} = \tau_{xz} = \tau_{zx} = \tau_{yz} = \tau_{zy} = 0. \end{cases} \quad (3B-7)$$

In equation 3B-7, the τ_p is a normal stress which is equivalent to $-u$. Using equations 3B-6 and 3B-7, equation 3B-1 can be simplified to

$$\frac{\partial \mathbf{v}}{\partial t} = - \begin{bmatrix} \frac{\partial v_x}{\partial t} \\ \frac{\partial v_y}{\partial t} \\ \frac{\partial v_z}{\partial t} \end{bmatrix} = - \begin{bmatrix} \frac{1}{\rho} \frac{\partial u}{\partial x} \\ \frac{1}{\rho} \frac{\partial u}{\partial y} \\ \frac{1}{\rho} \frac{\partial u}{\partial z} \end{bmatrix}, \quad (3B-8)$$

and equation 3B-5 can be simplified to

$$\mathbf{p} = \begin{bmatrix} p_x \\ p_y \\ p_z \end{bmatrix} = \begin{bmatrix} uv_x \\ uv_y \\ uv_z \end{bmatrix} = u\mathbf{v}, \quad (3B-9)$$

where the unit of u is $N \cdot m^{-2}$ and the unit of \mathbf{v} is $m \cdot s^{-1}$; thus, their product is $N \cdot s^{-1} \cdot m^{-1} = J \cdot s^{-1} \cdot m^{-2} = W \cdot m^{-2}$ which is the unit of p . From equation 3B-8, we can obtain

$$\mathbf{v} = \begin{bmatrix} v_x \\ v_y \\ v_z \end{bmatrix} = \begin{bmatrix} -\frac{1}{\rho} \int \frac{\partial u}{\partial x} dt \\ -\frac{1}{\rho} \int \frac{\partial u}{\partial y} dt \\ -\frac{1}{\rho} \int \frac{\partial u}{\partial z} dt \end{bmatrix} = -\frac{1}{\rho} \int \frac{\partial u}{\partial \mathbf{x}} dt. \quad (3B-10)$$

Inserting equation 3B-10 into 3B-9 gives

$$\mathbf{p} = -u \frac{1}{\rho} \int \frac{\partial u}{\partial \mathbf{x}} dt, \quad (3B-11)$$

which is exactly same as equation 3.21 (the dynamically-correct PV formula in acoustic media) and gives the propagation direction for both the pressure field u and the particle velocity \mathbf{v} in acoustic media. Combining equations 3B-6 and 3B-8 also gives

$$\begin{cases} \frac{\partial v_x}{\partial t} = -\frac{1}{\rho} \frac{\partial u}{\partial x}, & \frac{\partial v_y}{\partial t} = -\frac{1}{\rho} \frac{\partial u}{\partial y}, & \frac{\partial v_z}{\partial t} = -\frac{1}{\rho} \frac{\partial u}{\partial z}, \\ \frac{\partial u}{\partial t} = -\rho v_p^2 \left(\frac{\partial v_x}{\partial x} + \frac{\partial v_y}{\partial y} + \frac{\partial v_z}{\partial z} \right), \end{cases} \quad (3B-12)$$

which is an equivalent form of the acoustic equation 3.3. If the density is ignored, equation 3B-12 becomes

$$\begin{cases} \frac{\partial v_x}{\partial t} = -\frac{\partial u}{\partial x}, & \frac{\partial v_y}{\partial t} = -\frac{\partial u}{\partial y}, & \frac{\partial v_z}{\partial t} = -\frac{\partial u}{\partial z}, \\ \frac{\partial u}{\partial t} = -v_p^2 \left(\frac{\partial v_x}{\partial x} + \frac{\partial v_y}{\partial y} + \frac{\partial v_z}{\partial z} \right), \end{cases} \quad (3B-13)$$

which is an equivalent form of the scalar equation 3.4. Corresponding to the transition from equation 3B-12 to 3B-13, the PV equation 3B-11 also becomes equation 3.23 in which the density is gone.

Equation 3B-9 can also be used to calculate the PV of the separated normal stress and the P particle velocity in elastic media when Xiao and Leaney's (2010) approach is used to implement the P/S wave mode separation (Wang and McMechan 2015). This is because the P-wave decoupled equation of Xiao and Leaney (2010), which is based on Helmholtz theorem in elastic isotropic media, has the same form as equation 30 that is obtained by setting the shear modulus or S-velocity to be zero to simplify the elastic equations into the acoustic equation.

3.11 Appendix 3C “Data flows to calculate ADCIGs from RTM in acoustic media”

Now we combine the dynamically-correct MPV with our previous publications (Tang and McMechan, 2016, 2017c) to produce two standard flows to calculate ADCIGs from acoustic RTM. One uses the multidirectional propagation vectors of both source and receiver wavefields (Tang and McMechan, 2016, 2017c) to calculate the open angle for ADCIGs (for the PP reflection in acoustic media, half the open angle is equivalent to the reflection angle). The other flow combines the multidirectional source vector with the anti-truncation-artifact FT (ATFT) to calculate the incident angle for ADCIGs (for the PP reflection in acoustic media, the incident angle is equal to the reflection angle). To differentiate the ADCIGs obtained from the two flows, we define the ADCIGs calculated by the first flow as SR-ADCIGs ('S' denotes using the source propagation vector and 'R' denotes using the receiver propagation vector), and the ADCIGs calculated by the second flow as SI-ADCIGs. ('S' denotes using the source propagation vector

and 'I' means using the reflector-image normal). Correspondingly, the first flow is defined as the SR-flow and the second flow is defined as the SI-flow. The SR-flow is

- a) Calculate the source and receiver wavefields using the full wave equation.
- b) Use the dynamically-correct MPV in equations 3.24, 3.39, and 3.40 to calculate the multidirectional propagation vector. The decomposed pressure field can be recovered by equation 3.41.
- c) Calculate the RTM image (using the WD-AF imaging condition) and the SR-ADCIGs.

Table 3.1. A table of the SR-flow, the SI-flow and the SRSI flow.

NAMES	SR-FLOW	SI-FLOW	SRSI-FLOW
STEPS	(a), (b), (c)	(a), (b), (c'), (d)	(a), (b), (c''), (d)
KEY POINTS	Using the source and receiver propagation vectors to calculate ADCIGs	Using the source propagation (or polarization) vector and the reflector-image normal to calculate ADCIGs	A combination of the SR-flow and the SI-flow.
PRODUCTS	SR-ADCIGs	SI-ADCIGs	SR-ADCIGs and SI-ADCIGs

The SI-flow also uses the steps (a) and (b) in the SR-flow. Because it uses the source propagation/polarization-angle CIGs (SACIGs) and then transforms them into ADCIGs through ATFT (Tang and McMechan, 2017c), it starts to differ from the SR-flow at the third step;

c') Calculate the RTM image (using the WD-AF imaging condition) and SACIGs.

d) After migration, use the ATFT to transform SACIGs into SI-ADCIGs.

The SR- and SI-flows can be simply combined into a single SRSI-flow by combining (c) and (c'), which gives,

c'') Calculate the RTM image (using the WD-AF imaging condition), SR-ADCIGs and SACIGs.

A combination of steps (a), (b), (c'') and (d) is defined as the SRSI-flow, which can produce both SR-ADCIGs and SI-ADCIGs. See Table 3.1 for the steps included in each of the SR-, SI- and SRSI-flows.

CHAPTER 4

MULTIDIRECTIONAL-VECTOR-BASED ELASTIC REVERSE TIME MIGRATION AND ANGLE-DOMAIN COMMON-IMAGE GATHERS WITH APPROXIMATE WAVEFIELD DECOMPOSITION OF P AND S WAVES*

4.1 Summary

Elastic reverse time migration (E-RTM) has limitations when the migration velocities contain strong contrasts. First, the traditional scheme of P/S wave mode separation is based on Helmholtz's theorem; it contains an implicit assumption of constant shear modulus and thus requires smoothing the heterogeneous model to approximately satisfy a locally constant condition. Second, the vector-based imaging condition needs to use the reflection-image normal, and also cannot give the correct polarity of the PP image in all possible conditions. Third, the angle-domain common-image gathers (ADCIGs) calculated using Poynting vectors do not consider the wave interferences that happen at each reflector. We propose an improved data flow that involves three new contributions. The first contribution is an improved system of P/S wave mode separation that considers the converted wave generated at the current time, and thus does

* Tang C. and G. A. McMechan, 2018, Multidirectional-vector-based elastic reverse time migration and angle-domain common-image gathers with approximate wavefield decomposition of P and S waves: *Geophysics*, **83**, no. 1, S57-S79. Copyrighted by Society of Exploration Geophysicists. Permalink: <https://doi.org/10.1190/geo2017-0119.1>

Tang C. and G. A. McMechan, 2017, Elastic reverse time migration with an improved system of P/S wave mode separation in nonsmooth models: 87th International Meeting, SEG, Houston, 4696-4700. Copyrighted by Society of Exploration Geophysicists. Permalink: <https://doi.org/10.1190/segam2017-17789761.1>

Tang C. and G. A. McMechan, 2017, Multidirectional-vector-based elastic reverse time migration and angle-domain common-image gathers with approximate wavefield decomposition of p and s waves: 87th International Meeting, SEG, Houston, 4488-4493. Copyrighted by Society of Exploration Geophysicists. Permalink: <https://doi.org/10.1190/segam2017-17790704.1>

not require the constant-shear-modulus assumption. The second contribution is the new elastic imaging conditions based on multidirectional vectors; they can give the correct image polarity in all possible conditions without a priori knowledge of the reflector-image normal. The third contribution is two methods to calculate multidirectional propagation vectors for RTM images and ADCIGs: One is the elastic multidirectional Poynting vector and the other uses the sign of the wavenumber-over-frequency (\mathbf{k}/ω) ratio obtained from an amplitude-preserved approximate-propagation-angle-based wavefield decomposition to convert the particle velocities into multidirectional propagation vectors. The robustness of the improved data flow is shown by several 2D numerical examples. Extension of the schemes into 3D and amplitude-preserved imaging conditions are also possible.

4.2 Introduction

Reverse time migration (RTM), which the full wave equation for extrapolation (Baysal et al., 1983, McMechan, 1983, and Whitmore, 1983, for the initial idea of RTM for poststack data), has demonstrated its accuracy and robustness in imaging structurally complex regions. In the past decade, progress in prestack RTM is dramatic; several major issues such as the backscattering artifacts (e.g., Zhang and Sun, 2009; Liu et al., 2011; Tang and Wang, 2012a; Tang and McMechan, 2017c) and source-wavefield storage (e.g., Symes, 2007; Dussaud et al., 2008; Clapp, 2009; Tang and Wang, 2012b), have been addressed. These advances in the fundamental theory of the RTM complement the development in the computational capacity and the acquisition technology, to make the elastic RTM (E-RTM) increasingly feasible. In this chapter, we propose an improved data flow that addresses three important aspects of the E-RTM:

The P/S wave mode separation, the imaging conditions, and the angle-domain common image gathers (ADCIGs).

4.2.1 Separation of an elastic wave into P and S modes

To properly image the elastic properties of subsurface targets, separation of an elastic wave into P and S modes is required, which can be done based on the Helmholtz's theorem (e.g., Aki and Richards, 1980; Dellinger and Etgen, 1990; Ma and Zhu, 2003; Zhu, 2017). Methods of P/S wave mode separation can be generally divided into two types. The first applies divergence and curl operations to an elastic wave, to obtain pure P and S waves (e.g., Sun and Wang, 1999; Sun and McMechan, 2001). This directly uses the physical property of the P and S waves and is computationally efficient. However, the divergence and curl operations change the amplitude and phase which have been addressed in several publications (e.g., Sun and Chen, 2001; Sun et al., 2011). To correct both the phase and the amplitude in a single flow, Duan and Sava (2015) apply a time integration (or the equivalent operator in the frequency $[\omega]$ domain) to the source wavelet and to the observed data before extrapolation, followed by using the corresponding propagation velocity term to compensate the amplitude loss of the separated P or S wave after extrapolation. The divergence and curl operations can also be performed in the (local) wavenumber (\mathbf{k}) domain (Dellinger and Etgen, 1990; Zhang and McMechan, 2010), but this is very expensive and also involves the assumption of the constant elastic model in the local window.

The second type of P-S separation uses a system of decoupled equations. The current schemes for isotropic elastic media (Ma and Zhu, 2003; Zhang et al., 2007; Xiao and Leaney,

2010) are based on the corresponding Helmholtz's equations; their differences occur in the propagation equations (stress-based or elastodynamic equations) and in the numerical scheme (e.g., pseudo-spectral or staggered grid). Zhu (2017) separates the P and S modes by solving the Helmholtz equations, which has similarity to the scheme of Ma and Zhu (2003) but uses a fast Poisson solver.

However, the decoupling system based on Helmholtz's equations ignores the conversion between P and S waves at the current time, which will be discussed below. Thus, it has an implicit assumption that the shear modulus is constant, and thus requires a smooth shear modulus to approximately satisfy a locally constant condition.

4.2.2 Imaging conditions of the elastic RTM

The image calculated using unseparated source and receiver displacement vectors often contains cross-talk artifacts; these artifacts complicate the subsequent interpretation. Thus, the P/S wave mode separation is often implemented before imaging. Different combinations of the source P, source S, receiver P and receiver S waves give four types of reflection images: PP, PS, SP and SS.

There are two difficulties for the imaging condition. The first one is that the PS image changes polarity at normal incidence in isotropic media. A direct solution is to correct the polarity change based on rotation angles (Yan and Sava, 2008; Du and Zhu, 2012; Yan and Xie, 2012), which results in a close relationship between the elastic imaging conditions and ADCIGs. Because calculation of ADCIGs is often expensive, Duan and Sava (2015) propose scalar imaging conditions for PS and SP images, which need the normal to the reflection image.

However, calculation of the normal requires a priori information of the reflector locations and orientations. So it is still challenging to apply this method to imaging of the complex structure.

The second difficulty for the imaging condition relates to using the vector-based P/S wave mode separation (e.g., Ma and Zhu, 2003). The resulting P and S waves are vectors, but the images are required to be scalar; the modulus of the vector particle-velocity wavefield is the magnitude of the corresponding scalar wavefield, so the image-magnitude is easy to obtain (e.g., Wang and McMechan, 2015). Thus, the key issue is the polarity of the image at each grid point. Wang and McMechan (2015) use the polarization directions and the reflection-image normal to define the polarity of the PP and PS images; their method fails for the PP images with open angles larger than 90° . A similar approach is to use the dot product of the source and receiver vector wavefields to produce scalar images (Wang et al., 2016a; Zhu, 2017; Du et al., 2017), but this scheme does not preserve the amplitudes of the cross-correlated image. Du et al. (2017) also give a discussion about the polarity change of the PP image at open angle 90° because the dot product involves a scale factor that is the cosine value of the open angle of the PP reflection. The dot product has also been used by Shabelansky et al. (2017) in calculating the converted images. Gong et al. (2016) convert the vector waves into scalar values before applying the imaging condition.

4.2.3 Calculation of ADCIGs from E-RTM

In the previous subsection, the PP and PS imaging conditions are closely related to the calculation of ADCIGs in elastic media. Most of the methods to calculate ADCIGs in elastic media are extensions of those in acoustic media. The ADCIGs can be calculated from extended

images (Yan and Sava, 2008), by the energy flow direction (Dickens and Winbow, 2011; Gong et al., 2016; Yan and Dickens, 2016), or by local plane-wave decomposition (LPD) (Xie et al., 2002; Xu et al., 2011).

Using the Poynting vector (PV) (e.g., Yoon et al., 2011; Dickens and Winbow, 2011) to calculate propagation angles is efficient, but gives only a single direction per grid point per time step. Thus, the migration velocity model often needs to be smoothed to avoid wavefield interferences. To address this problem, a multidirectional PV (MPV) (Tang and McMechan, 2016) is proposed for acoustic media, which decomposes the wavefield into different approximate directions in the ω - \mathbf{k} domain and then calculates the PVs for each decomposed wavefield in the t - \mathbf{x} domain. Tang and McMechan (2017a) further supplement the MPV with an amplitude-preserving scheme to remove the Fourier truncation artifacts in the \mathbf{k} domain during the approximate-propagation-angle-based wave decomposition (approximate WD). These ideas can be expanded for elastic media by using an amplitude-preserving approximate WD to decompose P and S waves (both the stress tensor and the particle velocity) into different vector bins, and then calculating the PVs for each bin. A special case of the approximate WD is using two vector bins (up- and down-separation), which is applied by Suh and Cai (2009) to acoustic waves to remove the backscattering artifacts in RTM images (by cross-correlating the up/down-going source wavefield with down/up-going receiver wavefield), and by Wang et al. (2016b) to only the P and S particle velocities to (e.g.) improve the accuracy of PVs (by calculating them after the up/down separation) in constant/smooth velocity models.

4.2.4 The improvements in this chapter

The previous three subsections describe three important aspects of E-RTM; the P/S wave mode separation, imaging conditions, and calculation of ADCIGs. This chapter gives an improved data flow for E-RTM; this flow can work for non-smooth elastic models. First, we propose an improved system of P and S decoupled equations, which does not have the assumption of a constant shear modulus. This is involved in the P/S Wave Mode Separation section. Second, multidirectional-vector-based imaging conditions are proposed, which can give the correct polarity for all the possible conditions of PP, PS, SP and SS images without a priori knowledge of the reflection-image normal. Third, multidirectional propagation vectors, which can give multiple directions at wavefield overlaps, are calculated to give RTM images and ADCIGs. The second and third aspects are presented in the Multidirectional-vector-based Imaging Condition section.

4.3 Improved system of P/S wave mode separation

This section contains three subsections. The first subsection introduces the first-order hyperbolic system of elastodynamic equations, which is used to generate the elastic stress tensors and particle velocities. The second subsection introduces the current solutions of the P/S wave mode separation and the corresponding limitations. The third subsection addresses the limitation by proposing an improved system of the P/S wave mode separation with a consideration of the conversion between P and S waves at the current separation time.

4.3.1 The first-order hyperbolic system of elastodynamic equations

We use the first-order hyperbolic system of the elastodynamic equations in 2D elastic media (Virieux, 1986),

$$\frac{\partial v_x}{\partial t} = \frac{1}{\rho} \left(\frac{\partial \tau_{xx}}{\partial x} + \frac{\partial \tau_{zx}}{\partial z} \right), \quad (4.1)$$

$$\frac{\partial v_z}{\partial t} = \frac{1}{\rho} \left(\frac{\partial \tau_{xz}}{\partial x} + \frac{\partial \tau_{zz}}{\partial z} \right), \quad (4.2)$$

$$\frac{\partial \tau_{xx}}{\partial t} = (\lambda + 2\mu) \frac{\partial v_x}{\partial x} + \lambda \frac{\partial v_z}{\partial z}, \quad (4.3)$$

$$\frac{\partial \tau_{zz}}{\partial t} = (\lambda + 2\mu) \frac{\partial v_z}{\partial z} + \lambda \frac{\partial v_x}{\partial x}, \quad (4.4)$$

and

$$\frac{\partial \tau_{xz}}{\partial t} = \frac{\partial \tau_{zx}}{\partial t} = \mu \left(\frac{\partial v_x}{\partial z} + \frac{\partial v_z}{\partial x} \right), \quad (4.5)$$

where (v_x, v_z) is the particle velocity vector, $\begin{bmatrix} \tau_{xx} & \tau_{xz} \\ \tau_{zx} & \tau_{zz} \end{bmatrix}$ is the stress tensor, λ is the first Lamé parameter, μ is the shear modulus, ρ is the density, (x, z) is the location in space, and t is the time.

Inserting equations 4.3~4.5 into equations 4.1~4.2 gives,

$$\begin{aligned}\frac{\partial^2 v_x}{\partial t^2} &= \frac{1}{\rho} \left\{ \frac{\partial}{\partial x} \left[(\lambda + 2\mu) \frac{\partial v_x}{\partial x} + \lambda \frac{\partial v_z}{\partial z} \right] + \frac{\partial}{\partial z} \left[\mu \left(\frac{\partial v_x}{\partial z} + \frac{\partial v_z}{\partial x} \right) \right] \right\}, \\ \frac{\partial^2 v_z}{\partial t^2} &= \frac{1}{\rho} \left\{ \frac{\partial}{\partial x} \left[\mu \left(\frac{\partial v_x}{\partial z} + \frac{\partial v_z}{\partial x} \right) \right] + \frac{\partial}{\partial z} \left[(\lambda + 2\mu) \frac{\partial v_z}{\partial z} + \lambda \frac{\partial v_x}{\partial x} \right] \right\},\end{aligned}\tag{4.6}$$

which can be rewritten as (see Appendix 4A [Section 4.9])

$$\begin{aligned}\frac{\partial^2 v_x}{\partial t^2} &= \frac{1}{\rho} \left\{ \frac{\partial}{\partial x} \left[(\lambda + 2\mu) \left(\frac{\partial v_x}{\partial x} + \frac{\partial v_z}{\partial z} \right) \right] + \frac{\partial}{\partial z} \left[\mu \left(\frac{\partial v_x}{\partial z} - \frac{\partial v_z}{\partial x} \right) \right] + 2 \left(\frac{\partial \mu}{\partial z} \frac{\partial v_z}{\partial x} - \frac{\partial \mu}{\partial x} \frac{\partial v_z}{\partial z} \right) \right\}, \\ \frac{\partial^2 v_z}{\partial t^2} &= \frac{1}{\rho} \left\{ \frac{\partial}{\partial z} \left[(\lambda + 2\mu) \left(\frac{\partial v_x}{\partial x} + \frac{\partial v_z}{\partial z} \right) \right] + \frac{\partial}{\partial x} \left[\mu \left(\frac{\partial v_z}{\partial x} - \frac{\partial v_x}{\partial z} \right) \right] + 2 \left(\frac{\partial \mu}{\partial x} \frac{\partial v_x}{\partial z} - \frac{\partial \mu}{\partial z} \frac{\partial v_x}{\partial x} \right) \right\}.\end{aligned}\tag{4.7}$$

4.3.2 Implicit assumption in the traditional system of P and S decoupled equations

The elastic wave simulated by equations 4.1~4.5 includes both P and S waves. Based on Helmholtz's theorem (e.g., Aki and Richards, 1980; Dellinger and Etgen, 1990; Ma and Zhu, 2003), the displacement vectors of P and S waves can be obtained by (Xiao and Leaney, 2010),

$$\frac{\partial^2 \mathbf{u}_p}{\partial t^2} = \frac{1}{\rho} \left\{ \nabla \left[(\lambda + 2\mu) \nabla \cdot \mathbf{u} \right] \right\},\tag{4.8}$$

and

$$\frac{\partial^2 \mathbf{u}_s}{\partial t^2} = -\frac{1}{\rho} \left[\nabla \times (\mu \nabla \times \mathbf{u}) \right].\tag{4.9}$$

An equivalent implementation of equations 4.8 and 4.9 is to obtain the P stress tensor $\boldsymbol{\tau}^p$ and the S stress tensor $\boldsymbol{\tau}^s$ first and then use them to obtain the P displacement vector \mathbf{u}_p and the S displacement vector \mathbf{u}_s . The $\boldsymbol{\tau}^p$ contains only a normal stress,

$$\boldsymbol{\tau}^p = \begin{bmatrix} \tau_{xx}^p & \tau_{xz}^p \\ \tau_{zx}^p & \tau_{zz}^p \end{bmatrix} = (\lambda + 2\mu) \begin{bmatrix} \left(\frac{\partial u_x}{\partial x} + \frac{\partial u_z}{\partial z} \right) & 0 \\ 0 & \left(\frac{\partial u_x}{\partial x} + \frac{\partial u_z}{\partial z} \right) \end{bmatrix}, \quad (4.10)$$

and the $\boldsymbol{\tau}^s$ contains only shear stresses,

$$\boldsymbol{\tau}^s = \begin{bmatrix} \tau_{xx}^s & \tau_{xz}^s \\ \tau_{zx}^s & \tau_{zz}^s \end{bmatrix} = \mu \begin{bmatrix} 0 & \left(\frac{\partial u_z}{\partial x} - \frac{\partial u_x}{\partial z} \right) \\ \left(\frac{\partial u_x}{\partial z} - \frac{\partial u_z}{\partial x} \right) & 0 \end{bmatrix}. \quad (4.11)$$

To relate equations 4.10 and 4.11 with the first-order hyperbolic system (equations 4.1~4.5), we use the particle velocity vector (v_x, v_z) to replace the displacement vector (u_x, u_z) ,

$$\frac{\partial \boldsymbol{\tau}^p}{\partial t} = (\lambda + 2\mu) \begin{bmatrix} \left(\frac{\partial v_x}{\partial x} + \frac{\partial v_z}{\partial z} \right) & 0 \\ 0 & \left(\frac{\partial v_x}{\partial x} + \frac{\partial v_z}{\partial z} \right) \end{bmatrix}, \quad (4.12)$$

and,

$$\frac{\partial \boldsymbol{\tau}^s}{\partial t} = \mu \begin{bmatrix} 0 & \left(\frac{\partial v_z}{\partial x} - \frac{\partial v_x}{\partial z} \right) \\ \left(\frac{\partial v_x}{\partial z} - \frac{\partial v_z}{\partial x} \right) & 0 \end{bmatrix}. \quad (4.13)$$

Note, the (v_x, v_z) are the first-time derivatives (FTDs) of (u_x, u_z) . The P and S particle velocities (v_x^p, v_z^p) and (v_x^s, v_z^s) can be obtained by inserting equations 4.12 and 4.13 into equations 4.1 and 4.2,

$$\begin{aligned}\frac{\partial^2 v_x^p}{\partial t^2} &= \frac{1}{\rho} \left\{ \frac{\partial}{\partial x} \left[(\lambda + 2\mu) \left(\frac{\partial v_x}{\partial x} + \frac{\partial v_z}{\partial z} \right) \right] \right\}, \\ \frac{\partial^2 v_z^p}{\partial t^2} &= \frac{1}{\rho} \left\{ \frac{\partial}{\partial z} \left[(\lambda + 2\mu) \left(\frac{\partial v_x}{\partial x} + \frac{\partial v_z}{\partial z} \right) \right] \right\},\end{aligned}\tag{4.14}$$

and

$$\begin{aligned}\frac{\partial^2 v_x^s}{\partial t^2} &= \frac{1}{\rho} \left\{ \frac{\partial}{\partial z} \left[\mu \left(\frac{\partial v_x}{\partial z} - \frac{\partial v_z}{\partial x} \right) \right] \right\}, \\ \frac{\partial^2 v_z^s}{\partial t^2} &= \frac{1}{\rho} \left\{ \frac{\partial}{\partial x} \left[\mu \left(\frac{\partial v_z}{\partial x} - \frac{\partial v_x}{\partial z} \right) \right] \right\}.\end{aligned}\tag{4.15}$$

This scheme has similarity to that of Ma and Zhu (2003) but they use more simplified equations. Theoretically, if the decoupling system (equations 4.12~4.15) based on Helmholtz's theorem is correct, the summation of the P and S particle velocities should be equal to the total particle velocity;

$$\begin{cases} \frac{\partial^2 v_x}{\partial t^2} - \left(\frac{\partial^2 v_x^p}{\partial t^2} + \frac{\partial^2 v_x^s}{\partial t^2} \right) = 0, \\ \frac{\partial^2 v_z}{\partial t^2} - \left(\frac{\partial^2 v_z^p}{\partial t^2} + \frac{\partial^2 v_z^s}{\partial t^2} \right) = 0. \end{cases}\tag{4.16}$$

However, if we subtract equations 4.14 and 4.15 from equation 4.7, we obtain

$$\begin{cases} \frac{\partial^2 v_x}{\partial t^2} - \left(\frac{\partial^2 v_x^p}{\partial t^2} + \frac{\partial^2 v_x^s}{\partial t^2} \right) = \frac{2}{\rho} \left(\frac{\partial \mu}{\partial z} \frac{\partial v_z}{\partial x} - \frac{\partial \mu}{\partial x} \frac{\partial v_z}{\partial z} \right), \\ \frac{\partial^2 v_z}{\partial t^2} - \left(\frac{\partial^2 v_z^p}{\partial t^2} + \frac{\partial^2 v_z^s}{\partial t^2} \right) = \frac{2}{\rho} \left(\frac{\partial \mu}{\partial x} \frac{\partial v_x}{\partial z} - \frac{\partial \mu}{\partial z} \frac{\partial v_x}{\partial x} \right). \end{cases}\tag{4.17}$$

To satisfy the conservation principle in equation 4.16, we need

$$\begin{cases} \frac{\partial \mu}{\partial z} \frac{\partial v_z}{\partial x} = \frac{\partial \mu}{\partial x} \frac{\partial v_z}{\partial z}, \\ \frac{\partial \mu}{\partial x} \frac{\partial v_x}{\partial z} = \frac{\partial \mu}{\partial z} \frac{\partial v_x}{\partial x}. \end{cases} \quad (4.18)$$

Because we cannot assume the vector-particle components to be constant, we need

$$\frac{\partial \mu}{\partial x} = 0, \quad \frac{\partial \mu}{\partial z} = 0, \quad (4.19)$$

to satisfy equation 4.18 and further satisfy the conservation principle in equation 4.16. Equation 4.19 means that the shear modulus should be constant. Therefore, the decoupling system based on Helmholtz's theorem requires a constant or smooth (approximately locally constant) shear-modulus model. Corresponding to equation 4.17, we can also obtain

$$\frac{\partial \boldsymbol{\tau}}{\partial t} - \left(\frac{\partial \boldsymbol{\tau}^p}{\partial t} + \frac{\partial \boldsymbol{\tau}^s}{\partial t} \right) = 2\mu \begin{bmatrix} -\frac{\partial v_z}{\partial z} & \frac{\partial v_x}{\partial z} \\ \frac{\partial v_z}{\partial x} & -\frac{\partial v_x}{\partial x} \end{bmatrix}, \quad (4.20)$$

so the residual of the FTD of the stress tensor is also not zero. If we insert the residual in equation 4.20 into equation 4.1 and 4.2, we can obtain the residual in equation 4.17, because the residual in equation 4.17 is caused by inserting the pure P and S stress tensors in equations 4.12 and 4.13 into equations 4.1 and 4.2.

Thus, we have shown mathematically that the decoupling scheme based on Helmholtz's theorem assumes a constant shear-modulus. This decoupling system (equations 4.12~4.15) represents the extrapolation of pure P and S waves: the variation of the P particle velocity is generated by a pure P stress tensor (equations 4.12 and 4.14); the variation of the S particle

velocity is generated by a pure S stress tensor (equations 4.13 and 4.15). This scheme does not consider the conversion between P and S waves at the current separation time.

Figure 4.1 demonstrates the P and S waves obtained using the decoupling scheme based on Helmholtz's theorem in a velocity model with a sharp reflection boundary. There are two phenomena;

1. In the residual plots, there are apparent amplitude residuals at the reflector depths. The residual means that the summation of the P and S particle velocities is not equivalent to the total elastic particle velocity at these points (see the cyan arrows in Figure 4.1). This phenomenon is consistent with equation 4.17. (Note, in equations 4.14 and 4.15, the wave propagation is simulated by the elastic equations 4.1~4.5 and the Helmholtz theorem is used only to separate the elastic wave into P and S modes; thus, the error at the reflection point should not spread out to other locations as the wave propagates.)
2. The elastic waves propagate in oblique directions at the reflection points; so physically, the influence of the converted wave at the reflection points should be observed in both x - and z -components. In the z -component of the P wave and the x -component of the S wave, the converted waves that are generated at the current separation time are visible (see the blue arrows in Figure 4.1). However, in the x -component of the P wave and the z -component of the S wave, they are not visible (see the red arrows in Figure 4.1). This is inconsistent with the physical insight.

Xiao and Leaney (2010) use only the P stress tensor (equation 4.12) and obtain the S particle velocity by subtracting the P particle velocity from the total particle velocity. This

ensures that the summation of the P and S particle velocities is equal to total particle velocity, but it is equivalent to adding the residuals in equation 4.17 to the S wave. Thus, it is also inaccurate, because the contrast of the shear modulus also influences the P wave.

In summary, the traditional decoupling scheme based on Helmholtz's theorem (e.g., Ma and Zhu [2003] and Xiao and Leaney [2010]) has an implicit assumption of a constant shear modulus and does not consider the conversion between the P and S waves at the current separation time.

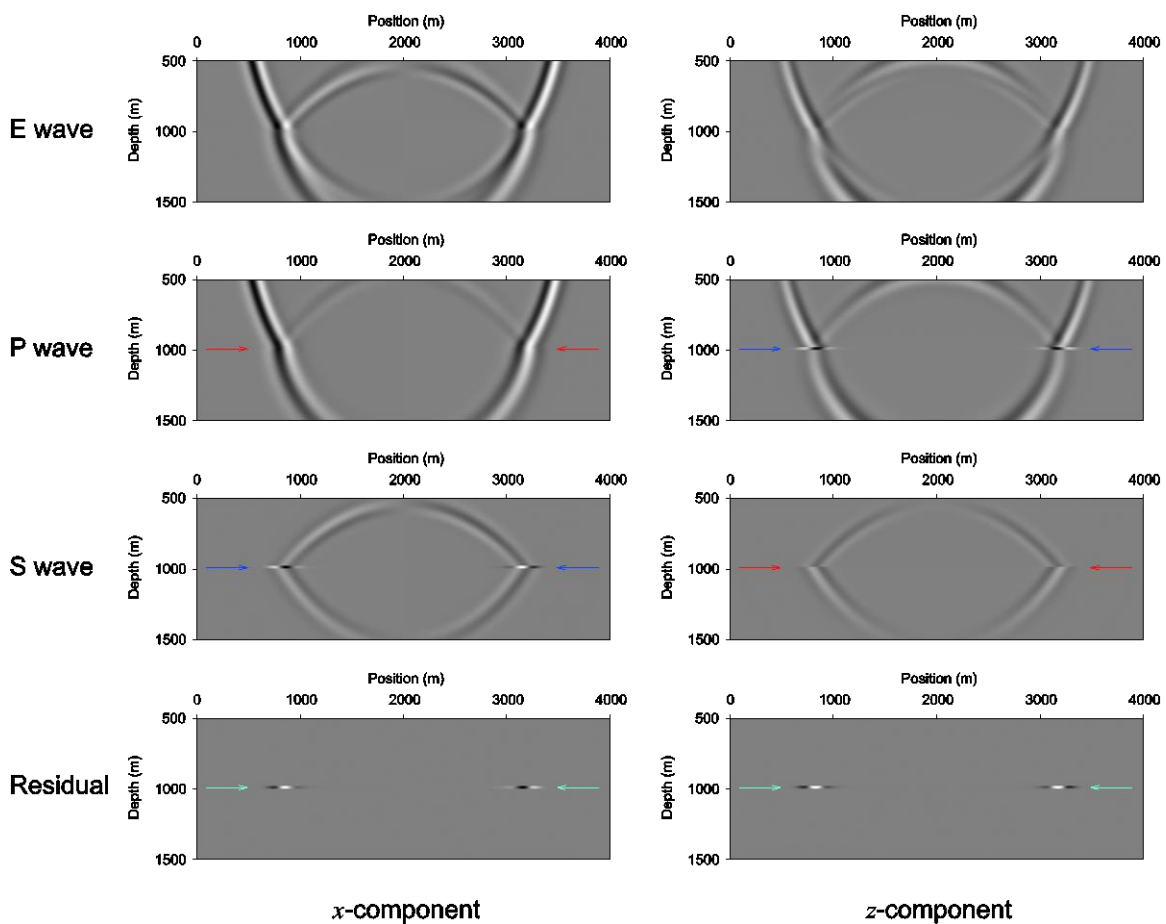


Figure 4.1. Snapshots of P and S particle velocities obtained using the traditional decoupling scheme in a heterogeneous medium with a single, flat reflector. The ‘E wave’ denotes the elastic wave. The residual is obtained by subtracting both the P and S particle velocities from the elastic particle velocity. The colored arrows point to the reflector depth. All the panels are plotted with the same amplitude scale.

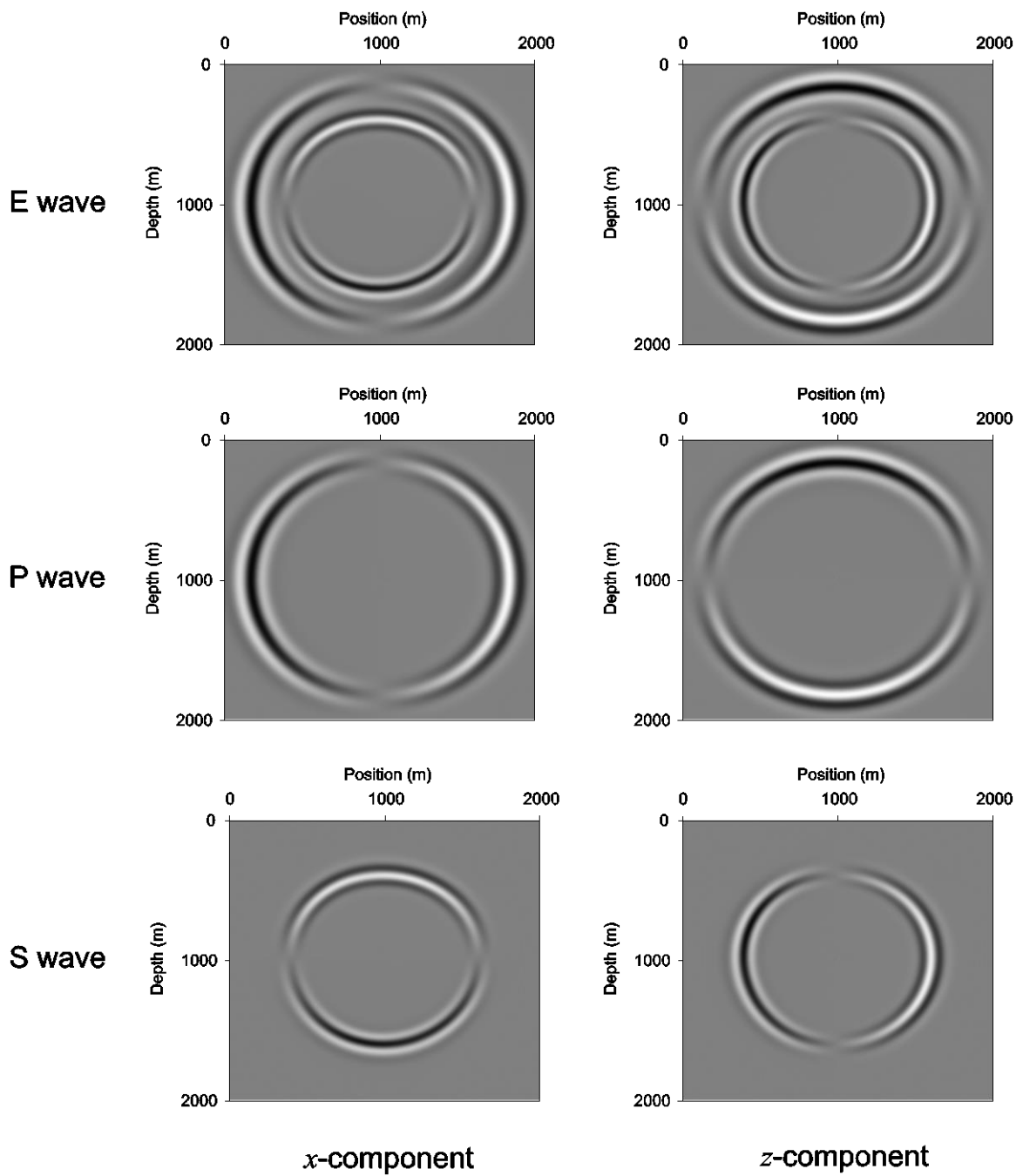


Figure 4.2. Snapshots of P and S particle velocities obtained using the new decoupling scheme in a homogeneous medium. The ‘E wave’ denotes the elastic wave. All the panels are plotted with the same amplitude scale.

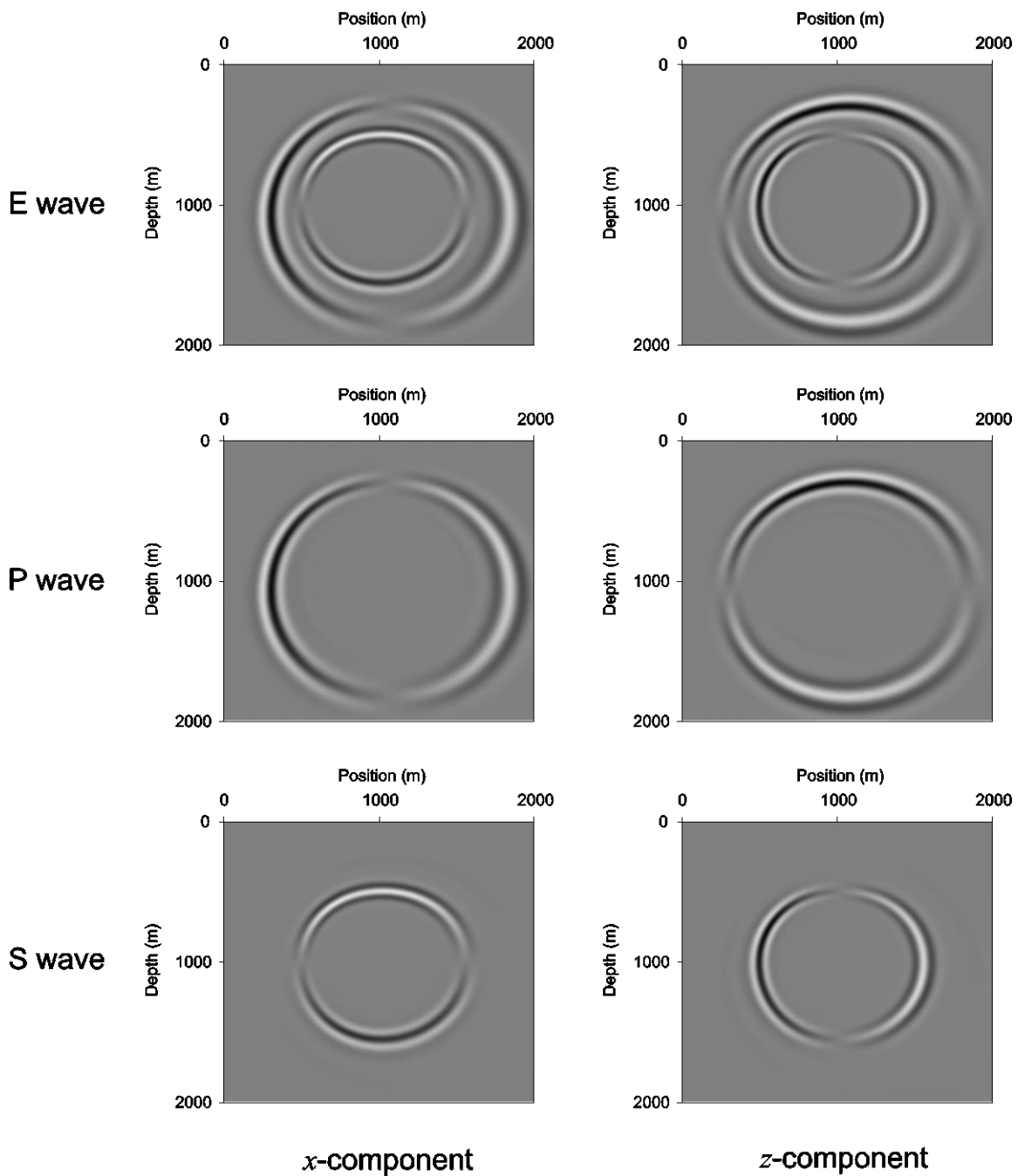


Figure 4.3. Snapshots of P and S particle velocities obtained using the new decoupling scheme in a heterogeneous and smooth medium. The ‘E wave’ denotes the elastic wave. All the panels are plotted with the same amplitude scale.

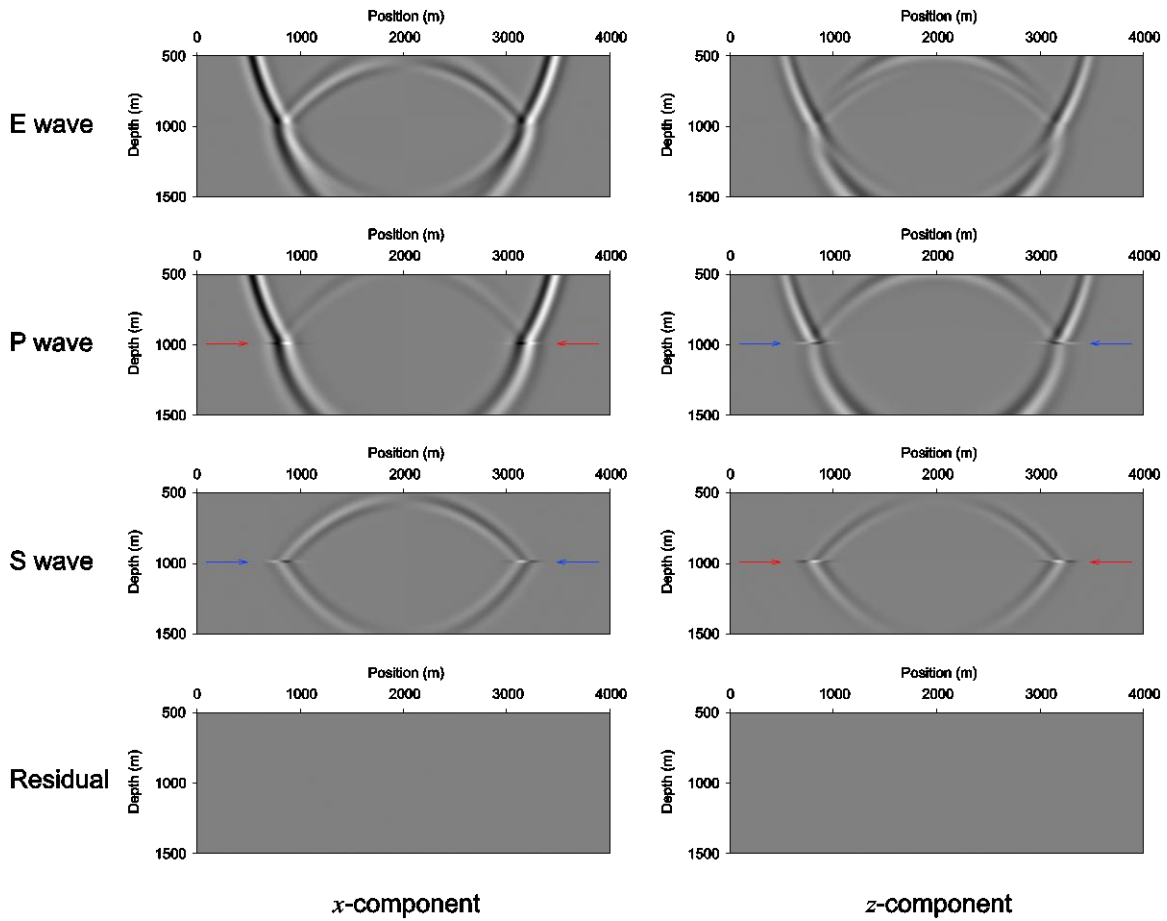


Figure 4.4. Snapshots of P and S particle velocities obtained using the new decoupling scheme in a heterogeneous medium with a single, flat reflector. The ‘E wave’ denotes the elastic wave. The residual is obtained by subtracting the P and S particle velocities from the elastic particle velocity. The colored arrows point to the reflector depth. All the panels are plotted with the same amplitude scale.

4.3.3 Improved decoupling system with a consideration of the conversion between P and S waves at the current separation time

An improvement can be applied to the traditional decoupling system (equations 4.14 and 4.15) to relax the assumption of constant shear-modulus. Because the shear-modulus contrast has an influence on both the P and S waves, we can split the residual in equation 4.17 into the decoupled equations 4.14 and 4.15, which gives

$$\begin{aligned}\frac{\partial^2 v_x^{p,tm}}{\partial t^2} &= \frac{1}{\rho} \left\{ \frac{\partial}{\partial x} \left[(\lambda + 2\mu) \left(\frac{\partial v_x}{\partial x} + \frac{\partial v_z}{\partial z} \right) \right] + \left(\frac{\partial \mu}{\partial z} \frac{\partial v_z}{\partial x} - \frac{\partial \mu}{\partial x} \frac{\partial v_z}{\partial z} \right) \right\}, \\ \frac{\partial^2 v_z^{p,tm}}{\partial t^2} &= \frac{1}{\rho} \left\{ \frac{\partial}{\partial z} \left[(\lambda + 2\mu) \left(\frac{\partial v_x}{\partial x} + \frac{\partial v_z}{\partial z} \right) \right] + \left(\frac{\partial \mu}{\partial x} \frac{\partial v_x}{\partial z} - \frac{\partial \mu}{\partial z} \frac{\partial v_x}{\partial x} \right) \right\},\end{aligned}\tag{4.21}$$

for the P wave and

$$\begin{aligned}\frac{\partial^2 v_x^{s,tm}}{\partial t^2} &= \frac{1}{\rho} \left\{ \frac{\partial}{\partial z} \left[\mu \left(\frac{\partial v_x}{\partial z} - \frac{\partial v_z}{\partial x} \right) \right] + \left(\frac{\partial \mu}{\partial z} \frac{\partial v_z}{\partial x} - \frac{\partial \mu}{\partial x} \frac{\partial v_z}{\partial z} \right) \right\}, \\ \frac{\partial^2 v_z^{s,tm}}{\partial t^2} &= \frac{1}{\rho} \left\{ \frac{\partial}{\partial x} \left[\mu \left(\frac{\partial v_z}{\partial x} - \frac{\partial v_x}{\partial z} \right) \right] + \left(\frac{\partial \mu}{\partial x} \frac{\partial v_x}{\partial z} - \frac{\partial \mu}{\partial z} \frac{\partial v_x}{\partial x} \right) \right\}.\end{aligned}\tag{4.22}$$

for the S wave. Superscript “*tm*” is used to distinguish the P and S variables of the improved scheme from those of the traditional scheme. Equations 4.21 and 4.22 correspond to splitting equation 4.20 into equations 4.12 and 4.13, which gives

$$\frac{\partial \boldsymbol{\tau}^{p,tm}}{\partial t} = \frac{\partial \boldsymbol{\tau}^p}{\partial t} + \mu \begin{bmatrix} -\frac{\partial v_z}{\partial z} & \frac{\partial v_x}{\partial z} \\ \frac{\partial v_z}{\partial x} & -\frac{\partial v_x}{\partial x} \end{bmatrix} = \begin{bmatrix} (\lambda + 2\mu) \left(\frac{\partial v_x}{\partial x} + \frac{\partial v_z}{\partial z} \right) - \mu \frac{\partial v_z}{\partial z} & \mu \frac{\partial v_x}{\partial z} \\ \mu \frac{\partial v_z}{\partial x} & (\lambda + 2\mu) \left(\frac{\partial v_x}{\partial x} + \frac{\partial v_z}{\partial z} \right) - \mu \frac{\partial v_x}{\partial x} \end{bmatrix},\tag{4.23}$$

for the P wave and

$$\frac{\partial \boldsymbol{\tau}^{s,tm}}{\partial t} = \frac{\partial \boldsymbol{\tau}^s}{\partial t} + \mu \begin{bmatrix} -\frac{\partial v_z}{\partial z} & \frac{\partial v_x}{\partial z} \\ \frac{\partial v_z}{\partial x} & -\frac{\partial v_x}{\partial x} \end{bmatrix} = \mu \begin{bmatrix} -\frac{\partial v_z}{\partial z} & \frac{\partial v_z}{\partial x} \\ \frac{\partial v_x}{\partial z} & -\frac{\partial v_x}{\partial x} \end{bmatrix},\tag{4.24}$$

for the S wave. Inserting equations 4.23 and 4.24 into equations 4.1 and 4.2 will give equations 4.21 and 4.22.

In the new system, the stress tensors and particle velocities of the P and S waves can be obtained by subtracting each other from the corresponding variable of the full elastic wave. Because the S stress tensor (equation 4.24) has a simpler expression than the P stress tensor (equation 4.23), we use equation 4.24 to implement P/S wave mode separation. The corresponding flow is

- a) Calculate the S stress tensor $\tau^{s,tm}$ using

$$\frac{\partial \tau^{s,tm}}{\partial t} = \begin{bmatrix} \frac{\partial \tau_{xx}^{s,tm}}{\partial t} & \frac{\partial \tau_{xz}^{s,tm}}{\partial t} \\ \frac{\partial \tau_{zx}^{s,tm}}{\partial t} & \frac{\partial \tau_{zz}^{s,tm}}{\partial t} \end{bmatrix} = \mu \begin{bmatrix} -\frac{\partial v_z}{\partial z} & \frac{\partial v_z}{\partial x} \\ \frac{\partial v_x}{\partial z} & -\frac{\partial v_x}{\partial x} \end{bmatrix}. \quad (4.25)$$

- b) If $\tau^{p,tm}$ is required, use

$$\tau^{p,tm} = \tau - \tau^{s,tm}, \quad (4.26)$$

to calculate it; otherwise, ignore this step.

- c) Insert $\tau^{s,tm}$ into the following equations (refer to equations 4.1 and 4.2)

$$\begin{aligned} \frac{\partial v_x^{s,tm}}{\partial t} &= \frac{1}{\rho} \left(\frac{\partial \tau_{xx}^{s,tm}}{\partial x} + \frac{\partial \tau_{zx}^{s,tm}}{\partial z} \right), \\ \frac{\partial v_z^{s,tm}}{\partial t} &= \frac{1}{\rho} \left(\frac{\partial \tau_{xz}^{s,tm}}{\partial x} + \frac{\partial \tau_{zz}^{s,tm}}{\partial z} \right), \end{aligned} \quad (4.27)$$

to calculate the S particle velocity $\mathbf{v}^{s,tm}$.

- d) Calculate P particle velocity $\mathbf{v}^{p,tm}$ using

$$\mathbf{v}^{p,tm} = \mathbf{v} - \mathbf{v}^{s,tm}. \quad (4.28)$$

In this data flow, P and S particle velocities are successfully decoupled. An alternative way to achieve this decomposition algorithm is described in Appendix 4B (Section 4.10), which corresponds to the divergence and curl operation.

Comparing the proposed flow with that of Ma and Zhu (2003), we can conclude:

1. When the shear modulus is constant, equations 4.21 and 4.22 of the improved system are equivalent to equations 4.14 and 4.15 of the traditional system. Figures 4.2 and 4.3 show that the new scheme works well for constant and smooth (approximately locally constant) models.
2. When the shear modulus has a strong contrast, the new decoupling scheme considers the conversion between the P and S waves at the current separation time. Figure 4.4 shows the decoupled result using the new scheme. Comparing with Figure 4.1, first, the residual obtained by subtracting the P and S particle velocities from the full elastic particle velocity is zero. Second, in both the x - and z -components of the P and S particle velocities, we can observe the converted waves that are generated at the reflection depths at the current separation time (compare the reflection points marked by red arrows in Figures 4.1 and 4.4). This fits with the physical insight; the wave propagates obliquely at these reflection points, and so the converted waves are generated in both x - and z -components at the reflection points (see red and blue arrows in Figure 4.4).

4.4 Multidirectional-vector-based imaging condition

This section involves three subsections. The first subsection defines improved elastic imaging conditions for PP, PS, SP and SS images. The PP and SS imaging conditions require the

sign of the open angle between the incident and reflected waves, which relates the elastic imaging conditions to the ADCIGs. Thus, the second subsection then uses the approximate WD to convert the particle velocities into multidirectional propagation vectors, because the difference between the particle velocity (the polarization vector) and the propagation vector is only the sign of \mathbf{k}/ω . Finally, the third subsection gives the corresponding elastic imaging conditions based on multidirectional polarization and propagation vectors.

4.4.1 Improved vector-based imaging conditions

In the “Introduction” section, we emphasize that the imaging conditions are very important for E-RTM. There are two issues of the imaging conditions here (take PP and PS images for example):

- i). Physically, both the PP and PS images need to be scalar, but the P and S particle velocities are vectors.
- ii). The PS image has a polarity change at normal incidence.

For problem (i), the magnitudes of the PP and PS images (I^{pp} and I^{ps}) are easy to obtain, e.g., for a cross-correlation imaging condition (e.g., Kaelin and Guitton, 2006)

$$|I^{pp}| = |\mathbf{v}_s^{p,tm}| |\mathbf{v}_r^{p,tm}|, \quad (4.29)$$

and

$$|I^{ps}| = |\mathbf{v}_s^{p,tm}| |\mathbf{v}_r^{s,tm}|, \quad (4.30)$$

where the subscripts s and r denote source and receiver, respectively. Thus, the key issue here is how to decide the polarity of I^{pp} and I^{ps} .

Physically, if both the source and receiver polarization vectors either share the same directions as, or have the opposite directions to, their propagation vectors, the polarity of I^{pp} is positive; otherwise (e.g., the source polarization vector shares the same direction as its propagation vector and the receiver polarization vector has the opposite direction to its propagation vector), the polarity of I^{pp} is negative. The polarity of I^{pp} is decided by the source P polarization vector $\mathbf{v}_s^{p,tm}$, the receiver P polarization vector $\mathbf{v}_r^{p,tm}$, and the open angle θ^{pp} between incident and reflected waves:

$$\text{sgn}^{pp} = \text{sgn}(I^{pp}) = -\text{sgn}(\cos \mathcal{G}^{pp} \cos \theta^{pp}) = -\text{sgn}(\mathbf{v}_s^{p,tm} \cdot \mathbf{v}_r^{p,tm} \cos \theta^{pp}), \quad (4.31)$$

where \mathcal{G}^{pp} is defined in equation 4C-1. Appendix 4C (Section 4.11) shows that equation 4.31 satisfies all the eight possible conditions of I^{pp} .

The I^{ps} has reversed polarities across normal incidence. To address this issue, the polarity of I^{ps} can be defined as follows: For an incident P wave with a polarization vector that shares the same direction as the propagation vector, if the polarization vector of the reflected vector S wave points to the reflection-image normal, the polarity of I^{ps} is positive; otherwise, it is negative. For an incident P wave with a polarization vector that has the opposite direction to the propagation vector, if the polarization vector of the reflected vector S wave points in the direction away from the reflection-image normal, the polarity of I^{ps} is positive; otherwise, it is negative.

The polarity of I^{ps} is decided by the source P polarization vector $\mathbf{v}_s^{p,tm}$ and the receiver S polarization vector $\mathbf{v}_r^{s,tm}$:

$$\text{sgn}^{ps} = \text{sgn}(I^{ps}) = -\text{sgn}(\cos \mathcal{G}^{ps}) = -\text{sgn}(\mathbf{v}_s^{p,tm} \cdot \mathbf{v}_r^{s,tm}), \quad (4.32)$$

where \mathcal{G}^{ps} is defined in equation 4D-1. Appendix 4D (Section 4.12) shows that equation 4.32 satisfies all the sixteen possible situations of the PS image.

A combination of equations 4.29 and 4.31 gives

$$I^{pp} = \text{sgn}^{pp} |I^{pp}| = -\text{sgn}(\mathbf{v}_s^{p,tm} \cdot \mathbf{v}_r^{p,tm} \cos \theta^{pp}) |\mathbf{v}_s^{p,tm}| |\mathbf{v}_r^{p,tm}|, \quad (4.33)$$

and a combination of equations 4.30 and 4.32 gives

$$I^{ps} = \text{sgn}^{ps} |I^{ps}| = -\text{sgn}(\mathbf{v}_s^{p,tm} \cdot \mathbf{v}_r^{s,tm}) |\mathbf{v}_s^{p,tm}| |\mathbf{v}_r^{s,tm}|. \quad (4.34)$$

The equations for SP and SS images are in Appendix 4E (Section 4.13).

Compared with the imaging conditions of Wang and McMechan (2015), equations 4.33 and 4.34 have two improvements.

- i'. Equation 4.33 can give the correct polarity of I^{pp} with open angles above 90° by adding the $\cos \theta^{pp}$ into sgn^{pp} .
- ii'. Equations 4.33 and 4.34 do not require calculation of the reflection-image normal.

Equations 4.33 and 4.34 address problems (i) and (ii) by separating the calculation of polarity and amplitude of an image. However, the I^{pp} in equation 4.33 requires calculation of propagation angles, which relates the vector-based imaging conditions to the calculation of

ADCIGs. Moreover, wavefield overlaps may influence the calculation of both the propagation and polarization (particle-velocity vector) directions, as addressed in the two subsections below.

4.4.2 Two methods to calculate the multidirectional propagation vectors

To calculate the P and S propagation vectors $(p_x^{p,tm}, p_z^{p,tm})$ and $(p_x^{s,tm}, p_z^{s,tm})$, an efficient way is using the PVs (Červený, 2001; Dickens and Winbow, 2011),

$$\begin{aligned} p_x^{p,tm} &= -(\tau_{xx}^{p,tm} v_x^{p,tm} + \tau_{xz}^{p,tm} v_z^{p,tm}), \\ p_z^{p,tm} &= -(\tau_{zx}^{p,tm} v_x^{p,tm} + \tau_{zz}^{p,tm} v_z^{p,tm}), \end{aligned} \quad (4.35)$$

for P waves and

$$\begin{aligned} p_x^{s,tm} &= -(\tau_{xx}^{s,tm} v_x^{s,tm} + \tau_{xz}^{s,tm} v_z^{s,tm}), \\ p_z^{s,tm} &= -(\tau_{zx}^{s,tm} v_x^{s,tm} + \tau_{zz}^{s,tm} v_z^{s,tm}), \end{aligned} \quad (4.36)$$

for S waves. Equations 4.35 and 4.36 give only a single direction and thus they do not work for wavefield overlaps that often occur in non-smooth migration models. To address this, we can extend the multidirectional scheme of Tang and McMechan (2016, 2017a) from an acoustic medium to an elastic medium, which gives

$$\begin{aligned} p_{x,i}^{p,tm} &= -(\tau_{xx,i}^{p,tm} v_{x,i}^{p,tm} + \tau_{xz,i}^{p,tm} v_{z,i}^{p,tm}), \\ p_{z,i}^{p,tm} &= -(\tau_{zx,i}^{p,tm} v_{x,i}^{p,tm} + \tau_{zz,i}^{p,tm} v_{z,i}^{p,tm}), \end{aligned} \quad (4.37)$$

and

$$\begin{aligned} p_{x,i}^{s,tm} &= -(\tau_{xx,i}^{s,tm} v_{x,i}^{s,tm} + \tau_{xz,i}^{s,tm} v_{z,i}^{s,tm}), \\ p_{z,i}^{s,tm} &= -(\tau_{zx,i}^{s,tm} v_{x,i}^{s,tm} + \tau_{zz,i}^{s,tm} v_{z,i}^{s,tm}), \end{aligned} \quad (4.38)$$

where e.g., $v_{x,i}^{p,tm}$ is obtained by decomposing $v_x^{p,tm}$ into several vector bins by using partial inverse Fourier transforms (FTs),

$$v_{x,i}^{p,tm}(t, \mathbf{x}) = \frac{1}{2\pi} \Re \left\{ \int_{-\infty}^{\infty} \left[\int_{\beta_{x,i-1}^{p,tm}}^{\beta_{x,i}^{p,tm}} \bar{V}_x^{p,tm}(\omega, \mathbf{k}) e^{-i\mathbf{k}\mathbf{x}} d\mathbf{k} \right] e^{i\omega t} d\omega \right\}, \quad (4.39)$$

Where \Re means taking only the real part, i is the reference number of the vector bin, and $\bar{V}_x^{p,tm}$ is the particle velocity in the ω - \mathbf{k} domain and can be obtained using a forward FT

$$\bar{V}_x^{p,tm}(\omega, \mathbf{k}) = \int_{-\infty}^{\infty} dt \int_{-\infty}^{\infty} d\mathbf{x} v_x^{p,tm}(t, \mathbf{x}) e^{i(\mathbf{k}\mathbf{x} - \omega t)}. \quad (4.40)$$

In equation 4.39, $\beta_x^{p,tm}$ is an ‘‘approximate’’ polar angle and can be calculated by

$$\beta_x^{p,tm} = \arctan \left(\frac{k_z^{p,tm}}{k_x^{p,tm}} \right). \quad (4.41)$$

The FTs in equations 4.39 and 4.40 are over the global space. Equations 4.39~4.41 decompose $v_x^{p,tm}$ into several approximate directions, which can also be applied to other variables in equations 4.37 and 4.38; then we can use the PV formulas (equations 4.37 and 4.38) to calculate the propagation directions for each decomposed wavefield. This two-step process is the basic structure of the MPV. Equation 4.39 is equivalent to (Tang and McMechan, 2016)

$$v_{x,i}^{p,tm}(t, \mathbf{x}) = \frac{1}{\pi} \Re \left\{ \int_{\beta_{x,i-1}^{p,tm}}^{\beta_{x,i}^{p,tm}} \left[\int_0^{+\infty} \bar{V}_x^{p,tm}(\omega, \mathbf{k}) e^{i\omega t} d\omega \right] e^{-i\mathbf{k}\mathbf{x}} d\mathbf{k} \right\}, \quad (4.42)$$

which means, the approximate WD in the \mathbf{k} domain only needs to be applied to the wavefields with positive frequencies. We use equation 4.42 in the implementation because it reduces the cost. Interested readers can also refer to Tang and McMechan (2016) for using complex-valued

extrapolation of the source wavelet and of the observed data using only the positive frequencies to save the I/O of the approximate WD, but this is not used in the implementation of this chapter.

Equations 4.40~4.42 describe an approximate WD for $v_{x,i}^{p,tm}$. To obtain an MPV for the P and S waves in elastic media, the approximate WD is required to be applied to each component of the stress tensor and the particle velocity (see equations 4.37 and 4.38), which is computationally expensive. A practical alternative is to decompose the P and S particle velocities $\mathbf{v}^{p,tm}$ and $\mathbf{v}^{s,tm}$ into $\mathbf{v}_i^{p,tm}$ and $\mathbf{v}_i^{s,tm}$, and then insert $\mathbf{v}_i^{p,tm}$ and $\mathbf{v}_i^{s,tm}$ into equations 4.23 and 4.24 to approximate the $\boldsymbol{\tau}_i^{p,tm}$ and $\boldsymbol{\tau}_i^{s,tm}$, respectively. Take the S stress tensor for example,

$$\frac{\partial \tilde{\boldsymbol{\tau}}_i^{s,tm}}{\partial t} = \mu \begin{bmatrix} -\frac{\partial v_{i,z}^{s,tm}}{\partial z} & \frac{\partial v_{i,z}^{s,tm}}{\partial x} \\ \frac{\partial v_{i,x}^{s,tm}}{\partial z} & -\frac{\partial v_{i,x}^{s,tm}}{\partial x} \end{bmatrix}, \quad (4.43)$$

where the “ \sim ” over $\boldsymbol{\tau}_i^{s,tm}$ means “approximate”. Thus, we only need to apply the approximate WD to $\mathbf{v}_i^{p,tm}$ and $\mathbf{v}_i^{s,tm}$. This approach also works in 3D.

Another way is to use the approximate WD to convert the decomposed particle velocities $\mathbf{v}_i^{p,tm}$ and $\mathbf{v}_i^{s,tm}$ into the propagation vectors $\mathbf{p}_i^{p,tm}$ and $\mathbf{p}_i^{s,tm}$. The particle velocities are also polarization vectors. When the approximate WD is applied to the particle velocities, it gives the sign of (\mathbf{k}/ω) , which can be used to convert the polarization vector (POV) into the propagation vector (PRV). In 2D, the propagation vector of a decomposed P particle velocity can be obtained using

$$\begin{aligned}
p_{x,i}^{p,tm}(t, \mathbf{x}) &= \text{sgn} \left[\left(\frac{k_x}{\omega} \right)_i \right] \cdot |v_{x,i}^{p,tm}(t, \mathbf{x})|, \\
p_{z,i}^{p,tm}(t, \mathbf{x}) &= \text{sgn} \left[\left(\frac{k_z}{\omega} \right)_i \right] \cdot |v_{z,i}^{p,tm}(t, \mathbf{x})|,
\end{aligned} \tag{4.44}$$

and the propagation vector of a decomposed S particle velocity can be obtained using

$$\begin{aligned}
p_{x,i}^{s,tm}(t, \mathbf{x}) &= \text{sgn} \left[\left(\frac{k_x}{\omega} \right)_i \right] \cdot |v_{x,i}^{s,tm}(t, \mathbf{x})|, \\
p_{z,i}^{s,tm}(t, \mathbf{x}) &= \text{sgn} \left[\left(\frac{k_z}{\omega} \right)_i \right] \cdot |v_{z,i}^{s,tm}(t, \mathbf{x})|,
\end{aligned} \tag{4.45}$$

because the propagation direction of an S wave is perpendicular to its particle velocity direction. Equations 4.44 and 4.45 contain the \mathbf{k}/ω in the t - \mathbf{x} domain; this involves the process from equations 4.40 to 4.42, which transforms the wavefield into the ω - \mathbf{k} domain (equation 4.40), performs the approximate WD and then transforms each decomposed wavefield back into the t - \mathbf{x} domain (equations 4.41 and 4.42). As indicated by equations 4.44 and 4.45, to convert the particle velocity into the propagation vector, the approximate WD needs at least four vector bins for a 2D case and eight vector bins for a 3D case (the extension of this method into 3D is discussed in Section 4.6). If we prefer to use only two vector bins (up and down) in 2D and two or four vectors in 3D, we can choose the first suggested approach which applies the approximate WDs to the P and S particle velocities and then inserts the decomposed P and S particle velocities into the corresponding decoupled equations (e.g., equations 4.23 and 4.24 for 2D) to obtain the decomposed P and S stress tensors (e.g., equation 4.43 for the S stress tensor in 2D).

The conversion in equations 4.44 and 4.45 has a flaw. To remove the Fourier truncation artifacts caused by angle truncation of the approximate WD in the \mathbf{k} domain (e.g., equation 4.42),

amplitude tapering needs to be done in the angle domain; to preserve the total amplitude, each pair of adjacent vector bins has a small shared amplitude-tapering window (Tang and McMechan, 2017c). The sign of \mathbf{k}/ω may not be correct for the part of the wavefields in the small shared windows that involve the quadrant boundaries, but the influence is very limited.

4.4.3 Multidirectional-vector-based imaging conditions for E-RTM and ADCIGs

To be consistent with the multidirectional propagation vector in the previous subsection, we use multidirectional-vector-based imaging conditions; thus, the PP imaging condition in equation 4.33 becomes

$$I_k^{pp} = -F(\theta_k^{pp}) [1 - \delta(i - j)] \operatorname{sgn}(\mathbf{v}_{s,i}^{p,m} \mathbf{v}_{r,j}^{p,m} \cos \theta_k) |\mathbf{v}_{s,i}^{p,m}| |\mathbf{v}_{r,j}^{p,m}|, \quad (4.46)$$

where i, j and k are reference numbers for the decomposed source wavefield, the decomposed receiver wavefield and the partial RTM images, respectively. Equation 4.46 uses a WD plus angle-filter (WD-AF) imaging condition (Tang and McMechan, 2017c) to remove the backscattering artifact. The $1 - \delta(i - j)$ means not cross-correlating the source and receiver wavefields in the same vector bins (δ denotes a delta function). The angle filter is

$$F(\theta_k^{pp}) = \begin{cases} 1, & \theta_k^{pp} < \theta_1, \\ \frac{1}{2} \left\{ 1 - \cos \left[\frac{\theta_2 - \theta_k^{pp}}{\theta_2 - \theta_1} \times \pi \right] \right\}, & \theta_1 \leq \theta_k^{pp} < \theta_2, \\ 0, & \theta_k^{pp} \geq \theta_2, \end{cases} \quad (4.47)$$

where θ_k^{pp} is the open angle of I_k^{pp} , and θ_1 and θ_2 are the threshold angles; we choose $\theta_1 = 120^\circ$ and $\theta_2 = 150^\circ$ in our examples. Both the delta function and the angle filter are for removing the backscattering artifacts.

Similarly, the PS imaging condition in equation 4.34 becomes

$$I_k^{ps} = -\text{sgn}(\mathbf{v}_{s,i}^{p,tm} \cdot \mathbf{v}_{r,j}^{s,tm}) |\mathbf{v}_{s,i}^{p,tm}| |\mathbf{v}_{r,j}^{s,tm}|. \quad (4.48)$$

Equations 4.46 and 4.48 work for wavefield overlaps because both the polarization and propagation vectors are multidirectional. For the corresponding SP and SS imaging conditions, see Appendix 4E (Section 4.13).

The entire PP and PS images are given by a summation of the corresponding partial images,

$$\begin{aligned} I^{pp} &= \sum_{k=1}^{k=K} I_k^{pp}, \\ I^{ps} &= \sum_{k=1}^{k=K} I_k^{ps}, \end{aligned} \quad (4.49)$$

where the K is the total number of partial images, which is $(M^2 - M)$ for the PP image and M^2 for the PS image. Here M is the number of vector bins for the approximate WD. Stacking I^{pp} and I^{ps} at all time steps of all the sources will produce the final PP and PS images.

Accordingly, the angle-domain imaging condition for PP ADCIGs is

$$I_k^{pp}(\bar{\theta}_k^{pp}) = -[1 - \delta(i-j)] \delta(\bar{\theta}_k^{pp} - \theta_k^{pp}) \text{sgn}(\mathbf{v}_{s,i}^{p,tm} \cdot \mathbf{v}_{r,j}^{p,tm} \cos \theta_k^{pp}) |\mathbf{v}_{s,i}^{p,tm}| |\mathbf{v}_{r,j}^{p,tm}|, \quad (4.50)$$

and the angle-domain imaging condition for PS ADCIGs is

$$I_k^{ps}(\bar{\theta}_k^{ps}) = -\delta(\bar{\theta}_k^{ps} - \theta_k^{ps}) \text{sgn}(\mathbf{v}_{s,i}^{p,tm} \cdot \mathbf{v}_{r,j}^{s,tm}) |\mathbf{v}_{s,i}^{p,tm}| |\mathbf{v}_{r,j}^{s,tm}|. \quad (4.51)$$

where $\bar{\theta}_k^{pp}$ and $\bar{\theta}_k^{ps}$ are the open angles for sorting PP and PS ADCIGs, and θ_k^{pp} and θ_k^{ps} are the open angles calculated by

$$\begin{cases} \theta_k^{pp} = \pi - \cos\left(\frac{\mathbf{p}_{s,i}^{p,tm} \cdot \mathbf{p}_{r,j}^{p,tm}}{|\mathbf{p}_{s,i}^{p,tm}| |\mathbf{p}_{r,j}^{p,tm}|}\right), \\ \theta_k^{ps} = \pi - \cos\left(\frac{\mathbf{p}_{s,i}^{p,tm} \cdot \mathbf{p}_{r,j}^{s,tm}}{|\mathbf{p}_{s,i}^{p,tm}| |\mathbf{p}_{r,j}^{s,tm}|}\right), \end{cases} \quad (4.52)$$

Equations 4.50 and 4.51 are theoretical expressions. In implementation, because $\bar{\theta}_k^{pp}$ and $\bar{\theta}_k^{ps}$ often need to be equally-spaced, a Gaussian-weighting function can be used to replace the delta function to binning the calculated θ_k^{pp} and θ_k^{ps} into several $\bar{\theta}_k^{pp}$ and $\bar{\theta}_k^{ps}$ within a small window (Tang and McMechan, 2017a). For the corresponding SP and SS imaging conditions, see Appendix 4E (Section 4.13).

The approximate WD is not cheap, but the method is proposed for elastic imaging with non-smooth, structurally complicated migration models. For smooth models with relatively simple structure, because most source wavefields are down-going and most of the receiver wavefields are up-going, application of the proposed method may not be necessary. However, even for smooth migration models with relatively simple structures, backscattering artifacts may appear in the shallow part of the migration image because of the tomographic waves near the surface; thus, applying an up-down separation before imaging may still improve the image especially in the near-surface region (e.g., Wang et al., 2016b).

For models with a varied complication of the structures (e.g., in the horizontal direction for recording the data on the surface), due to the limited illumination of each source, some sources give high-amplitude images for simple structures and some give the high-amplitude images for complicated structures. If there is a pre-knowledge, it is also possible to apply different numbers of vector bins to the image corresponding to different sources.

4.5 Examples

This section uses both simple and complicated models to illustrate the proposed methods. The entire data flow is presented in Figure 4.5. Because the P/S wave mode separation has been illustrated in the “Theory” section (Figures 4.1 to 4.4), we start with illustrating the multidirectional polarization/propagation vectors for overlapping wavefields, then use two simple models to compare the elastic imaging conditions, and finally apply the data flow to a complicated portion of the Marmousi2 model (Martin et al., 2006). All the multidirectional-vector examples use four vector bins for the approximate WD. For the multidirectional-vector-based RTM examples, both the source and receiver wavefields use four vector bins and thus there are twelve partial images (refer to equations, 4.46, 4.48, 4.50 and 4.51).

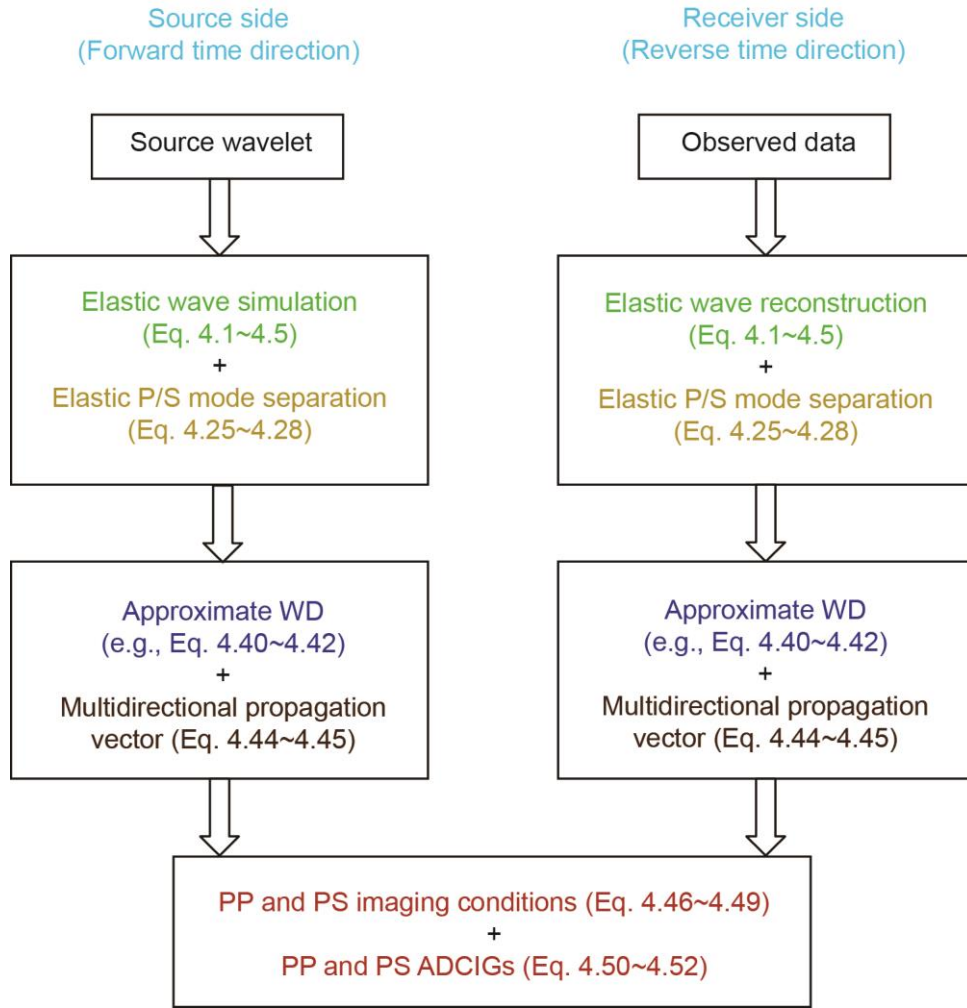


Figure 4.5. The proposed data flow.

4.5.1 Calculating the polarization and propagation vectors for wavefield overlaps

Figures 4.6~4.8 illustrate the effectiveness of the proposed method for calculating multidirectional propagation vectors when wavefields overlap. Figure 4.6 shows a snapshot with PS, PP and SS wavefield overlaps. Here, the PS overlap denotes that a P wave overlaps with an S wave, the PP overlap denotes that a P wave overlaps with a P wave, and the SS overlap denotes that an S wave overlaps with an S wave. Because the polarization and propagation vectors of

both the x - and z -component of the particle velocities are same, we plot only the x -component of particle velocities in Figures 4.6~4.8.

In Figure 4.6, the polarization vectors (see the red arrows) are chaotic and cannot give the correct directions at the wavefield overlaps. A comparison of the full elastic, the P, and the S waves shows that using P/S wave mode separation improves the result by separating the PS wavefield overlaps, which is a commonsense aspect (e.g., used by Wang and McMechan [2015]); however, in the P and S wave snapshots, the PP and SS wavefield overlaps still remain.

In Figure 4.7, using the approximate WD can separate these wavefield overlaps; thus, the polarization directions of both the P and S particle velocities are correct. However, these polarization directions are not the propagation directions. By using equations 4.44 and 4.45 to convert the polarization directions to propagation directions, we obtain Figure 4.8, which gives the correct propagation directions.

4.5.2 PP and PS images for two simple models with a flat reflector interface

Two simple elastic models with a flat reflecting interface between two layers (Figure 4.9) are used to illustrate the proposed procedure. Figure 4.9a contains positive PP and PS reflectivity. Figures 4.10 and 4.11 show the PP and PS images obtained using four imaging conditions. There is a single source that locates at the midpoint of the surface; the synthetic data is observed by the 500 receivers at the surface, the range of which is from 0 to 5000 m.

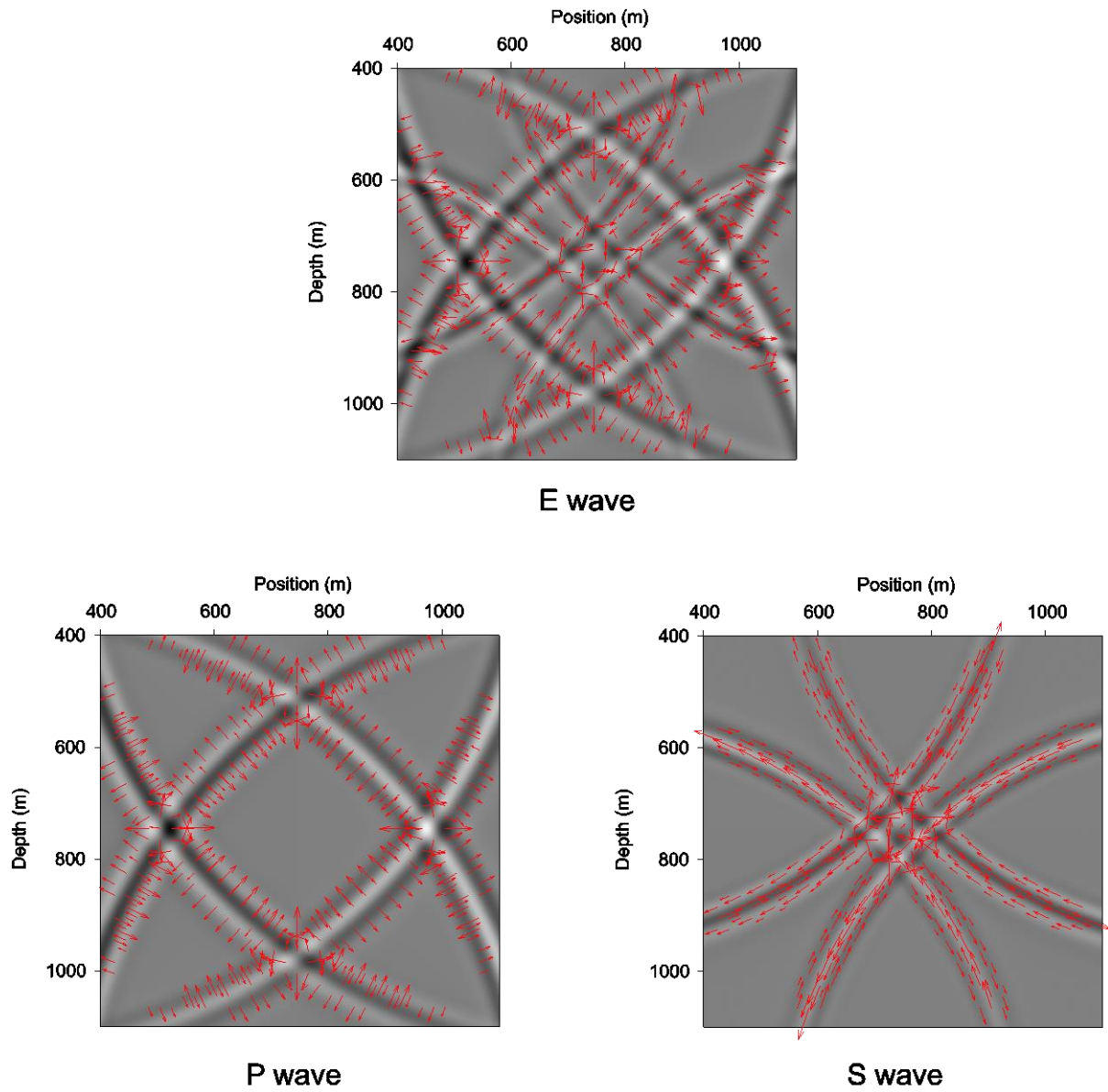


Figure 4.6. Wavefield snapshots of the x -component of an elastic (E) particle velocities and the separated P and S particle velocities. The arrows denote the polarization directions defined by the particle velocities.

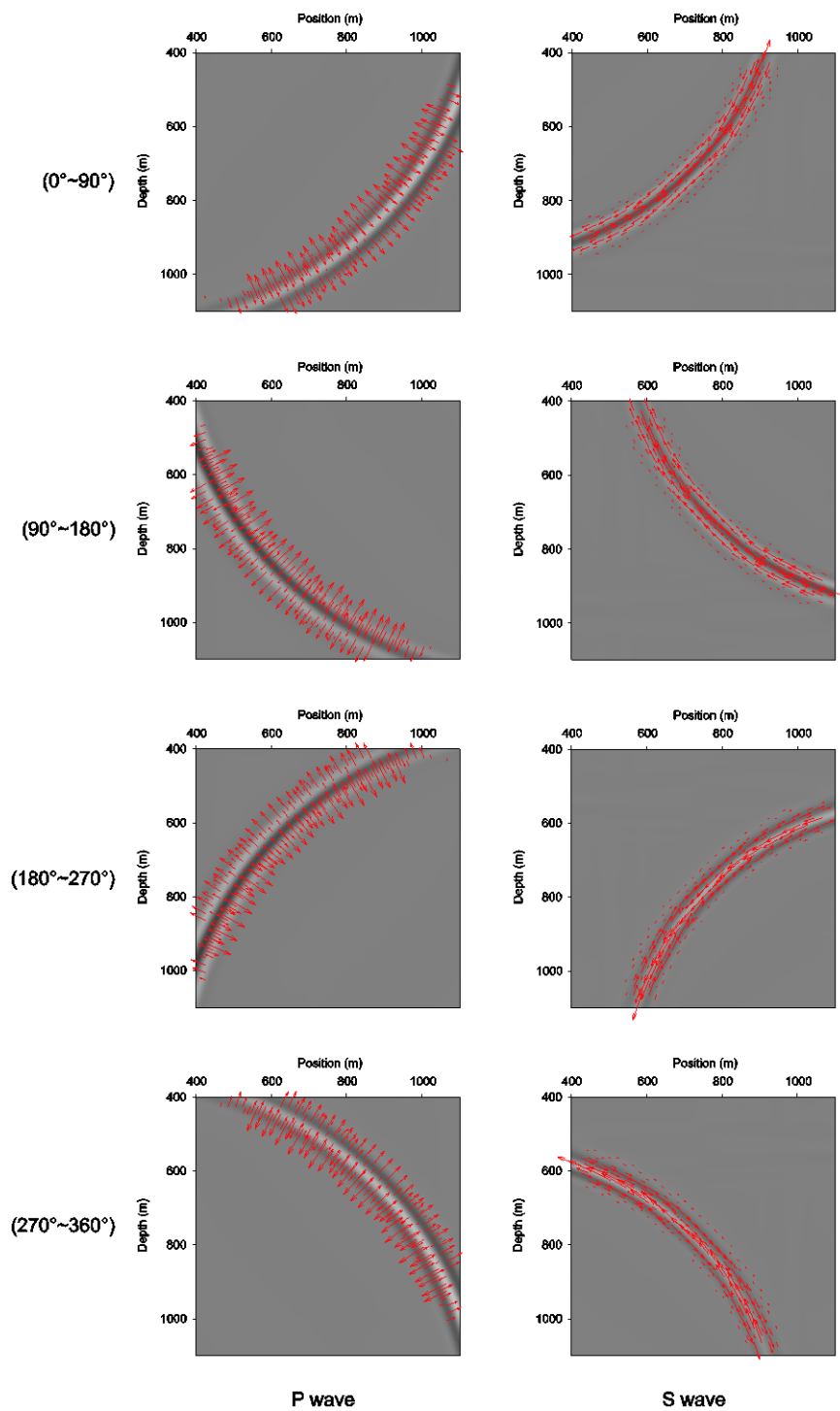


Figure 4.7. Wavefield snapshots of the x -component of the decomposed P and S particle velocities. The arrows denote the polarization directions defined by the particle velocities.

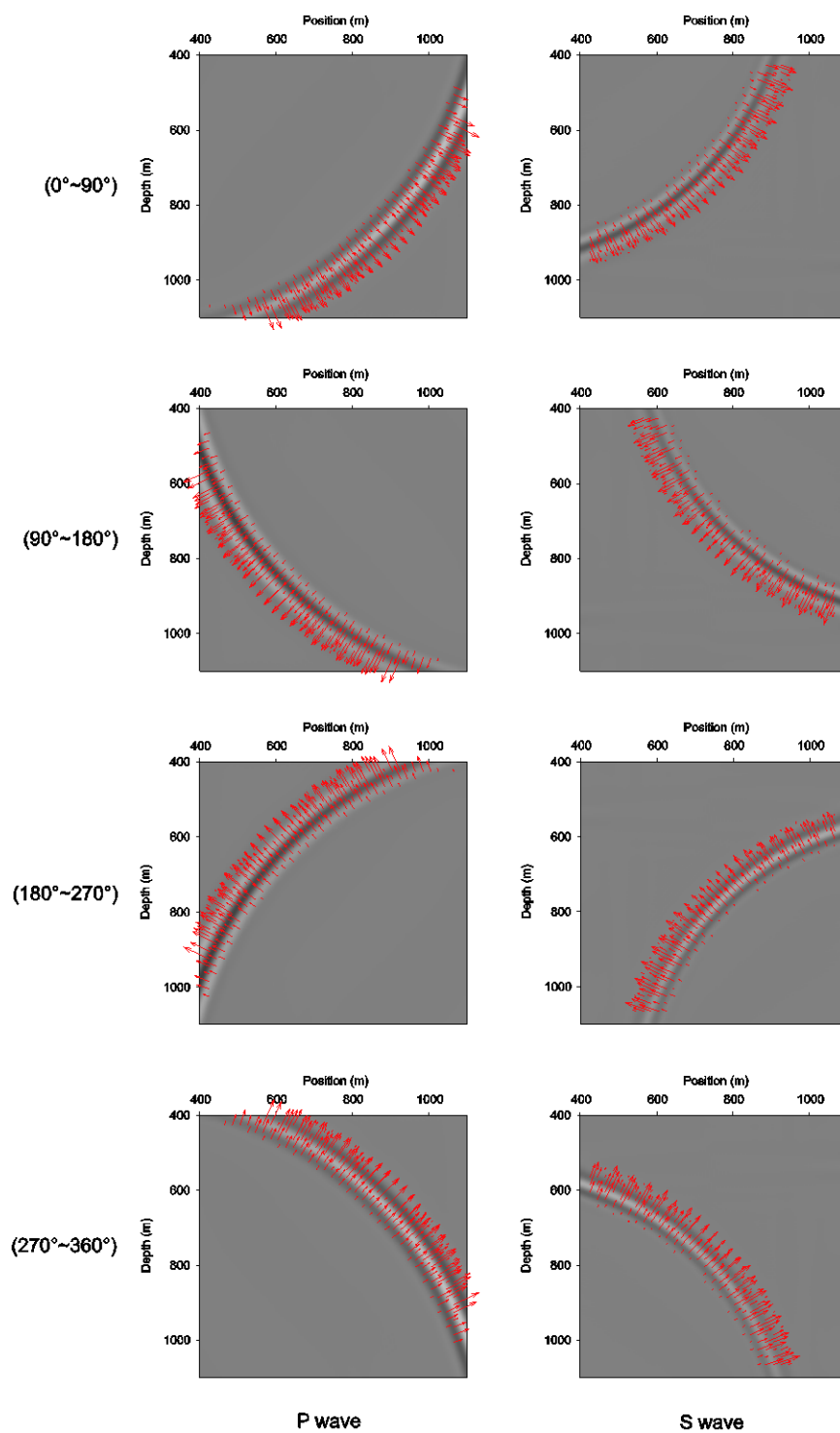


Figure 4.8. Snapshots of the x -component of decomposed P and S particle velocities. The arrows denote the polarization directions defined by the particle velocities.

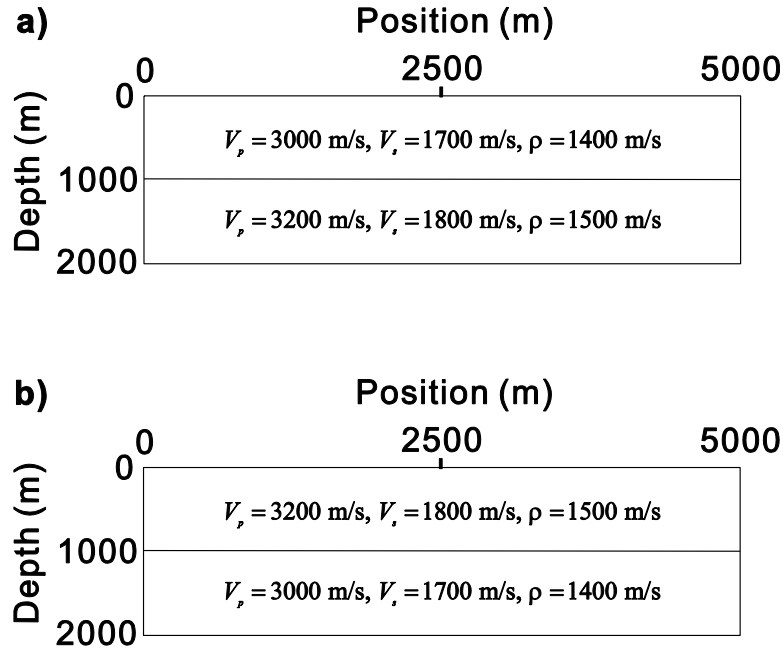


Figure 4.9. Schematic diagram of two simple elastic models.

In Figure 4.10a, using scalar wavefields obtained using a divergence operator can give the correct polarity of the PP image, but the divergence operator does not preserve the amplitude of the wavefields. In Figure 4.10b, the image produced by cross-correlating x -component of $\mathbf{v}_s^{p,tm}$ and $\mathbf{v}_r^{p,tm}$ has invisible amplitude at small reflection angles. In Figure 4.10c, cross-correlating z -component of $\mathbf{v}_s^{p,tm}$ and $\mathbf{v}_r^{p,tm}$ gives a reverse polarity of the PP reflectivity. Both the images in Figure 4.10b and 4.10c have weaker amplitude than that in Figure 4.10d, because 4.10b and 4.10c cross-correlate uses only x - or z -component of $\mathbf{v}_s^{p,tm}$ and $\mathbf{v}_r^{p,tm}$. In Figure 4.10d, using the multidirectional-vector-based imaging condition (equation 4.46) gives the correct PP polarity and also removes the backscattering artifacts in Figure 4.10a.

For the PS images in Figure 4.11a, using the scalar wavefields obtained using divergence and pseudo-curl operators generates an image with a polarity reversal at the normal incidence.

Note, here we directly use $\left(\frac{\partial v_x}{\partial z} - \frac{\partial v_z}{\partial x}\right)$ as a pseudo-curl operator to directly generate a scalar S wave for the comparison. In Figures 4.11b and 4.11c, Cross-correlating x - or z -component of the vector particle velocities cannot give the correct polarity of the PS reflectivity. The multidirectional-vector-based imaging condition in equation 4.48 provides the correct PS image in Figure 4.11d.

Figures 4.12 and 4.13 provide the PP and PS images that use the velocity model in Figure 4.9b which contains a negative PP/PS reflectivity. The same conclusions can be obtained here. The red lines in Figures 4.10d and 4.12d mark the image points at open angle of 90° , where the phase of the PP images is continuous. Figures 4.10~4.13 verify that the multidirectional-vector-based imaging conditions in equations 4.46 and 4.48 are correct. In Figures 4.10~4.13, the PS image has much larger illumination aperture than the PP image, because the PS reflection angle is smaller than the PP reflection angle at each image point.

4.5.3 Applying the proposed flow to a complicated portion of the Marmousi2 model

We apply the proposed flow (Figure 4.5) to synthetic data obtained from the elastic model in Figure 4.14. The target region for imaging and calculating ADCIGs starts at 500 m depth, which is a complicated portion of the Marmousi2 model.

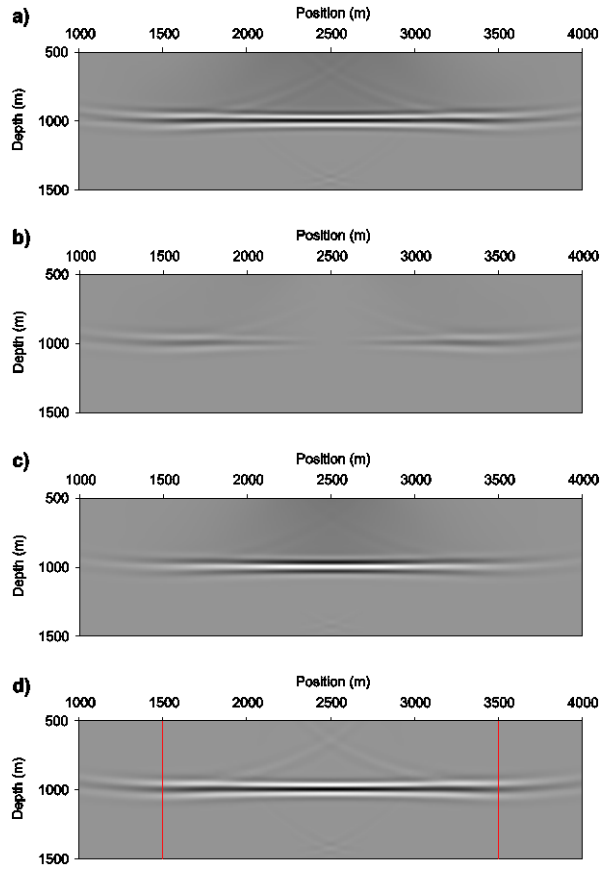


Figure 4.10. PP images using the elastic model in Figure 4.9a which contains a positive reflectivity. (a) Using P particle velocities decomposed by divergence operator. (b) Cross-correlating the x -component of the $\mathbf{v}_s^{p,lm}$ with the x -component of $\mathbf{v}_r^{p,lm}$. (c) Cross-correlating the z -component of the $\mathbf{v}_s^{p,lm}$ with the z -component of $\mathbf{v}_r^{p,lm}$. (d) Using the multidirectional-vector-based imaging condition for the PP image. The two red lines mark the open angle of 90° . Panels (b) ~ (d) are plotted with the same amplitude scale. Panel (a) is plotted with a different scale because the divergence operator changes the amplitudes of the wavefields. The low-wavenumber noise above the reflector in Panel (a) is the backscattering artifacts.

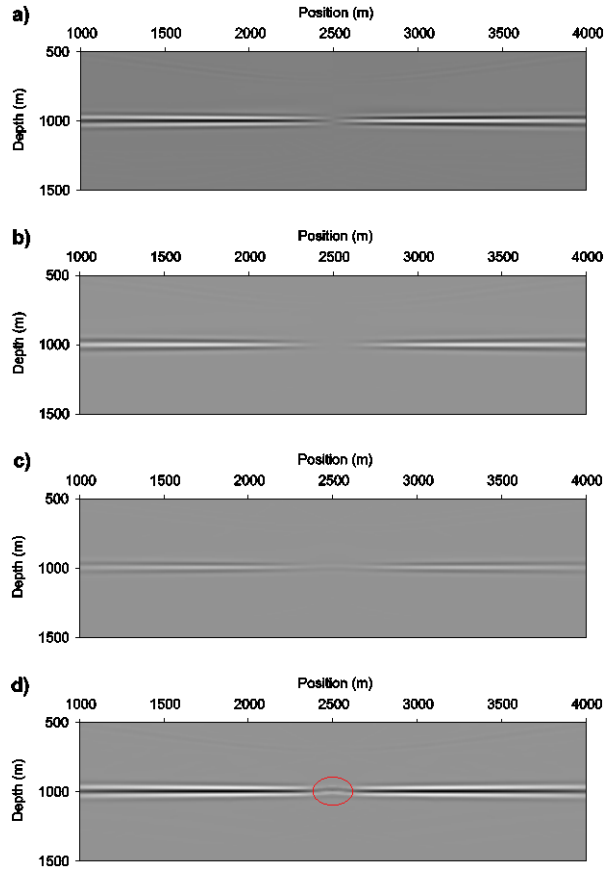


Figure 4.11. PS images using the elastic model in Figure 4.9a which contains a positive reflectivity. (a) Using P and S particle velocities decomposed by divergence and pseudo-curl operators. (b) Cross-correlating the x -component of the $\mathbf{v}_s^{p,tm}$ with the x -component of $\mathbf{v}_r^{s,tm}$. (c) Cross-correlating the z -component of the $\mathbf{v}_s^{p,tm}$ with the z -component of $\mathbf{v}_r^{s,tm}$. (d) Using the multidirectional-vector-based imaging condition for PS image. Panels (b) ~ (d) are plotted with the same amplitude scale. Panel (a) is plotted with a different scale because the divergence and pseudo-curl operators change the amplitudes of the wavefields. The minor phase-shift in the red oval in panel (d) is caused by the minor phase-shift at the top of z -component of the S-wave at normal incidence.

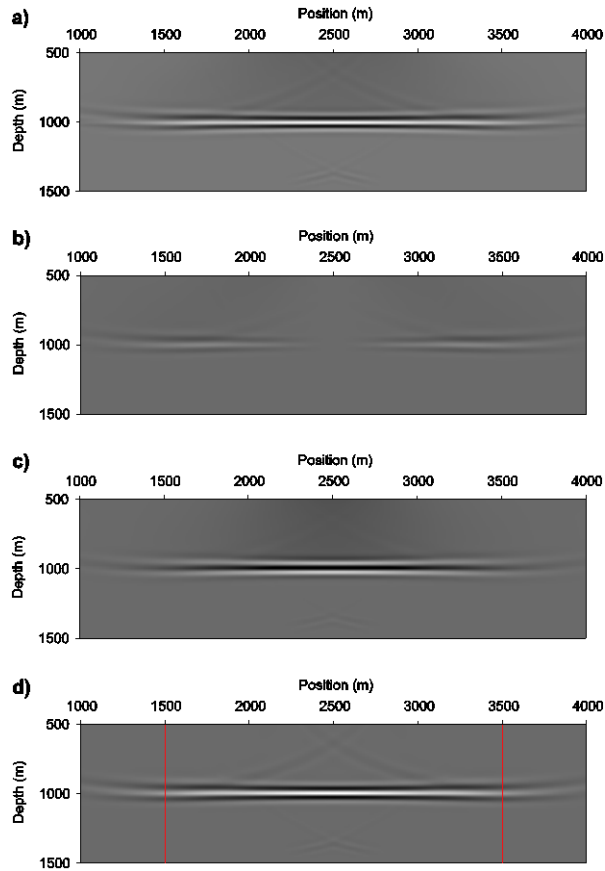


Figure 4.12. PP images using the elastic model in Figure 4.9b which contains a negative reflectivity. Refer to the caption of Figure 4.10 for other discussion of the four panels.

In this numerical example, both the horizontal and vertical grid intervals are 10 m. Each model of Figure 4.14 contains 401x201 grids. There are 200 shots located from 20 m to 4000 m along the surface. For each shot, 401 receivers record the data along the surface. The offset range is from -2000 m to 2000 m. The source wavelet is a Ricker wavelet with a dominant frequency of 25 Hz. The time interval is 1 ms; 3200 time steps are recorded at each receiver.

The simulation of the elastodynamic equations uses a staggered grid (Virieux, 1984; Nguyen and McMechan, 2015), which can effectively improve the accuracy of first time and space derivatives. The finite differencing (FD) uses 8th-order for the spatial derivative and 2nd-

order for the time derivative. To reduce the strong reflection at the four grid edges of the 2D model, the convolutional perfect matched layer (C-PML) absorbing boundary (Komatitsch and Martin, 2007) is used.

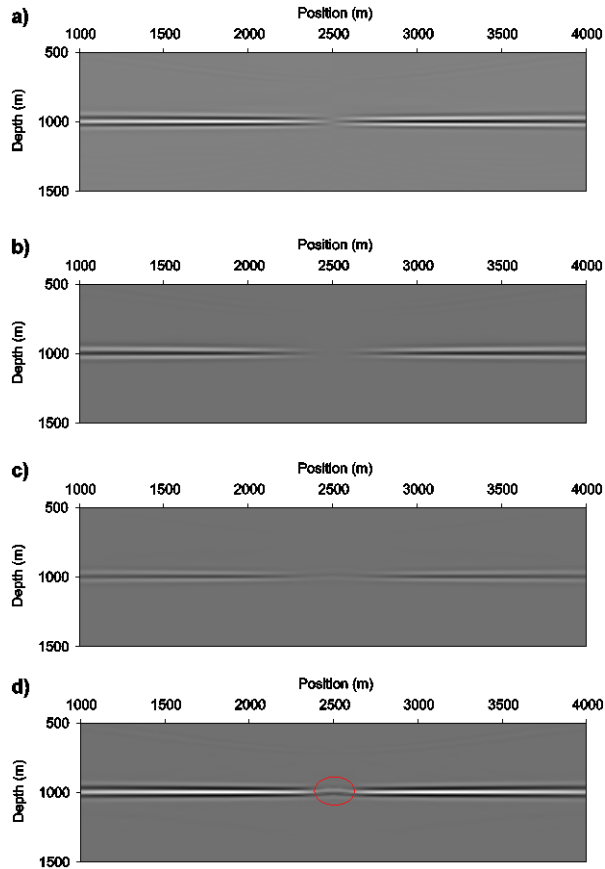


Figure 4.13. PS images using the elastic model in Figure 4.9b which contains a negative reflectivity. Refer to the caption of Figure 4.11 for other discussion of the four panels.

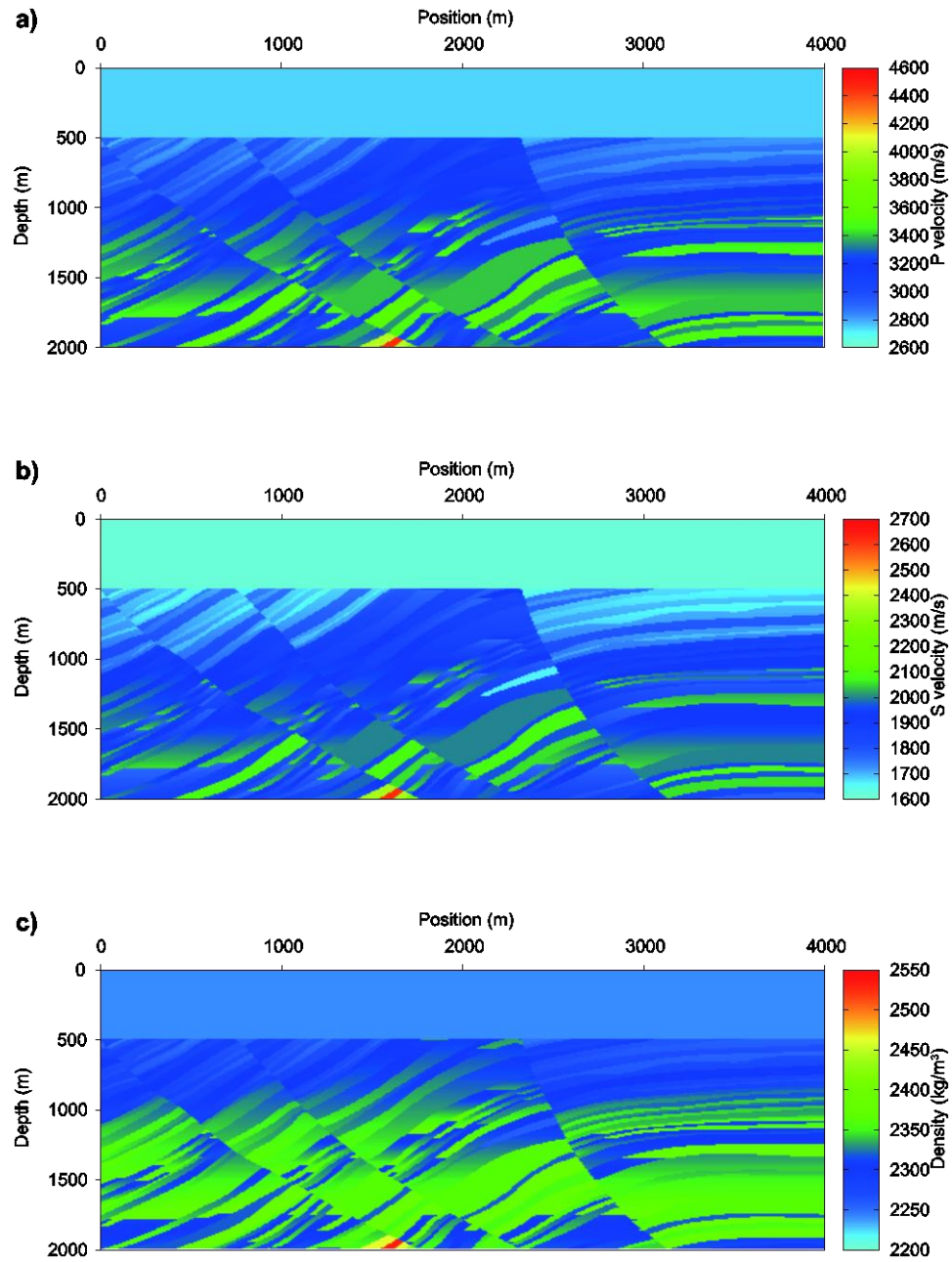


Figure 4.14. A complicated portion of Marmousi2 model with a constant elastic layer added at the top. (a) The P velocity. (b) The S velocity. (c) The density.

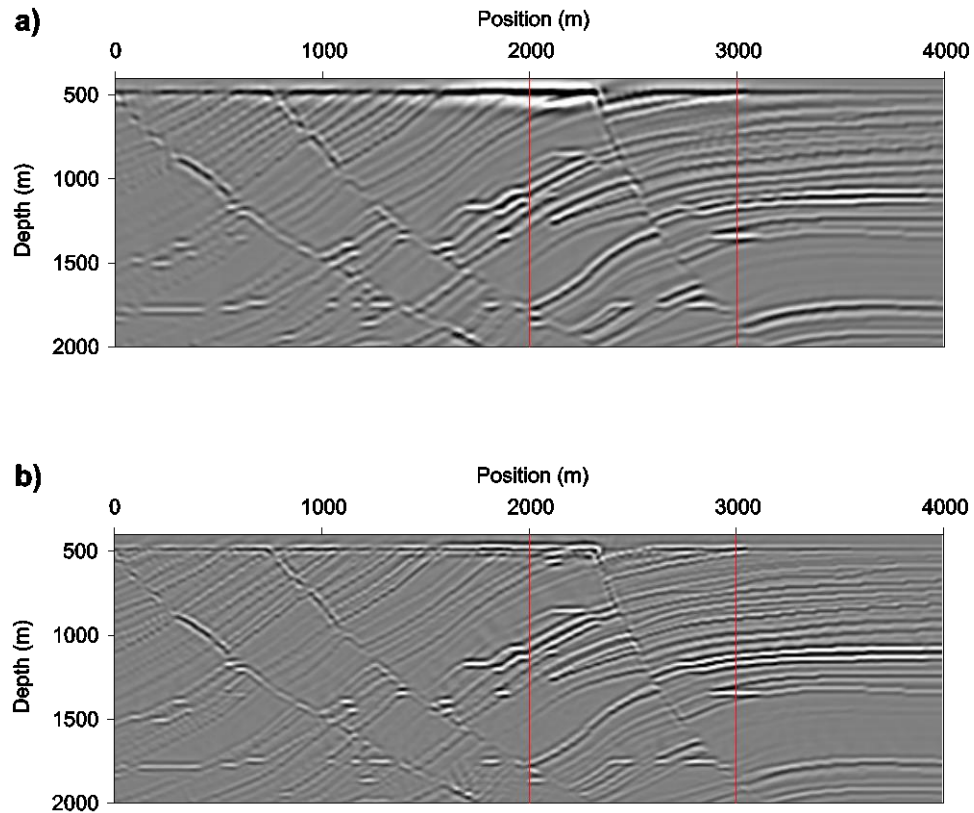


Figure 4.15. (a) PP image and (b) PS image obtained by using the proposed flow with the true migration velocity in Figure 4.14. The region between the two red lines define the location of the PP and PS ADCIGs in Figures 4.16 and 4.17.

Figures 4.15 and 4.16 show the PP and PS images and representative ADCIGs obtained using the proposed data flow with the true P and S migration velocity. These images and ADCIGs have high quality. The PS image and ADCIGs have higher resolution than the PP image and ADCIGs, because the S-velocity is lower than the P-velocity, which means the dominant wavenumber of the S wave is larger than that of the P wave. In Figure 4.16, the PP ADCIGs have much larger magnitudes than the PS ADCIGs near normal incidence, because the reflection energy of the converted S wave is weak at normal incidence. The phenomena shown in

the PP and PS images and the ADCIGs in Figures 4.15 and 4.16 are consistent with the physical truth.

The PP and PS ADCIGs using an 8% low velocity are shown in Figure 4.17. The ADCIGs are sensitive to the incorrect velocity; most of the gathers curve upward. The phases of both the PP and PS ADCIGs are continuous, which facilitates the calculation of curvatures for subsequent migration velocity analysis.

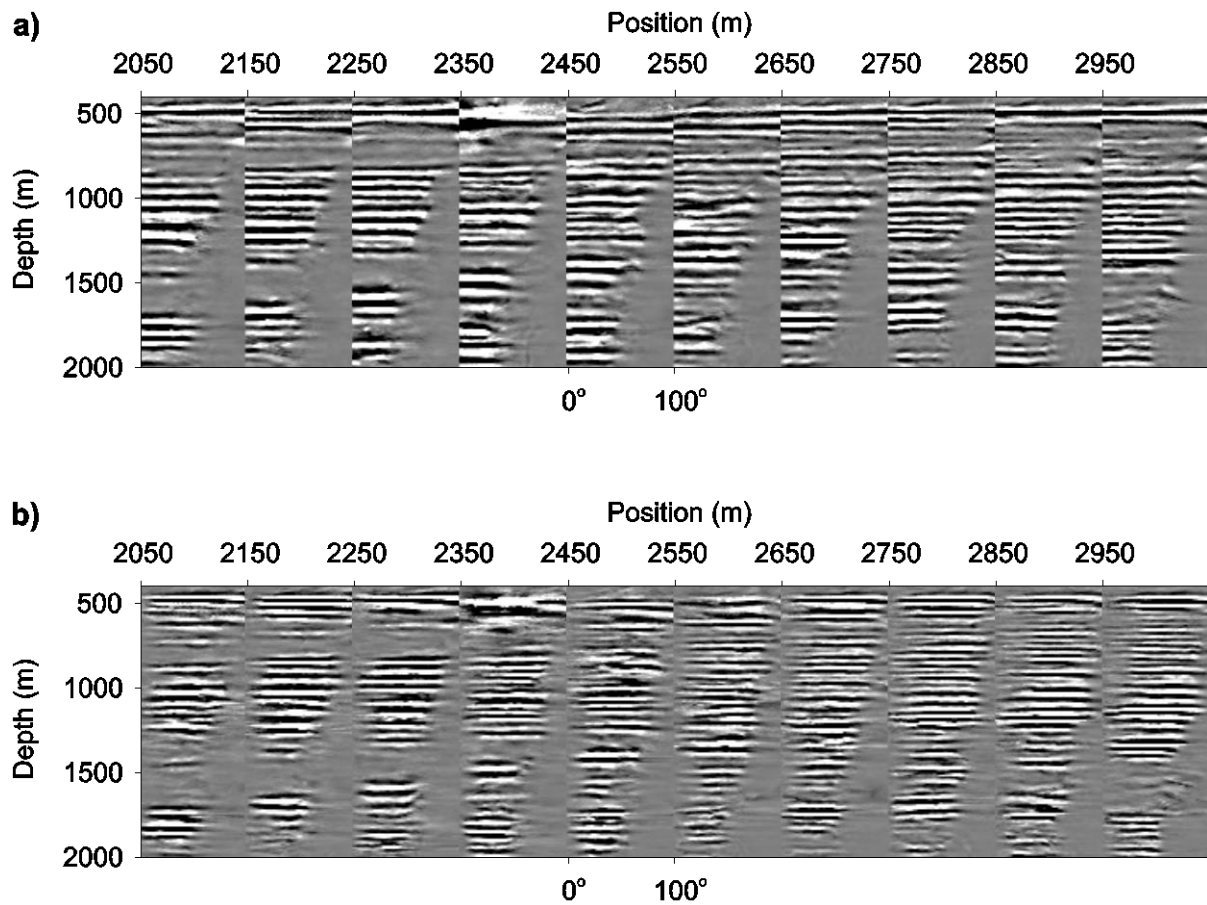


Figure 4.16. (a) PP ADCIGs and (b) PS ADCIGs obtained by using the proposed method with the true migration velocity (see Figure 4.14 for the elastic model and Figure 4.15 for the corresponding stacked images). The range of open angles is from 0° to 100°.

4.6 Discussion and future developments

In this section, we discuss the extension of our schemes into 3D, the amplitude-preserved imaging conditions, and the combination of the multidirectional source vector and reflection-image normal to calculate elastic ADCIGs. The implementations of these applications are left for potential future developments.

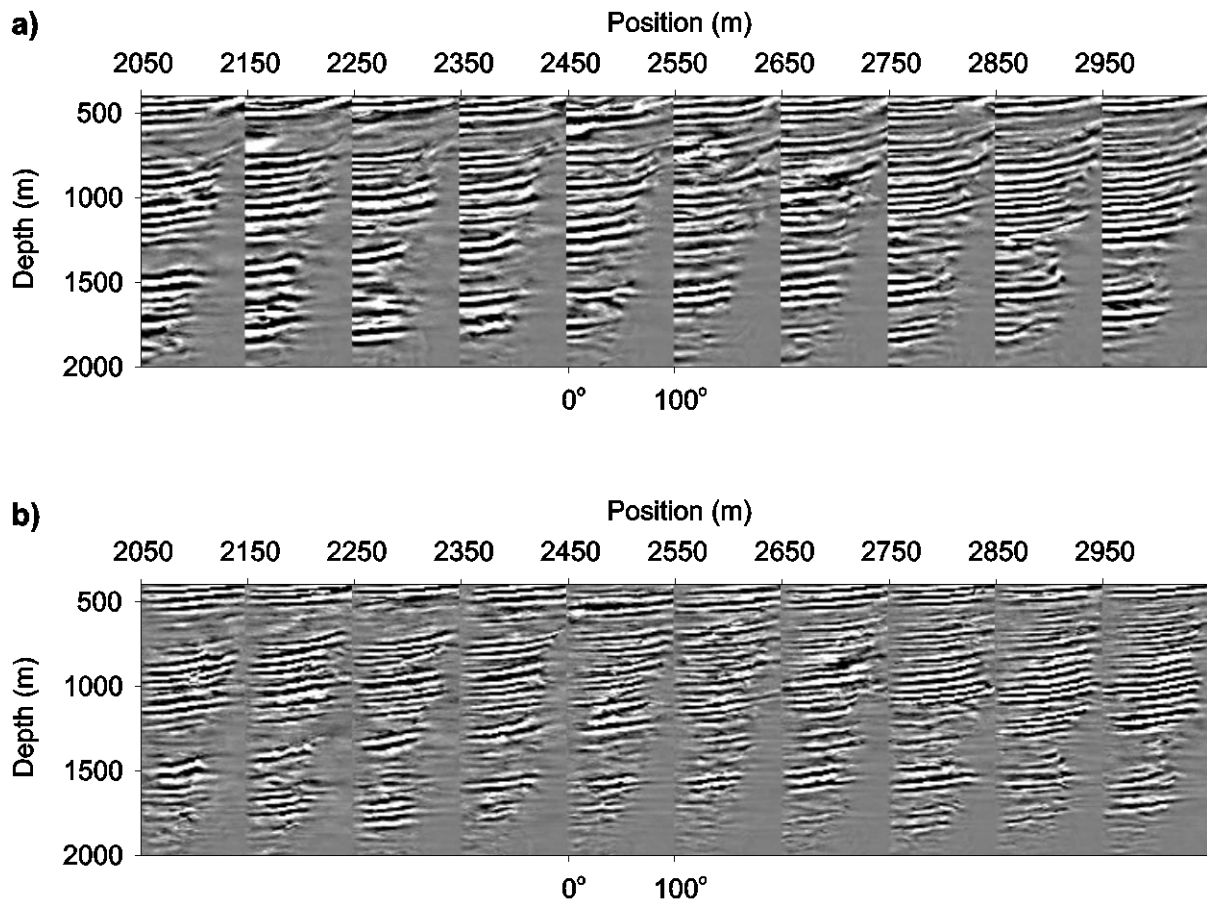


Figure 4.17. (a) PP ADCIGs and (b) PS ADCIGs obtained by using the proposed method with an 8% low migration velocity of the elastic model in Figure 4.14. The range of open angles is from 0° to 100° .

4.6.1 Extension of the P/S wave mode separation into 3D

Derivation of the decoupling system of P and S waves in 3D can be performed with the following steps.

(I). Obtain the $\partial\tau^p/\partial t$ and $\partial\tau^s/\partial t$ from the Helmholtz's equation in 3D, which corresponds to equations 4.12 and 4.13 in 2D.

(II). Calculate the residual

$$\left(\frac{\partial\tau}{\partial t}\right)_{resi} = \frac{\partial\tau}{\partial t} - \left(\frac{\partial\tau^p}{\partial t} + \frac{\partial\tau^s}{\partial t}\right), \quad (4.53)$$

which corresponds to equation 4.20 in 2D.

(III). Calculate $\tau^{p,m}$ and $\tau^{s,m}$ in 3D,

$$\begin{aligned} \frac{\partial\tau^{p,m}}{\partial t} &= \frac{\partial\tau^p}{\partial t} + \frac{1}{2}\left(\frac{\partial\tau}{\partial t}\right)_{resi}, \\ \frac{\partial\tau^{s,m}}{\partial t} &= \frac{\partial\tau^s}{\partial t} + \frac{1}{2}\left(\frac{\partial\tau}{\partial t}\right)_{resi}, \end{aligned} \quad (4.54)$$

which corresponds to equations 4.23 and 4.24 in 2D.

(IV). Substitute equation 4.54 into the 3D elastodynamic equations to obtain the equations for calculating $\mathbf{v}^{p,m}$ and $\mathbf{v}^{s,m}$, which corresponds to inserting equations 4.23 and 4.24 into equations 4.1 and 4.2 to obtain equations 4.21 and 4.22 in 2D.

Following this derivation, we obtain

$$\frac{\partial \tau^{s,tm}}{\partial t} = \mu \begin{bmatrix} \frac{\partial \tau_{xx}^{s,tm}}{\partial t} & \frac{\partial \tau_{xy}^{s,tm}}{\partial t} & \frac{\partial \tau_{xz}^{s,tm}}{\partial t} \\ \frac{\partial \tau_{yx}^{s,tm}}{\partial t} & \frac{\partial \tau_{yy}^{s,tm}}{\partial t} & \frac{\partial \tau_{yz}^{s,tm}}{\partial t} \\ \frac{\partial \tau_{zx}^{s,tm}}{\partial t} & \frac{\partial \tau_{zy}^{s,tm}}{\partial t} & \frac{\partial \tau_{zz}^{s,tm}}{\partial t} \end{bmatrix} = \mu \begin{bmatrix} -\left(\frac{\partial v_y}{\partial y} + \frac{\partial v_z}{\partial z}\right) & \frac{\partial v_y}{\partial x} & \frac{\partial v_z}{\partial x} \\ \frac{\partial v_x}{\partial y} & -\left(\frac{\partial v_x}{\partial x} + \frac{\partial v_z}{\partial z}\right) & \frac{\partial v_z}{\partial y} \\ \frac{\partial v_x}{\partial z} & \frac{\partial v_y}{\partial z} & -\left(\frac{\partial v_x}{\partial x} + \frac{\partial v_y}{\partial y}\right) \end{bmatrix}, \quad (4.55)$$

in 3D. Then the flow of P/S wave mode separation in 3D can be easily obtained by using equations 4.55 to replace equation 4.25 and using

$$\begin{cases} \frac{\partial v_x^{s,tm}}{\partial t} = \frac{1}{\rho} \left(\frac{\partial \tau_{xx}^{s,tm}}{\partial x} + \frac{\partial \tau_{yx}^{s,tm}}{\partial y} + \frac{\partial \tau_{zx}^{s,tm}}{\partial z} \right), \\ \frac{\partial v_y^{s,tm}}{\partial t} = \frac{1}{\rho} \left(\frac{\partial \tau_{xy}^{s,tm}}{\partial x} + \frac{\partial \tau_{yy}^{s,tm}}{\partial y} + \frac{\partial \tau_{zy}^{s,tm}}{\partial z} \right), \\ \frac{\partial v_z^{s,tm}}{\partial t} = \frac{1}{\rho} \left(\frac{\partial \tau_{xz}^{s,tm}}{\partial x} + \frac{\partial \tau_{yz}^{s,tm}}{\partial y} + \frac{\partial \tau_{zz}^{s,tm}}{\partial z} \right), \end{cases} \quad (4.56)$$

to replace equation 4.27 in the data flow (a)~(d) for 2D. The method in Appendix 4B (Section 4.10) (using $-1/\omega^2$) can also be applied to P/S wave mode separation of elastic particle velocities in 3D. Note, the S-wave in 3D may include both the SV and SH waves and separating them may require extra information; e.g., the normal to the reflector plane in the reflection image. This normal may need to be calculated in the \mathbf{k} domain because of complications of the reflection image (e.g., intersections), especially for 3D real data. Some scatters may also complicate the calculation of the normal to the reflector plane because the scattered waves do not satisfy Snell's law.

4.6.2 Extension of the multidirectional propagation vector into 3D

The multidirectional-vector-based imaging conditions (equations 4.46, 4.48 and 4E-3 and 4E-4) can be directly applied to 3D. Note, in physics, the PS and SP images in 3D are P-SV and SV-P images. This is because, (i) the S wave converted from a P wave should be an SV wave, (ii) the S wave that generates the converted P wave should also be an SV wave, and (iii) an SH wave generates only the SH wave. Thus, the imaging conditions for PS and SP images (equation 4.48 and 4E-1) still work in 3D.

The extension of calculating multidirectional propagation vector in 3D is discussed in this subsection. For the conversion from POV to PRV (equations 4.44 and 4.45), the extension of (P wave) equation 4.44 from 2D into 3D is

$$\begin{cases} p_{x,i}^{p,tm}(t, \mathbf{x}) = \text{sgn} \left[\left(\frac{k_x}{\omega} \right)_i \right] \cdot |v_{x,i}^{p,tm}(t, \mathbf{x})|, \\ p_{y,i}^{p,tm}(t, \mathbf{x}) = \text{sgn} \left[\left(\frac{k_y}{\omega} \right)_i \right] \cdot |v_{y,i}^{p,tm}(t, \mathbf{x})|, \\ p_{z,i}^{p,tm}(t, \mathbf{x}) = \text{sgn} \left[\left(\frac{k_z}{\omega} \right)_i \right] \cdot |v_{z,i}^{p,tm}(t, \mathbf{x})|. \end{cases} \quad (4.57)$$

The extension of equation 4.45 from 2D into 3D is

$$\begin{cases} p_{x,i}^{s,tm}(t, \mathbf{x}) = \text{sgn} \left[\left(\frac{k_x}{\omega} \right)_i \right] \cdot |\gamma_{x,i}^{s,tm}(t, \mathbf{x})|, \\ p_{y,i}^{s,tm}(t, \mathbf{x}) = \text{sgn} \left[\left(\frac{k_y}{\omega} \right)_i \right] \cdot |\gamma_{y,i}^{s,tm}(t, \mathbf{x})|, \\ p_{z,i}^{s,tm}(t, \mathbf{x}) = \text{sgn} \left[\left(\frac{k_z}{\omega} \right)_i \right] \cdot |\gamma_{z,i}^{s,tm}(t, \mathbf{x})|, \end{cases} \quad (4.58)$$

where $\boldsymbol{\gamma}_i^{s,tm}$ is a vector that is parallel to the propagation direction and satisfies

$$\boldsymbol{\gamma}_i^{s,tm} \cdot \mathbf{v}_i^{s,tm} = 0. \quad (4.59)$$

In 3D, deciding $\boldsymbol{\gamma}_i^{s,tm}$ from $\mathbf{v}_i^{s,tm}$ requires extra information, such as the normal to the reflector.

Thus, we propose a three-step process to decide $\boldsymbol{\gamma}_i^{s,tm}$. Take a PS image as an example:

- A). Use the PS imaging condition (equation 4.48) to obtain the 3D PS image. Calculate the normal to the local reflector-image plane.
- B). Use the $\mathbf{v}_i^{s,tm}$ and the normal to the PS reflection-image plane to decide the normal of the PS reflection plane (the local plane that contains the incident P and the reflected S waves).
- C). Use the normal to the reflection plane to convert $\mathbf{v}_i^{s,tm}$ to $\boldsymbol{\gamma}_i^{s,tm}$.

Then we can use equation 4.58 to convert $\boldsymbol{\gamma}_i^{s,tm}$ into $\mathbf{p}_i^{s,tm}$.

As an alternative, the multidirectional propagation vector of a P or S wave in 3D can also be obtained using the 3D MPV equations (corresponding to equations 4.37 and 4.38 in 2D):

$$P_{\chi,i}^{p,tm} = -\left(\tau_{\chi x,i}^{p,tm} v_{x,i}^{p,tm} + \tau_{\chi y,i}^{p,tm} v_{y,i}^{p,tm} + \tau_{\chi z,i}^{p,tm} v_{z,i}^{p,tm}\right), \quad (4.60)$$

and

$$P_{\chi,i}^{s,tm} = -\left(\tau_{\chi x,i}^{s,tm} v_{x,i}^{s,tm} + \tau_{\chi y,i}^{s,tm} v_{y,i}^{s,tm} + \tau_{\chi z,i}^{s,tm} v_{z,i}^{s,tm}\right), \quad (4.61)$$

where $\chi = x, y, z$ to obtain the x -, y - and z - components of the MPV; $\boldsymbol{\tau}_i^{p,tm}$ and $\boldsymbol{\tau}_i^{s,tm}$ can be approximated by inserting $\mathbf{v}_i^{p,tm}$ and $\mathbf{v}_i^{s,tm}$ into the 3D decoupled equations (e.g., equation 4.55 for obtaining $\boldsymbol{\tau}_i^{s,tm}$), which corresponds to equation 4.43 in 2D, and so the approximate WD needs to be applied only to $\mathbf{v}^{p,tm}$ and $\mathbf{v}^{s,tm}$. After obtaining the propagation vectors of the source and receiver wavefields, equation 4.52 can be directly used to calculate the open angle in 3D; for calculation of the azimuth angle in 3D, refer to Tang and McMechan (2017a).

4.6.3 Discussion on the amplitude-preserved imaging conditions

In this chapter, we use the cross-correlation imaging condition as an example to illustrate the multidirectional-vector-based imaging condition. This imaging condition does not produce amplitudes that are consistent with amplitude-versus-angle (AVA) theory. Here, we also provide multidirectional-vector-based deconvolution imaging conditions (in the ω domain) which can improve the amplitude balance because the deconvolution imaging condition (e.g., Zhang et al. 2005) is consistent with the physical concept of the reflectivity,

$$\left\{ \begin{array}{l} I_k^{pp}(\omega, \mathbf{x}) = -[1 - \delta(i - j)] F(\theta_k^{pp}) \operatorname{sgn}(\mathbf{v}_{s,i}^{p,tm} \cdot \mathbf{v}_{r,j}^{p,tm} \cos \theta_k^{pp}) \frac{|\mathbf{v}_{r,j}^{p,tm}(\omega, \mathbf{x})|}{|\mathbf{v}_{s,i}^{p,tm}(\omega, \mathbf{x})|}, \\ I_k^{ps}(\omega, \mathbf{x}) = -\operatorname{sgn}(\mathbf{v}_{s,i}^{p,tm} \cdot \mathbf{v}_{r,j}^{s,tm}) \frac{|\mathbf{v}_{r,j}^{s,tm}(\omega, \mathbf{x})|}{|\mathbf{v}_{s,i}^{p,tm}(\omega, \mathbf{x})|}, \\ I_k^{sp}(\omega, \mathbf{x}) = -\operatorname{sgn}(\mathbf{v}_{s,i}^{s,tm} \cdot \mathbf{v}_{r,j}^{p,tm}) \frac{|\mathbf{v}_{r,j}^{p,tm}(\omega, \mathbf{x})|}{|\mathbf{v}_{s,i}^{s,tm}(\omega, \mathbf{x})|}, \\ I_k^{ss}(\omega, \mathbf{x}) = -[1 - \delta(i - j)] F(\theta_k^{ss}) \operatorname{sgn}(\mathbf{v}_{s,i}^{s,tm} \cdot \mathbf{v}_{r,j}^{s,tm} \cos \theta_k^{ss}) \frac{|\mathbf{v}_{r,j}^{s,tm}(\omega, \mathbf{x})|}{|\mathbf{v}_{s,i}^{s,tm}(\omega, \mathbf{x})|}. \end{array} \right. \quad (4.62)$$

The corresponding angle-domain imaging condition is

$$\left\{ \begin{array}{l}
I_k^{pp}(\bar{\theta}_k^{pp}, \omega, \mathbf{x}) = -[1 - \delta(i - j)] \delta(\bar{\theta}_k^{pp} - \theta_k^{pp}) \operatorname{sgn}(\mathbf{v}_{s,i}^{p,tm} \cdot \mathbf{v}_{r,j}^{p,tm} \cos \theta_k^{pp}) \frac{|\mathbf{v}_{r,j}^{p,tm}(\omega, \mathbf{x})|}{|\mathbf{v}_{s,i}^{p,tm}(\omega, \mathbf{x})|}, \\
I_k^{ps}(\bar{\theta}_k^{ps}, \omega, \mathbf{x}) = -\delta(\bar{\theta}_k^{ps} - \theta_k^{ps}) \operatorname{sgn}(\mathbf{v}_{s,i}^{p,tm} \cdot \mathbf{v}_{r,j}^{s,tm}) \frac{|\mathbf{v}_{r,j}^{s,tm}(\omega, \mathbf{x})|}{|\mathbf{v}_{s,i}^{p,tm}(\omega, \mathbf{x})|}, \\
I_k^{sp}(\bar{\theta}_k^{sp}, \omega, \mathbf{x}) = -\delta(\bar{\theta}_k^{sp} - \theta_k^{sp}) \operatorname{sgn}(\mathbf{v}_{s,i}^{s,tm} \cdot \mathbf{v}_{r,j}^{p,tm}) \frac{|\mathbf{v}_{r,j}^{p,tm}(\omega, \mathbf{x})|}{|\mathbf{v}_{s,i}^{s,tm}(\omega, \mathbf{x})|}, \\
I_k^{ss}(\bar{\theta}_k^{ss}, \omega, \mathbf{x}) = -[1 - \delta(i - j)] \delta(\bar{\theta}_k^{ss} - \theta_k^{ss}) \operatorname{sgn}(\mathbf{v}_{s,i}^{s,tm} \cdot \mathbf{v}_{r,j}^{s,tm} \cos \theta_k^{ss}) \frac{|\mathbf{v}_{r,j}^{s,tm}(\omega, \mathbf{x})|}{|\mathbf{v}_{s,i}^{s,tm}(\omega, \mathbf{x})|}.
\end{array} \right. \quad (4.62)$$

For both equations 4.61 and 4.62, the image at each spatial location is a summation of all the partial images at each k of each ω of each source; all the vectors are in the ω domain. Note the amplitude-preserving imaging condition has a single-arrival assumption (or requires the number of arrivals at all the grid points to be the same, which requires applying the deconvolution imaging condition to each arrival then calculating the average value at each grid point) and also requires a good migration velocity model. To improve the stability of equations 4.61 and 4.62, we approximate them as

$$\left\{ \begin{array}{l}
I_k^{pp}(\omega, \mathbf{x}) = -[1 - \delta(i - j)] F(\theta_k^{pp}) \operatorname{sgn}(\mathbf{v}_{s,i}^{p,tm} \cdot \mathbf{v}_{r,j}^{p,tm} \cos \theta_k^{pp}) \frac{|\mathbf{v}_{s,i}^{p,tm}(\omega, \mathbf{x})| |\mathbf{v}_{r,j}^{p,tm}(\omega, \mathbf{x})|}{|\mathbf{v}_s^{p,tm}(\omega, \mathbf{x})|^2}, \\
I_k^{ps}(\omega, \mathbf{x}) = -\operatorname{sgn}(\mathbf{v}_{s,i}^{p,tm} \cdot \mathbf{v}_{r,j}^{s,tm}) \frac{|\mathbf{v}_{s,i}^{p,tm}(\omega, \mathbf{x})| |\mathbf{v}_{r,j}^{s,tm}(\omega, \mathbf{x})|}{|\mathbf{v}_s^{p,tm}(\omega, \mathbf{x})|^2}, \\
I_k^{sp}(\omega, \mathbf{x}) = -\operatorname{sgn}(\mathbf{v}_{s,i}^{s,tm} \cdot \mathbf{v}_{r,j}^{p,tm}) \frac{|\mathbf{v}_s^{s,tm}(\omega, \mathbf{x})| |\mathbf{v}_{r,j}^{p,tm}(\omega, \mathbf{x})|}{|\mathbf{v}_s^{s,tm}(\omega, \mathbf{x})|^2}, \\
I_k^{ss}(\omega, \mathbf{x}) = -[1 - \delta(i - j)] F(\theta_k^{ss}) \operatorname{sgn}(\mathbf{v}_{s,i}^{s,tm} \cdot \mathbf{v}_{r,j}^{s,tm} \cos \theta_k^{ss}) \frac{|\mathbf{v}_{s,i}^{s,tm}(\omega, \mathbf{x})| |\mathbf{v}_{r,j}^{s,tm}(\omega, \mathbf{x})|}{|\mathbf{v}_s^{s,tm}(\omega, \mathbf{x})|^2},
\end{array} \right. \quad (4.63)$$

and

$$\left\{ \begin{array}{l}
I_k^{pp}(\bar{\theta}_k^{pp}, \omega, \mathbf{x}) = -[1 - \delta(i - j)] \delta(\bar{\theta}_k^{pp} - \theta_k^{pp}) \operatorname{sgn}(\mathbf{v}_{s,i}^{p,tm} \cdot \mathbf{v}_{r,j}^{p,tm} \cos \theta_k^{pp}) \frac{|\mathbf{v}_{s,i}^{p,tm}(\omega, \mathbf{x})| |\mathbf{v}_{r,j}^{p,tm}(\omega, \mathbf{x})|}{|\mathbf{v}_s^{p,tm}(\omega, \mathbf{x})|^2}, \\
I_k^{ps}(\bar{\theta}_k^{ps}, \omega, \mathbf{x}) = -\delta(\bar{\theta}_k^{ps} - \theta_k^{ps}) \operatorname{sgn}(\mathbf{v}_{s,i}^{p,tm} \cdot \mathbf{v}_{r,j}^{s,tm}) \frac{|\mathbf{v}_{s,i}^{p,tm}(\omega, \mathbf{x})| |\mathbf{v}_{r,j}^{s,tm}(\omega, \mathbf{x})|}{|\mathbf{v}_s^{p,tm}(\omega, \mathbf{x})|^2}, \\
I_k^{sp}(\bar{\theta}_k^{sp}, \omega, \mathbf{x}) = -\delta(\bar{\theta}_k^{sp} - \theta_k^{sp}) \operatorname{sgn}(\mathbf{v}_{s,i}^{s,tm} \cdot \mathbf{v}_{r,j}^{p,tm}) \frac{|\mathbf{v}_{s,i}^{s,tm}(\omega, \mathbf{x})| |\mathbf{v}_{r,j}^{p,tm}(\omega, \mathbf{x})|}{|\mathbf{v}_s^{s,tm}(\omega, \mathbf{x})|^2}, \\
I_k^{ss}(\bar{\theta}_k^{ss}, \omega, \mathbf{x}) = -[1 - \delta(i - j)] \delta(\bar{\theta}_k^{ss} - \theta_k^{ss}) \operatorname{sgn}(\mathbf{v}_{s,i}^{s,tm} \cdot \mathbf{v}_{r,j}^{s,tm} \cos \theta_k^{ss}) \frac{|\mathbf{v}_{s,i}^{s,tm}(\omega, \mathbf{x})| |\mathbf{v}_{r,j}^{s,tm}(\omega, \mathbf{x})|}{|\mathbf{v}_s^{s,tm}(\omega, \mathbf{x})|^2},
\end{array} \right. \quad (4.64)$$

respectively, where the source P/S wavefields in the denominators are not approximate-angle-decomposed wavefields.

Because of the assumption mentioned in last paragraph, we suggest applying these deconvolution imaging conditions in a short optimal time window including only a single arrival at each grid point. The central point of this window can be at the excitation time. We suggest that each grid point of each source should have only one excitation time which can be calculated by picking the maximum amplitude over all the decomposed source P/S wavefields of all the time steps at this grid point. Note in the non-smooth migration model, magnitude picking should be done after applying the approximate WD to the source wavefield because the picking cannot be accurate at wavefield overlaps. For a smooth migration model, the excitation time can be calculated through either the ray tracing (e.g., Chang and McMechan, 1986) or picking the maximum amplitude of all the decomposed source wavefields of all the time steps at each grid point.

The optimal time window is variable at each grid point. The wavefields in these windows can be saved through three steps: First, calculate the excitation time for each grid point and output an excitation-time table (e.g., by picking the time step with the maximum magnitude during the source wavefield propagation); second, use this excitation-time table to decide the starting and ending time steps of the optimal time window for each grid point; third, perform source-wavefield simulation and receiver-wavefield reconstruction, during which the source and receiver wavefields are saved in the short optimal window for each grid point. This approach also works for acoustic media which often uses stress tensors to calculate the PP reflection image. Because the deconvolution imaging condition is consistent with the physical concept of the reflectivity, it has more advantages in viscoacoustic or viscoelastic RTMs and full waveform inversions (FWIs) (refer to Tang and McMechan [2017d] for the application of deconvolution imaging condition in the FWI) in attenuated media than the cross-correlation imaging condition which is the product of the source and receiver wavefields. This is because the amplitudes of the source wavefields progressively decrease with an increased length of the wave path in visco media, which often leads to weak amplitudes in the deep region of the reflection image obtained from the cross-correlation imaging condition.

Because the elastic AVA has a high requirement of the amplitude accuracy (which is easy to be influenced by the migration velocity, noise, attenuation, multi-pathing, wavefield overlaps, anisotropy and so on), it is difficult to be implemented in practice. Therefore, the deconvolution imaging condition can be used to improve the amplitude balance of the reflection image which is obtained from the cross-correlation imaging condition but is often difficult to give accurate

reflection-image amplitudes in a medium with complicated geological structures, especially for 3D real data.

If we want to apply the deconvolution imaging condition to the wavefields at all the time steps rather than in the optimal time window, to improve the stability of the deconvolution imaging condition in practice where the migration velocity is often not incorrect, equations 4.63 and 4.64 can be approximated (refer to the work of Tang and McMechan [2017d]) by

$$\begin{aligned}
I_k^{pp}(\mathbf{x}) &= -[1 - \delta(i - j)] F(\theta_k^{pp}) \operatorname{sgn}(\hat{\mathbf{v}}_{s,i}^{p,tm} \cdot \hat{\mathbf{v}}_{r,j}^{p,tm} \cos \theta_k^{pp}) \frac{\int |\hat{\mathbf{v}}_{s,i}^{p,tm}(t, \mathbf{x})| |\hat{\mathbf{v}}_{r,j}^{p,tm}(t, \mathbf{x})| dt}{\int |\hat{\mathbf{v}}_s^{p,tm}(t, \mathbf{x})|^2 dt}, \\
I_k^{ps}(\mathbf{x}) &= -\operatorname{sgn}(\hat{\mathbf{v}}_{s,i}^{p,tm} \cdot \hat{\mathbf{v}}_{r,j}^{s,tm}) \frac{\int |\hat{\mathbf{v}}_{s,i}^{p,tm}(t, \mathbf{x})| |\hat{\mathbf{v}}_{r,j}^{s,tm}(t, \mathbf{x})| dt}{\int |\hat{\mathbf{v}}_s^{p,tm}(t, \mathbf{x})|^2 dt}, \\
I_k^{sp}(\mathbf{x}) &= -\operatorname{sgn}(\hat{\mathbf{v}}_{s,i}^{s,tm} \cdot \hat{\mathbf{v}}_{r,j}^{p,tm}) \frac{\int |\hat{\mathbf{v}}_{s,i}^{s,tm}(\omega, \mathbf{x})| |\hat{\mathbf{v}}_{r,j}^{p,tm}(\omega, \mathbf{x})| dt}{\int |\hat{\mathbf{v}}_s^{s,tm}(\omega, \mathbf{x})|^2 dt}, \\
I_k^{ss}(\mathbf{x}) &= -[1 - \delta(i - j)] F(\theta_k^{ss}) \operatorname{sgn}(\hat{\mathbf{v}}_{s,i}^{s,tm} \cdot \hat{\mathbf{v}}_{r,j}^{s,tm} \cos \theta_k^{ss}) \frac{\int |\hat{\mathbf{v}}_{s,i}^{s,tm}(\omega, \mathbf{x})| |\hat{\mathbf{v}}_{r,j}^{s,tm}(\omega, \mathbf{x})| dt}{\int |\hat{\mathbf{v}}_s^{s,tm}(\omega, \mathbf{x})|^2 dt},
\end{aligned} \tag{4.65}$$

and

$$\begin{aligned}
I_k^{pp}(\bar{\theta}_k^{pp}, \mathbf{x}) &= -[1 - \delta(i - j)] \delta(\bar{\theta}_k^{pp} - \theta_k^{pp}) \operatorname{sgn}(\mathbf{v}_{s,i}^{p,tm} \cdot \mathbf{v}_{r,j}^{p,tm} \cos \theta_k^{pp}) \frac{\int |\mathbf{v}_{s,i}^{p,tm}(\omega, \mathbf{x})| |\mathbf{v}_{r,j}^{p,tm}(\omega, \mathbf{x})| dt}{\int |\mathbf{v}_s^{p,tm}(\omega, \mathbf{x})|^2 dt}, \\
I_k^{ps}(\bar{\theta}_k^{ps}, \mathbf{x}) &= -\delta(\bar{\theta}_k^{ps} - \theta_k^{ps}) \operatorname{sgn}(\mathbf{v}_{s,i}^{p,tm} \cdot \mathbf{v}_{r,j}^{s,tm}) \frac{|\mathbf{v}_{s,i}^{p,tm}(\omega, \mathbf{x})| |\mathbf{v}_{r,j}^{s,tm}(\omega, \mathbf{x})|}{\int |\mathbf{v}_s^{p,tm}(\omega, \mathbf{x})|^2 dt}, \\
I_k^{sp}(\bar{\theta}_k^{sp}, \mathbf{x}) &= -\delta(\bar{\theta}_k^{sp} - \theta_k^{sp}) \operatorname{sgn}(\mathbf{v}_{s,i}^{s,tm} \cdot \mathbf{v}_{r,j}^{p,tm}) \frac{|\mathbf{v}_{s,i}^{s,tm}(\omega, \mathbf{x})| |\mathbf{v}_{r,j}^{p,tm}(\omega, \mathbf{x})|}{\int |\mathbf{v}_s^{s,tm}(\omega, \mathbf{x})|^2 dt}, \\
I_k^{ss}(\bar{\theta}_k^{ss}, \mathbf{x}) &= -[1 - \delta(i - j)] \delta(\bar{\theta}_k^{ss} - \theta_k^{ss}) \operatorname{sgn}(\mathbf{v}_{s,i}^{s,tm} \cdot \mathbf{v}_{r,j}^{s,tm} \cos \theta_k^{ss}) \frac{|\mathbf{v}_{s,i}^{s,tm}(\omega, \mathbf{x})| |\mathbf{v}_{r,j}^{s,tm}(\omega, \mathbf{x})|}{\int |\mathbf{v}_s^{s,tm}(\omega, \mathbf{x})|^2 dt},
\end{aligned} \tag{4.66}$$

respectively, where the $\hat{\cdot}$ denotes deconvolving the wavefield with the source wavelet.

If the wavelet deconvolution is ignored, the deconvolution imaging condition is approximately equivalent to the reflection-over-incidence (ROI) imaging condition in the t domain (e.g., Kaelin and Guitton, 2006), which is also difficult to stabilize in practice. To improve the stability, Nguyen and McMechan (2015) pick the maximum magnitude from the reconstructed source wavefield over all the time steps at each grid point, and then apply the ROI imaging condition only to the time step with the maximum amplitude, which is also included in the vector-based imaging condition of Wang and McMechan (2015); but picking of the maximum amplitude involves an assumption of no wavefield overlaps at each time step, and thus requires a smooth model to work. Our improved vector-based imaging condition (refer to equations 4.33, 4.34, 4E-1 and 4E-2) can also be combined with the scheme of Nguyen and McMechan (2015) in a smooth elastic model.

4.6.4 Combining multidirectional source vector with the reflection-image normal to calculate RTM ADCIGs

In practice, because the simulated source wavefield is more stable than the reconstructed receiver wavefield, Tang and McMechan (2017a) propose an improved flow to use the multidirectional source vector and the reflection-image normal to calculate ADCIGs. This idea can also be easily extended to elastic data by using the proposed method to calculate the source-angle-domain CIGs (SACIGs) and then to use the anti-truncation-artifact FT (ATFT) to convert the SACIGs into the incident-angle-domain CIGs (refer to Tang and McMechan [2017a]).

4.7 Conclusions

We propose an improved data flow for the E-RTM and ADCIGs in non-smooth elastic models; this flow contains three main aspects. First, the original Helmholtz-theorem-based system of P and S decoupled equations does not consider the wave mode conversion at the current separation time and thus requires a constant or smooth (approximately locally constant) shear-modulus model; the proposed improved decoupling system relaxes this assumption. Second, the proposed multidirectional-vector-based elastic imaging conditions can give the correct polarities of the E-RTM images in non-smooth models, including the PP and SS images with open angles above 90° ; the imaging conditions do not need calculation of the reflection-image normal. Third, we propose two schemes to calculate the multidirectional propagation vectors in nonsmooth elastic models: one is the elastic MPV and the other converts the particle velocities into multidirectional propagation vectors by using the sign of (\mathbf{k}/ω) in the approximate WD. Numerical 2D examples show that the proposed flow can produce high-quality

E-RTM images and ADCIGs. Extension of these methods into 3D and amplitude-preserved imaging conditions are also possible.

4.8 Acknowledgments

The computational resources are provided by the Texas Advanced Computing Center (TACC) and the UT Dallas Geophysical Consortium (UTD GC). A research assistantship is provided via the financial support of the Sponsors of the UTD GC. We also appreciate the comments from Associate Editor V. Vinje and four anonymous reviewers.

4.9 Appendix 4A “The transformation of equation 4.6 to equation 4.7”

Equation 4.6 is equivalent to

$$\begin{aligned}\frac{\partial^2 v_x}{\partial t^2} &= \frac{1}{\rho} \left\{ \frac{\partial}{\partial x} \left[(\lambda + 2\mu) \left(\frac{\partial v_x}{\partial x} + \frac{\partial v_z}{\partial z} \right) \right] + \frac{\partial}{\partial z} \left[\mu \left(\frac{\partial v_x}{\partial z} - \frac{\partial v_z}{\partial x} \right) \right] + 2 \left[\frac{\partial}{\partial z} \left(\mu \frac{\partial v_z}{\partial x} \right) - \frac{\partial}{\partial x} \left(\mu \frac{\partial v_z}{\partial z} \right) \right] \right\}, \\ \frac{\partial^2 v_z}{\partial t^2} &= \frac{1}{\rho} \left\{ \frac{\partial}{\partial z} \left[(\lambda + 2\mu) \left(\frac{\partial v_x}{\partial x} + \frac{\partial v_z}{\partial z} \right) \right] + \frac{\partial}{\partial x} \left[\mu \left(\frac{\partial v_z}{\partial x} - \frac{\partial v_x}{\partial z} \right) \right] + 2 \left[\frac{\partial}{\partial x} \left(\mu \frac{\partial v_x}{\partial z} \right) - \frac{\partial}{\partial z} \left(\mu \frac{\partial v_x}{\partial x} \right) \right] \right\}.\end{aligned}\tag{4A-1}$$

Because

$$\begin{aligned}\frac{\partial}{\partial z} \left(\mu \frac{\partial v_z}{\partial x} \right) - \frac{\partial}{\partial x} \left(\mu \frac{\partial v_z}{\partial z} \right) &= \frac{\partial \mu}{\partial z} \frac{\partial v_z}{\partial x} - \frac{\partial \mu}{\partial x} \frac{\partial v_z}{\partial z}, \\ \frac{\partial}{\partial x} \left(\mu \frac{\partial v_x}{\partial z} \right) - \frac{\partial}{\partial z} \left(\mu \frac{\partial v_x}{\partial x} \right) &= \frac{\partial \mu}{\partial x} \frac{\partial v_x}{\partial z} - \frac{\partial \mu}{\partial z} \frac{\partial v_x}{\partial x},\end{aligned}\tag{4A-2}$$

equation 4A-1 is equivalent to

$$\begin{aligned}\frac{\partial^2 v_x}{\partial t^2} &= \frac{1}{\rho} \left\{ \frac{\partial}{\partial x} \left[(\lambda + 2\mu) \left(\frac{\partial v_x}{\partial x} + \frac{\partial v_z}{\partial z} \right) \right] + \frac{\partial}{\partial z} \left[\mu \left(\frac{\partial v_x}{\partial z} - \frac{\partial v_z}{\partial x} \right) \right] + 2 \left(\frac{\partial \mu}{\partial z} \frac{\partial v_z}{\partial x} - \frac{\partial \mu}{\partial x} \frac{\partial v_z}{\partial z} \right) \right\}, \\ \frac{\partial^2 v_z}{\partial t^2} &= \frac{1}{\rho} \left\{ \frac{\partial}{\partial z} \left[(\lambda + 2\mu) \left(\frac{\partial v_x}{\partial x} + \frac{\partial v_z}{\partial z} \right) \right] + \frac{\partial}{\partial x} \left[\mu \left(\frac{\partial v_z}{\partial x} - \frac{\partial v_x}{\partial z} \right) \right] + 2 \left(\frac{\partial \mu}{\partial x} \frac{\partial v_x}{\partial z} - \frac{\partial \mu}{\partial z} \frac{\partial v_x}{\partial x} \right) \right\},\end{aligned}\tag{4A-3}$$

which is equation 4.7.

4.10 Appendix 4B “An alternative approach to achieve equations 4.21 and 4.22”

Equations 4.21 and 4.22 are equivalent to

$$\begin{aligned}\bar{V}_x^{p,tm} &= -\frac{1}{\rho\omega^2} \left\{ \frac{\partial}{\partial x} \left[(\lambda + 2\mu) \left(\frac{\partial \bar{V}_x}{\partial x} + \frac{\partial \bar{V}_z}{\partial z} \right) \right] + \left(\frac{\partial \mu}{\partial z} \frac{\partial \bar{V}_z}{\partial x} - \frac{\partial \mu}{\partial x} \frac{\partial \bar{V}_z}{\partial z} \right) \right\}, \\ \bar{V}_z^{p,tm} &= -\frac{1}{\rho\omega^2} \left\{ \frac{\partial}{\partial z} \left[(\lambda + 2\mu) \left(\frac{\partial \bar{V}_x}{\partial x} + \frac{\partial \bar{V}_z}{\partial z} \right) \right] + \left(\frac{\partial \mu}{\partial x} \frac{\partial \bar{V}_x}{\partial z} - \frac{\partial \mu}{\partial z} \frac{\partial \bar{V}_x}{\partial x} \right) \right\},\end{aligned}\tag{4B-1}$$

for the P wave and

$$\begin{aligned}V_x^{s,tm} &= -\frac{1}{\rho\omega^2} \left\{ \frac{\partial}{\partial z} \left[\mu \left(\frac{\partial \bar{V}_x}{\partial z} - \frac{\partial \bar{V}_z}{\partial x} \right) \right] + \left(\frac{\partial \mu}{\partial z} \frac{\partial \bar{V}_z}{\partial x} - \frac{\partial \mu}{\partial x} \frac{\partial \bar{V}_z}{\partial z} \right) \right\}, \\ V_z^{s,tm} &= -\frac{1}{\rho\omega^2} \left\{ \frac{\partial}{\partial x} \left[\mu \left(\frac{\partial \bar{V}_z}{\partial x} - \frac{\partial \bar{V}_x}{\partial z} \right) \right] + \left(\frac{\partial \mu}{\partial x} \frac{\partial \bar{V}_x}{\partial z} - \frac{\partial \mu}{\partial z} \frac{\partial \bar{V}_x}{\partial x} \right) \right\},\end{aligned}\tag{4B-2}$$

for the S wave in the ω domain. Here the \bar{V} denotes the particle velocity in the ω domain.

Equations 4B-1 and 4B-2 provide an alternative way of obtaining equations 4.21 and 4.22 from equations 4.25~4.28 as follows:

- a'). Apply a $-\frac{1}{\omega^2}$ operator to the source wavelet (or to the observed data for wavefield reconstruction).

- b'). Using the modified source wavelet from (a') to calculate the full elastic particle velocity in the time domain.
- c'). Apply the operation in the brace of equations 4B-1 and 4B-2 to the full elastic particle velocity. This step has some similarities to divergence and curl operations.

The $-1/\omega^2$ can also be applied to the elastic particle velocity rather than to the source wavelet (especially when the wavefields are extrapolated in the ω domain), but it is more expensive if the wavefields are extrapolated in the time domain.

4.11 Appendix 4C “The polarity of the PP image”

This Appendix verifies that equation 4.31 can give a correct polarity for the PP images in all the eight possible conditions, which are shown in Figures 4.18 and 4.19. In these two figures, the label S is the propagation from the source to the reflection point; the label R is the propagation from the reflection point to the receiver. The \mathcal{G}^{pp} in equation 4.31 is the angle between the source-P and receiver-P polarization vectors,

$$\mathcal{G}^{pp} = \cos^{-1} \left(\frac{\mathbf{v}_s^{p,tm} \cdot \mathbf{v}_r^{p,tm}}{|\mathbf{v}_s^{p,tm}| |\mathbf{v}_r^{p,tm}|} \right), \quad (4C-1)$$

so

$$\text{sgn}(\cos \mathcal{G}^{pp}) = \text{sgn}(\mathbf{v}_s^{p,tm} \cdot \mathbf{v}_r^{p,tm}). \quad (4C-2)$$

Figure 4.18 shows four possible polarization situations when the PP reflectivity is positive. In Figures 4.18a and 4.18c

$$\cos \mathcal{G}^{pp} < 0, \quad \cos \theta^{pp} > 0, \quad (4C-3)$$

so equation 4.31 becomes

$$\text{sgn}(I^{pp}) = -\text{sgn}(\mathbf{v}_s^{p,tm} \cdot \mathbf{v}_r^{p,tm} \cos \theta) = 1, \quad (4C-4)$$

which satisfies the physical truth that the PP reflectivity is positive.

In Figure 4.18b and 4.18d,

$$\cos \mathcal{G}^{pp} > 0, \quad \cos \theta^{pp} < 0, \quad (4C-5)$$

so equation 4.31 becomes

$$\text{sgn}(I^{pp}) = -\text{sgn}(\mathbf{v}_s^{p,tm} \cdot \mathbf{v}_r^{p,tm} \cos \theta^{pp}) = 1, \quad (4C-6)$$

which satisfies the physical truth that the PP reflectivity is positive.

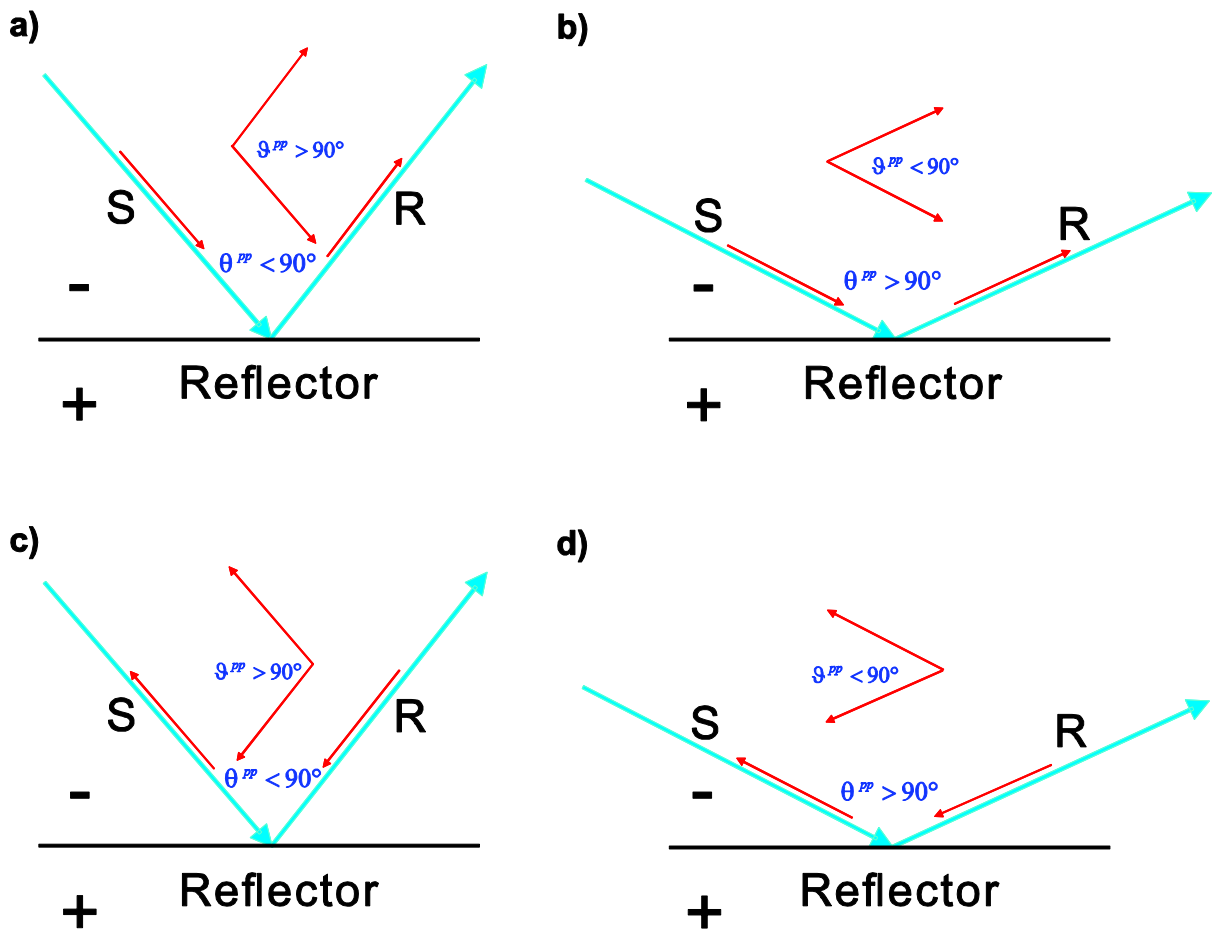


Figure 4.18. Schematic diagram of four representative situations of PP images when the PP reflectivity is positive. The ‘-’ and ‘+’ denote lower and higher P impedances, respectively. The cyan arrows denote the propagation directions and the red arrows denote the polarization directions. θ^{pp} is the open angle between source and receiver propagation vectors (see equation 4.52). ϑ^{pp} is the angle between source P and receiver P polarization vectors (see equation 4C-1). Panels (a) and (c) show two possible polarization situations with the open angle θ^{pp} below 90° ; Panels (b) and (d) show two possible polarization situations with the open angle θ^{pp} above 90° .

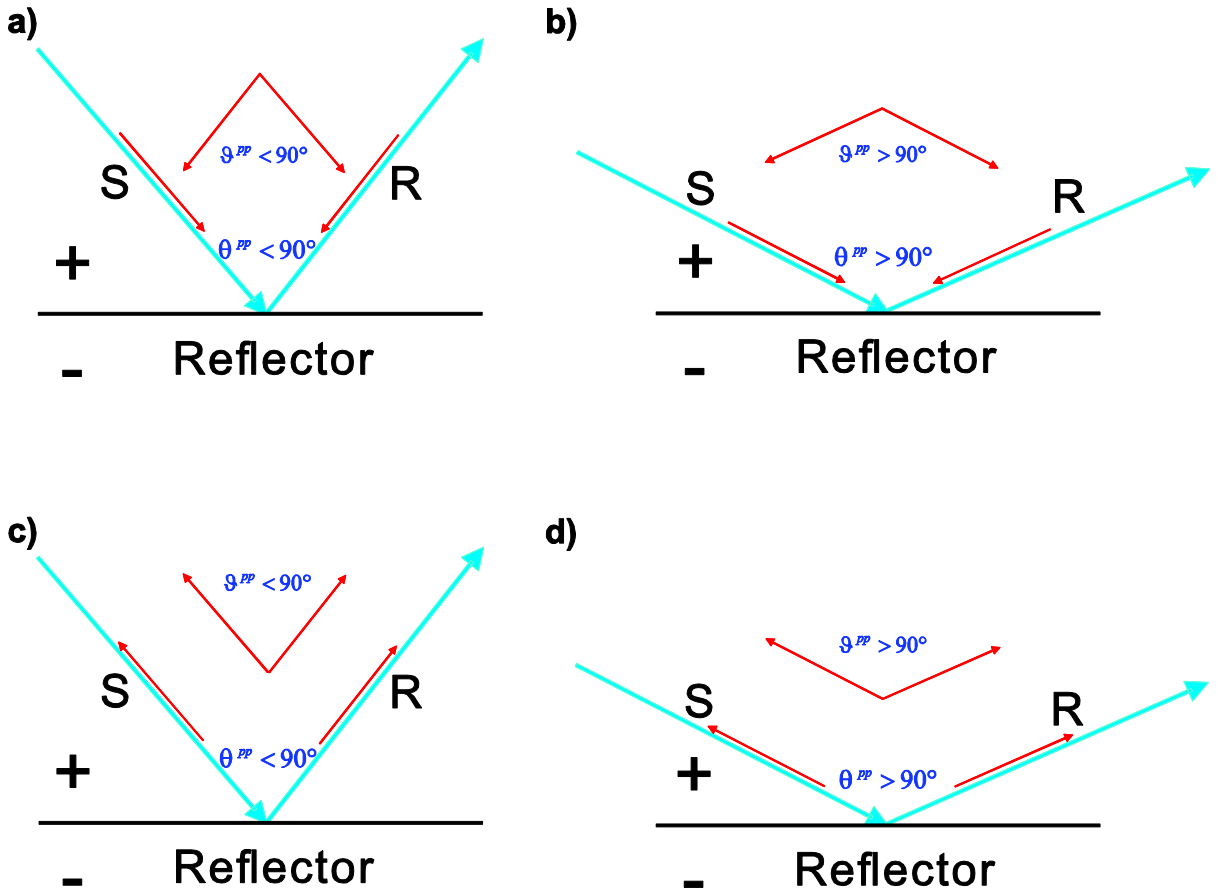


Figure 4.19. Schematic diagram of four representative situations of PP images when the PP reflectivity is negative. Panels (a) and (c) show two possible polarization situations with the open angle θ^{pp} below 90° ; Panels (b) and (d) show two possible polarization situations with the open angle θ^{pp} above 90° . \mathcal{G}^{pp} is the angle between two P polarization vectors (see equation 4C-1).

Figure 4.19 shows four possible polarization situations when the PP reflectivity is negative. In Figures 4.19a and 4.19c,

$$\cos \mathcal{G}^{pp} < 0, \quad \cos \theta^{pp} < 0, \quad (4C-7)$$

so equation 4.31 becomes

$$\text{sgn}(I^{pp}) = -\text{sgn}(\mathbf{v}_s^{p,tm} \cdot \mathbf{v}_r^{p,tm} \cos \theta^{pp}) = -1, \quad (4C-8)$$

which satisfies the physical truth that the PP reflectivity is negative.

In Figure 4.19b and 4.19d,

$$\cos \mathcal{G}^{pp} > 0, \quad \cos \theta^{pp} > 0, \quad (4C-9)$$

so equation 4.31 becomes

$$\text{sgn}(I^{pp}) = -\text{sgn}(\mathbf{v}_s^{p,tm} \cdot \mathbf{v}_r^{p,tm} \cos \theta^{pp}) = -1, \quad (4C-10)$$

which satisfies the physical truth that the PP reflectivity is negative.

4.12 Appendix 4D “The polarity of the PS image”

This Appendix verifies that equation 4.32 can give a correct polarity of the PS image in all the possible situations. In Figures 4.20~4.22, the label S is the propagation from the source to the reflection point; the label R is the propagation from the reflection point to the receiver.

The \mathcal{G}^{ps} in equation 4.32 is the angle between the source-P and receiver-S polarization vectors,

$$\mathcal{G}^{ps} = \cos^{-1} \left(\frac{\mathbf{v}_s^{p,tm} \cdot \mathbf{v}_r^{s,tm}}{|\mathbf{v}_s^{p,tm}| |\mathbf{v}_r^{s,tm}|} \right), \quad (4D-1)$$

and so

$$\text{sgn}(\cos \mathcal{G}^{ps}) = \text{sgn}(\mathbf{v}_s^{p,tm} \cdot \mathbf{v}_r^{s,tm}). \quad (4D-2)$$

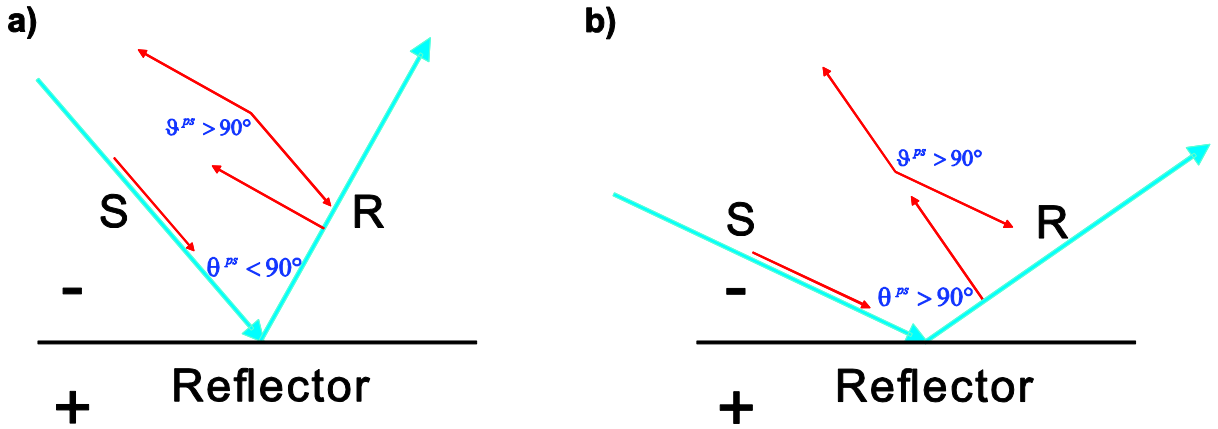


Figure 4.20. Schematic diagram of two representative situations of PS images when the PS reflectivity is positive. The ‘-’ and ‘+’ denote lower and higher (P and S) impedances, respectively. Panel (a) shows a possible polarization situation with the open angle θ_{ps} below 90° ; Panel (b) shows a possible polarization situation with the open angle θ_{ps} above 90° . In both the two panels, the source P wave is on the left side and the receiver S wave is on the right side. The blue arrows denote the propagation directions and the red arrows denote the polarization directions.

The polarity of the PS image is independent of the open angle θ^{ps} of the source and receiver propagation vectors. For example, in Figure 4.20, panels (a) and (b) present two possible situations of the open angles (below or above 90°). For both situations, $\cos \mathcal{G}^{ps} < 0$, so

$$\text{sgn}(I^{ps}) = -\text{sgn}(\cos \mathcal{G}^{ps}) = -\text{sgn}(\mathbf{v}_s^{p,tm} \cdot \mathbf{v}_r^{s,tm}) = 1, \quad (4D-3)$$

which satisfy the physical truth that the PS reflectivity is possible. Thus, the polarity of the PS image in Figure 4.20 is independent of the open angle θ^{ps} ; this rule also exists for other situations. Therefore, regardless of θ^{ps} , the PS images have eight possible polarization conditions that are shown in Figures 4.21 and 4.22.

In Figure 4.21, the PS reflectivity is positive. There are four possible polarization conditions. For equation 4.32, all of these conditions give a unified result,

$$\text{sgn}(I^{ps}) = -\text{sgn}(\cos \mathcal{G}^{ps}) = -\text{sgn}(\mathbf{v}_s^{p,tm} \cdot \mathbf{v}_r^{s,tm}) = 1, \quad (4D-4)$$

which satisfy the physical truth that the PS reflectivity is possible.

In Figure 4.22, the PS reflectivity is negative. There are four possible polarization conditions. For equation 4.32, all of these conditions give a unified result,

$$\text{sgn}(I^{ps}) = -\text{sgn}(\cos \mathcal{G}^{ps}) = -\text{sgn}(\mathbf{v}_s^{p,tm} \cdot \mathbf{v}_r^{s,tm}) = -1, \quad (4D-5)$$

which satisfy the physical truth that the PS reflectivity is negative.

4.13 Appendix 4E “The imaging conditions for the SP and SS images”

Corresponding to equations 4.31 and 4.32, the imaging conditions are

$$I^{sp} = -\text{sgn}(\mathbf{v}_s^{s,tm} \cdot \mathbf{v}_r^{p,tm}) \left| \mathbf{v}_s^{s,tm} \right| \left| \mathbf{v}_r^{p,tm} \right|, \quad (4E-1)$$

for the SP image and

$$I^{ss} = -\text{sgn}(\mathbf{v}_s^{s,tm} \cdot \mathbf{v}_r^{s,tm} \cos \theta) \left| \mathbf{v}_s^{s,tm} \right| \left| \mathbf{v}_r^{s,tm} \right|, \quad (4E-2)$$

for the SS image.

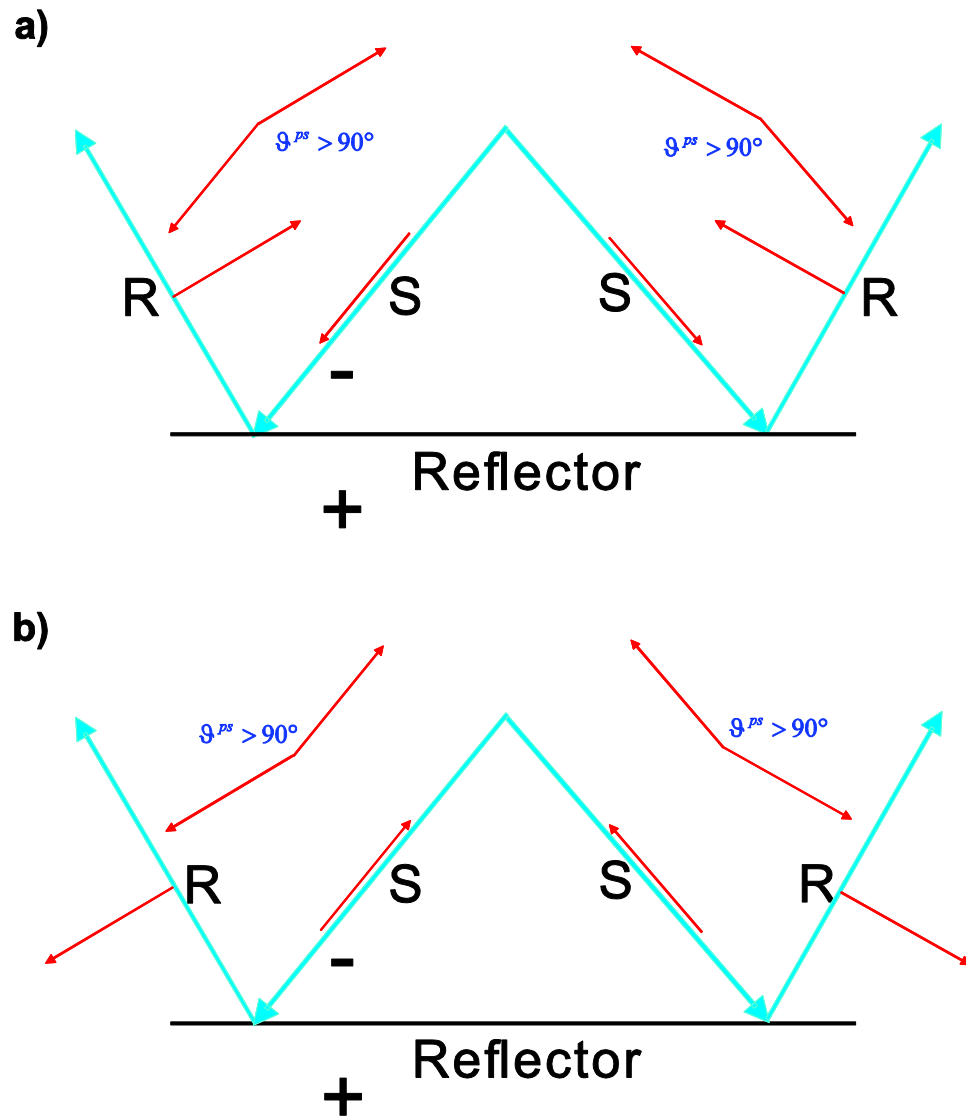


Figure 4.21. Schematic diagram of four representative polarization situations of PS images when the PS reflectivity is positive. In panel (a), the polarization direction of the source P wave is the same as its propagation direction. In panel (b), the polarization direction of the source P wave is opposite to its propagation direction.

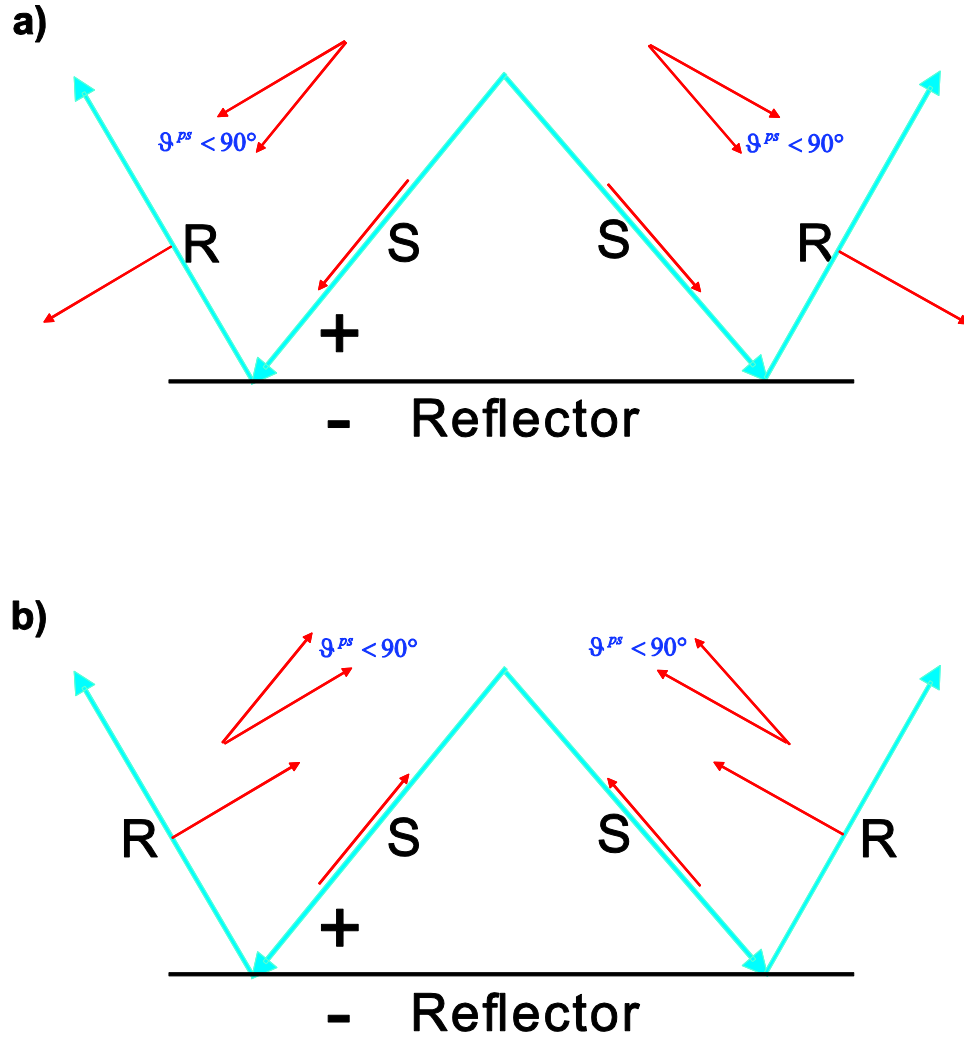


Figure 4.22. Schematic diagram of four representative polarization situations of PS images when the PS reflectivity is negative. In panel (a), the polarization direction of the source P wave is the same as its propagation direction. In panel (b), the polarization direction of the source P wave is opposite to its propagation direction.

Corresponding to equations 4.46 and 4.48, the multidirectional-vector-based imaging conditions are

$$I_k^{sp} = -\text{sgn}(\mathbf{v}_{s,i}^{s,tm} \cdot \mathbf{v}_{r,j}^{p,tm}) \|\mathbf{v}_{s,i}^{s,tm}\| \|\mathbf{v}_{r,j}^{p,tm}\|, \quad (4E-3)$$

for the SP image and

$$I_k^{ss} = -F(\theta_i^{ss})[1 - \delta(i - j)] \operatorname{sgn}(\mathbf{v}_{s,i}^{s,tm} \cdot \mathbf{v}_{r,j}^{s,tm} \cos \theta_k) \left| \mathbf{v}_{s,i}^{s,tm} \right| \left| \mathbf{v}_{r,j}^{s,tm} \right|, \quad (4E-4)$$

for the SS image, where the θ_i^{ss} is defined below. The entire SP and SS images are given by a summation of the corresponding partial images (refer to equation 4.49).

Corresponding to equations 4.50 and 4.51, the multidirectional-vector-based imaging conditions in the angle domain are

$$I_k^{sp}(\bar{\theta}_k^{sp}) = -\delta(\bar{\theta}_k^{sp} - \theta_k^{sp}) \operatorname{sgn}(\mathbf{v}_{s,i}^{s,tm} \cdot \mathbf{v}_{r,j}^{p,tm}) \left| \mathbf{v}_{s,i}^{s,tm} \right| \left| \mathbf{v}_{r,j}^{p,tm} \right|, \quad (4E-5)$$

for the SP ADCIGs and

$$I_k^{ss}(\bar{\theta}_k^{ss}) = -[1 - \delta(i - j)] \delta(\bar{\theta}_k^{ss} - \theta_k^{ss}) \operatorname{sgn}(\mathbf{v}_{s,i}^{s,tm} \cdot \mathbf{v}_{r,j}^{s,tm} \cos \theta_k^{ss}) \left| \mathbf{v}_{s,i}^{s,tm} \right| \left| \mathbf{v}_{r,j}^{s,tm} \right|, \quad (4E-6)$$

for the SS ADCIGs, where $\bar{\theta}_k^{sp}$ and $\bar{\theta}_k^{ss}$ are the open angles for sorting SP and SS ADCIGs, and θ_k^{sp} and θ_k^{ss} are the open angles calculated by

$$\begin{aligned} \theta_k^{sp} &= \pi - \cos^{-1} \left(\frac{\mathbf{p}_{s,i}^{s,tm} \cdot \mathbf{p}_{r,j}^{p,tm}}{\left| \mathbf{p}_{s,i}^{s,tm} \right| \left| \mathbf{p}_{r,j}^{p,tm} \right|} \right), \\ \theta_k^{ss} &= \pi - \cos^{-1} \left(\frac{\mathbf{p}_{s,i}^{s,tm} \cdot \mathbf{p}_{r,j}^{s,tm}}{\left| \mathbf{p}_{s,i}^{s,tm} \right| \left| \mathbf{p}_{r,j}^{s,tm} \right|} \right). \end{aligned} \quad (4E-7)$$

CHAPTER 5

FROM CLASSICAL REFLECTIVITY-TO-VELOCITY INVERSION TO FULL WAVEFORM INVERSION USING PHASE-MODIFIED AND DECONVOLVED REVERSE-TIME-MIGRATION IMAGES*

5.1 Summary

To obtain a physical understanding of gradient-based descent methods in full waveform inversion (FWI), we find a connection between the FWI gradient and the image provided by reverse time migration (RTM): The gradient uses the residual data as a virtual source, and RTM uses the observed data directly as the boundary condition, so the FWI gradient is similar to a time integration of the RTM image using the residual data, which physically converts the phase of the reflectivity to the phase of the velocity. Therefore, the gradient-based FWI can be connected to the classical reflectivity-to-velocity/impedance inversion (RVI). We propose a new FWI scheme that provides a self-contained and physically-intuitive derivation which naturally establishes a connection between the amplitude-preserved RTM, the Zoeppritz equations (AVA inversion) and RVI, and combines them into a single framework to produce a preconditioned inversion formula. In this scheme, the relative velocity update is a phase-modified and deconvolved RTM image obtained with the residual data. Consistent with the deconvolution, the

* Tang C. and G. A. McMechan, 2017, From classical reflectivity-to-velocity inversion to full-waveform inversion using phase-modified and deconvolved reverse time migration images: *Geophysics*, 82, no. 1, S31-S49. Copyrighted by Society of Exploration Geophysicists. Permalink: <https://doi.org/10.1190/geo2016-0033.1>

Tang C. and G. A. McMechan, 2016, From classical reflectivity-to-velocity inversion to full-waveform inversion using phase-modified and deconvolved reverse-time-migration images: 86th International Meeting, SEG, Dallas, 1141-1145. Copyrighted by Society of Exploration Geophysicists. Permalink: <https://doi.org/10.1190/segam2016-13879375.1>

multi-scale approach applies a gradually-widening low-pass frequency filter to the deconvolved wavelet at early iterations, and then uses the unfiltered deconvolved wavelet for the final iterations. Numerical tests show that the new method makes a significant improvement to the quality of the inversion result.

5.2 Introduction

Full waveform inversion (FWI) has emerged as a viable technology for depth model building and has started to be applied in production. The initial idea of FWI is proposed by Lailly (1983) and Tarantola (1984); the goal is to find the optimal parameter updates to minimize the difference between the predicted and observed data. The update in each iteration of FWI is the negative product of an inverse Hessian matrix and a gradient of the objective function. Because the Hessian matrix is both complicated and large, it is difficult to invert, so gradient-based descent methods are widely used. Based on a derivation using the adjoint-state method (Tarantola, 1984; Plessix, 2006), the gradient is a cross-correlation of the second time derivative of a forward-time extrapolated wavefield from the source, and a reverse-time extrapolated residual wavefield from the receivers; the latter uses the difference between the predicted data and the observed data as a virtual source. Because the $-\partial/\partial t^2$ is equivalent to a ω^2 in the frequency domain, the FWI gradient is kinematically similar to a reverse-time-migration (RTM) image using the cross-correlation imaging condition (e.g., Chattopadhyay and McMechan, 2008) with the residual data as the boundary condition to reconstruct the receiver wavefield. This leads to the classical statement that “reverse time migration is the first iteration of full waveform inversion” (Mora, 1989).

Compared to traditional tomographic methods, FWI provides higher resolution and accuracy, but unfortunately, also incurs increased uncertainty and instability. Cycle-skipping dictates that FWI can succeed only when the phase difference between the predicted and observed data is within a half wavelength (Mora, 1989). Thus, low-frequency data are required when the initial velocity model does not fit the real data within half a wavelength, and inversion needs to proceed continuously from low to high frequency (Bunks et al., 1995), to satisfy the half wavelength condition progressively at each scale. Multi-scale FWI is easier and more natural when wavefield extrapolation is in the frequency domain (Pratt et al., 1998) or the Laplace-domain (Shin and Cha, 2008). For FWI using extrapolation in the time (t) domain (time-domain FWI), a low-pass or band-pass frequency filter is required. In practice, high-quality low-frequency data are very difficult to obtain. Therefore, tomographic and large-reflection-angle images are separated or enhanced to update the background velocity in early iterations (Tang et al., 2013c; Díaz and Sava, 2013; Alkhalifah, 2015); adaptive FWI approaches have also been developed (Warner and Guasch, 2014; Jiao et al., 2015), which try to match the predicted and observed data before back-propagating the residual between them.

The objective functions of all the FWI methods discussed above are implemented by minimization of the difference between the predicted data and the observed data; thus, they are often defined as data-domain FWI. These methods have high accuracy but require low-frequency data or a good initial velocity model. To overcome these problems and to balance the accuracy and stability, image-domain inversion algorithms are developed, which can be generally divided into two types. The first uses extended images (Symes and Carazzone, 1991; Sava and Biondi, 2004; Shen and Symes, 2008, Yang and Sava, 2011) to establish new objective functions. These

methods can make use of the kinematic information and thus can deal with less accurate initial models than when using the dynamic characteristics (the phase and amplitude). Therefore, they are expected to be more stable in establishing the background model but may be less accurate than data-domain FWI. The second type of image-domain FWI uses demigration to calculate the predicted data and uses only the reflection signal to update velocities (Xu et al., 2012). These methods make use of the fact that the locations, of the reflectors in the reflection images obtained from RTM, are more accurate than those in the initial velocity model. However, if the reflection image does not have (relatively) true amplitudes and correct phases, it may have a negative influence on the predicted data calculated by demigration.

Similar to parameter inversions, there are also algorithms to invert reflection images. Their objective functions are similar to FWI, but use the reflection image as the inversion target. Generally, there are two categories: least-squares (LS) migration and amplitude-preserved (AP) migration. The LS migration (Nemeth et al., 1999; Zhang et al., 2015) uses demigration to calculate the predicted data, and thus suffers from problems similar to those of the second type of image-domain inversions. It is usually used to calculate the amplitude-preserved image, especially when illumination compensation and multiples are considered. The LS migration can be combined with FWI to obtain a more accurate update (Yao et al., 2014). Unlike the LS migration, the angle-domain amplitude-preserved RTM (AP-RTM) (e.g., Xu et al., 2011) does not need iterations. The main difference between the AP-RTM and FWI, is that the predicted data has a linear relation with the reflectivity (in AP-RTM) but a nonlinear relation with the velocity (in FWI). So, the inverse Hessian for the AP-RTM can be explicitly calculated while that for FWI cannot. Zhang et al. (2014) extend the AP-RTM into impedance inversion. Innanen

(2014) uses the amplitude-variation-with-offset (AVO) relation to approximate the inverse Hessian for pre-critical reflection FWI. Qin et al. (2015) also derive a preconditioned FWI formula using the AP-RTM.

Gradient-based FWI does not use the inverse Hessian but is widely used because of its efficiency. Conjugate gradients, such as PR (Polak and Ribière, 1969), are usually used to increase the convergence rate of steepest-descent methods (Virieux and Operto, 2009). A spectral-shaping filter has also been developed to improve the convergence (Lazaratos et al., 2011; Plessix and Li, 2013). To obtain a more accurate solution of FWI, approximations of the Hessian matrix have also been developed, such as the Limited-memory Broyden–Fletcher–Goldfarb–Shanno (L-BFGS) method (e.g., Nocedal, 1980), the truncated-Newton method (Métivier et al., 2012) and the Gauss-Newton method (Pratt et al., 1998); inversion formulas using the preconditioned Hessian have also been proposed (Lee et al., 2010; Qin et al., 2015; Tang and Lee, 2015). Beside the problem of calculating the inverse Hessian matrix, the linear Born assumption in FWI also may not give a good approximation of multiple scattering and thus direct nonlinear inversion methods are being developed (Wu et al., 2014; Wu et al., 2015). Solving these problems (e.g., the inverse Hessian) is very expensive; their solutions also involve other assumptions. Therefore, gradient-based descent FWI is still the most common approach and connecting this approach with a clear physical meaning is important.

In this chapter, to obtain a physical understanding of the steepest-descent FWI, we establish a relation between the FWI gradient and the RTM image and show that there is a phase-transformation operator in the FWI gradient, which converts the phase of an RTM reflection image (obtained with the residual data) to the phase of the velocity update. Based on this, we

connect the FWI with the classical reflectivity-to-velocity/impedance inversion (Peterson et al., 1955; Oldenburg et al., 1983) and propose a new scheme. It provides a self-contained and physically-intuitive derivation that naturally relates several previously published schemes (Innanen, 2014; Zhang et al., 2014; Qin et al. 2015) and combines them into a single framework.

5.3 Theory

This section is divided into three subsections. The first subsection introduces the relation between the FWI gradient and the RTM image, and proves that the nature of steepest-descent FWI is a reflectivity-to-velocity inversion (RVI). Based on this relationship, in the second subsection, we use the RVI to derive a new inversion formula, which uses a phase-modified and deconvolved RTM image (obtained by using the residual data). The third subsection contains a discussion of the wavelet deconvolution.

5.3.1 The relation between the FWI gradient and the RTM image

In this subsection, we prove a relation between reverse time migration (RTM) and the gradient of full waveform inversion (FWI), and point out the difference between the boundary conditions of the propagation equations to obtain them.

Consider an acoustic isotropic example. When the receivers are on the surface, the wave-propagation equations and boundary conditions of RTM in acoustic media are

$$\begin{cases} \frac{1}{v^2} \frac{\partial^2 u_s(t, \mathbf{x})}{\partial t^2} = \nabla^2 u_s(t, \mathbf{x}) + \delta(\mathbf{x} - \mathbf{x}_s) F(t), \\ d_{cal}(t, x, y, \mathbf{x}_s) = u_s(t, x, y, z = 0), \end{cases} \quad (5.1)$$

for the source wavefield and

$$\begin{cases} \frac{1}{v^2} \frac{\partial^2 u_r(t, \mathbf{x})}{\partial t^2} = \nabla^2 u_r(t, \mathbf{x}), \\ u_r(t, x, y, z=0) = d_{obs}(t, x, y, \mathbf{x}_s), \end{cases} \quad (5.2)$$

for the receiver wavefield. In equations 5.1 and 5.2, u_s and u_r are the source and receiver wavefields, respectively. \mathbf{x} and \mathbf{x}_s are the locations of an image point and of the source, respectively. ∇^2 is a Laplacian operator. $F(t)$ is the source, which is a time integration of the injection pressure: $\int_0^t f(t') dt'$ (where f is the injection pressure). $\delta(\)$ is a delta function. d_{cal} and d_{obs} are the predicted and observed data at the receivers, respectively; they can also be written as \mathbf{d}_{cal} and \mathbf{d}_{obs} to represent the data matrices. v is the propagation velocity of the pressure wave and t is the time.

The objective function of the conventional FWI is an L2 norm:

$$C(\mathbf{m}) = \frac{1}{2} \delta \mathbf{d}^T \delta \mathbf{d}, \quad (5.3)$$

where \mathbf{m} is the model parameter, T is the transposition operator, and $\delta \mathbf{d}$ is the residual between the calculated and the observed data,

$$\delta \mathbf{d} = \mathbf{d}_{cal} - \mathbf{d}_{obs}. \quad (5.4)$$

The relation between the model update $\delta \mathbf{m}$ and $C(\mathbf{m})$ can be obtained by expanding $C(\mathbf{m})$ into a Taylor series of the background model \mathbf{m}_0 . Based on Virieux and Operto's (2009) derivation,

$$\delta \mathbf{m} = -\frac{1}{2} H^{-1} J = -\frac{1}{2} \left[\frac{\partial^2 C(\mathbf{m})}{\partial \mathbf{m}^2} \right]^{-1} \left[\frac{\partial C(\mathbf{m})}{\partial \mathbf{m}} \right] \Big|_{\mathbf{m}=\mathbf{m}_0}. \quad (5.5)$$

The Hessian matrix H is difficult to invert, so the most common implementation uses only the gradient J , and searches for a step length μ_k to define the model update:

$$\mathbf{m}_{k+1} = \mathbf{m}_k - \mu_k \left[\frac{\partial C(\mathbf{m})}{\partial \mathbf{m}} \Big|_{\mathbf{m}=\mathbf{m}_k} \right], \quad (5.6)$$

where k is the iteration number. Considering only the velocity, for a single source at \mathbf{x}_s and a single receiver at \mathbf{x}_r , the gradient at location \mathbf{x} in equation 5.6 can be expressed in convolutional form as (see Appendix 5A [Section 5.7]):

$$\frac{\partial C(\mathbf{x}_s, \mathbf{x}, \mathbf{x}_r; v)}{\partial v} \Big|_{v=v_0} = \int dt \frac{2}{v^3} \frac{\partial^2 u_s}{\partial t^2} [G(\mathbf{x}, \mathbf{x}_r; -t) * \delta \mathbf{d}], \quad (5.7)$$

where v_0 is the background velocity, and $G(\mathbf{x}, \mathbf{x}_r; -t)$ is the Green's function from the image point \mathbf{x} to the receiver \mathbf{x}_r , through time $-t$. Based on the reciprocity theorem,

$$G(\mathbf{x}_r, \mathbf{x}; t) = G(\mathbf{x}, \mathbf{x}_r; -t), \quad (5.8)$$

where $G(\mathbf{x}_r, \mathbf{x}; t)$ is the Green's function from \mathbf{x}_r to \mathbf{x} , through time t . The convolution $G(\mathbf{x}_r, \mathbf{x}; t) * \delta \mathbf{d}$ is an adjoint-state source using the residual data, the wavefield from which propagates in the reverse-time direction from the maximum recording time T to zero. Because of equation 5.8, if the \mathbf{x}_s and \mathbf{x}_r are omitted for simplification (in our implementation, the gradient is stacked over multiple sources and receivers), equation 5.7 can be written as

$$\left. \frac{\partial C(\mathbf{x}, v)}{\partial v} \right|_{v=v_0} = \int \frac{1}{v_0^3} \frac{\partial^2 u_s(t, \mathbf{x})}{\partial t^2} g_r(t, \mathbf{x}) dt, \quad (5.9)$$

where g_r is obtained from

$$\begin{cases} \frac{1}{v^2} \frac{\partial^2 g_r(t, \mathbf{x})}{\partial t^2} = \nabla^2 g_r(t, \mathbf{x}), \\ g_r(t, x, y, z=0) = \int_t^T \delta d(t', x, y, \mathbf{x}_s) dt'. \end{cases} \quad (5.10)$$

In practice, a surface-energy-compensation term $\frac{\cos \alpha_r}{v_r}$ should be included in the boundary condition (Zhang et al., 2014); here α_r is the propagation angle and v_r is the propagation velocity at the surface receiver location. The time-integration in equation 5.10 is equivalent to multiplying by $\frac{1}{i\omega}$ in the ω domain (here ω is the angular frequency and i is $\sqrt{-1}$), so equations 5.9 and 5.10 are equivalent to (see Appendix 5B [Section 5.8])

$$\left. \frac{\partial C(\mathbf{x}, v)}{\partial v} \right|_{v=v_0} = \Re \left[\int \frac{1}{v_0^3} i\omega U_s(\omega, \mathbf{x}) \bar{H}_r(\omega, \mathbf{x}) d\omega \right], \quad (5.11)$$

and

$$\begin{cases} \frac{1}{v^2} \frac{\partial^2 h_r(t, \mathbf{x})}{\partial t^2} = \nabla^2 h_r(t, \mathbf{x}), \\ h_r(t, x, y, z=0) = \delta d(t, x, y, \mathbf{x}_s). \end{cases} \quad (5.12)$$

where \bar{H}_r means the complex-conjugate of H_r and \Re means taking the real part; U_s and H_r are the Fourier transforms (FTs) of u_s and h_r , respectively. Equation 5.12 is very similar to

equation 5.2 (the propagation equation for the receiver side in RTM); both of them are in the reverse-time direction, and the only difference is that equation 5.2 uses the observed data as the boundary condition, while equation 5.12 uses the residual data as the boundary condition.

By comparing equations 5.2 and 5.10, we conclude that the differences of the boundary conditions between RTM and the FWI gradient are: RTM uses the observed data directly for the boundary condition (equation 5.2), while the FWI gradient uses the time integration of the residual data (an adjoint-state source) as the boundary condition (equation 5.10). The time integration works as a phase transformation operator $\frac{1}{i\omega}$, which transforms the phase of the reflectivity into that of the velocity.

Based on equations 5.9 and 5.10, equation 5.6 becomes

$$v_{k+1}(\mathbf{x}) = v_k(\mathbf{x}) - \mu_k \frac{1}{v_k^3(\mathbf{x})} \left(\int \frac{\partial^2 u_s(t, \mathbf{x})}{\partial t^2} g_r(t, \mathbf{x}) dt \right). \quad (5.13)$$

Here, the $-\frac{\partial^2}{\partial t^2}$ (or ω^2) does not change the main polarity of the wavelet-phase but performs as a high-pass frequency filter (Figure 5.1). Therefore, the core of steepest-descent FWI is a phase transformation from the reflectivity to the velocity.

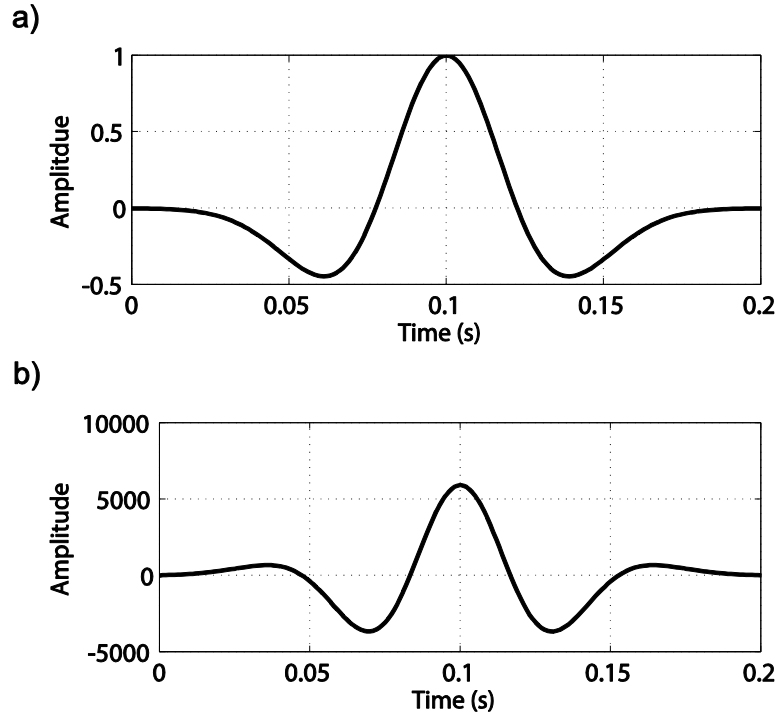


Figure 5.1. Ricker wavelet (Panel a) and the negative of its second time derivative (Panel b) have similar phases, but a) has longer wavelength than b), which means the dominant frequency of a) is lower than that of b).

5.3.2 FWI based on reflectivity-to-velocity inversion

In the previous subsection, we conclude that the FWI gradient is similar to the classical reflectivity-to-velocity inversion (RVI) (Peterson et al., 1955). In this subsection, we derive a new FWI formula based on RVI.

There is a relation between the reflectivity and the impedance,

$$R = \frac{I_2 - I_1}{I_2 + I_1} = \frac{\rho_2 v_2 - \rho_1 v_1}{\rho_2 v_2 + \rho_1 v_1}, \quad (5.14)$$

where R is the reflectivity of the model, I_1 is the impedance of upper layer, I_2 is the impedance of lower layer, and ρ is the density. Note, the R in equation 5.14 is a property of the model and

is independent of the reflection angle. Assuming constant density (as we are considering only velocity inversion in this chapter), equation 5.14 becomes

$$R = \frac{v_2 - v_1}{v_2 + v_1}, \quad (5.15)$$

which can also be written as

$$R = \frac{\Delta v}{2v_a}, \quad (5.16)$$

where v_a is the average velocity of the two layers, and Δv is the difference between the velocities of the two layers. Equation 5.16 can be further changed to

$$R = \frac{\Delta x_i}{2} \frac{1}{v_a} \frac{\Delta v}{\Delta x_i} = A \frac{1}{v_a} \frac{dv}{dx_i}, \quad (5.17)$$

where Δx_i is a small unit interval in the reflector normal direction, and we define a scale factor

A to replace $\frac{\Delta x_i}{2}$.

Now, define the forward and inverse FTs between the t - \mathbf{x} and ω - \mathbf{k} domains as

$$\begin{cases} \bar{U}(\omega, \mathbf{k}) = \int_{-\infty}^{\infty} dt \int_{-\infty}^{\infty} d\mathbf{x} u(t, \mathbf{x}) e^{i(\mathbf{kx} - \omega t)}, \\ u(t, \mathbf{x}) = \int_{-\infty}^{\infty} d\omega \int_{-\infty}^{\infty} d\mathbf{k} \bar{U}(\omega, \mathbf{k}) e^{i(-\mathbf{kx} + \omega t)}, \end{cases} \quad (5.18)$$

where \mathbf{k} is the wavenumber; the $(2\pi)^{-1}$ is ignored here because it can be included in the scale factor (or step length), which can be obtained by a steepest-descent search in inversion (e.g., Pica et al, 1990). So, we have

$$i\omega \leftrightarrow \frac{\partial}{\partial t}, \quad -i\mathbf{k} \leftrightarrow \frac{\partial}{\partial \mathbf{x}}, \quad (5.19)$$

where \leftrightarrow means an equivalence between time (or space) and frequency (or wavenumber) domains; the opposite signs of ω and \mathbf{k} are because of the definitions of the FTs in equation 5.18.

Because of equation 5.19, equation 5.17 becomes

$$R = -\frac{A}{v_a} ik_i v, \quad (5.20)$$

where k_i is the wavenumber from a 1D FT along the reflector normal direction, and (see Appendix 5C [Section 5.9] for the relation between $|k_i|$ and $|\mathbf{k}_{ref}|$)

$$|k_i| = |\mathbf{k}_{ref}| = \beta |\mathbf{k}|. \quad (5.21)$$

where \mathbf{k}_{ref} and \mathbf{k} are the wavenumbers of the reflection image and of the propagating wavefield, respectively. Here β is a global scale factor. In equation 5.21, we assume a deconvolved source (or a deconvolution imaging condition) is used. For the cross-correlation imaging condition using the source wavelet, the relation between $|\mathbf{k}_{ref}|$ and $|\mathbf{k}|$ includes a $\cos\theta$ (where θ is the reflection angle) (Zhang and Sun, 2009; Alkhalifah, 2015). For equation 5.20, if we use the reflectivity to calculate the velocity, we obtain

$$\frac{v}{v_a} = -\frac{1}{A} \frac{R}{ik_i}. \quad (5.22)$$

The amplitude-preserved reflection image, which is consistent with the amplitude variation with (reflection) angle (AVA) theory, can be obtained (approximately) by using a deconvolution imaging condition (Zhang et al, 2005; Zhang and Sun, 2009)

$$R'(\mathbf{x}, \theta) = \iint \frac{U_r(\mathbf{x}, \omega)}{U_s(\mathbf{x}, \omega)} \delta(\theta' - \theta) d\omega d\theta', \quad (5.23)$$

where R' is an angle-dependent reflection coefficient at reflection angle θ . The reflectivity R in equation 5.22 is theoretically equivalent to the reflection coefficient R' at normal incidence. θ' is the reflection angle calculated from the propagation vectors of the source and receiver wavefields (e.g., see equation 5.8 of Tang and McMechan, 2016); the propagation vector can be calculated by the local plane-wave decomposition (Xu et al. 2011) in the ω - \mathbf{k} domain or by the multidirectional slowness vector (Tang and McMechan, 2016) in the t - \mathbf{x} domain (including approximate wave decomposition in ω - \mathbf{k}). A wavelet deconvolution is automatically involved in equation 5.23. There are two points that need to be noted:

1. To obtain the reflectivity R from the angle-dependent reflection coefficients R' , for each image point, a least-squares estimate of R is calculated to fit the AVA curve of R' .
2. Equation 5.23 assumes the ideal condition of a primary reflection from one source. However, because of the limited illumination of a single source, the images are usually stacked over many source gathers and involve multiple arrivals. Therefore, the so-called “true-amplitude” RTM image assumes a balanced illumination and contains the “relative” reflection coefficients, which require a scale factor μ to become the “true” reflection coefficients. Using the cross-correlation imaging condition (e.g., Chattopadhyay and

McMechan, 2008) is more stable than equation 5.23 in implementation and will be discussed later in this subsection.

The derivation below is to obtain a new inversion formula; the inversion is an iterative process, and a scale factor is adjusted in a steepest-descent search at each iteration. To obtain an approximate true reflectivity, we can use the approach proposed by Aki and Richards (1980) to linearize the angle-dependent reflection-coefficient equation (Appendix 5D [Section 5.10]),

$$R(\mathbf{x}) = \frac{1}{N} \int R'(\mathbf{x}, \theta) \cos^2 \theta d\theta, \quad (5.24)$$

where N is explained in Appendix 5D [Section 5.10]. The Aki-Richards equation is also used by Innanen (2014) to approximate the inverse Hessian in reflection FWI. Substituting equation 5.23 into 5.24 gives (refer to Point II above for the generation of μ)

$$R(\mathbf{x}) = \mu \mathcal{R} \left[\iint \frac{U_r(\mathbf{x}, \omega)}{U_s(\mathbf{x}, \omega)} \cos^2 \theta d\omega d\theta \right], \quad (5.25)$$

where N^{-1} is included in the scale factor μ , which is added because the RTM image is often stacked over common-source gathers (refer to Point II above). For simplification, we do not add an integration over sources in equation 5.25. Substituting equation 5.25 into 5.22 gives

$$\frac{v}{v_a} = -\mu \mathcal{R} \left\langle \iint F^{-1} \left\{ \frac{1}{ik_i} F \left[\frac{U_r(\mathbf{x}, \omega)}{U_s(\mathbf{x}, \omega)} \cos^2 \theta \right] \right\} d\omega d\theta \right\rangle. \quad (5.26)$$

at location \mathbf{x} , where F is a local spatial FT from the \mathbf{x} domain to the \mathbf{k} domain, and F^{-1} is the corresponding inverse FT. In equation 5.26, the k_i from equation 5.22 is inside the integration, because this integration is obtained from a least-squares estimation of the true reflectivity R to fit

a set of angle-dependent reflection coefficients R' (See Appendix 5D [Section 5.10]), each of which corresponds to a solution of R .

Because of equation 5.1, we have

$$\omega^2 = |\mathbf{k}|^2 v_0^2, \quad (5.27)$$

where v_0 is the background velocity. Based on the definition of the FTs (equation 5.18), we obtain the relation between ω and the wavenumber k_w along the wavefront (propagation) direction (Tang and McMechan, 2016),

$$\omega = k_w v_0. \quad (5.28)$$

Because of equation 5.21, and also because k_w and k_i should have the same sign,

$$\omega = \beta^{-1} k_i v_0. \quad (5.29)$$

Although equation 5.28 requires a constant v_0 , k_w is only used to connect k_i and ω , both of which are independent of v_0 , and thus there is not a constant-velocity assumption for equation 5.29. Substituting equation 5.29 into 5.26 gives (including β^{-1} in μ)

$$\frac{v}{v_a} = -\mu v_0 \Re \left[\iint \frac{U_r(\mathbf{x}, \omega) \cos^2 \theta}{i \omega U_s(\mathbf{x}, \omega)} d\omega d\theta \right]. \quad (5.30)$$

In the process from equation 5A-6 to 5A-7 (see Appendix 5A [Section 5.7]), a velocity perturbation will lead to a perturbation of the predicted data and also the generation of a residual, and there is a condition that the velocity perturbation is small enough that the subsequent data residual is within a half period. Similarly, if the velocity perturbation is small enough that the

subsequent change in the reflector location is within a half wavelength (which corresponds to the half period condition in the derivation of the FWI gradient), the influence of the velocity perturbation on the deconvolution in equation 5.30 can be ignored in the derivation because the subsequent phase difference between the two reflectivity images (obtained by using predicted and observed data) can be gradually decreased by iterations. Thus, from equation 5.30, we obtain

$$\frac{\delta v'}{v_0} = -\mu v_{0a} \Re \left[\iint \frac{H_r(\mathbf{x}, \omega) \cos^2 \theta}{i\omega U_s(\mathbf{x}, \omega)} d\omega d\theta \right], \quad (5.31)$$

where $\delta v'$ is the velocity perturbation and v_{0a} is the v_a for the background velocity. The H_r is the FT of h_r , which is calculated by using the residual data as the boundary condition for reverse-time extrapolation (equation 5.12). The sign of the velocity update δv should be opposite to that of the velocity perturbation $\delta v'$, and this corresponds to the update direction being opposite to the gradient (equation 5.6) in steepest-descent FWI, so

$$\frac{\delta v}{v_0} = -\frac{\delta v'}{v_0} = \mu v_{0a} \Re \left[\iint \frac{H_r(\mathbf{x}, \omega) \cos^2 \theta}{i\omega U_s(\mathbf{x}, \omega)} d\omega d\theta \right]. \quad (5.32)$$

If we use the time integration (the adjoint-state source) to replace the $\frac{1}{i\omega}$, equation 5.32 becomes

(refer to equations 5.9-5.12)

$$\frac{\delta v}{v_0} = \mu v_{0a} \Re \left[\iint \frac{G_r(\mathbf{x}, \omega)}{U_s(\mathbf{x}, \omega)} \cos^2 \theta d\omega d\theta \right], \quad (5.33)$$

where G_r (corresponding to g_r in the t domain) is calculated by equation 5.10, which uses the residual data as an adjoint-state source. In summary, the “half wavelength” conditions in the FWI gradient (equation 5.9) and in the RVI-based FWI (equation 5.33) are

1. The derivation of the FWI gradient (equation 5.9) requires the phase difference between predicted and observed data to be within half a wavelength (refer to equations 5A-6 and 5A-7 in Appendix 5A [Section 5.7]).
2. The RVI-based FWI (equation 5.33) requires the phase difference between the reflectivity images obtained from the predicted and observed data should be within half a wavelength (refer to equations 5.30 and 5.31).

Mathematically, the RVI-based FWI is equivalent to using the L2-norm of the difference between the reflectivity images obtained from predicted and observed data as the objective function and using the physical insight of RVI to give a preconditioned gradient (See Appendix 5E [Section 5.11]).

In equations 5.32 and 5.33, the $\cos^2 \theta$ enhances the reflection signal. To avoid calculating ADCIGs, we ignore this term, which increases the weight of the long-wavelength tomographic signal (Tang et al., 2013c), which will be discussed below. The v_{0a} is the average velocity of the two layers that constitute the reflector, so it does not influence the local phase of the velocity update δv around that reflector, which determines the update direction of the inversion. If we use the average velocity for the whole (target) model to approximate v_{0a} , priority is given to the update of the low velocities, and equation 5.33 becomes

$$\frac{\delta v}{v_0} = \mu \mathfrak{R} \left[\int \frac{G_r(\mathbf{x}, \omega)}{U_s(\mathbf{x}, \omega)} d\omega \right]. \quad (5.34)$$

where v_{oa} is included in the scale factor μ . Equation 5.34 is similar to the inversion formula of Qin et al. (2015) (See Appendix 5F [Section 5.12]), and can also be rewritten as,

$$\frac{\delta v}{v_0} = \mu \mathfrak{R} \left[\int \frac{\bar{U}_s(\mathbf{x}, \omega) G_r(\mathbf{x}, \omega)}{U_s(\mathbf{x}, \omega) \bar{U}_s(\mathbf{x}, \omega)} d\omega \right] = \mu \mathfrak{R} \left[\int \frac{U_s(\mathbf{x}, \omega) \bar{G}_r(\mathbf{x}, \omega)}{S(\omega) \bar{S}(\omega)} \cdot \frac{1}{G(\mathbf{x}_s, \mathbf{x}) \bar{G}(\mathbf{x}_s, \mathbf{x})} d\omega \right], \quad (5.35)$$

where $G(\mathbf{x}_s, \mathbf{x})$ is the Green's function from the source \mathbf{x}_s to an image point \mathbf{x} , and $S(\omega)$ is the zero-phase source wavelet in the ω domain. FWI is an iterative process which is strongly related to the local phase of the RTM image; $[G(\mathbf{x}_s, \mathbf{x}) \bar{G}(\mathbf{x}_s, \mathbf{x})]^{-1}$ is a spreading-energy term and has little influence on the local phase, so equation 5.35 becomes

$$\frac{\delta v}{v_0} = \mu \mathfrak{R} \left[\int \frac{U_s(\mathbf{x}, \omega) \bar{G}_r(\mathbf{x}, \omega)}{S(\omega) \bar{S}(\omega)} d\omega \right], \quad (5.36)$$

which is approximately equivalent to

$$\frac{\delta v}{v_0} = \mu I_p = \mu \int \hat{u}_s(\mathbf{x}, t) \hat{g}_r(\mathbf{x}, t) dt, \quad (5.37)$$

in the t domain. A comparison between the results using equations 5.34 and 5.37 is shown in Appendix 5F [Section 5.12]. The wavefields \hat{u}_s and \hat{g}_r (where ‘ \wedge ’ means ‘deconvolved’) can be obtained by using the deconvolved source wavelet for modelling and the deconvolved residual data for wavefield reconstruction, respectively. The I_p is a phase-modified and deconvolved (residual) RTM image. When the term involving the reflection angle is ignored, Equation 5.36 or

5.37 is equivalent to using the cross-correlation imaging condition (e.g., Chattopadhyay and McMechan, 2008) of the source and residual wavefields that are both deconvolved to replace equation 5.23, and also has similarities with Zhang et al.'s (2014) equation for inverting only the velocity. Equations 5.34 (which is similar to equation 5F-1 in Appendix 5F [Section 5.12]) and 5.36 also indicate that the essential difference between the inversion formulas of Qin et al. (2015) and Zhang et al. (2014) relates to the different imaging conditions used to obtain the amplitude-preserved RTM image; the former corresponds to the deconvolution imaging condition and the latter corresponds to the cross-correlation imaging condition.

We will discuss the influence of the deconvolution operator in equation 5.37 in the next subsection, so now we write it as

$$\frac{\delta v}{v_0} = \mu \int u_s(\mathbf{x}, t) g_r(\mathbf{x}, t) dt, \quad (5.38)$$

and compare it with equation 5.13. Equation 5.38 uses the full waveform for inversion and thus can also be regarded as an FWI formula. There are two differences between equations 5.13 and 5.38. First, the ω^2 or $-\frac{\partial^2}{\partial t^2}$ in equation 5.13 is removed in equation 5.38; second, the velocity term $\frac{1}{v_0^3}$ in the right side of equation 5.13 is modified to v_0 in equation 5.38 (moving v_0 from the left to the right side of equation 5.38).

The derivation of equation 5.38 is directly from the reflection-coefficient equation 5.15 and has a clear physical meaning, which can be interpreted into the following physical process. First, subtract the reflectivity image obtained by using predicted data from that obtained by using the

observed data, to produce a residual image; then apply a reflectivity-to-velocity inversion to this residual image to obtain an update; and finally search for a scale factor to add this update to the background velocity. Note, this description is only for physical interpretation; in implementation, we do not need to calculate two RTM images for subtraction. Instead, the subtraction of reflectivity images in the first step and the phase transformation $(i\omega)^{-1}$ in the second step, can be achieved in a single step, using a time integration of the residual data as a boundary condition of the reverse-time extrapolation from the receivers (equation 5.10).

Refracted and turning waves are usually removed in RTM imaging, because the source and receiver wavefields cross-correlate along these wave paths (when the migration velocity is correct) and thus create artifact-images (Liu et al., 2011). However, we need to use these waves in equation 5.38 (the FWI formula). This is because the initial velocity in FWI is incorrect, and so the source and residual wavefields of the refracted and turning waves will not propagate on the same path; thus, they will have large opening angles, and are similar to a large-reflection-angle image. These images have long wavelengths that are useful to establish the background velocity in the shallow part of the model because the error of the reflector locations in these long-wavelength images are more likely to satisfy the half-wavelength condition. Note that, when the velocities along a wave path of refracted or turning waves become correct, the residual data for this wave path will be zero, and thus a cross-correlation of the source and the residual wavefields along this wave path in FWI will not generate artifacts as in RTM.

In the early iterations, because the refracted and turning waves have high amplitudes in the residual data, they have higher weight in the inversion and contribute more to the update of the

background velocity. As the inversion proceeds, these waves become better fitted (between the predicted and observed data) and thus their residuals become smaller, so the reflection signals then have higher weight in the inversion and produce more accurate velocities. Moreover, as discussed in the previous subsection, the core of the traditional steepest-descent FWI formula (equation 5.13) also involves a transformation from the phase of the reflectivity to the phase of velocity, which is similar to the reflectivity-to-velocity inversion; a common-sense aspect of steepest-descent FWI is that the refracted and turning waves are useful and give long-wavelength updates (Sirgue, 2006; Tang et al., 2013c). Therefore, we include the refracted and turning waves in the velocity update.

Equation 5.38 means that “a relative velocity perturbation $\frac{\Delta v}{v_0}$ is equal to a phase-modified

RTM image obtained with the residual data”, and the scale factor (the step length) of this image is adjusted by a steepest-descent search. The difference between using a first time derivative (equation 5.13) and a time integration (in equation 5.38, the time integration is included in g_r) is clearly seen in Figures 5.2 and 5.3. In Figure 5.2a, the reflectivity (at 0.1 s) is caused by a velocity change at 0.1s. Because the reflectivity is positive, the velocity before 0.1 s should be lower than that after 0.1 s. However, Figure 5.2b (taking a first time derivative of Figure 5.2a) does not fit well with this physical phenomenon, because it changes sign three times (implying three reflectors), while Figure 5.2c (taking a time integration) fits well with this phenomenon and has only one reflector at 0.1 s. A related comparison is shown in Figure 5.3; compared to the first time derivative in Figure 5.3d, the update given by time integration in Figure 5.3e fits better with the ideal update in Figure 5.3c. The difference between Figure 5.3c and Figure 5.3e is because of

the limited frequency bandwidth and side-lobes (in the amplitude spectrum) of the wavelet in Figure 3e; therefore, wavelet deconvolution (see equations 5.36 and 5.37) needs to be done to the wavelets of the reflection image (to obtain Figure 5.3f), which is introduced in the next subsection.

5.3.3 Using deconvolved source and residual data for inversion

In the previous subsection, the relative velocity update is obtained by applying a reflectivity-to-velocity inversion to the residual image. In equation 5.38, the seismic wavelet always has a limited frequency bandwidth and side-lobes in the amplitude spectrum, which leads to a wavelet-like velocity update (Figure 5.3e). This causes artificial velocity layers and complicates local minima. To be consistent with the physical truth of the true reflectivity, the wavelets used in the inversion need to be deconvolved (equation 5.37 and Figure 5.3f).

Figure 5.4 demonstrates the result of applying deconvolution to a Ricker wavelet. Strictly speaking, the deconvolution with the zero-phase source wavelet (see equation 5.37) does not enlarge the frequency band, but it can enlarge the “effective” frequency bandwidth by balancing (flattening) the spectral amplitude over the existing frequency band (compare Figures 5.4c and 5.4d).

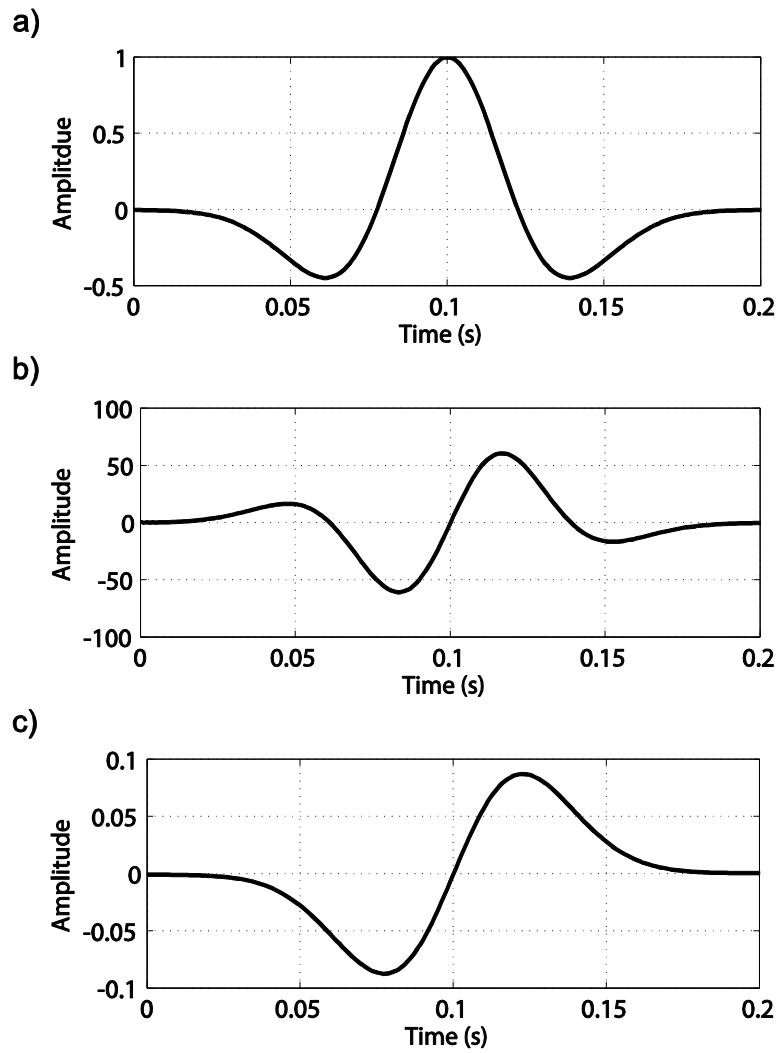


Figure 5.2. Ricker wavelet a), its first time derivative b), and its time integration c). In b), the polarity of the wavelet changes three times, which correspond to three reflectors; while in (c), the polarity of the wavelet changes only at 0.1 s, which corresponds to a positive reflectivity at 0.1 s and thus is consistent with a).

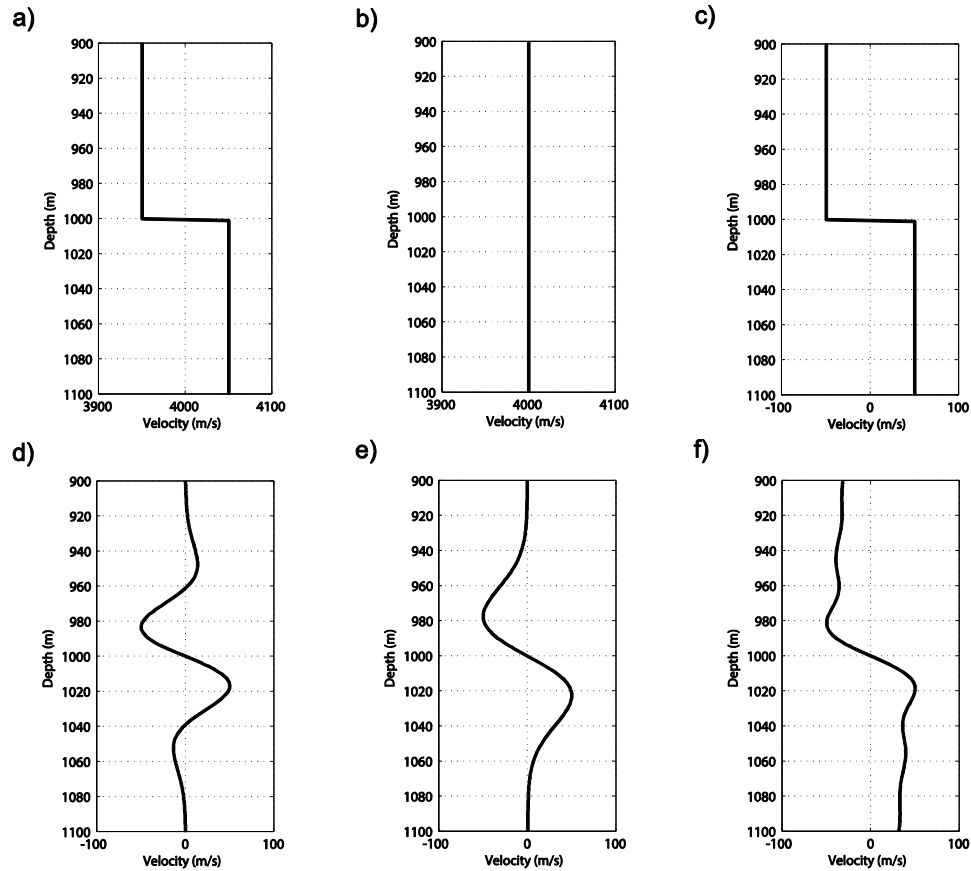


Figure 5.3. Schematic diagram for comparison of different phases in FWI. For a true model in a) and an initial model in b), the ideal velocity update is in c). Using the first time derivative of the residual image gives an update in d), using the time integration gives an update in e), and using a deconvolution and a time integration gives an update in f).

For better interpretation, we combine the comparisons in Figures 5.3 and 5.4. The difference between applying a phase-transformation operator $(i\omega)^{-1}$ to the original wavelet (Figure 5.4a) and to the deconvolved wavelet (Figure 5.4b) is shown in Figures 5.3e and 5.3f, respectively. Figure 5.3f is more similar to the ideal update (Figure 5.3c) than Figure 5.3e, because Figure 5.4b is more similar to a spike than Figure 5.4a, and it has a better magnitude balance in the spectrum (compare Figure 5.4c and 5.4d). The deconvolution operator in

equations 5.36 and 5.37 is also part of the spectral-shaping of Plessix and Li (2013), but their formula gives only a partial compensation (see Appendix 5G [Section 5.13]).

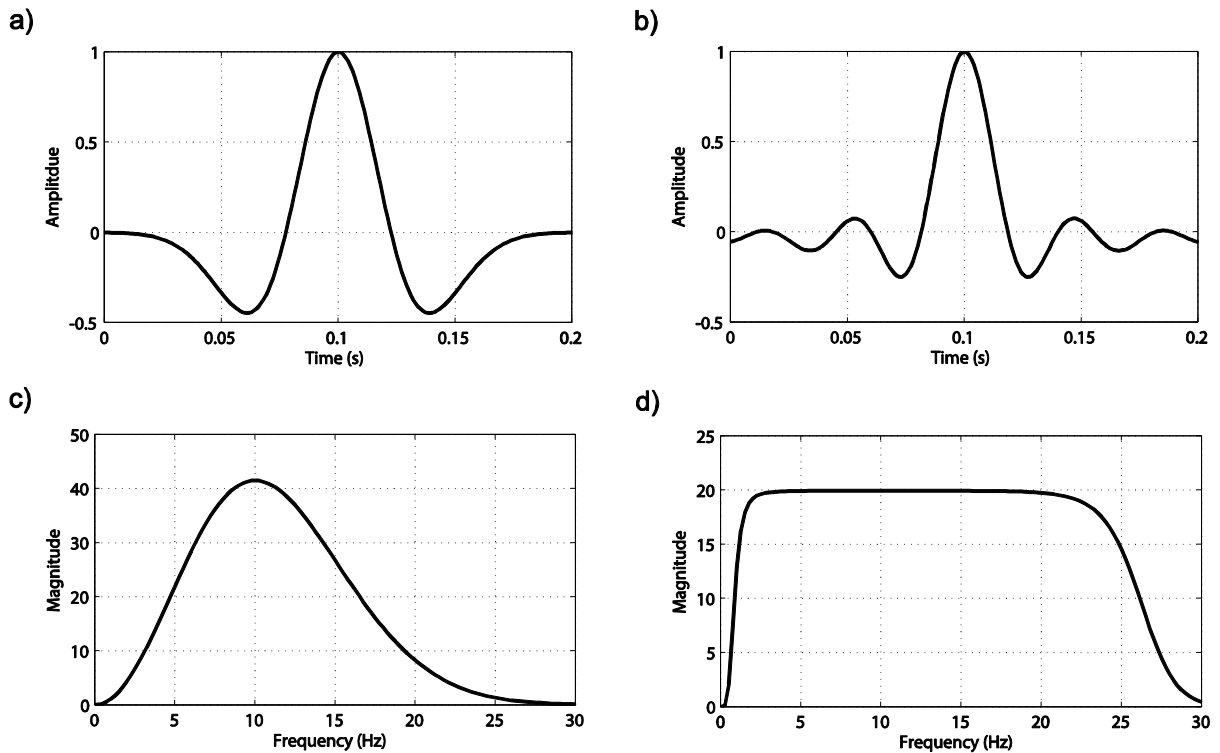


Figure 5.4. For a Ricker wavelet in a), deconvolving it with a zero-phase Ricker wavelet with the same dominant frequency will give a wavelet in b). The spectrum of a) is in c); the spectrum of b) is in d). The phase comparison between time integration of a) and b) is seen in Figures 5.3e and 5.3f.

5.4 Examples

To be consistent with the deconvolution of the source wavelet and the residual data (in Section 5.3), the multi-scale approach is divided into two parts. First, we apply a low-pass frequency filter to the source wavelet and the residual data that are both deconvolved, and use the filtered data to update the background velocity. As the inversion proceeds, we increase the cut-off frequency of the low-pass frequency filter to gradually increase the frequency bandwidth

and thus improve the resolution of the image result while avoiding cycle-skipping. Finally, we use the source wavelet and residual data that are both deconvolved to invert for the details of the velocity model. During this two-part process, the width of the “effective” frequency bandwidth of the deconvolved wavelet is progressively increased to the maximum. To improve the convergence, we combine Hestenes-Stiefel with Dai–Yuan algorithms (Hager and Zhang, 2006; Yang et al., 2015) to give a non-linear conjugate update δc_i ,

$$\delta c_i = \begin{cases} (I_p)_i + \beta_i \delta c_{i-1}, & i \geq 1, \\ (I_p)_i, & i = 0, \end{cases} \quad (5.39)$$

where

$$\beta_i = \max \left[0, \min \left(\beta_i^{HS}, \beta_i^{DY} \right) \right], \quad (5.40)$$

where

$$\begin{cases} \beta_i^{HS} = - \frac{\langle (I_p)_i, (I_p)_i - (I_p)_{i-1} \rangle}{\langle \delta c_{i-1}, (I_p)_i - (I_p)_{i-1} \rangle}, \\ \beta_i^{DY} = - \frac{\langle (I_p)_i, (I_p)_i \rangle}{\langle \delta c_{i-1}, (I_p)_i - (I_p)_{i-1} \rangle}, \end{cases} \quad (5.41)$$

where $\langle \rangle$ means an inner product. So, equation 5.37 becomes

$$\frac{\delta v}{v_0} = \mu \delta c_i, \quad (5.42)$$

In the following two subsections, we compare the inversion results obtained from the conjugate-gradient-based FWI using a steepest-descent to search for the step length (S-FWI) (equation 5.13

plus HS-DY), the FWI using phase-modified RTM images (P-FWI) (equation 5.38 plus HS-DY), and the FWI using phase-modified and deconvolved RTM images (PD-FWI) (equation 5.37 plus HS-DY). The HS-DY algorithm is defined in equations 5.39-5.42 (by using equation 5.37 as an example). The step length μ can be obtained by applying a linear steepest-descent search algorithm developed by Pica et al. (1990). In PD-FWI, The step-length search can be applied to the predicted and observed data that are both deconvolved (and filtered in the first-part of the multi-scale approach). During the inversions, we do not set any predetermined nonzero bounds of the inverted velocity within the target inversion area.

5.4.1 Examples based on the SEG overthrust model

We now use 2D examples to illustrate the performance of the proposed FWI. The first example uses a complicated part of the SEG overthrust model. The grid intervals in both horizontal and vertical directions are 25 m. The source uses a seismic wavelet obtained by stacking Ricker wavelets from 12 Hz to 25 Hz (Figure 5.5); the resulting dominant frequency is about 16.7 Hz. The true velocity model is in Figure 5.6a; to remove the influence of the direct wave in the residual, we put a sediment layer at the top, the velocity of which is constant at 2500 m/s and is assumed to be known. The target area starts at 500 m depth. The initial model (Figure 5.6b) has only a 1D velocity variation in depth. This initial model is made in two steps: First, we smooth the true model by 20 iterations using the average velocity within a 21x21 (grid points) window as the velocity at the center point of that window; then, we use the average velocity in the horizontal direction as the velocity for each depth.

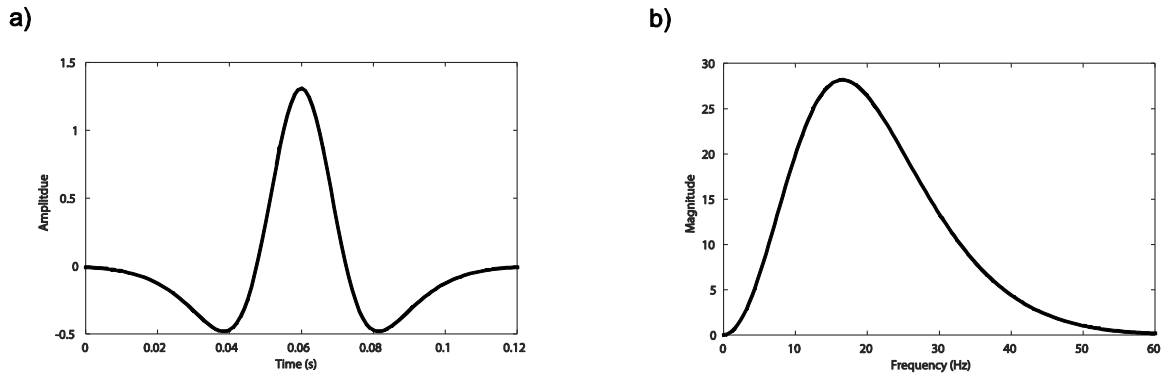


Figure 5.5. The source wavelet a) and its spectrum b) used for the SEG overthrust model.

There are 60 sources at horizontal locations from -1400 to 4500 m. The receivers are to the right of each source, and the offset range (the locations of receivers relative to that of the corresponding source) is from 100 to 3000 m. The cut-off frequencies (COFs) for the low-pass frequency filter are 4, 6, 8, 12, and 16 Hz, and the spectral amplitudes are tapered over a width of 4 Hz around these COFs. For example, for a COF at 4 Hz, the taper starts at 2 Hz ends at 6 Hz. We perform 20 iterations for each scale, and then do another 80 iterations using the unfiltered data. So the total number is 180.

We compare the inversion results obtained by using S-FWI, P-FWI and PD-FWI in Figure 5.6. The P-FWI solution (Figure 5.6d) gives a more accurate velocity than S-FWI (Figure 5.6c), but some parts of the velocity are still underestimated; the velocity from PD-FWI (Figure 5.6e) is even more accurate and gives a result that is very similar to the true model (Figure 5.6a). The different accuracy of velocities also leads to different accuracy of the locations of reflector boundaries, especially in the deep part of the model (see the arrows in Figure 5.6). In addition, artificial layers are seen in Figure 5.6d; for example, there are underestimated velocity layers (artificial layers) within the high-velocity layer indicated by the red and blue arrows, which are

caused by the limited frequency bandwidth and the side-lobes of the spectrum of the seismic wavelet (refer to Figures 5.3c, 5.3e and 5.3f). These artificial layers become less apparent in Figure 5.6e, which uses a source wavelet and residual data that are both deconvolved.

Figure 5.7 shows more detailed velocity profiles at horizontal locations 1000, 2000, 3000 and 4000 m. The P-FWI (Figure 5.7b) gives a more accurate velocity than the S-FWI (Figure 5.7a); PD-FWI (Figure 5.7c) works even better and gives a nearly perfect inversion result. The differences between the three methods are most significant in the velocity profiles at 1000 m, because the structure is relatively complicated there (see Figure 5.6a). In the PD-FWI result (Figure 5.7c), there are still some small velocity fluctuations because the frequency bandwidth is still limited, but the magnitudes of these fluctuations are very small. The bottom of the model is well inverted by using PD-FWI (Figure 5.7c), although no reflection comes from below. This is because, in equation 5.15, if the velocity of the upper layer and the reflectivity of the reflector are known, the velocity below the reflector can be calculated; although the derivation from equation 5.15 to 5.37 (or 5.42) has several assumptions, the inversion result at the bottom of the model can be gradually improved by iterations.

Figure 5.8 shows the results of S-FWI, P-FWI and PD-FWI at different iterations and provides more comparison details; the multi-scale method updates the velocity gradually, from large scale (the background) to small scale (the details). Comparison of the results at the same iteration number (e.g., iteration 60) also show that P-FWI (Figure 5.8b) works better than S-FWI (Figure 5.8a), and PD-FWI (Figure 5.8c) works even better.

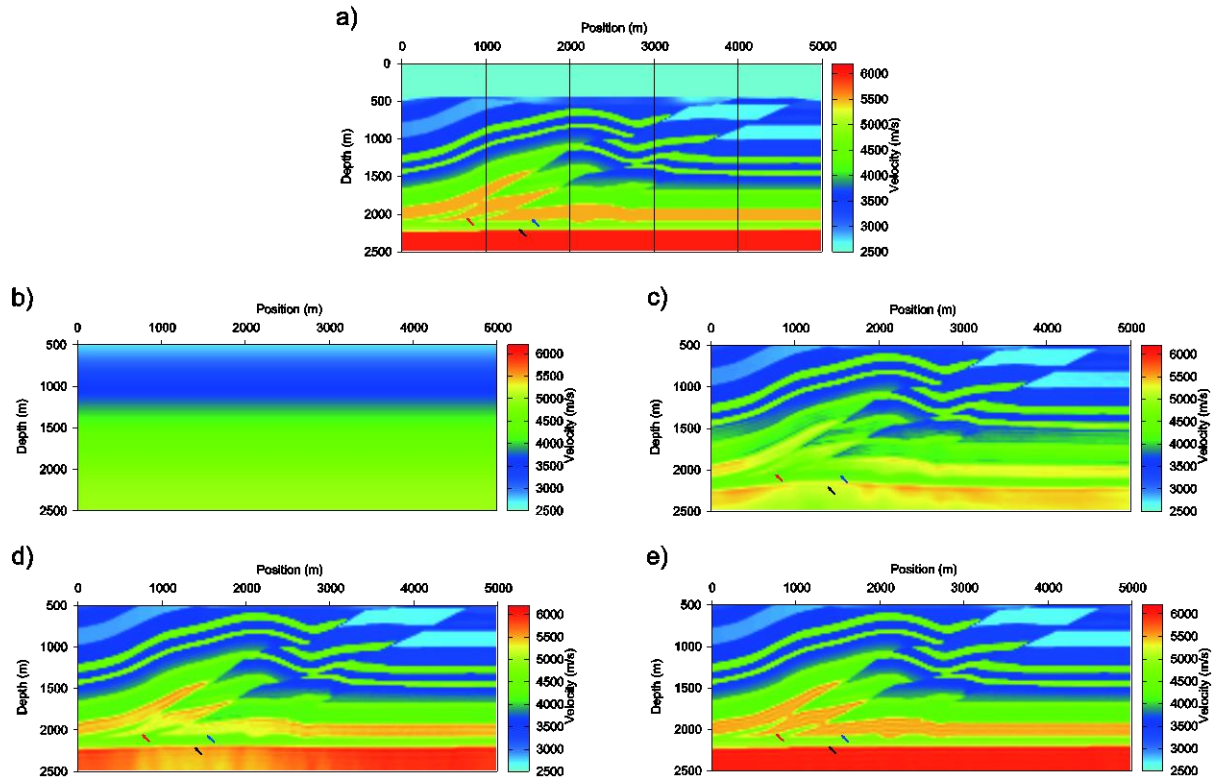


Figure 5.6. Comparison of inversion results obtained by using three methods on a complicated portion of the SEG overthrust model. a) The true model. b) The initial model. c) the S-FWI result. d) the P-FWI result. e) the PD-FWI result. The red, black and blue arrows point to three reflector boundaries, respectively. The four black lines in a) denote the locations for the velocity profiles in Figure 5.7, which show more details for comparison.

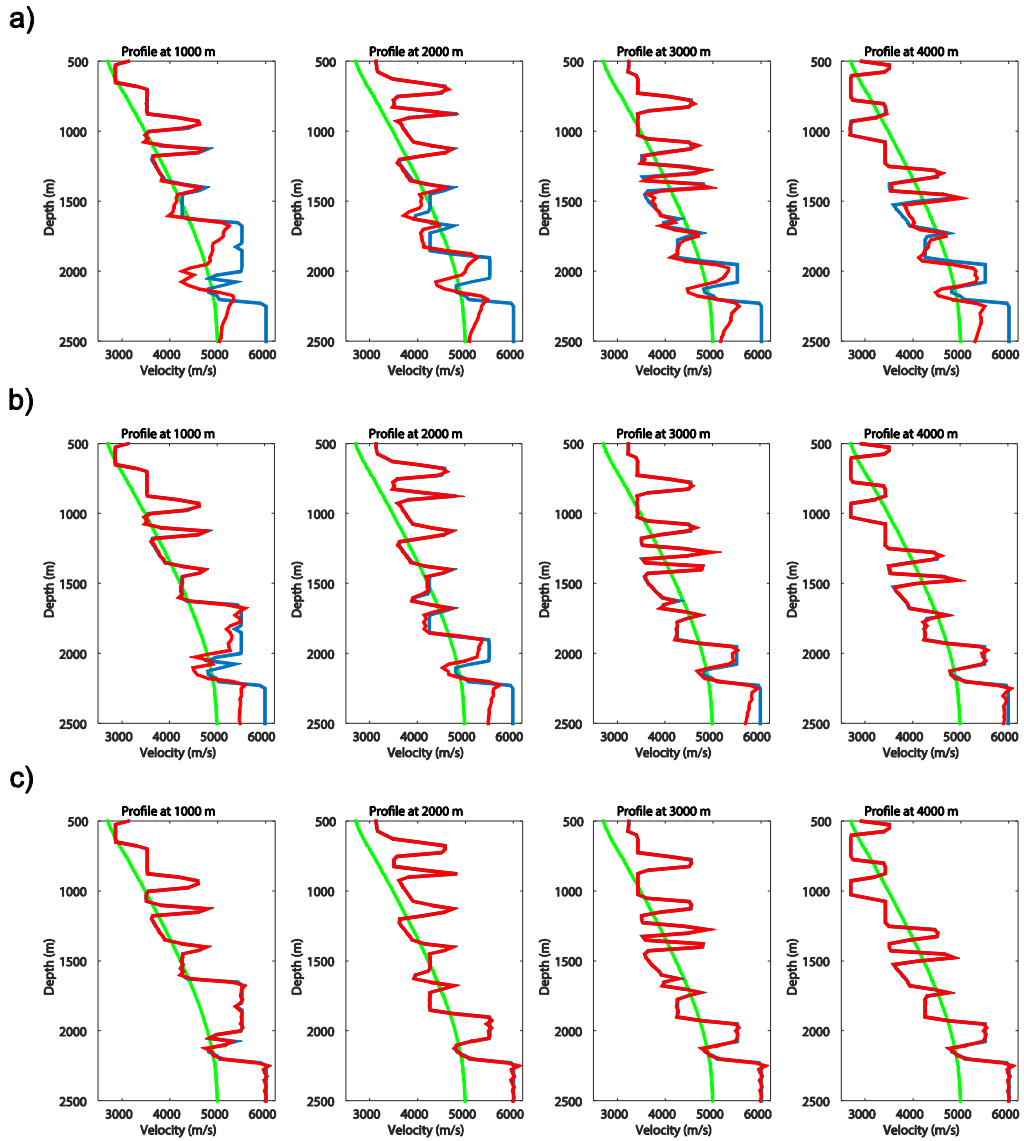


Figure 5.7. Comparison of velocity profiles obtained with S-FWI (Panel a), P-FWI (Panel b), and PD-FWI (Panel c), for the SEG overthrust model. The blue line is the true velocity, the green line is the initial velocity, and the red line is the inverted velocity.

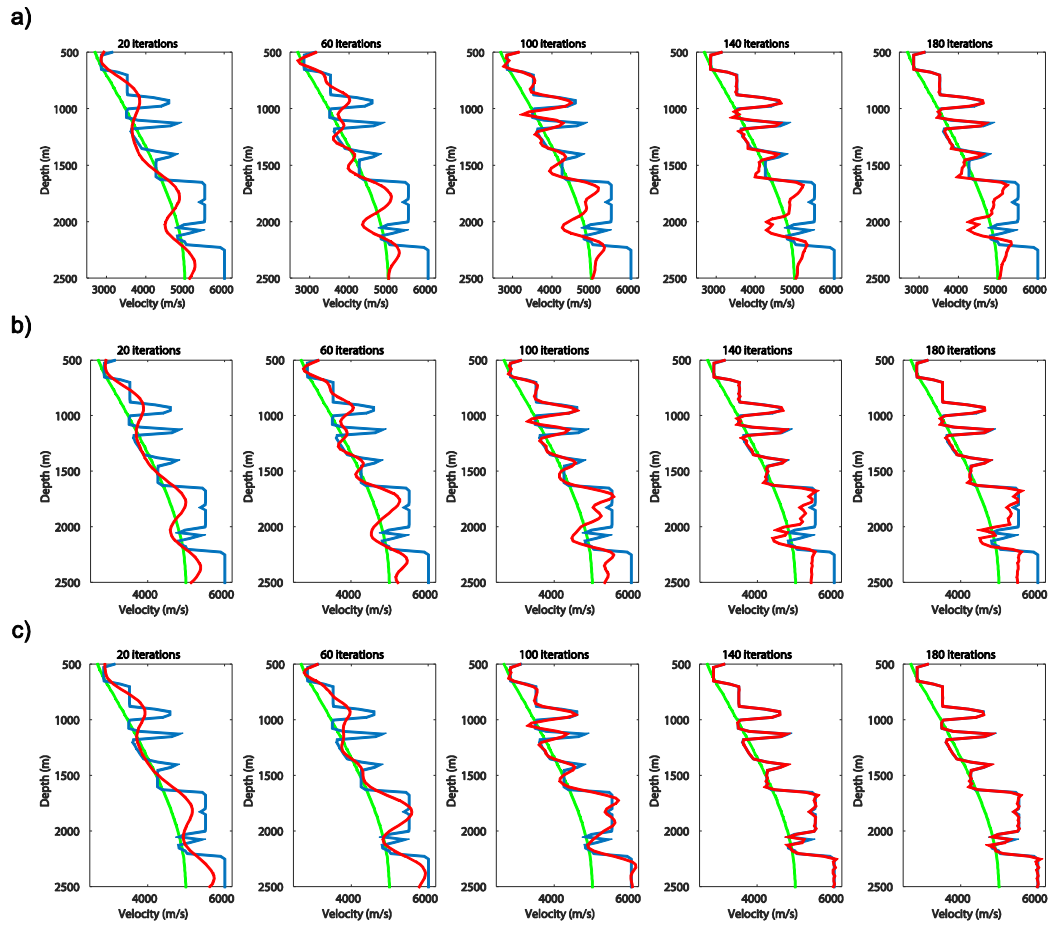


Figure 5.8. Velocity profiles at different iterations of S-FWI (Panel a), P-FWI (Panel b), and PD-FWI (Panel c), for the SEG overthrust model. The horizontal location of these velocity profiles is 1000 m (see Figure 5.6a). The blue line is the true velocity, the green line is the initial velocity, and the red line is the inverted velocity.

Figure 5.9 shows the average velocity residuals (the errors between the true and inverted velocities) of S-FWI, P-FWI and PD-FWI as a function of iteration number. The velocity residual decreases from S-FWI, to P-FWI, to PD-FWI. Comparison of (relative) total data residuals of the three methods is shown in Figure 5.10, in which PD-FWI has the smallest value.

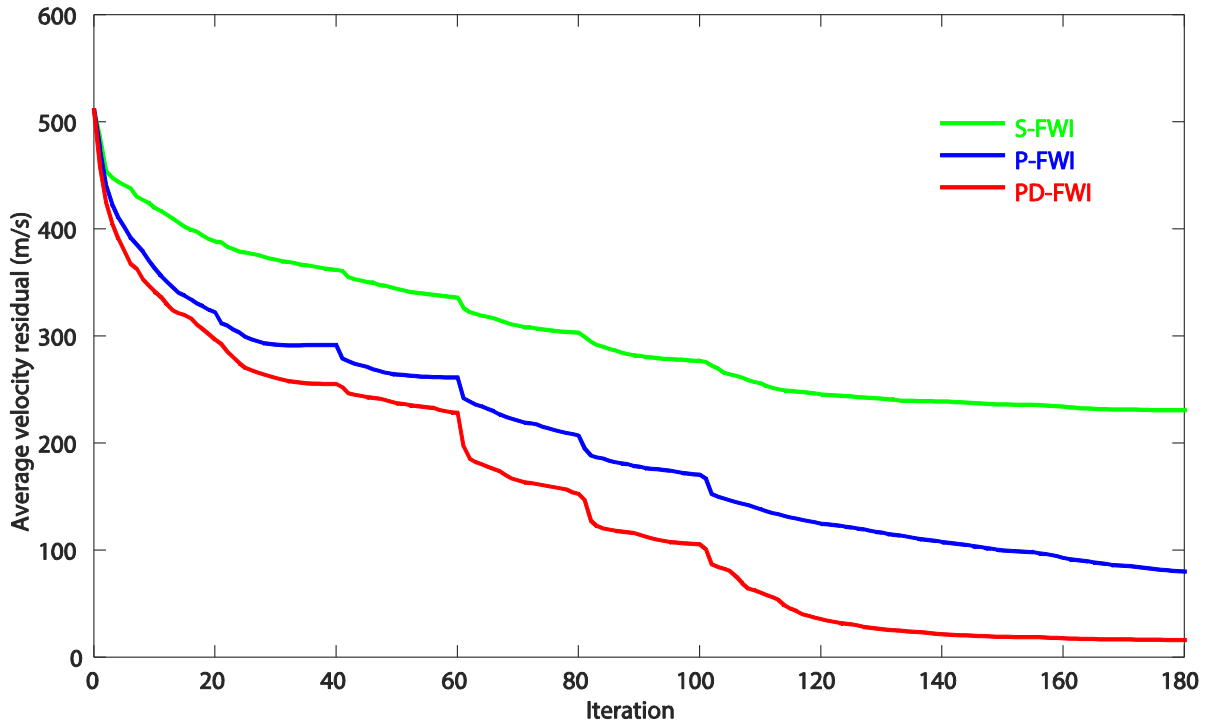


Figure 5.9. Comparison of average velocity residual between the true and inverted velocities obtained with S-FWI, P-FWI, and PD-FWI, for the SEG overthrust model.

5.4.2 Examples based on the Marmousi model

The second example uses a complicated part of the Marmousi model as the target area for inversion. The grid intervals are 25 m x 25 m. The source is a Ricker wavelet with a dominant frequency of 12 Hz (Figure 5.11). The true velocity model is in Figure 5.12a. The velocity of the water layer is 1500 m/s, and the target area for inversion starts at 500 m depth. The initial model (Figure 5.12b) is obtained by smoothing the true model by 20 iterations using the average velocity within a 21x11 (grid points) window as the velocity at the center point of that window. There are 90 sources at horizontal locations from -2900 to 6000 m. The receivers are to the right side of each source, and the offset range is from 100 to 3000 m. For the low-pass frequency filter, the selected COFs and taper window are the same as in the SEG overthrust model example in the

previous subsection. For each scale, twenty iterations are performed, followed by another 40 iterations using the unfiltered data, so the total number of iterations is 140.

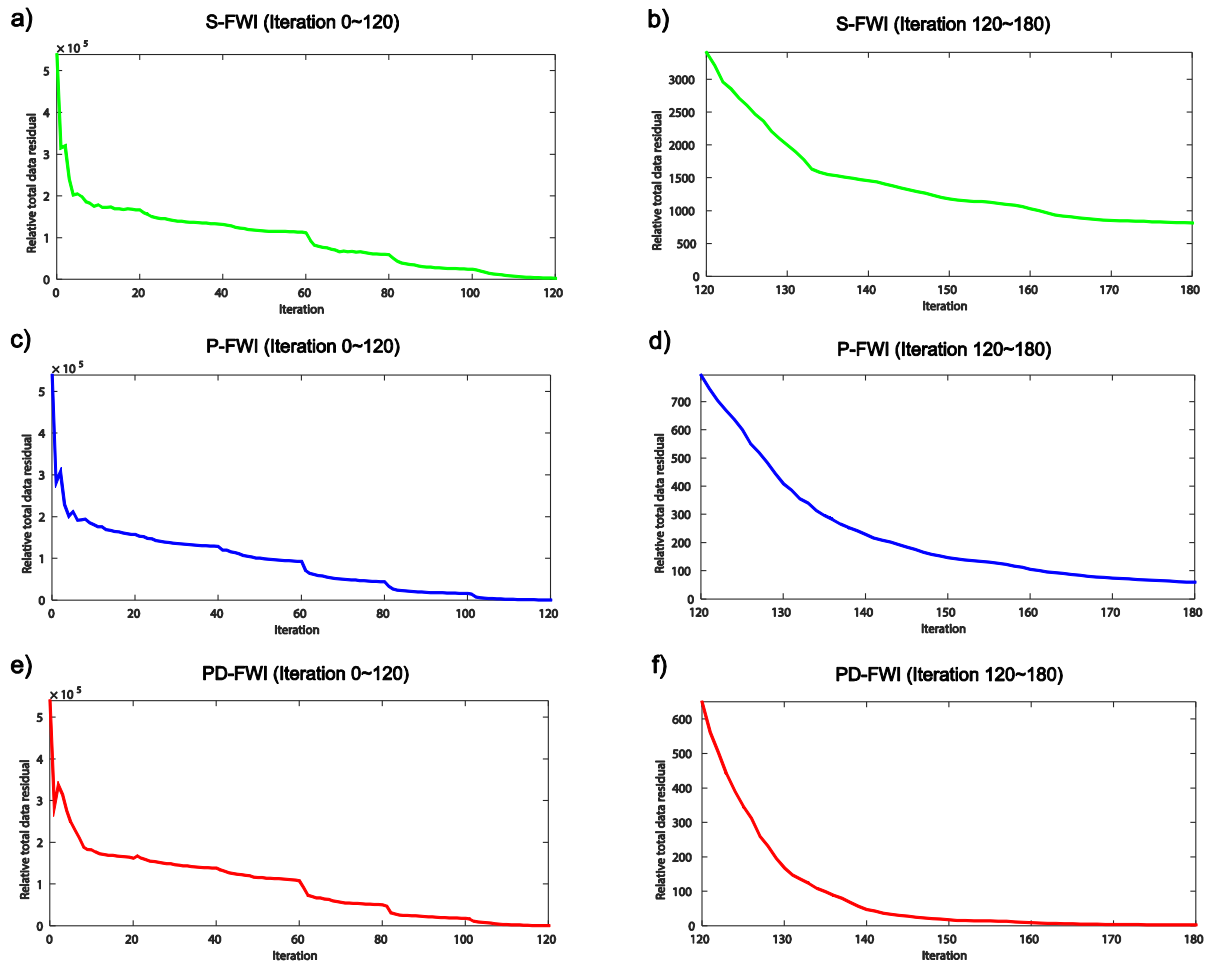


Figure 5.10. Comparison of (relative) total data residuals between predicted and observed data obtained with S-FWI (Panels a and b), P-FWI (Panels c and d), and PD-FWI (Panels e and f), for the SEG overthrust model. The total data residual is a summation of the square of the residual over every time, of every receiver, of every shot.

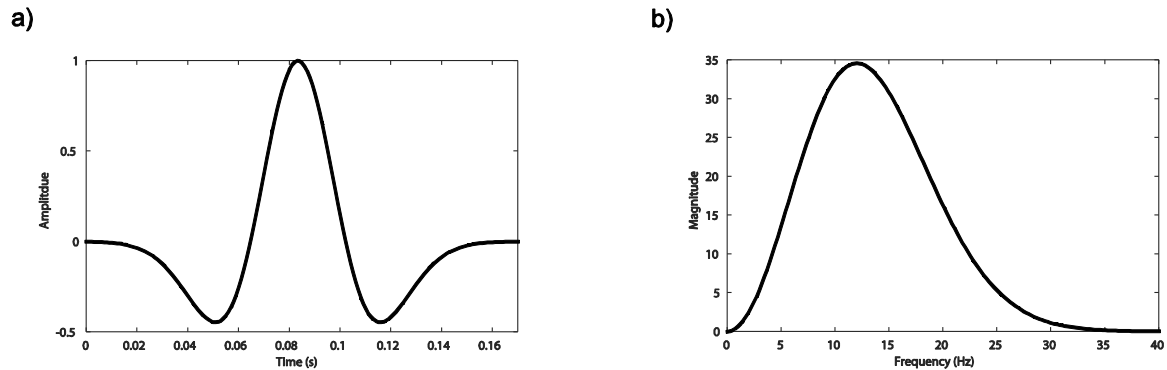


Figure 5.11. The source wavelet a) and its spectrum b) used for the Marmousi model.

The true model (Figure 5.12a) includes three layers (in red) with very high velocity contrast to the adjacent layers, which is the main challenge for this inversion. S-FWI (Figure 5.12c) fails to give an accurate inversion result including the three high-velocity layers; P-FWI (Figure 5.12d) performs better and partially recovers the high-velocity structures; PD-FWI (Figure 5.12e) gives the best result, and successfully inverts the three high-velocity layers.

The velocity profiles in Figure 5.13 provide more details for comparison. We choose the three horizontal locations 1000, 2500, and 4000 m; each of these passes through one of the three high-velocity layers (see the vertical black lines in Figure 5.12a). Figure 5.14 shows the average velocity residual for the S-FWI, P-FWI, and PD-FWI results as a function of iteration number. The comparisons in Figures 5.13 and 5.14 further quantitatively support the conclusions obtained from Figure 5.12.

5.5 Conclusions

This chapter illustrates the relation between RTM and FWI by noting that the core of gradient-based FWI is a phase transformation from the reflectivity to the velocity, and provides an improved iterative inversion algorithm based on the physical insight of the reflectivity-to-

velocity inversion. Compared with the steepest-descent FWI, the new algorithm removes the high-pass frequency filter ω^2 and compensates the velocity term. Moreover, we use a source wavelet and residual data that are both deconvolved to obtain the reflectivity-image residual. By using the deconvolution, the amplitudes within the frequency band of the spectrum are well balanced, and thus the “effective” frequency bandwidth of the wavelet is enlarged.

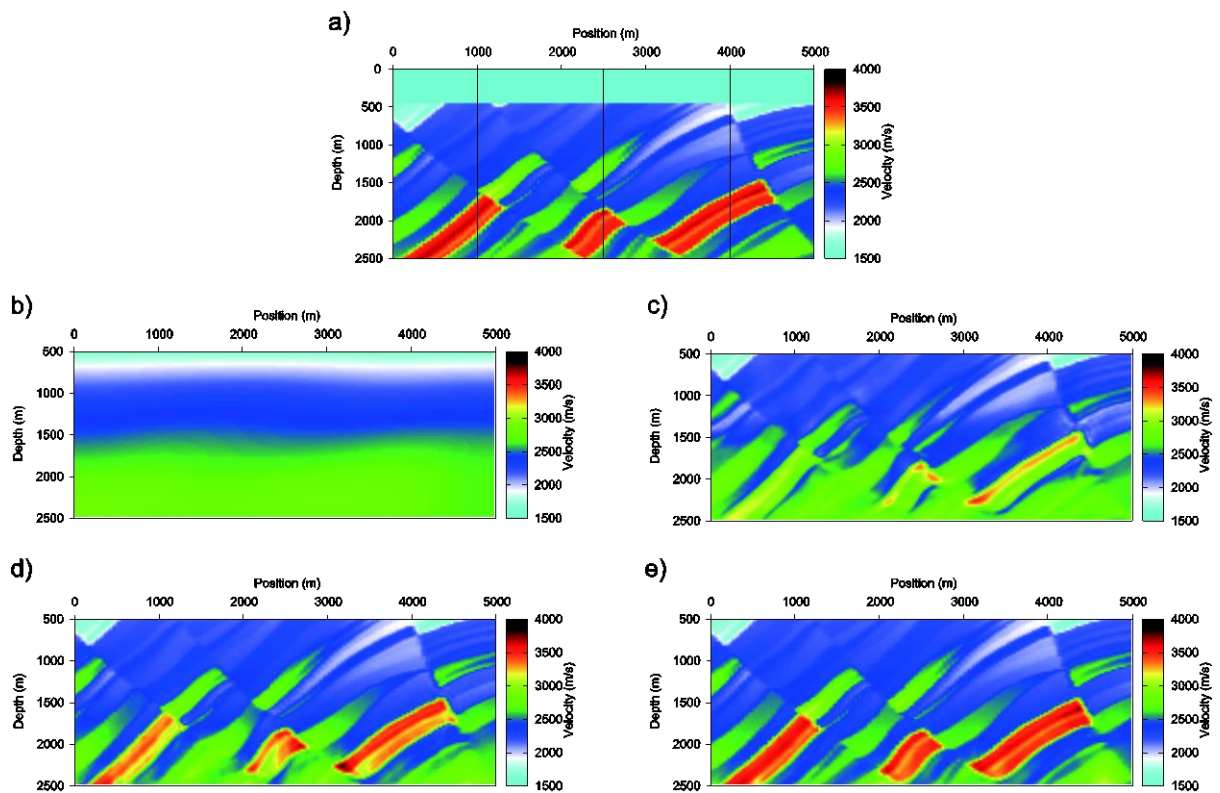


Figure 5.12. Comparison of inversion results obtained by using three methods on a complicated portion of the Marmousi model. a) The true model, b) The initial model, c) the S-FWI result, d) the P-FWI result, e) the PD-FWI result. The three black lines in a) denote the locations for the velocity profiles in Figure 5.13, which show more details for comparison.

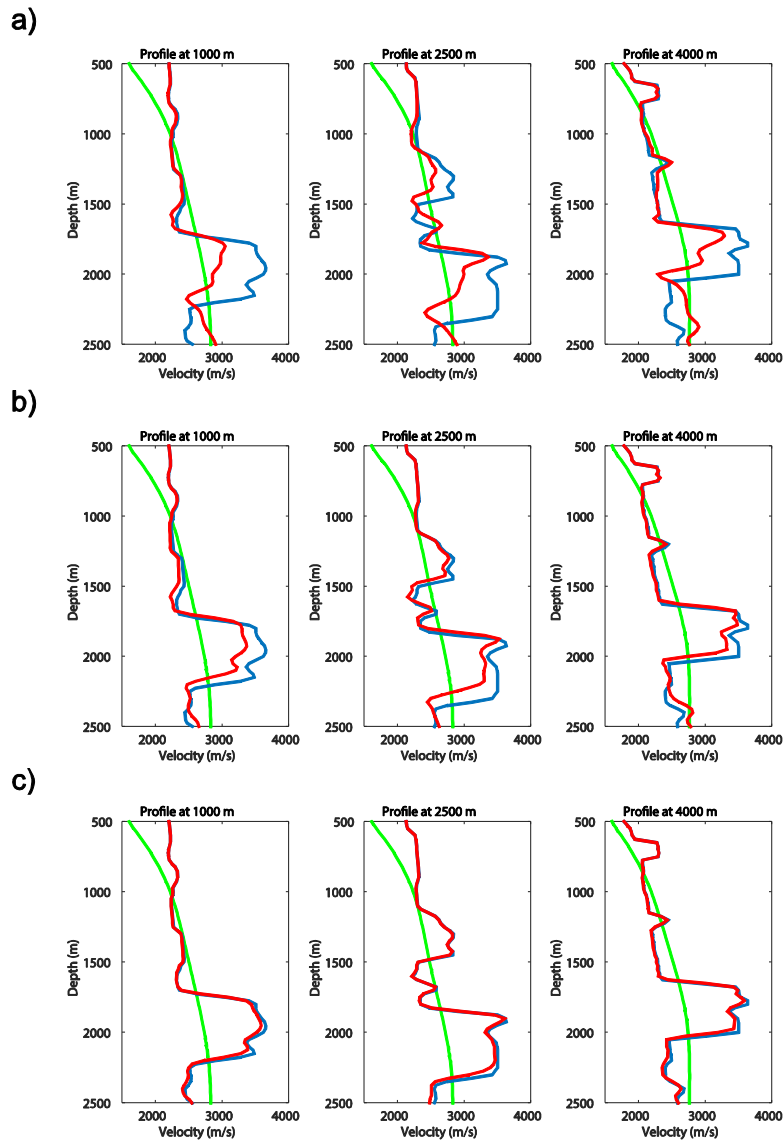


Figure 5.13. Comparison of velocity profiles obtained with S-FWI (Panel a), P-FWI (Panel b), and PD-FWI (Panel c), for the Marmousi model. The blue line is the true velocity, the green line is the initial velocity, and the red line is the inverted velocity.

In summary, the new scheme is that, the relative velocity update is a phase-modified and deconvolved RTM image obtained with the residual data, and the scale factor of this image is adjusted by a steepest-descent search. Numerical examples show this scheme can give a

significant improvement to the inverted velocity, compared with the traditional conjugate-gradient-based descent FWI.

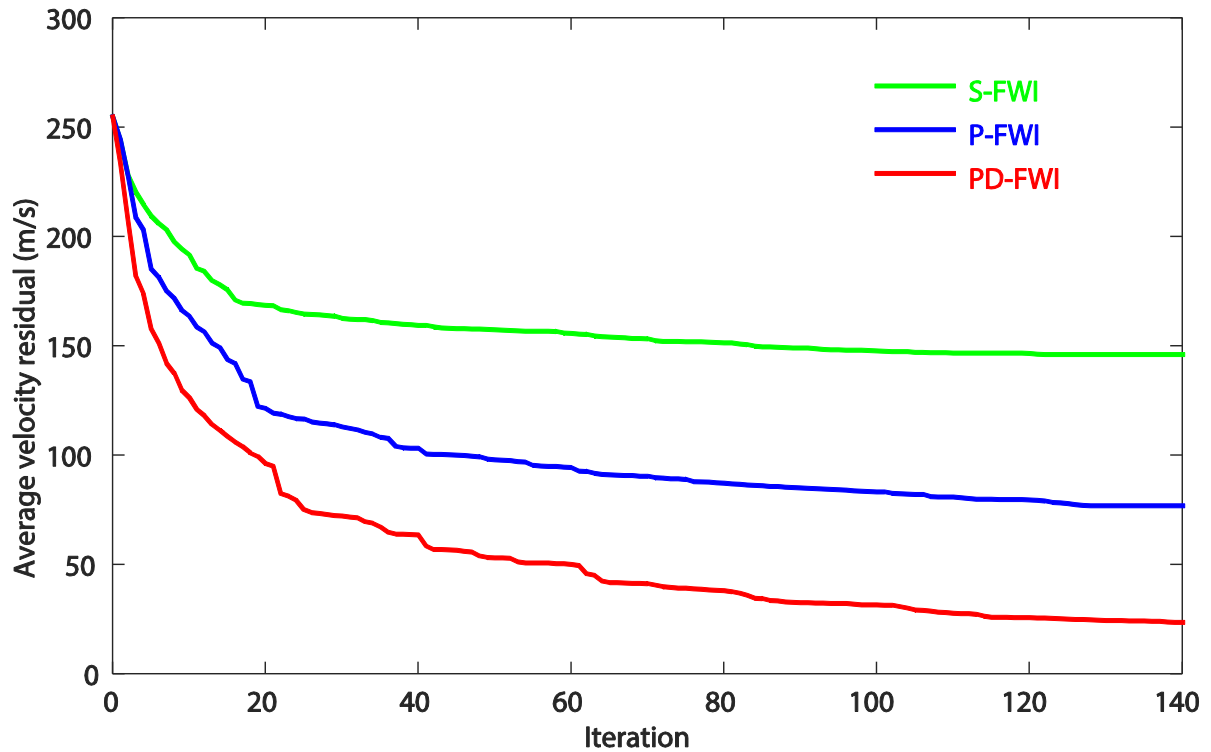


Figure 5.14. Comparison of average velocity residuals between the true and inverted velocities obtained with S-FWI, P-FWI, and PD-FWI, for the Marmousi model.

5.6 Acknowledgments

The computational resources are provided by Total USA, the Texas Advanced Computing Center (TACC) and the UT Dallas Geophysical Consortium (UTD GC). A research assistantship is provided via the financial support of the Sponsors of the UTD GC. Tang is grateful for the help of Bertrand Duquet and Fuchun Gao during his visit to Total. We also appreciate the valuable comments from Associate Editor Anatoly Baumstein, Yu Zhang, Paul Williamson and one anonymous reviewer.

5.7 Appendix 5A “Half wavelength” condition in deriving the FWI gradient”

If there is a velocity perturbation Δv , from equation 5.1, we obtain

$$\frac{1}{(v + \Delta v)^2} \frac{\partial^2 (u_s + \Delta u_s)}{\partial t^2} = \frac{\partial^2 (u_s + \Delta u_s)}{\partial \mathbf{x}^2} + \delta(\mathbf{x} - \mathbf{x}_s) F(t), \quad (5A-1)$$

where Δu_s is the resulting wavefield perturbation. If the velocity perturbation is small enough,

$$\frac{1}{(v + \Delta v)^2} = \frac{1}{v^2} - \frac{2\Delta v}{v^3} + o(\Delta v), \quad (5A-2)$$

where high-order terms $o(\Delta v)$ can be ignored. Subtracting equation 5.1 from 5A-1 gives

$$\frac{1}{v^2} \frac{\partial^2 \Delta u_s}{\partial t^2} - \frac{\partial^2 \Delta u_s}{\partial \mathbf{x}^2} = \frac{\partial^2 u_s}{\partial t^2} \frac{2\Delta v}{v^3}. \quad (5A-3)$$

For a primary reflection, equation 5.1 can be replaced by

$$u_s(\mathbf{x}_s, \mathbf{x}, \mathbf{x}_r; t) = \int_0^t dt' F(\mathbf{x}_s) G(\mathbf{x}_s, \mathbf{x}; t') R(\mathbf{x}) G(\mathbf{x}, \mathbf{x}_r; t - t'), \quad (5A-4)$$

where $u_s(\mathbf{x}_s, \mathbf{x}, \mathbf{x}_r; t)$ is the pressure field at location \mathbf{x}_r and time t in the wave path from \mathbf{x}_s to \mathbf{x} and then to \mathbf{x}_r (through time t); this equation also involves the cases of primary refraction and direct waves by setting $R(\mathbf{x}) = 1.0$. Equation 5A-4 is equivalent to a convolution form,

$$u_s(\mathbf{x}_s, \mathbf{x}, \mathbf{x}_r; t) = F_s(\mathbf{x}_s, \mathbf{x}; t) * G(\mathbf{x}, \mathbf{x}_r; t), \quad (5A-5)$$

where F_s is the source on the exploding-reflector;

$$F_s(\mathbf{x}_s, \mathbf{x}; t) = F(\mathbf{x}_s; t) G(\mathbf{x}_s, \mathbf{x}; t) R(\mathbf{x}). \quad (5A-6)$$

In the first-order Born approximation, we assume that the background model is correct and the wavefield perturbation produced by a velocity perturbation is not influenced by other velocity perturbations. Thus, the perturbation of u_s (defined as Δu_s) has a linear relationship with the perturbation of F_s (defined as ΔF_s) in equation 5A-5, which means we assume the velocity perturbation does not influence the convolution and the Green's function G in equation 5A-5. This linear assumption can be relaxed to a "half wavelength" condition for inversion of a single parameter (the velocity in the present context), because, as the inversion proceeds, the phase of Δu_s will gradually move closer to that of u_s , by updating the velocity. Thus, from equation 5A-5,

$$\Delta u_s(\mathbf{x}_s, \mathbf{x}, \mathbf{x}_r; t) = \Delta F_s(\mathbf{x}_s, \mathbf{x}; t) * G(\mathbf{x}, \mathbf{x}_r; t). \quad (5A-7)$$

Substituting 5A-3 into 5A-7 gives

$$\delta d_{cal}(\mathbf{x}_s, \mathbf{x}, \mathbf{x}_r; t) = \Delta u_s(\mathbf{x}_s, \mathbf{x}, \mathbf{x}_r; t) = \frac{2\Delta v}{v^3} \frac{\partial^2 u_s(\mathbf{x}_s, \mathbf{x}; t)}{\partial t^2} * G(\mathbf{x}, \mathbf{x}_r; t), \quad (5A-8)$$

which can be rewritten as

$$\frac{\partial d_{cal}(\mathbf{x}_s, \mathbf{x}, \mathbf{x}_r; t)}{\partial v} = \frac{2}{v^3} \frac{\partial^2 u_s(\mathbf{x}_s, \mathbf{x}; t)}{\partial t^2} * G(\mathbf{x}, \mathbf{x}_r; t). \quad (5A-9)$$

Because the observed data are independent of the estimated velocity model, the gradient of the objective function (equation 5.3) with respect to velocity is

$$\begin{aligned}
\frac{\partial C(\mathbf{x}_s, \mathbf{x}, \mathbf{x}_r; v_0)}{\partial v} &= \int dt \frac{\partial d_{cal}(\mathbf{x}_s, \mathbf{x}, \mathbf{x}_r; t)}{\partial v} \delta d(\mathbf{x}_s, \mathbf{x}, \mathbf{x}_r; t) \\
&= \int dt \left[\frac{2}{v^3} \frac{\partial^2 u_s(\mathbf{x}_s, \mathbf{x}; t)}{\partial t^2} * G(\mathbf{x}, \mathbf{x}_r; t) \right] \delta d(\mathbf{x}_s, \mathbf{x}_r; t).
\end{aligned} \tag{5A-10}$$

By using the relation,

$$\int dt [f(t) * g(t)] h(t) = \int dt f(t) [g(-t) * h(t)], \tag{5A-11}$$

equation 5A-10 becomes

$$\left. \frac{\partial C(\mathbf{x}_s, \mathbf{x}, \mathbf{x}_r; v)}{\partial v} \right|_{v=v_0} = \int dt \frac{2}{v^3} \frac{\partial^2 u_s(\mathbf{x}_s, \mathbf{x}; t)}{\partial t^2} [G(\mathbf{x}, \mathbf{x}_r; -t) * \delta d], \tag{5A-12}$$

which is equation 5.7 if we use the matrix expression $\delta \mathbf{d}$.

5.8 Appendix 5B “Derivation from equations 5.9 and 5.10 to 5.11 and 5.12”

Equations 5.9 and 5.10 in the t domain correspond to

$$\left. \frac{\partial C(v)}{\partial v} \right|_{v=v_0} = -\Re \left[\int \frac{1}{v_0^3} \omega^2 U_s(\omega, \mathbf{x}) \bar{G}_r(\omega, \mathbf{x}) d\omega \right], \tag{5B-1}$$

and

$$\begin{cases} -\frac{\omega^2}{v^2} G_r(\omega, \mathbf{x}) = \frac{\partial^2 G_r(\omega, \mathbf{x})}{\partial \mathbf{x}^2}, \\ G_r(\omega, x, y, z=0) = \frac{1}{i\omega} \delta d(\omega, x, y, \mathbf{x}_s). \end{cases} \tag{5B-2}$$

in the ω domain, respectively. Here G_r is the FT of g_r (from the t domain to the ω domain).

Defining

$$H_r(\omega, \mathbf{x}) = i\omega G_r(\omega, \mathbf{x}), \quad (5B-3)$$

and substituting it into equations 5B-1 and 5B-2 gives

$$\left. \frac{\partial C(v)}{\partial v} \right|_{v=v_0} = -\Re \left[\int \frac{1}{v_0^3} \omega^2 U_s(\omega, \mathbf{x}) \frac{\bar{H}_r(\omega, \mathbf{x})}{i\omega} d\omega \right], \quad (5B-4)$$

and

$$\begin{cases} -\frac{\omega^2}{v^2} \frac{H_r(\omega, \mathbf{x})}{i\omega} = \frac{\partial^2 \left[\frac{H_r(\omega, \mathbf{x})}{i\omega} \right]}{\partial \mathbf{x}^2}, \\ \frac{H_r(\omega, x, y, z=0)}{i\omega} = \frac{1}{i\omega} \delta d(\omega, x, y, \mathbf{x}_s). \end{cases} \quad (5B-5)$$

Equations 5B-4 and 5B-5 can be simplified to

$$\left. \frac{\partial C(\mathbf{x}, v)}{\partial v} \right|_{v=v_0} = \Re \left[\int \frac{1}{v_0^3} i\omega U_s(\omega, \mathbf{x}) \bar{H}_r(\omega, \mathbf{x}) d\omega \right], \quad (5B-6)$$

and

$$\begin{cases} -\frac{\omega^2}{v^2} H_r(\omega, \mathbf{x}) = \frac{\partial^2 H_r(\omega, \mathbf{x})}{\partial \mathbf{x}^2}, \\ H_r(\omega, x, y, z=0) = \delta d(\omega, x, y, \mathbf{x}_s). \end{cases} \quad (5B-7)$$

Equation 5B-6 is equation 5.11, and equation 5B-7 (in the ω domain) is equivalent to equation 5.12 (in the t domain).

5.9 Appendix 5C “Relation between $|k_i|$ and $|\mathbf{k}_{ref}|$ ”

In equation 5.17, the Δx_i is defined as a small unit interval in the reflector normal direction, and thus

$$\Delta x_i = \Delta x_x = \Delta x_y = \Delta x_z. \quad (5C-1)$$

Because

$$(\Delta v_i)^2 = (\Delta v_x)^2 + (\Delta v_y)^2 + (\Delta v_z)^2, \quad (5C-2)$$

we obtain

$$\left(\frac{\Delta v_i}{\Delta x_i}\right)^2 = \left(\frac{\Delta v_x}{\Delta x_x}\right)^2 + \left(\frac{\Delta v_y}{\Delta x_y}\right)^2 + \left(\frac{\Delta v_z}{\Delta x_z}\right)^2, \quad (5C-3)$$

which can be approximated by

$$k_i^2 = k_{ref-x}^2 + k_{ref-y}^2 + k_{ref-z}^2 = |\mathbf{k}_{ref}|^2, \quad (5C-4)$$

in the \mathbf{k} domain. Equation 5C-4 gives

$$k_i = |\mathbf{k}_{ref}|, \quad (5C-5)$$

which is the first part of equation 5.21.

5.10 Appendix 5D “The relationship between the true reflectivity and the angle-dependent reflectivities”

The relation between the true reflectivity R and the angle-dependent reflectivity $R'(\theta)$ is defined by the Zoeppritz equations; an important linear approximation of the Zoeppritz equations in elastic media is the Aki-Richards equations (Aki and Richards, 1980). In acoustic media, considering only the PP image and ignoring the terms involving S-velocity, the Aki-Richards equations are simplified to a single equation

$$\frac{1}{2 \cos^2 \theta} \frac{\Delta v}{v} + \frac{1}{2} \frac{\Delta \rho}{\rho} = R'(\theta), \quad (5D-1)$$

where Δv and $\Delta \rho$ are differences of the velocity and density between the two adjacent layers that constitute the reflector. Because only velocity inversion is considered in this chapter, equation 5D-1 is simplified to

$$R = \frac{\Delta v}{2v} = R'(\theta) \cos^2 \theta. \quad (5D-2)$$

In equation 5D-2, for each reflection angle θ , there is a reflection coefficient $R'(\theta)$ and thus there is a solution for R . We approximate R by using a least-squares estimation from the overdetermined system (equation 5D-2), which is

$$R = \frac{1}{N} \int R'(\theta) \cos^2 \theta d\theta, \quad (5D-3)$$

where N is the number of equations in the system (5D-2). The N^{-1} can be included in a scale factor μ . Although the Aki-Richards approximation has limitations as it requires small velocity

contrasts and small reflection angles (say, up to 35° or so), the FWI is an iterative process and the velocity is inverted gradually as iterations proceed, and thus we can use this approximation in the derivation.

5.11 Appendix 5E “Using the reflectivity-image residual as the objective function”

The objective function using the reflectivity-image residual R_{res} is

$$l = R_{res}^T R_{res} = (R_{cal} - R_{obs})^T (R_{cal} - R_{obs}), \quad (5E-1)$$

where R_{cal} and R_{obs} are the reflectivity images obtained by using predicted and observed data to calculate the U_r in equation 5.23, respectively. The velocity update is

$$\Delta v = -\frac{1}{2} H^{-1} J = -\frac{1}{2} \left(\frac{\partial^2 l}{\partial v^2} \right)^{-1} \frac{dl}{dv}, \quad (5E-2)$$

where H is the Hessian and J is the Jacobian derivative. Because R_{obs} is independent of the migration velocity, we obtain

$$J = \frac{dl}{dv} = 2R_{res} \frac{d(R_{cal} - R_{obs})}{dv} = 2R_{res} \frac{dR_{cal}}{dv}. \quad (5E-3)$$

Because of equations 5.20 and 5.29, if we use the “half-wavelength condition” from equation 5.30 to 5.31, we obtain

$$\frac{dR_{cal}}{dv} = -A \frac{i\omega}{v_a v_0}, \quad (5E-4)$$

and thus

$$J = -2A \frac{i\omega}{v_a v_0} R_{res}. \quad (5E-5)$$

Substituting equation 5E-5 into 5E-2 gives

$$\Delta v = \mu H^{-1} \frac{R_{res} i\omega}{v_a v_0}, \quad (5E-6)$$

where μ is the step length (the A in equation 5E-5 is included in μ). The RVI-based FWI (equation 5.33) can be explained as using geophysical insight to give a preconditioned gradient (involving an approximation and simplification of H^{-1}) for inversion.

5.12 Appendix 5F “A transformation of Qin et al.’s (2015) formula”

Considering only the real-valued velocity in acoustic media, the inversion formula given by Qin et al. (2015) is

$$\delta v = \mu v_0^3 \Re \left(\int \frac{i}{\omega^3} \frac{\frac{\partial H_r}{\partial \mathbf{x}} \frac{\partial \bar{U}_s}{\partial \mathbf{x}} + H_r \frac{\partial^2 \bar{U}_s}{\partial \mathbf{x}^2}}{U_s \bar{U}_s} d\omega \right), \quad (5F-1)$$

which can be reformulated as

$$\delta v = -\mu v_0^3 \Re \left\{ \int \frac{i}{\omega^3} \frac{F^{-1}[\mathbf{k}_s \mathbf{k}_r F(\bar{U}_s H_r)] + F^{-1}[\mathbf{k}_s^2 F(\bar{U}_s H_r)]}{U_s \bar{U}_s} d\omega \right\}, \quad (5F-2)$$

in the \mathbf{k} domain. Here \mathbf{k}_s and \mathbf{k}_r are the (local) wavenumbers of the source and residual wavefields, respectively; the meanings of F and F^{-1} are defined in equation 5.26. When the source wavelet is well estimated,

$$|\mathbf{k}_s| = |\mathbf{k}_r| = |\mathbf{k}|, \quad (5F-3)$$

and thus equation 5F-2 can be written as

$$\delta v = -\mu v_0^3 \Re \left\{ \int \frac{i}{\omega^3} \frac{F^{-1} \left[2\mathbf{k}^2 \cos^2 \gamma F(H_r) \right]}{U_s} d\omega \right\}, \quad (5F-4)$$

where γ is the open angle between \mathbf{k}_s and \mathbf{k}_r . If we ignore the $\cos^2 \gamma$ and include the ‘2’ in the step length μ ; equation 5F-4 can be written as

$$\delta v = \mu v_0 \Re \left\{ \int F^{-1} \left[\left(\frac{v_0^2 \mathbf{k}^2}{\omega^2} \right) F \left(\frac{1}{i\omega} \frac{H_r}{U_s} \right) \right] d\omega \right\}. \quad (5F-5)$$

Because of equation 5.27, equation 5F-5 becomes

$$\delta v = \mu v_0 \Re \left(\int \frac{1}{i\omega} \frac{H_r}{U_s} d\omega \right). \quad (5F-6)$$

Because $\frac{1}{i\omega}$ can be replaced by using a time integration of the residual data (equation 5.10),

equation 5F-6 becomes

$$\frac{\delta v}{v_0} = \mu \Re \left(\int \frac{G_r}{U_s} d\omega \right), \quad (5F-7)$$

which is equation 5.34.

A comparison of the results using equations 5.34 and 5.37 is shown in Figure 5.15. In Section 5.4 “Examples”, the PD-FWI corresponds to equation 5.37. In Figure 5.15, because both the two FWI algorithms use phase-modified and deconvolved RTM images, we define the one

that uses the deconvolution imaging condition (equation 5.34) as PD-FWI-DIC and define the one that uses the cross-correlation imaging condition (equation 5.37) as PD-FWI-CIC. Both of them use the HS-DY algorithm defined by equations 5.39-5.42 (which use equation 5.37 as an example for the definition). The PD-FWI-CIC here is the PD-FWI in Section 5.4 “Examples”, and Figure 5.15b is Figure 5.7c.

Figure 5.15b is slightly better than Figure 5.15a because equation 5.37 is more stable than equation 5.34 in implementation. Equation 5.34 requires a damping threshold value as the iteration proceeds, because of the instability of the denominator (note, the implementation of equation 5.34 uses its equivalent form in the first part of equation 5.35); equation 5.37 has a fixed threshold value in the wavelet deconvolution because the zero-phase source wavelet is stable.

5.13 Appendix 5G “A comparison with the spectral shaping method”

The spectral shaping method is proposed by Lazaratos et al. (2011) and Plessix and Li (2013). Plessix and Li (2013) apply a spectral filter

$$f_d = \frac{\omega^{-\beta/2}}{S(\omega)}, \quad (5G-1)$$

to the observed data, where β is a coefficient and $S(\omega)$ is defined in equation 5.35. Equation 5G-1 includes a deconvolution operator $S^{-1}(\omega)$ and a spectral shaping operator $\omega^{-\beta/2}$ to compensate for the propagation effect. The goal of this method is to make the spectrum of the gradient more similar to that of a desired update. Substituting equation 5G-1 into the FWI gradient (equation 5.13 in the ω domain) gives

$$\left. \frac{\partial C(v)}{\partial v} \right|_{v=v_0} = \frac{2}{v_0^3} \Re \left\{ \int \omega^2 U_s(\omega) \left[\frac{\omega^{-\beta/2}}{S(\omega)} \bar{G}_r(\omega) \right] d\omega \right\}. \quad (5G-2)$$

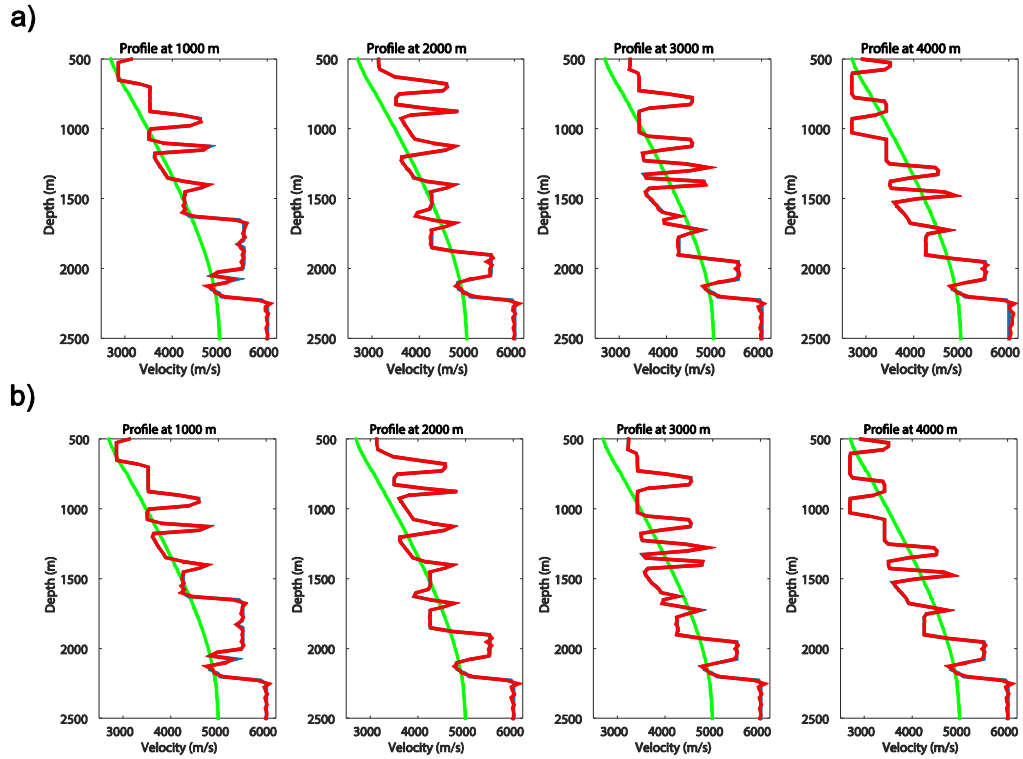


Figure 5.15. Inverted velocity profiles obtained by using a) PD-FWI-DIC and b) PD-FWI-CIC on a complicated portion of the SEG overthrust model (Figure 5.6a). The blue line is the true velocity, the green line is the initial velocity, and the red line is the inverted velocity.

Compared to our inversion formula (equation 5.37),

1. Equation 5G-2 includes only one deconvolution term for the residual data; while equation 5.37 requires deconvolutions for both the source wavelet and residual data, to obtain a deconvolved residual image.

2. Equation 5G-2 does not compensate the velocity term v_0^{-3} in the FWI gradient; while equation 5.37 compensates it by v_0^4 , which gives a velocity term v_0 .
3. In equation 5G-2, the β can be either adaptive or fixed during the inversion; Plessix and Li (2013) suggest using $\beta = 2$ for 2D acquisition.

The spectral shaping method is not a preconditioned inverse Hessian; it still requires solving the inverse Hessian matrix to compensate the velocity and frequency terms (Plessix and Li, 2013). If the inverse Hessian can be well estimated, we may not need a spectral shaping.

CHAPTER 6

**FROM CLASSICAL REFLECTIVITY-TO-IMPEDANCE INVERSION TO FULL
WAVEFORM IMPEDANCE INVERSION USING PHASE-MODIFIED,
DECONVOLVED REVERSE-TIME-MIGRATION IMAGES
AND ROCK-PHYSICS INFORMATION***

6.1 Summary

Full waveform inversion (FWI) is based on a strongly approximate solution of a mathematical problem. To connect it with physical concepts, previously we used the classical reflectivity-to-velocity inversion to derive an FWI formula, which suggests that the relative velocity update is a phase-modified and deconvolved reverse-time-migration (RTM) image using the residual data. In this chapter, we extend this method from P-velocity inversion into P-impedance inversion. During the extension, a difficult point is that the P-impedance is a product of P-velocity and density; updates of the two parameters have a trade-off during the inversion process. In our system, solving this trade-off is similar to an amplitude-versus-angle (AVA) inversion. However, the accurate AVA information is hard to obtain in practice; the AVA inversion also requires the angle-domain common-image gathers (ADCIGs) to be (nearly) flat, which poses a much stricter constraint on the accuracy of the background P-velocity than the half-wavelength condition for single-parameter (P-velocity) FWI. To proceed, we combine our formula with rock physics constraints by which the relation between the P-velocity and density

* Tang C. and G. A. McMechan, 2017, From classical reflectivity-to-impedance inversion to full waveform impedance inversion using phase-modified, deconvolved reverse-time-migration image and rock-physics information: 87th International Meeting, SEG, Houston, 1578-1582. Copyrighted by Society of Exploration Geophysicists. Permalink: <https://doi.org/10.1190/segam2017-17791370.1>

can be approximated. Thus, we can invert only the P-impedance and use it to estimate the P-velocity and density in each iteration. So, we convert the multi-parameter inversion (P-velocity and density) into single-parameter inversion (P-impedance). Extension of this method into elastic media is also given. In the real world, the rock-physics relationship is complicated, probabilistic and condition-dependent; we suggest addressing this via Machine Learning, by building and progressively modifying a database of statistical multi-parameter (P and S velocities, density, attenuation, etc.) relations that can be navigated with a search engine (e.g., like Google) to dynamically determine (e.g., non-linear interpolation) the solution with the highest probability and its nonuniqueness. This implies a major, multi-year effort. A stable amplitude-preserved RTM formula is also given as an approximation to the deconvolution imaging condition.

6.2 Introduction

Classical full waveform inversion (FWI) (e.g., Tarantola, 1984) defines a mathematical problem to minimize an L2 norm of the residual data. The mathematical complexity of the problem forces ignorance of several terms during the derivation. To relate the FWI process with physical concepts, Tang and McMechan (2017b) [see Chapter 5] use a classical reflectivity-to-velocity inversion to derive an improved FWI formula. In this Chapter, we extend this method into P-impedance inversion in acoustic media. Most of the references have been given in Chapter 5. We will mention some references (e.g., Zhang et al., 2014; Qin and Lambaré, 2016; Duan and Sava, 2016) as we explain the theory.

During the extension, the inversion involves two parameters (P-velocity and density); separation of the trade-off between them requires high-accuracy amplitude versus (reflection)

angle (AVA) information and flat angle-domain common-image gathers (ADCIGs) with consistent wavenumber along the angle axis. Both of them are hard to obtain for a practical FWI; particularly the latter requirement means the half-wavelength condition of single-parameter FWI does not work for multi-parameter inversion. To proceed, we propose to use rock physics information to obtain the density from the P-velocity. Then the multi-parameter inversion is converted into a single-parameter inversion. We also give the extension of this method to elastic media.

6.3 Full waveform impedance inversion

In acoustic media, the relation between the true reflectivity (that is independent of the reflection angle) and the impedance is defined as below (used by, e.g., Peterson et al. [1955]),

$$R = \frac{I_2 - I_1}{I_1 + I_2} = \frac{\Delta I}{2I_a} = \frac{\rho_2 v_2 - \rho_1 v_1}{\rho_1 v_1 + \rho_2 v_2}, \quad (6.1)$$

where R is the PP reflectivity (at normal incidence); I_1 and I_2 are P-impedances of the upper and lower layers; ΔI is the impedance contrast and I_a is the average impedance; v is the P-velocity and ρ is the density. Using the same definition of Fourier transforms (FTs) as Tang and McMechan (2017a) (Chapter 5), equation 6.1 can be reformed approximately as

$$R = \frac{\Delta x_i}{2} \frac{1}{I_a} \frac{\Delta I}{\Delta x_i} = A \frac{1}{I_a} \frac{dI}{dx_i} = -A \frac{1}{I_a} ik_i I, \quad (6.2)$$

where the Δx_i and k_i are a small unit interval and the wavenumber in the reflector-normal direction, respectively; A is a scale value. We can rewrite equation 6.2 as

$$\frac{I}{I_a} = -\frac{1}{A} \frac{R}{ik_i}, \quad (6.3)$$

where R can be approximately obtained from the amplitude-preserved (AP) reverse time migration (RTM) (Tang and McMechan, 2017b)

$$R(\mathbf{x}) = \mu \int R'(\mathbf{x}, \theta) \cos^2 \theta d\theta = \mu \Re \left[\iint \frac{U_r(\mathbf{x}, \omega, \theta)}{U_s(\mathbf{x}, \omega, \theta)} \cos^2 \theta d\omega d\theta \right], \quad (6.4)$$

where μ is a scale factor, \Re means taking the real part, θ is the reflection angle, R' is the angle-dependent reflectivity, and U_s and U_r are the FTs of source wavefield u_s and receiver wavefield u_r , which are obtained by using the observed data directly as the boundary condition,

$$\begin{cases} \frac{\partial^2 u_r(t, \mathbf{x})}{\partial t^2} - \rho v^2 \frac{\partial}{\partial \mathbf{x}} \left[\frac{1}{\rho} \frac{\partial u_r(t, \mathbf{x})}{\partial \mathbf{x}} \right] = 0, \\ u_r(t, x, y, z=0) = d_{obs}(t, x, y, \mathbf{x}_s), \end{cases} \quad (6.5)$$

where d_{obs} is the observed data, \mathbf{x}_s is the source location, and t is the time. Inserting equation 6.4 into equation 6.3 gives

$$\frac{I}{I_a} = -\mu \Re \left\langle \iint F^{-1} \left\{ \frac{1}{ik_i} F \left[\frac{U_r(\mathbf{x}, \omega, \theta)}{U_s(\mathbf{x}, \omega, \theta)} \cos^2 \theta \right] \right\} d\omega d\theta \right\rangle, \quad (6.6)$$

where F is a forward FT from the \mathbf{x} to the \mathbf{k} domain; A^{-1} is included in μ . Based on a half-wavelength assumption (Tang and McMechan, 2017b), we can obtain

$$\frac{\delta I}{I_a} = \mu \Re \left\langle \iint \frac{v_0}{i\omega} \frac{H_r(\mathbf{x}, \omega, \theta)}{U_s(\mathbf{x}, \omega, \theta)} \cos^2 \theta d\omega d\theta \right\rangle. \quad (6.7)$$

where δI is the impedance update and H_r is an FT of h_r that is obtained by using the residual data (calculated data minus observed data) directly as the boundary condition of equation 6.5.

Equation 6.7 can be written as

$$\frac{\delta I}{I_a} = \mu v_0 \Re \left[\iint \frac{G_r(\mathbf{x}, \omega, \theta)}{U_s(\mathbf{x}, \omega, \theta)} \cos^2 \theta d\omega d\theta \right], \quad (6.8)$$

where G_r is the FT of g_r that is obtained using

$$\begin{cases} \frac{\partial^2 g_r(t, \mathbf{x})}{\partial t^2} - \rho v^2 \frac{\partial}{\partial \mathbf{x}} \left[\frac{1}{\rho} \frac{\partial g_r(t, \mathbf{x})}{\partial \mathbf{x}} \right] = 0, \\ g_r(t, x, y, z=0) = \int_t^T \delta d(t', x, y, \mathbf{x}_s) dt'. \end{cases} \quad (6.9)$$

6.4 From impedance to velocity and density

Equation 6.8 is a full waveform impedance inversion, but equation 6.9 requires P-velocity and density for wavefield extrapolation. Based on the Aki and Richards (1980) equation, we can separate the P-impedance update in equation 6.8 into

$$\frac{\delta v}{v_a} + \cos^2 \theta \frac{\delta \rho}{\rho_a} = \mu v_0 \Re \left[\int \frac{G_r(\mathbf{x}, \omega, \theta)}{U_s(\mathbf{x}, \omega, \theta)} \cos^2 \theta d\omega \right], \quad (6.10)$$

which has similarity with the formulas of Zhang et al. (2014) and Qin and Lambaré (2016). Solving $\delta v/v_a$ and $\delta \rho/\rho_a$ requires a least-squares solution to satisfy the AVA. However, implementation of equation 6.10 is very difficult at the current stage, because

- (I). Equation 6.10 requires high accuracy of the AVA information. However, the deconvolution imaging condition is often not stable in practice; this imaging condition assumes a single

reflection at each grid point for one sources, but the image in practice contains multipaths and is also often stacked over several sources. In a complicated structure, each image point often does not have a balanced illumination at each angle.

(II). Stable least-squares estimation from equation 6.10 requires the ADCIGs to be flat. This means we may need the velocity above the reflection image to be correct, which results in a correct image location. Thus, the half-wavelength condition does not work for the multi-parameter inversion in equation 6.10, because, if the ADCIGs are not flat, the least-squares estimation is difficult to be stable.

(III). The Aki-Richards equation is a linear approximation of Zoeppritz equations and works only for small angles (say, up to 35°).

So it is difficult to implement equation 6.10 at the current stage, but the real world does involve more parameters than V_p . To proceed, we propose to use rock physics information to convert the P-impedance (in equation 6.8) into P-velocity and density. For example, Gardner et al. (1974) propose that the P-velocity and density have the following relation,

$$\rho = 310V_p^{0.25}, \quad (6.11)$$

where the unit of V_p is m/s and the unit of ρ is kg/m³. The V_p here is the v in equations 6.1~6.10.

Based on equation 6.11, we have

$$V_p = (I_p/310)^{0.8}. \quad (6.12)$$

In the real world, the relation between V_p and ρ is certainly much more complicated than Gardner's relation. The rock-physics relationship between V_p and ρ is strongly non-linear and

probabilistic. It also depends on different geological conditions such as lithology, pressure, porosity, and so on. With the development of the computer science, one way to address this is via Machine learning, by building and progressively modifying a large database of statistical multi-parameter (V_p , V_s , ρ , attenuation, etc.) relations that can be navigated with a fast search engine (e.g., like Google) to dynamically determine (e.g., non-linear interpolation) the solution with the highest probability and its nonuniqueness, which also has the potential for defining uncertainty (or risk) in using the FWI result for subsequent interpretation. The significance of this approach is using rock-physics relationships to reduce the multi parameters (e.g., V_p , V_s , ρ) to a single one (e.g. I_p) for inversion, in which the half-wavelength criterion can be applied. Establishing this database and search engine is beyond the scope of the present study, as it implies a major, multi-year effort. In the example section below, we assume that the constraint defined by equation 6.11 is accurate, and show the results of combining this with an approximate implementation of equation 6.8. A different approach of using a physical constraint is to include it in the objective function of P- and S-velocity tomography, as shown by Duan and Sava (2016).

6.5 A practical implementation for AP-RTM

The FWI implementation in equation 6.8 requires a deconvolution imaging condition and calculation of reflection angles. As explained in section 6.4, the angle-dependent deconvolution imaging condition involves several assumptions which are hard to satisfy in FWI. To simplify the implementation, we ignore the angle dependence and involve the $\cos^2 \theta$ in the global scale μ , and thus equation 6.4 is simplified to

$$R(\mathbf{x}) = \mu \int \frac{U_r(\mathbf{x}, \omega)}{U_s(\mathbf{x}, \omega)} d\omega = \mu \mathfrak{R} \left[\int \frac{U_s(\mathbf{x}, \omega) \bar{U}_r(\mathbf{x}, \omega)}{U_s^2(\mathbf{x}, \omega)} d\omega \right], \quad (6.13)$$

The U_s or U_s^2 in the denominator still cause an instability, especially when the velocity is incorrect, an image point with a large U_r may not have a large U_s and then the instability occurs. To stabilize it, we propose a practical scheme below. The first step is to rewrite equation 6.13 as (Tang and McMechan, 2017b)

$$R(\mathbf{x}) = \mu \mathfrak{R} \left[\int \frac{U_s(\mathbf{x}, \omega) \bar{U}_r(\mathbf{x}, \omega)}{S^2(\mathbf{x}_s, \omega)} [G(\mathbf{x}_s, \mathbf{x}, \omega)]^{-2} d\omega \right], \quad (6.14)$$

where the S is the source wavelet and $G(\mathbf{x}_s, \mathbf{x}, \omega)$ is the Green's function from \mathbf{x}_s to \mathbf{x} . Equation 6.14 involves two parts; one is the convolution imaging condition with source wavelet deconvolution and the other is the spreading loss compensation (Tang and McMechan, 2017b). Assuming the source wavelet is known, the instability issue focuses mainly on the second part (the spreading loss compensation). To stabilize equation 6.14, we use an approximate formula,

$$R(\mathbf{x}) = \mu \mathfrak{R} \left\{ \frac{\int [U_s(\mathbf{x}, \omega) \bar{U}_r(\mathbf{x}, \omega) / S^2(\omega)] d\omega}{\int [U_s^2(\mathbf{x}, \omega) / S^2(\omega)] d\omega} \right\}, \quad (6.15)$$

where the denominator is an approximation of the spreading loss $[G(\mathbf{x}_s, \mathbf{x}, \omega)]^2$. Equation 6.15 is equivalent to

$$R(\mathbf{x}) = \mu \frac{\int \hat{u}_s(\mathbf{x}, t) \hat{u}_r(\mathbf{x}, t) dt}{\int |\hat{u}_s(\mathbf{x}, t)|^2 dt}, \quad (6.16)$$

which is similar to the source-normalized cross-correlation imaging condition (e.g., Kaelin and Guitton, 2006) but it uses the deconvolved source and receiver wavefields (\hat{u}_s and \hat{u}_r ; the $\hat{}$ means ‘deconvolved’). In complicated media, it is possible that an image point is not illuminated by a particular source. Therefore, to increase the stability of equation 6.16, we use

$$R(\mathbf{x}) = \mu \frac{\int \hat{u}_s(\mathbf{x}, t) \hat{u}_r(\mathbf{x}, t) dt}{\int |\hat{u}_s(\mathbf{x}, t)|^2 dt + \varepsilon^2 A}, \quad (6.17)$$

for each source, which ε^2 is a small positive value and A can be, e.g., an average or a maximum value of $\int |\hat{u}_s(\mathbf{x}, t)|^2 dt$ in the global space. The cross-correlation in the numerator involves backscattering artifacts, which can be removed by using a wave decomposition plus angle-filter imaging condition (Tang and McMechan, 2017c),

$$R(\mathbf{x}) = \mu \frac{\int \sum_{i=0, j=0}^{M-1, N-1} F(\theta) \delta(i-j) \hat{u}_{s,i}(\mathbf{x}, t) \hat{u}_{r,j}(\mathbf{x}, t) dt}{\int |\hat{u}_s(\mathbf{x}, t)|^2 dt + \varepsilon^2 A}, \quad (6.18)$$

where i and j are the reference numbers of the decomposed source and receiver wavefields, respectively; $F(\theta)$ is an (reflection or open) angle filter.

However, in FWI, removing the backscattering and tomographic signal may not be necessary; see the discussion of Section 5.3.2. Thus, based on the process from equation 6.4 to equation 6.17, equation 6.8 becomes

$$\frac{\delta I}{I_a} = \mu \frac{v_0 \int \hat{u}_s(\mathbf{x}, t) \hat{g}_r(\mathbf{x}, t) dt}{\int |\hat{u}_s(\mathbf{x}, t)|^2 dt + \varepsilon^2 A}. \quad (6.19)$$

The I_a is difficult to obtain; it can be approximated by using I_0 or the global average of the I_0 . The latter is used in our implementation, in which I_a can be included in the scale factor μ . If we ignore the spreading loss compensation, equation 6.19 becomes

$$\frac{\delta I}{I_a} = \mu v_0 \int \hat{u}_s(\mathbf{x}, t) \hat{g}_r(\mathbf{x}, t) dt, \quad (6.20)$$

which enhances the magnitude for short wave paths from the source. This generally gives priority to the shallow parts and the near-offset data. The proposed scheme can also be combined with some algorithms, such as adaptive matching (e.g., Zhu and Fomel, 2016) and/or layer stripping (e.g., Masoni et al. 2016), to relax the half-wavelength condition. The layer stripping can be applied to either the residual data (in time) or the image (in depth), which often requires a tapering function at cut-off boundaries to avoid artifacts.

6.6 Examples

Here we provide a 2D example using a complicated portion of the SEG overthrust model. The true I_p model is obtained using the density in equation 6.11; see Figure 6.1a. To remove the effect of the direct wave, we add a constant layer (2500 m/s) at the top and so the target region is below 500 m depth. The initial I_p model is in Figure 6.1b. There are 200 sources from 40 to 4000 m; each source corresponds to 401 receivers with a migration aperture from -2000 to 2000 m. Some algorithms (nonlinear conjugate, step-length searching and multi-scale scheme) are applied to improve equations 6.19 and 6.20; refer to the paper of Tang and McMechan (2017a) for details. Thus, when we mention using equation 6.19 or 6.20 below (including the figure captions), we actually mean using the corresponding equation as the core of the FWI

implementation. We use 20 iterations for each of five tapering windows with central frequencies (4, 6, 8, 12 and 16 Hz) with a width of 4Hz, and finally run another 80 iterations using the unfiltered data. So, the total iteration number is 180. To maintain stability of the finite-difference extrapolation, we set a maximum value for the I_p , which corresponds to the P-velocity at 7000 m/s. Moreover, the I_p must be positive. Figures 6.1c and 6.1d contains the results using equations 6.19 and 6.20; both have good quality and they are very similar. Actually Figure 6.1c is slightly better than Figure 6.1d, because Figure 6.2 shows that Figure 6.1c has a slightly lower average relative I_p residual than Figure 6.1d. Figure 6.3 shows an I_p profile in Figure 6.1c, where the inverted I_p almost overlaps with the true I_p . In summary, Figures 6.1~6.3 show that the proposed FWI flow inverts an accurate I_p model.

6.7 Extension of the proposed flow into elastic media

The proposed flow can be extended into elastic media. As there are both P- and S-impedances, equation 6.8 becomes

$$\begin{cases} \frac{\delta I_p}{I_{p,a}} = \mu_p v_{p,0} \Re \left[\iint \frac{G_{r,P}(\mathbf{x}, \omega)}{U_{s,P}(\mathbf{x}, \omega)} \cos^2 \theta_{pp} d\omega d\theta_{pp} \right], \\ \frac{\delta I_s}{I_{s,a}} = \mu_s v_{s,0} \Re \left[\iint \frac{G_{r,S}(\mathbf{x}, \omega)}{U_{s,S}(\mathbf{x}, \omega)} \cos^2 \theta_{ss} d\omega d\theta_{ss} \right], \end{cases} \quad (6.21)$$

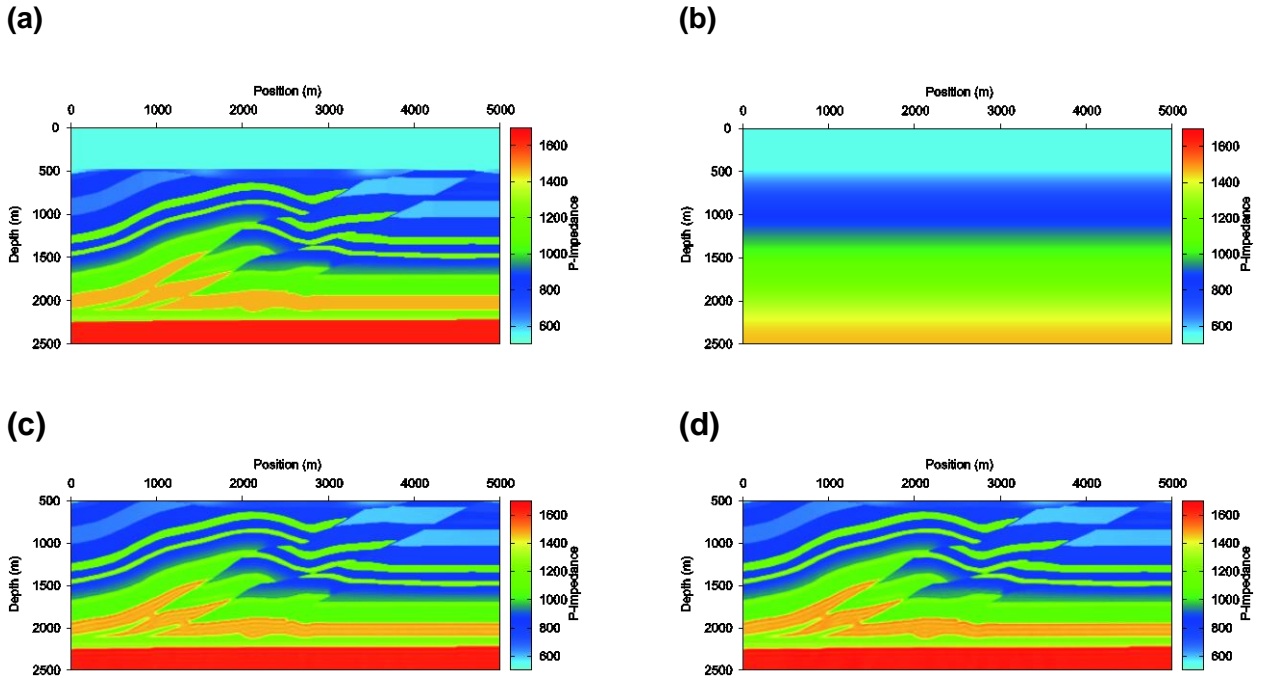


Figure 6.1. (a) and (b) are the true and initial P-impedance models. (c) and (d) are inverted results using equations 6.19 and 6.20, respectively. The unit of P-impedance used in Figures 6.1 and 6.3 is $\text{kg} \cdot \text{cm}^{-2} \cdot \text{s}^{-1}$.

which use PP and SS images. Here the upper-case ‘*P*’ and ‘*S*’ in the subscripts denote P and S waves, respectively. Obtaining V_p , V_s and ρ from I_p and I_s requires rock-physics knowledge. In practice, because the P-wave signal is often more reliable than the S-wave signal, a choice is inverting only the P-impedance and using the rock-physics information to obtain V_p , V_s and ρ for the elastic wave extrapolation, from which we can obtain the decomposed P wave for the phase-modified and deconvolved PP image (using residual data). It is easy to use the P stress tensors to obtain the PP image. If the vector P and S particle-velocities are used, please refer to Tang and McMechan (2018) for obtaining the scalar PP and SS images. Using the rock-physics

relationship to reduce the number of parameters in inversion can also be used in classical FWI frame for inverting the velocity.

6.8 Conclusion

We derive a new formula for full waveform impedance inversion based on the classical reflectivity-to-impedance inversion, which suggests that the impedance update is a phase-modified and deconvolved RTM image obtained using the residual data which is then multiplied by the background velocity and the I_a . To obtain the P-velocity and density for wave extrapolation, we propose to use the rock-physics relationship to obtain them from P-impedance. Because of the complexity of this relationship in practice, we suggest using Machine Learning by establishing a large database and using a fast, dynamic search engine, to support this scheme, in which the number of parameters that needs to be inverted is decreased. Furthermore, we suggest a scheme to stabilize the implementation of the deconvolution imaging condition. The numerical example shows that our method works well for the P-impedance inversion in acoustic media. Extension of the method into elastic media is also given.

6.9 Acknowledgments

The computational resources are provided by Total USA, the Texas Advanced Computing Center (TACC) and the UT Dallas Geophysical Consortium (UTD GC). A research assistantship is provided via the financial support of the Sponsors of the UTD GC.

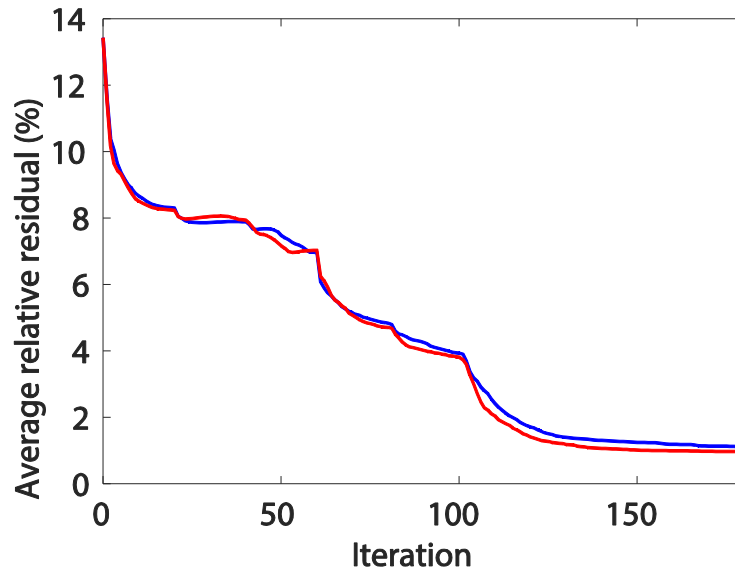


Figure 6.2. Average P-impedance relative residual (shown in percentage) versus iteration number. This relative residual is obtained by averaging $|I_{p,result} - I_{p,true}| / I_{p,true}$ in the global space. The red and blue lines corresponding to Figure 6.1c (using equation 6.19) and Figure 6.1d (using equation 6.20), respectively.

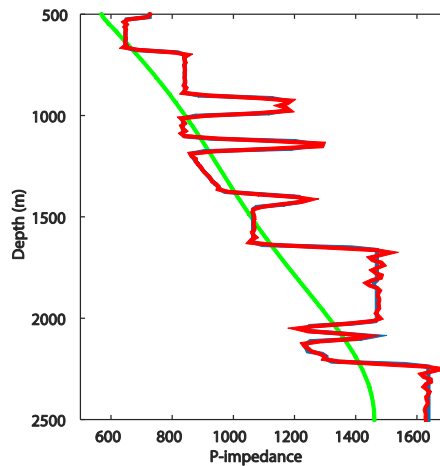


Figure 6.3. P-impedance profile at horizontal locations 2000 m. The blue, green and red lines denote the true, initial and inverted P-impedance (Figure 6.1c).

CHAPTER 7

CONCLUDING REMARKS

7.1 Conclusions

We give three main contributions to the calculation of angle-domain common-image gathers (ADCIGs) from reverse time migration (RTM) in acoustic media. First, we discover a relationship between the slowness vectors in the t - \mathbf{x} domain and the ω - \mathbf{k} domain, which can be connected by the Fourier transform. This discovery explains why the PV in the t - \mathbf{x} domain can give only a single direction per grid point per time step and why the SV in the ω - \mathbf{k} domain can provide multiple directions. Based on this, we propose the multidirectional Poynting vector, which consists of two steps. First, we decompose the wavefield into several vector bins in the ω - \mathbf{k} domain. This spatial FT is for the full space; it cannot give the accurate local propagation directions in a heterogeneous model. Thus, in the second step, we use the PV to calculate the propagation directions of each decomposed wavefield in the t - \mathbf{x} domain. We also prove that the decomposition results of the positive- and negative-frequency wavefields are conjugated. Because we need only the real part of the decomposition result, we only need to apply the approximate WD to the analytic (positive-frequency) wavefield. When the memory is not enough to save the full wavefields in the t - \mathbf{x} domain, we can also use the complex-valued extrapolation of the analytic source wavelet and analytic recorded data to obtain the analytic source and receiver wavefields. An amplitude-preserved tapering scheme in the angle domain has also been given to reduce the Fourier truncation artifacts. A wavefield decomposition plus angle-filter imaging condition is proposed to reduce the backscattering artifacts.

The second contribution of calculating ADCIGs from acoustic RTM is to give a dynamically-correct MPV. The dynamically-correct PV is a product of the reciprocal of the density, the pressure field (PF), and a factor that is obtained by applying both a time integration and a space derivative to the PF. We then combine the dynamically-correct PV with the multidirectional scheme to give a dynamically-correct MPV. A scheme to improve the efficiency of this dynamically-correct MPV is also given; compared to the kinematically-correct MPV, this scheme improves the result without introducing much more computational complexity.

The third contribution is to develop an improved data flow, which separates the calculation of ADCIGs into two parts: one is during the migration and the other one is after the migration. During the migration, we use the time-shift MPV (or the dynamically-correct MPV) to calculate the source-propagation-angle-domain CIGs (SACIGs). After migration, we suggest using an anti-truncation-artifacts Fourier transform to transform SACIGs into ADCIGs in the \mathbf{k} domain. During this process, the normal of each partial reflector image from SACIGs is used.

We also propose an improved data flow to address the three issues of RTM: the P/S wave mode separation, the imaging conditions, and the calculation of ADCIGs. First, we give an improved decoupling system of the P/S wave mode separation, which considers the energy conversion at the reflectors and thus relaxes the assumption of a (locally) constant shear modulus. Second, we propose improved imaging conditions based on multidirectional vectors. These imaging conditions can give the correct polarity for the PP and SS images with open angles beyond 90° and can also correct the polarity change at normal incidence of the PS and SP images without knowledge of the reflector normal. In numerical tests, we use this flow to produce PP

and PS images, and they have high quality. For the ADCIG calculation, we propose two schemes to calculate the multidirectional propagation vectors. The first one is based on a natural extension of the MPV from acoustic media to elastic media. To decrease the cost, we suggest decomposing only the P/S particle velocities and then inserting the decomposed P/S particle velocities into the decoupling system to obtain the corresponding decomposed P/S stress tensor. The second scheme directly uses the approximate WD to transform the particle velocities into multidirectional propagation vectors.

We also make progress in full waveform inversion (FWI). We propose a new FWI scheme that provides a self-contained and physically-intuitive derivation which establishes a natural connection between the amplitude-preserved RTM, the Zoeppritz equations (the AVA inversion) and the reflectivity-to-impedance inversion, and combines them into a single framework to produce a preconditioned inversion formula. This derivation suggests that the relative impedance update is a phase-modified and deconvolved RTM image using the residual data. To obtain the P-velocity and density for wave extrapolation, we propose to use the rock-physics relationship to separate the P-impedance into them. We also suggest using machine learning to address the complexity of this relationship in the real world. When we consider the velocity only, the impedance inversion formula becomes the velocity inversion formula, which provides high-quality inversion results in the examples. The impedance inversion method also has the potential to be extended into elastic media.

7.2 Future work

The future work may involve (but is not limited to) improving the current algorithms in this dissertation (including extending them for use with more complicated media), developing new algorithms for the RTM and FWI in the anisotropic and viscous media, using machine learning to improve the seismic imaging and inversion, and developing algorithms to calculate the true-amplitude, or relative-amplitude-preserved, reflectivity image.

REFERENCES

- Aki, K., and P. Richards, 1980, Quantitative seismology: Theory and methods: W.H. Freeman and Co.
- Alkhalifah, T., 2015, Efficient scattering angle filtering for Full waveform inversion: 85th Annual International Meeting, SEG, Expanded Abstracts, 1138-1142.
- Baysal, E., D. D. Kosloff, and J. W. C. Sherwood, 1983, Reverse time migration: *Geophysics*, **48**, no. 11, 1514-1524.
- Berkhout, A. J., 1985, Seismic migration, imaging of acoustic energy by wave field extrapolation (Third Edition): Elsevier Science Limited, ISBN: 9780444425478.
- Biondi, B., and W. Symes, 2004, Angle-domain common-image gathers for migration velocity analysis by wavefield continuation imaging: *Geophysics*, **69**, no. 5, 1283-1298.
- Böhmer, C. G., 2016, Introduction to General Relativity and Cosmology: World Scientific Publishing Europe Ltd. ISBN: 978-1-78634-117-4.
- Bunks, C., F. M. Saleck, S. Zaleski, and G. Chavent, 1995, Multiscale seismic waveform inversion: *Geophysics*, 60, no. 5, 1457–1473.
- Červený, V., 2001, Seismic ray theory: Cambridge University Press. ISBN: 9780521018227.
- Chattopadhyay S. and G. A. McMechan, 2008, Imaging conditions for prestack reverse-time migration: *Geophysics*, **73**, no. 3, S81-S89.
- Claerbout J. F., 1971, Toward a unified theory of reflector mapping: *Geophysics*, **36**, no. 3, 467-481.
- Chang, W. F., and G. A. McMechan, 1986, Reverse-time migration of offset VSP data using the excitation time imaging condition, *Geophysics*, 51, no. 1, 67-84.
- Clapp, R. G., 2009, Reverse time migration with random boundaries: 79th Annual International Meeting, SEG, Expanded Abstracts, 2809-2813.
- Dellinger, J., and J. Etgen, 1990, Wave-field separation in two-dimensional anisotropic media: *Geophysics*, **55**, 914-919.
- Díaz, E., and P. Sava, 2015, Wavefield tomography using reverse time migration backscattering: *Geophysics*, **80**, no. 1, R57-R69.
- Dickens, T. A., and G. A. Winbow, 2011, RTM angle gathers using Poynting vectors: 81th Annual International Meeting, SEG, Expanded Abstracts, 3109-3113.
- Du, Q., and Y. Zhu, 2012, Polarity reversal correction for elastic reverse time migration: *Geophysics*, **77**, no. 2, S31-S41.
- Du Q., C. Guo, Q. Zhao, X. Gong, C. Wang, and X. Li, 2017, Vector-based elastic reverse time migration based on scalar imaging condition: *Geophysics*, **82**, no. 2, S111-S127.

- Duan, Y., and P. Sava, 2015. Scalar imaging condition for elastic reverse time migration: *Geophysics*, **80**, no. 4, S127-S136.
- Duan, Y., and P. Sava, 2016, Elastic wavefield tomography with physical model constraints, *Geophysics*, **81**, no. 6, R447-R456.
- Dussaud, E., W. W. Symes, P. Williamson, L. Lemaistre, P. Singer, B. Denel, and A. Cherrett, 2008, Computational strategies for reverse-time migration: 78th Annual International Meeting, SEG, Expanded Abstracts, 2267-2771.
- Fomel, S. 2004, Theory of 3-D angle gathers in wave-equation imaging: 74th Annual International Meeting, SEG, Expanded Abstracts, 1053-1056.
- Fomel, S., L. Ying, and X. Song, 2013, Seismic wave extrapolation using lowrank symbol approximation: *Geophysical Prospecting*, **61**, no. 3, 526-536.
- Gardner, G. H. F., L. W. Gardner, and A. R. Gregory, 1974, Formation velocity and density—the diagnostic basics for stratigraphic traps: *Geophysics*, **39**, no. 6, 770-780.
- Gong, T., B. D. Nguyen, and G. A. McMechan, 2016, Polarized wavefield magnitudes with optical flow for elastic angle-domain common-image gathers: *Geophysics*, **81**, no. 4, S239-S251.
- Gray, S. H., and N. Bleistein, 2009, True-amplitude Gaussian-beam migration: *Geophysics*, **74**, no. 2, S11-S23.
- Hager, W. W., and H. Zhang, 2006, A survey of nonlinear conjugate gradient methods: *Pacific Journal of Optimization*, **2**, 35–58.
- Hu, L., and G. A. McMechan, 1987, Wavefield transformations of vertical seismic profiles: *Geophysics*, **52**, no. 3, 307-321.
- Jin, H., G. A. McMechan, and H. Guan, 2014, Comparison of methods for extracting ADCIGs from RTM: *Geophysics*, **79**, no. 3, S89-S103.
- Kaelin B. and A. Guitton, 2006, Imaging condition for reverse time migration: 76th Annual International Meeting, SEG, Expanded Abstracts, S19-S23.
- Komatitsch, D. and R. Martin, 2007, An unsplit convolutional perfectly matched layer improved at grazing incidence for the seismic wave equation: *Geophysics*, **72**, no. 5, SM155-SM167.
- Jiao K., D. Sun, X. Cheng, D. Vigh, 2015, Adjustive full waveform inversion: 85th Annual International Meeting, SEG, Expanded Abstracts, 1091-1095.
- Innanen K. A., 2014, Reconciling seismic AVO and precritical reflection FWI - Analysis of the inverse Hessian: 84th Annual International Meeting, SEG, Expanded Abstracts, 1022-1027.
- Lailly, P., 1983, The seismic inverse problem as a sequence of before stack migrations: Conference on Inverse Scattering, Theory and Application, Society for Industrial and Applied Mathematics, Expanded Abstracts, 206–220.

- Lazaratos, S., I. Chikichev, and K. Wang, 2011, Improving the convergence rate of full wavefield inversion using spectral shaping: 81st Annual International Meeting, SEG, Expanded Abstracts, 2428-2432.
- Lee, S., J. R. Krebs, J. E. Anderson, A. Baumstein, and D. Hinkley, 2010, Subsurface parameter estimation in full wavefield inversion and reverse time migration: 80th Annual International Meeting, SEG, Expanded Abstracts, 1065-1069.
- Liu, F., G. Zhang, S. A. Morton, and J. P. Leveille, 2011, An effective imaging condition for reverse-time migration using wavefield decomposition: *Geophysics*, **76**, no. 1, S29-S39.
- Ma, D., and G. Zhu, 2003, Numerical modeling of P wave and S wave separation in elastic wavefield (In Chinese): *Oil Geophysical Prospecting*, **38**, 482-486.
- Martin G. S., R. Wiley, and K. J. Marfurt, 2006, Marmousi2: An elastic upgrade for Marmousi: *The Leading Edge*, **25**, 156-166.
- Masoni, I., J.-L. Boelle, R. Brossier, and J. Virieux, 2016, Layer stripping FWI for surface waves: 86th Annual International Meeting, SEG, Expanded Abstracts, 1369-1373.
- McGarry R. and Y. Qin, 2013, Direction-vector-based angle gathers from anisotropic elastic RTM: 83rd Annual International Meeting, SEG, Expanded Abstracts, 3820-3824.
- McMechan, G. A., 1983, Migration by extrapolation of time-dependent boundary values: *Geophysical Prospecting*, **31**, no. 3, 413-420.
- Métivier, L., R. Brossier, J. Virieux, and S. Operto, 2012, The truncated Newton method for full waveform inversion: 82nd Annual International Meeting, SEG, Expanded Abstracts, doi: 10.1190/segam2012-0981.1.
- Mora, P., 1989, Inversion = migration + tomography: *Geophysics*, **54**, no. 12, 1575-1586.
- Morse, P. M., and H. Feshbach, 1953, *Methods of theoretical physics*: McGraw-Hill.
- Nemeth, T., C. Wu, and G. T. Schuster, 1999, Least-squares migration of incomplete reflection data: *Geophysics*, **64**, no. 1, 208-221.
- Nocedal, J., 1980, Updating quasi-Newton matrices with limited storage: *Mathematics of Computation*, **35**, 773-782.
- Nguyen, B. D., and G. A. McMechan, 2015, Five ways to avoid storing source wavefield snapshots in 2D elastic prestack reverse time migration: *Geophysics*, **80**, no. 1, S1-S18.
- Oldenburg, D. W., T. Scheuer, and S. Levy, 1983, Recovery of the acoustic impedance from reflection seismograms: *Geophysics*, **48**, no. 10, 1318-1337.
- Peterson, R. A., W. R. Fillipone, and F. B. Coker, 1955, The synthesis of seismograms from well log data: *Geophysics*, **20**, no. 3, 516-538.
- Pica A., J. P. Diet, and A. Tarantola, 1990, Nonlinear inversion of seismic reflection data in a laterally invariant medium. *Geophysics*, **55**, no. 3, 284-292.

- Plessix, R.-E., 2006, A review of the adjoint-state method for computing the gradient of a functional with geophysical applications: *Geophysical Journal International*, **167**, no. 2, 495–503.
- Plessix, R.-E., and Y. Li, 2013, Waveform acoustic impedance inversion with spectral shaping: *Geophysical Journal International*, **195**, no. 1, 1-14.
- Polak, E., and G. Ribière, 1969, Note sur la convergence de méthodes de directions conjuguées: *Revue Française d'Informatique et de Recherche Opérationnelle*, **16**, 35–43.
- Poynting, J. H., 1884, On the Transfer of Energy in the Electromagnetic Field: *Philosophical Transactions of the Royal Society of London*, 175, 343–361.
- Pratt, R. G., C. Shin, and G. Hick, 1998, Gauss-Newton and full Newton methods in frequency-space seismic waveform inversion: *Geophysical Journal International*, **133**, no. 2, 341–362.
- Proakis, J., 1995, *Digital Communications (Third Edition)*: McGraw-Hill Inc, ISBN: 0-07-113814-5.
- Qin, B., T. Allemand, and G. Lambaré, 2015, Full waveform inversion using preserved amplitude reverse time migration: 85th Annual International Meeting, SEG, Expanded Abstracts, 1252-1257.
- Qin, B., and G. Lambaré, 2016, Joint inversion of velocity and density in preserved-amplitude full-waveform inversion: 86th Annual International Meeting, SEG, Expanded Abstracts, 1325-1330.
- Rabben T. K., and B. Ursin, 2011, AVA inversion of the top Utsira Sand reflection at the Sleipner field: *Geophysics*, **76**, no. 3, C53-C63.
- Richardson A. and A. E. Malcolm, 2015, Separating a wavefield by propagation direction: 85th Annual International Meeting, SEG, Expanded Abstracts, 4185-4189.
- Sava, P., and B. Biondi, 2004, Wave-equation migration velocity analysis. I: Theory: *Geophysical Prospecting*, **52**, no. 6, 593–606.
- Sava, P. C., and S. Fomel, 2003. Angle-domain common-image gathers by wavefield continuation methods: *Geophysics*, **68**, no. 3, 1065-1074.
- Sava, P. C., and S. Fomel, 2006, Time-shift imaging condition in seismic migration: *Geophysics*, **71**, no. 6, S209-S217.
- Sava, P. C., and I. Vlad, 2011, Wide-azimuth angle gathers for wave-equation migration: *Geophysics*, **76**, no. 3, S131-S141.
- Shabelansky, A. H., A. Malcolm, and M. Fehler, 2017, Converted-wave seismic imaging: Amplitude-balancing source-independent imaging conditions: *Geophysics*, **82**, no. 2, S99-S109.

- Shen H., S. Mothi, and U. Albertin, 2011, Improving subsalt imaging with illumination based weighting of RTM 3D angle gathers: 81st Annual International Meeting, SEG, Expanded Abstracts, 3206-3211.
- Shen, P., and W. W. Symes, 2008, Automatic velocity analysis via shot profile migration: *Geophysics*, **73**, no. 5, VE49–VE59.
- Shin, C., and Y. H. Cha, 2008, Waveform inversion in the Laplace domain: *Geophysical Journal International*, **173**, no. 3, 922–931.
- Sirgue, L., 2006, The importance of low frequency and large offset in waveform inversion: 68th Annual International Conference and Exhibition, EAGE, Expanded Abstracts, A037.
- Soubaras, R., 2003, Angle gathers for shot-record migration by local harmonic decomposition: 73rd Annual International Meeting, SEG, Expanded Abstracts, 889-892.
- Sun R., J. Chow, and K. J. Chen, 2001, Phase correction in separating P- and S-waves in elastic data: *Geophysics*, **66**, 1515-1518.
- Sun R., and G. A. McMechan, 2001, Scalar reverse-time depth migration of prestack elastic seismic data: *Geophysics*, **66**, 1519-1527.
- Sun, R., G. A. McMechan, and H. Chuang, 2011, Amplitude balancing in separating P and S waves in 2D and 3D elastic seismic data: *Geophysics*, **76**, no. 3, S103-S113.
- Sun, R., and A. Wang, 1999, Scalar reverse-time depth migration of prestack elastic seismic data: 69th Annual International Meeting, SEG, Expanded Abstracts, 1457-1460.
- Suh, S. Y., and J. Cai, 2009, Reverse-time migration by fan filtering plus wavefield decomposition: 79th Annual International Meeting, SEG, Expanded Abstracts, 2804-2808.
- Symes, W. W., 2007, Reverse time migration with optimal checkpointing: *Geophysics*, **72**, no. 5, SM213-SM221.
- Symes, W., and J. Carazzone, 1991, Velocity inversion by differential semblance optimization: *Geophysics*, **56**, no. 5, 654–663.
- Tang C. and G. A. McMechan, 2015a, Time-shift multi-direction slowness vector for computing angle gathers from reverse-time migration—Part I: Multi-direction slowness vector: 85th Annual International Meeting, SEG, Expanded Abstracts, 4360-4364.
- Tang C. and G. A. McMechan, 2015b, Time-shift multi-direction slowness vector for computing angle gathers from reverse-time migration—Part II: Conjugate relation, complex-valued extrapolation, and time shift: 85th Annual International Meeting, SEG, Expanded Abstracts, 4365-4369.
- Tang, C. and G. A. McMechan, 2016. Multidirectional slowness vector for computing angle gathers from reverse time migration: *Geophysics*, **81**, no. 2, S55-S68.
- Tang, C., G. A. McMechan, and D. Wang, 2017a. Two algorithms to stabilize the multidirectional Poynting vector for calculating angle gathers from reverse time migration: *Geophysics*, **82**, no. 2, S129-S141.

- Tang, C. and G. A. McMechan, 2017b, From classical reflectivity-to-velocity inversion to full-waveform inversion using phase-modified and deconvolved reverse time migration images: *Geophysics*, **82**, no. 1, S31-S49.
- Tang C. and G. A. McMechan, 2017c, Combining multidirectional source vector with anti-truncation-artifact Fourier transform to calculate angle gathers from reverse time migration in two steps: *Geophysics*, **82**, no. 5, S359-S376.
- Tang C. and G. A. McMechan, 2017d, From classical reflectivity-to-impedance inversion to full waveform impedance inversion using phase-modified, deconvolved reverse-time-migration image and rock-physics information: 87th International Meeting, SEG, Houston, 1578-1582.
- Tang C. and G. A. McMechan, 2018, Multidirectional-vector-based elastic reverse time migration and angle-domain common-image gathers with approximate wavefield decomposition of P and S waves: *Geophysics*, **83**, no. 1, S57-S79.
- Tang, C. and D. Wang, 2012a, Reverse time migration with source wavefield reconstruction and wavefield decomposition: *Global Geology*, **31**, no. 4, 803-812. (In Chinese)
- Tang, C. and D. Wang, 2012b, Reverse time migration with source wavefield reconstruction in target imaging region: 74th Annual International Conference and Exhibition, EAGE, Extended Abstracts, P272.
- Tang, C., D. Wang, and H. Jiang, 2013a, RTM angle gathers with Gaussian weighted time-lapse Poynting vectors and receiver wavefield reconstruction in forward time direction: 83rd Annual International Meeting, SEG, Expanded Abstracts, 3779-3783.
- Tang, B., S. Xu, and Y. Zhang, 2011, Aliasing in RTM 3D angle gathers: 81st Annual International Meeting, SEG, Expanded Abstracts, 3310-3314.
- Tang, B., S. Xu, and Y. Zhang, 2013b, 3D angle gathers with plane-wave reverse-time migration: *Geophysics*, **78**, no. 2, S117-S123.
- Tang, Y., S. Lee, A. Baumstein, and D. Hinkley, 2013c, Tomographically enhanced full wavefield inversion: 83rd Annual International Meeting, SEG, Expanded Abstracts, 1037-1041.
- Tang, Y., and S. Lee, 2015, Preconditioning full waveform inversion with phase - encoded Hessian. 85th Annual International Meeting, SEG, Expanded Abstracts, 1034-1038.
- Tarantola, A., 1984, Inversion of seismic reflection data in the acoustic approximation: *Geophysics*, **49**, no. 8, 1259-1266.
- Versteeg, R., 1994, The Marmousi experience: Velocity model determination on a synthetic complex data set: *The Leading Edge*, **13**, no. 9, 927-936.
- Virieux, J., 1984, SH-wave propagation in heterogeneous media; velocity-stress finite-difference method: *Geophysics*, **49**, 1933-1957.
- Virieux, J., 1986, P-SV wave propagation in heterogeneous media; velocity-stress finite-difference method: *Geophysics*, **51**, 889-901.

- Virieux, J., and S. Operto, 2009, An overview of full-waveform inversion in exploration geophysics: *Geophysics*, **74**, no. 6, WCC1–WCC26.
- Vyas, M., D. Nichols, and E. Mobley, 2011, Efficient RTM angle gathers using source directions: 81st Annual International Meeting, SEG, Expanded Abstracts, 3104-3108.
- Wang, C., J. Cheng, and B. Arntsen, 2016a, Scalar and vector imaging based on wave mode decoupling for elastic reverse time migration in isotropic and transversely isotropic media: *Geophysics*, **81**, no. 5, S383-S398.
- Wang, W., and G. A. McMechan, 2015, Vector-based elastic reverse time migration: *Geophysics*, **80**, no. 6, S245-S258.
- Wang, W., G. A. McMechan, C. Tang, and F. Xie, 2016b, Up/down and P/S decompositions of elastic wavefields using complex seismic traces with applications to calculating Poynting vectors and angle-domain common-image gathers from reverse time migrations: *Geophysics*, **81**, no. 4, S181-S194.
- Warner M., and L. Guasch, 2014, Adaptive Waveform Inversion: Theory: 84th Annual International Meeting, SEG, Expanded Abstracts, 1089-1093.
- Whitmore, N. D, 1983, Iterative depth migration by backward time propagation: 75th Annual International Meeting, SEG, Expanded Abstracts, 382-385.
- Wu, R., C. Hu, and B. Wang, 2014, Nonlinear sensitivity operator and inverse thin-slab propagator for tomographic waveform inversion: 84th Annual International Meeting, SEG, Expanded Abstracts, 928-933.
- Wu, R., B. Wang, and M. Jakobsen, 2015, Green's function and T-matrix reconstruction using surface data for direct nonlinear inversion: 85th Annual International Meeting, SEG, Expanded Abstracts, 1286-1291.
- Xiao, X., and W. S. Leaney, 2010, Local vertical seismic profiling (VSP) elastic reverse-time migration and migration resolution: Salt-flank imaging with transmitted P-to-S waves: *Geophysics*, **75**, no. 2, S35-S49.
- Xie, X., and R. Wu, 2002, Extracting angle domain information from migrated wavefield: 72nd Annual International Meeting, SEG, Expanded Abstracts, 1360-1363.
- Xie, X., 2015, An angle-domain wavenumber filter for multi-scale full-waveform inversion: 85th Annual International Meeting, SEG, Expanded Abstracts, 1132-1137.
- Xu, S., D. Wang, F. Chen, Y. Zhang, and G. Lambaré, 2012, Full waveform inversion for reflected seismic data: 74th Annual International Conference and Exhibition, EAGE, Extended Abstracts, W024.
- Xu, S., Y. Zhang, and G. Lambaré, 2010, Antileakage Fourier transform for seismic data regularization in higher dimensions: *Geophysics*, **75**, no. 6, WB113-WB120.
- Xu, S., Y. Zhang, D. Pham, and G. Lambaré, 2005, Antileakage Fourier transform for seismic data regularization: *Geophysics*, **70**, no. 4, V87-V95.

- Xu, S., Y. Zhang, and B. Tang, 2011, 3D angle gathers from reverse time migration: *Geophysics*, **76**, no. 2, S77-S92.
- Yan J., and T. A. Dickens, 2016. Reverse time migration angle gathers using Poynting vectors: *Geophysics*, **81**, no. 6, S511-S522.
- Yan, J., and W. Ross, 2013, Improving the stability of angle gather computation using Poynting vectors: 83rd Annual International Meeting, SEG, Expanded Abstracts, Expanded Abstracts, 3784-3788.
- Yan, J., and P. C. Sava, 2008, Isotropic angle-domain elastic reverse-time migration, *Geophysics*, **73**, no. 6, S229-S239.
- Yan, R., and X. Xie, 2012, An angle-domain imaging condition for elastic reverse time migration and its application to angle gather extraction: *Geophysics*, **77**, no. 5, S105-S115.
- Yan, R., H. Guan, X. Xie, and R. Wu, 2014, Acquisition aperture correction in the angle domain toward true-reflection reverse time migration: *Geophysics*, **79**, no. 6, S241-S250.
- Yang, P., J. Gao, and B. Wang, 2015, A graphics processing unit implementation of time-domain full-waveform inversion: *Geophysics*, **80**, no. 3, F31-F39.
- Yang, T., and P. Sava, 2011, Wave-equation migration velocity analysis with time-shift imaging: *Geophysical Prospecting*, **59**, no. 4, 635–650.
- Yao, G., M. Warner, and A. Siverton, 2014, Reflection FWI for both Reflectivity and Background Velocity: 76th Annual International Conference and Exhibition, EAGE, Extended Abstracts, E106.
- Yoon, K., M. Guo, J. Cai, and B. Wang, 2011, 3D RTM angle gathers from source wave propagation direction and dip of reflector: 81st Annual International Meeting, SEG, Expanded Abstracts, 3136-3140.
- Yoon, K., K. J. Marfurt, and W. Starr, 2004, Challenges in reverse-time migration: 74th Annual International Meeting, SEG, Expanded Abstracts, 1057-1060.
- Zhang, J., Z. Tian, and C. Wang, 2007, P and S wave-separated elastic wave-equation numerical modeling using 2D staggered grid: 77th Annual International Meeting, SEG, Expanded Abstracts, 2104-2109.
- Zhang, Q., 2014, RTM angle gathers and Specular Filter (SF) RTM using optical flow: 84th Annual International Meeting, SEG, Expanded Abstracts, 3816-3820.
- Zhang, Q., and G. A. McMechan, 2010, 2D and 3D elastic wavefield vector decomposition in the wavenumber domain for VTI media: *Geophysics*, **75**, no. 3, D13-D26.
- Zhang, Q., and G. A. McMechan, 2011, Direct vector-field method to obtain angle-domain common-image gathers from isotropic acoustic and elastic reverse-time migration: *Geophysics*, **76**, no. 5, WB135–WB149.

- Zhang, S., G. Schuster, and Y. Luo, 2012, Angle-domain migration velocity analysis using wave-equation reflection traveltime inversion: 82nd Annual International Meeting, SEG, Expanded Abstracts, 1-6.
- Zhang, Y., L. Duan, and Y. Xie, 2015, A stable and practical implementation of least-squares reverse time migration: *Geophysics*, **80**, no. 1, V23-V31.
- Zhang, Y., A. Ratcliffe, G. Roberts, and L. Duan, 2014, Amplitude-preserving reverse time migration: From reflectivity to velocity and impedance inversion: *Geophysics*, **79**, no. 6, S271–S283.
- Zhang, Y., and J. Sun, 2009, Practical issues in reverse time migration: true-amplitude gathers, noise removal and harmonic-source encoding: *First Break*, **26**, 29-35.
- Zhang, Y. and G. Zhang, 2009, One-step extrapolation method for reverse time migration: *Geophysics*, **74**, no. 4, A29–A33.
- Zhang, Y., G. Zhang and N. Bleistein, 2005, Theory of true amplitude one-way wave equations and true amplitude common-shot migration: *Geophysics*, **70**, no. 4, E1-10.
- Zhang, Y., G. Zhang, D. Yingst, and J. Sun, 2007, Explicit marching method for reverse-time migration: 77th Annual International Meeting, SEG, Expanded Abstracts, 2300-2304.
- Zhao, L., B. Feng, and H. Wang, 2012, Efficient RTM angle gathers using source propagation direction and reflector normal direction: 82nd Annual International Meeting, SEG, Expanded Abstracts, doi: 10.1190/segam2012-1160.1.
- Zhu, H., 2017, Elastic wavefield separation based on the Helmholtz decomposition: *Geophysics*, **82**, no. 2, S173-S183.
- Zhu, H., and S. Fomel, 2016, Building good starting models for full-waveform inversion using adaptive matching filtering misfit: *Geophysics*, **81**, no. 5, U61-U72.

BIOGRAPHICAL SKETCH

Chen Tang received a Bachelor's degree in Applied Geophysics in 2010 and a Master's degree in Seismic Exploration in 2013, both from Jilin University. Since 2013, he has been a PhD candidate at The University of Texas at Dallas; his supervisor is Professor George A. McMechan, the awardee of 'Maurice Ewing Medal' (2012) and 'Virgil Kauffman Gold Medal' (1997) from SEG. Chen received the 'University Outstanding Graduation Thesis Award' (2010) from Jilin University, the 'Outstanding Student Paper Award' (2012) from the Chinese Geophysical Society, and the first 'National Graduate Scholarship' (2012) from the Chinese Ministry of Education. His research interests include full waveform inversion, reverse time migration and their implementations in a variety of models (acoustic, elastic, anisotropic and attenuating). He is a student member of SEG.

CURRICULUM VITAE

Chen Tang

Ph.D. candidate and Research assistant at The University of Texas at Dallas.

ROC 1.503, 800 W Campbell Rd, Richardson, TX 75080

LinkedIn: <https://www.linkedin.com/in/chen-tang-a8aa6268> .

Resume updated on April 5, 2018.

EDUCATION

- Ph.D. Candidate in Geophysics (Subsurface Imaging), University of Texas at Dallas.
 1. Advisor: George A. McMechan, Ida M. Green Professor at UT Dallas.
 2. Dates of Admission and Expected Graduation: AGU 2013—MAY 2018.
 3. Dissertation: From multidirectional-vector-based seismic reverse time migration to angle-domain common-image gathers to full waveform inversion using phase-modified and deconvolved images in acoustic and elastic media.
- Master in Geo-Exploration and Information Technology (Seismic Exploration); Jilin University; 2010—2013. Thesis: Time-domain reverse time migration and angle gathers construction.
- Bachelor in Exploration Technology and Project (Applied Geophysics); Jilin University; 2006—2010. Thesis: Anisotropic migration in transversely isotropic media.

WORK EXPERIENCES

1. May 15, 2017 – August 15, 2017, ExxonMobil Upstream Research Company.
 - a. Geoscience Intern, Full Waveform Inversion, Seismic Acquisition & Imaging.
 - b. Research Area: Q-Compensated full waveform inversion.

SELECTED ACTIVITIES & VOLUNTEER

1. Reviewer, Geophysics, Society of Exploration Geophysicists (SEG).
2. Reviewer, Geophysical Prospecting, European Association of Geoscientists and Engineers (EAGE).
3. Reviewer, Physics of the Earth and Planetary Interiors.
4. Reviewer, Journal of Geophysics and Engineering.
5. President, SEG Student Chapter at UT Dallas, 2017.
6. Treasurer, SEG Student Chapter at UT Dallas, 2014.

SELECTED AWARDS

1. SEG/Chevron Student Leadership Symposium Travel Grant, Society of Exploration Geophysicists, 2017.
2. SEG/ExxonMobil Student Education Program Travel Grant, Society of Exploration Geophysicists, 2015.
3. SEG Foundation Travel Grant, Society of Exploration Geophysicists, 2014.
4. First “National Graduate Scholarship”, Chinese Ministry of Education, 2012.
5. “Outstanding Student Paper Award”, Chinese Geophysical Society, 2012.
6. “University Outstanding Graduation Thesis Award”, Jilin U., 2010.

RESEARCH INTERESTS

1. Using machine learning (especially neural network) to analyze big seismic data.
2. Wave propagation, imaging and inversion in attenuating or/and anisotropic media.
3. Full waveform inversion.
4. Amplitude-preserved reverse time migration and angle-domain common-image gathers.
5. Ray/beam-based migration and tomography.
6. High performance computing.

FULL LIST OF ARTICLES

1. **Tang C.** and G. A. McMechan, 2018, The dynamically-correct formula of Poynting vector for acoustic media with application in calculating the multidirectional propagation vector to produce angle gathers from reverse time migration: *Geophysics*. (Accepted)
2. **Tang C.** and G. A. McMechan, 2018, Multidirectional-vector-based elastic reverse time migration and angle-domain common-image gathers with approximate wavefield decomposition of P and S waves: *Geophysics*, **83**, no. 1, S57-S79.
3. **Tang C.** and G. A. McMechan, 2017, Combining multidirectional source vector with anti-truncation-artifact Fourier transform to calculate angle gathers from reverse time migration in two steps: *Geophysics*, **82**, no. 5, S359-S376.
4. **Tang C.**, G. A. McMechan, and D. Wang, 2017, Two algorithms to stabilize multidirectional Poynting vectors for calculating angle gathers from reverse time migration: *Geophysics*, **82**, no. 2, S129-S141.
5. **Tang C.** and G. A. McMechan, 2017, From classical reflectivity-to-velocity inversion to full-waveform inversion using phase-modified and deconvolved reverse time migration images: *Geophysics*, **82**, no. 1, S31-S49.
6. Wang W., G. A. McMechan, **C. Tang** and F. Xie, 2016, Up/down and P/S decompositions of elastic wavefields using complex seismic traces with applications to calculating Poynting vectors and ADCIGs from reverse-time migration: *Geophysics*, **81**, no. 4, S181-S194.
7. **Tang C.** and G. A. McMechan, 2016, Multidirectional slowness vector for computing angle

- gathers from reverse time migration: *Geophysics*, **81**, no. 2, S11-S24.
8. **Tang C.** and D. Wang, 2012, Reverse time migration with source wavefield reconstruction and wavefield decomposition: *Global Geology*, **31**, No. 4, 803-812. (In Chinese)
 9. Wang D., Z. Tong, **C. Tang** and H. Zhu, 2010, An iterative curvelet thresholding algorithm for seismic random noise Attenuation: *Applied Geophysics*, **7**, No. 4, 315-324.
 10. **Tang C.** and D. Wang, 2010, An iterative method to solve the vertical wavenumber of phase-shift migration in transversely isotropic media: *Journal of Jilin University (Earth Science Edition)*, **40**, 58-62. (In Chinese)

FULL LIST OF ABSTRACTS AT INTERNATIONAL CONFERENCES

1. **Tang C.** and G. A. McMechan, 2017, From classical reflectivity-to-impedance inversion to full waveform impedance inversion using phase-modified, deconvolved reverse-time-migration image and rock-physics information: 87th International Meeting, **SEG**, Houston, 1578-1582.
2. **Tang C.** and G. A. McMechan, 2017, Multidirectional-vector-based elastic reverse time migration and angle-domain common-image gathers with approximate wavefield decomposition of p and s waves: 87th International Meeting, **SEG**, Houston, 4488-4493.
3. **Tang C.** and G. A. McMechan, 2017, Elastic reverse time migration with an improved system of p/s wave mode separation in nonsmooth models: 87th International Meeting, **SEG**, Houston, 4696-4700.
4. **Tang C.** and G. A. McMechan, 2016, From classical reflectivity-to-velocity inversion to full-waveform inversion using phase-modified and deconvolved reverse-time-migration images: 86th International Meeting, **SEG**, Dallas, 1141-1145.
5. **Tang C.** and G. A. McMechan, 2016, Combining multidirectional-source vector with revised antileakage Fourier transform to calculate angle gathers from reverse time migration in two steps: 86th International Meeting, **SEG**, Dallas, 4378-4382.
6. **Tang C.** and G. A. McMechan, 2016, Two algorithms to stabilize multidirectional Poynting vectors for calculating angle gathers from reverse time migration: 86th International Meeting, **SEG**, Dallas, 4388-4392.
7. **Tang C.** and G. A. McMechan, 2015, Time-shift multidirection slowness vector for computing angle gathers from reverse time migration: Part 1 - Multidirection slowness vector: 85th International Meeting, **SEG**, New Orleans, 4360-4364.
8. **Tang C.** and G. A. McMechan, 2015, Time-shift multidirection slowness vector for computing angle gathers from reverse time migration: Part 2 - Conjugate relation, complex-valued extrapolation, and time shift: 85th International Meeting, **SEG**, New Orleans, 4365-4369.
9. **Tang C.**, 2014, Combining source direction vectors with wavefield decomposition to calculate angle gathers: 84th International Meeting, **SEG**, Denver, 3831-3836.
10. **Tang C.**, D. Wang and H. Jiang, 2013, RTM angle gathers with Gaussian weighted time-lapse Poynting vectors and receiver wavefield reconstruction in forward time direction. 83rd International Meeting, **SEG**, Houston, 3779-3783.
11. **Tang C.** and D. Wang, 2013, RTM Angle Gathers with the Time-lapse Poynting Vector and

- Wavefield Reconstruction: 75th International Conference, **EAGE**, London, We P09 07.
12. **Tang C.**, 2012, Time-lapse Poynting vector for RTM angle gathers: 28th International Meeting, **CGS** (Chinese Geophysical Society), Beijing. (In Chinese)
 13. **Tang C.** and D Wang, 2012, Reverse time migration based on source wavefield reconstruction and wavefield decomposition in target region: 28th International Meeting, **CGS** (Chinese Geophysical Society), Beijing. (In Chinese)
 14. **Tang C.** and D. Wang, 2012, Reverse time migration with source wavefield reconstruction in target imaging region: 74th International Conference, **EAGE**, Copenhagen, P272.

Google Scholar Citations <http://scholar.google.com/citations?hl=en&user=sKQYr58AAAAJ>